Two-Pion Correlation Measurements for 14.6 A·GeV/c ^{28}Si+X and 11.6 A·GeV/c ^{197}Au+Au

by

Ron A. Soltz

B.S., Massachusetts Institute of Technology (1987)
M.A., Columbia University (1989)

Submitted to the Department of Physics
in partial fulfillment of the requirements for the degree of

Doctor of Philosophy

at the

MASSACHUSETTS INSTITUTE OF TECHNOLOGY

May 1994

Author .....
Department of Physics
April 11, 1994

Certified by .....
George S.F. Stephans
Principal Research Scientist, Laboratory for Nuclear Science
Thesis Supervisor

Certified by .....
Wit Busza
Professor, Department of Physics
Thesis Co-supervisor

Accepted by .....
George F. Koster
Chairman, Physics Graduate Committee

Two-Pion Correlation Measurements for 14.6 A· GeV/c ^{28}Si+X and 11.6 A· GeV/c ^{197}Au+Au

by

Ron A. Soltz

Submitted to the Department of Physics
on April 11, 1994, in partial fulfillment of the
requirements for the degree of
Doctor of Philosophy

Abstract

Two-pion correlation functions have been measured in the central rapidity regions (1.5<y<2.0) for 14.6 A · GeV/c Si+Au $\rightarrow 2\pi^-$+X (central and peripheral), Si+Al $\rightarrow 2\pi^+$+X (central and minimum bias), Si+Au $\rightarrow 2\pi^+$+X (central), and 11.6 A · GeV/c Au+Au $\rightarrow 2\pi^-$+X (central) systems. Two-dimensional fits in R-τ and R_T-R_L were performed for these systems for different cuts in the total charged particle multiplicity and forward energy. The R, R_T, and R_L radius parameters for systems involving the Si projectile were found to increase with increasing charged particle multiplicity. These parameters were observed to scale linearly with $A_{pp}^{1/3}$, where A_{pp} is the number of projectile participants as calculated from the forward energy deposition.

The correlation functions were also fit to several three-dimensional functions. In all cases these fits proved to be consistent with the results of the two-dimensional fits. Events generated from the RQMD cascade code indicate that pions within experimental acceptance are produced from a region that is smaller than the entire region of pion production. A direct measure of the RQMD source for pions within the acceptance show qualitative agreement with the observed scaling.

A minimization function was developed which is derived from the Poisson fluctuations in both the actual and background distributions. Progress was made in understanding the errors of event-mixed background distributions. An empirical study confirms that fluctuations within a bin are indeed Poisson for typical backgrounds generated during this analysis.

Thesis Supervisor: George S.F. Stephans
Title: Principal Research Scientist, Laboratory for Nuclear Science

Thesis Co-supervisor: Wit Busza
Title: Professor, Department of Physics

for Susan,

for David,

for my parents

Contents

List of Figures

Chapter 1

Introduction

1.1 Heavy Ion Physics

To study collisions of relativistic heavy ions at AGS energies is to study the physics of complex and little understood systems. We expect heavy ion collisions in this energy regime to compress nuclear matter to densities several times that of normal nuclear matter. The theory of strong interactions, Quantum Chromo-Dynamics (QCD), suggests that at such high densities the hadron-bound quarks may become deconfined, creating a phase transition to a plasma of quarks and gluons [Mül85]. The search for this new state of matter, the quark-gluon plasma (QGP), is the primary motivation for studying these collisions. However, many of the calculations which predict such a phase transition require certain assumptions which are not easily transferred to the case of colliding nuclei. Furthermore, detecting this phase transition in the laboratory is no easy task. If formed, the QGP will eventually hadronize (the quarks will combine into hadrons). This stage of the collision may erase much of the information regarding the existence and nature of the plasma phase. Our aspirations for finding this phase transition rest with the observation of certain signatures which can survive the hadronization stage. Despite the difficulty involved, there is no doubt that the high density systems created in these collisions are truly uncharted territory. Even without QGP formation, there is a great deal to be learned about what occurs during these collisions. The most interesting result may be one which has not been anticipated.

1.1.1 The Holy Grail

The Running Coupling

The belief that heavy ion collisions will produce the quark-gluon plasma comes from the property of QCD known as asymptotic freedom. This refers to the behavior of the running coupling in perturbative QCD, which diminishes at large momentum transfer or short distances. Conversely, at large distances the coupling becomes singular (blows up). This property, known as confinement, restricts the quarks to objects (such as nucleons) which have no net color charge. However, when the coupling becomes large, perturbation theory is no longer valid. This property of QCD is still an area of active research.

If we take normal nuclear matter and compress it and heat it, we expect that eventually the constituent quarks will become deconfined, and the plasma will be created. This is what we are attempting with collisions of heavy ions at the AGS, where the center-of-mass energy per nucleon is 2.7 GeV for a symmetric collision with the Si beam. As will be discussed in the following section, at significantly higher energies, the two colliding nuclei pass through one another. In this case the phase transition would not be brought about through compression of the nuclei, but through heating the vacuum region between the nuclei as they depart the collision zone.

Predicting the Phase Transition

While the behavior of the running coupling from perturbative QCD leads us to believe that very high densities or temperatures will lead to the QGP, perturbative QCD does not lend itself to predicting at what values of the temperature and density a phase transition will occur. A quick estimate can be derived by calculating the thermodynamics of a gas of non-interacting quarks and gluons. The boundary condition is established by setting the pressure equal to the vacuum pressure from the MIT bag model [Mül85]. Incorporating some uncertainty into the true value of the coupling (allowing for some interaction) leads to a critical energy density in the range of 0.5–2 GeV/fm^3. More detailed calculations involving Monte Carlo evaluation of the QCD Lagrangian on a lattice (lattice QCD) yield similar values [JCS86], although these calculations are mainly concerned with the behavior of the gluons. Nevertheless, a collision which increases the energy density of normal nuclear matter ($\sim$0.14 GeV/fm^3) by tenfold easily attains this critical range.

1.1.2 Relativistic Heavy Ion Collisions

Current Experimental Programs

Research on relativistic heavy ion collisions is currently underway at the Brookhaven AGS and CERN SPS accelerators. The AGS began accelerating beams of O and Si at 14.6 $A \cdot GeV/c$ in 1986 and was upgraded to handle Au beams at 11.6 $A \cdot GeV/c$ in the spring of 1992. The SPS began with beams of S at 200 $A \cdot GeV/c$ and will begin accelerating Pb beams in the fall of 1994. Each lab is planning a new colliding facility (RHIC and LHC) which will collide nucleons of 100 $A \cdot GeV/c$ (higher for LHC) in the center of mass frame, and probe a different regime for plasma formation. An extrapolation from p+Pb collisions at 100 GeV suggests that in a central collision the proton will lose on average 2.5 units of rapidity [BG84]. The nucleon-nucleon center of mass rapidities for the AGS Si beams and the SPS S beams are 1.72 and 3.03, respectively. Thus the AGS, and to a lesser extent the SPS offer a unique opportunity to study compressed nuclear matter and the chance to observe QGP formation in the baryon rich regime.

Report from the Field

We now come to the question of how one would detect the formation of the quark-gluon plasma if it were formed. A thorough review of each of the proposed signatures of the QGP is beyond the scope of this thesis. Instead we present a brief synopsis of the present status of some of the initially proposed signatures in Table 1.1. For a complete review of the current situation see [GR93, ESO94]. Clearly, no conclusive evidence for the QGP has yet been seen. However, the story behind these

Signature	Measurement	Reason for Caution
strangeness enhancement	Increase in K/π yield	associated production from multiple collisions can produce same signal
anti-particle enhancement	observed	difficulty separating production and absorption
J/ψ suppression	observed	difficulty separating absorption from suppression
large source/long lifetime	none	

Table 1.1: Present status of some of the QGP signatures.

signatures underscores the need to carefully understand what transpires in heavy ion collisions, even for classes of events which are not likely candidates for producing the QGP. While the search for

the QGP is the primary reason for studying these collisions, it is not the only reason. It would make an interesting historical survey to tabulate the number of truly significant scientific experiments according to those that found what they were looking for, and those that found something else. This is not to say that we should abandon the search for the QGP so that we may improve our chances of finding it! Rather, now that we have created these fantastic events in the laboratory, let us try to understand them before we move on.

1.2 The Source

Bose-Einstein correlations are a natural tool for use in understanding heavy ion collisions, where simple geometric considerations go a long way in explaining many aspects of the data. Specifically, Bose-Einstein correlations between identical pions with low relative momentum provide a measure of their relative separation at the points of their last interaction. It is hoped that this quantity can be simply related to entire region of pion emission. In the event of QGP formation, the hadronization stage will likely be accompanied by a rapid expansion.[1] There are also models in which the hadronization occurs slowly, leading to long lifetimes [Pra86]. Bose-Einstein correlations will be sensitive to either one of these signatures. In the absence of both the QGP and a simple relation between the measured separation of pions and the full extent of the source, the two-pion correlation will at the very least provide valuable constraints for models which purport to accurately describe the collision process.

1.2.1 Bose-Einstein Statistics

There are many ways to demonstrate the way in which Bose-Einstein statistics lead to a momentum correlation for two-particles originating from a finite source. Simply put, the symmetrization of the multi-particle wave function for bosons leads to an enhanced probability that more than one boson will be in the same state. If we consider only two particles, then it is twice as likely that the two particles will be found in the same state. If we localize two single-particle states to a region δx, then there is an enhanced probability that their momentum difference is of the order $\delta p = \hbar/\delta x$. This relation can be set in a more rigorous form by calculating the pair correlation function using second quantized operators. The probability for two particles to have momenta $\mathbf{p}_1$, $\mathbf{p}_2$ can be expressed in

[1] The loss of color degrees of freedom associated with confinement will lead to a decrease in entropy unless the hadronization is accompanied by expansion [Bus94].

terms of the single particle density operators (see Appendix A),

$$\begin{aligned} P(\mathbf{p}_1,\mathbf{p}_2) &= \frac{\langle N|\rho(\mathbf{p}_1)\rho(\mathbf{p}_2)|N\rangle}{\langle N|N\rangle} \\ &= \left\{\int \frac{(2\pi)^3 d\mathbf{x}^3}{V^3}\frac{\langle N|\rho(\mathbf{x})|N\rangle}{\langle N|N\rangle}\right\}^2 \\ &\quad + \left\{\int \frac{(2\pi)^3 d\mathbf{x}^3}{V^3}\frac{\langle N|\rho(\mathbf{x})|N\rangle}{\langle N|N\rangle} e^{i(\mathbf{p}_1-\mathbf{p}_2)\cdot\mathbf{x}}\right\}^2 . \end{aligned} \tag{1.1}$$

The second term in Eq. 1.1 is an interference term, which is the Fourier Transform of the spatial distribution of the two particles where the F.T. is a function of the relative momentum of the two particles. It is important to note that this interference is different from Young's double slit interference. The latter is a result of quantum mechanical interference of the alternate paths of one particle, while the former results from the quantum statistical interference of two particles.[2] Thus, if we can accurately measure the momenta of two particles originating from a collision, then we can relate the relative momentum distribution to a parameterized source distribution and thereby measure the source.

1.2.2 First Observation

HBT

Hanbury Brown and Twiss proposed the first use of two-particle correlations to measure a source size. In this case the particles were photons used to measure the angular diameter of a stellar radio source [BT54]. They later applied this technique to the visual spectrum with a measurement of the angular diameter of Sirius [BT56]. In addition to noting their ground-breaking work, there are several points to be made in reference to this first use of intensity interferometry as it was called at the time. First the effect can be understood solely in terms of classical concepts. A thorough investigation of both classical and quantum aspects can be found in [Zaj82] and [BT57], and will not be presented here. Second, this is not only the first, but also the most faithful use of this technique. All of the effects yet to be discussed which pose problems for the measurement of a collision source with pion pairs are absent for the case of photons radiated from a star. A full account of the application and history of this technique in astronomy can be found in [Bro74].

[2] Vasili Vutsadakis was not the first person to note this, but he explains it rather well in his PhD thesis [Vut92].

GGLP

Goldhaber, Goldhaber, Lee and Pais (GGLP) were the first to use this technique in the context of accelerator collisions [G+60]. They observed that the opening angle distributions of identical pions produced in proton-antiproton annihilations at 1.05 GeV/c disagreed with predictions from a statistical model of pion production [G+59]. Their work is instructive in both the way in which the symmetrization effects were parameterized, and the interpretation given to their results. Rather than attempt to separate out effects of symmetrization as is now commonly done, they instead modified the statistical model to incorporate the Bose-Einstein correlation, and then compared the model prediction to the data for several assumed source sizes. They were somewhat dismayed, however, at the discrepancy between the radius used by the model to match the angular distributions of the pion pairs and the radius needed by the model to accurately reproduce the observed mean pion multiplicities. A statement concerning this would apply equally well to models presently used in heavy ion collisions,

> ... an adequate model should at the same time give a reasonable account of all combined aspects of the annihilation process.

The authors were also wary of the potential effects of the di-pion interaction. In concluding they state that at the very least, the present work shows that the effects of Bose-Einstein symmetrization cannot be neglected in a study of this interaction.

This paper also contains a simpler and more intuitive derivation of the correlation function in terms of the F.T. of the source. Kopylov and co-workers, who were the first to make the connection between the work of HBT and GGLP [Gri71], then gave it a more general context (as well as the picture in Fig. 1-1) .

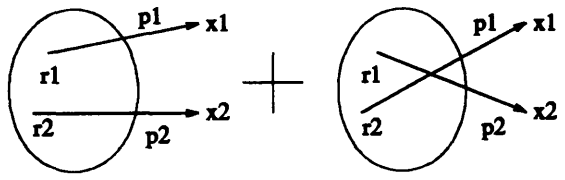

Figure 1-1: Two indistinguishable processes by which two particles are emitted from points $\vec{r}_1$, $\vec{r}_2$ in the source with momentum $\vec{p}_1$, $\vec{p}_2$ that are detected at space points $\vec{x}_1$, $\vec{x}_2$.

We start with the probability of detecting two bosons of momentum p_1, p_2 at the space points x_1, x_2 which have been emitted from points r_1, r_2 in the source. We assume that the particles are

well approximated by plane waves (i.e. no final state interactions). Our inability to distinguish which source point emitted which particle leads to the following symmetrized probability,

$$\begin{aligned} P(p_1,p_2;r_1,r_2) &= \psi(p_1,p_2;r_1,r_2)^*\psi(p_1,p_2;r_1,r_2) \\ &= \{\frac{1}{\sqrt{2}}[e^{ip_1\cdot(x_1-r_1)+ip_2\cdot(x_2-r_2)} + e^{ip_1\cdot(x_1-r_2)+ip_2\cdot(x_2-r_1)}]\}^2 \\ &= 1+\cos(p_2-p_1)\cdot(r_2-r_1) \end{aligned} \tag{1.2}$$

Integrating over the source,

$$\begin{aligned} P(p_1,p_2) &= \int dr_1{}^4 dr_2{}^4 g(r_1,p_1)g(r_2,p_2)[1+\cos(p_2-p_1)\cdot(r_2-r_1)] \\ &\quad \textbf{Assume}: g(r,p)=\rho(r)f(p) \\ &= 1+|\tilde{\rho}(p_2-p_1)|^2. \end{aligned} \tag{1.3}$$

This relation is identical to Eq. A.2 ($\tilde{\rho}$ is the F.T. of the source distribution). In addition to being simpler than the derivation of the pair correlation function in Appendix A, this derivation illustrates another important assumption: that the source distribution can be factored separately into a momentum distribution and a space-time distribution. A source distribution which does not satisfy this condition is said to exhibit dynamical correlations. The effects of these correlations on the two-particle correlation function will be discussed Chapters 2 and 6.

1.2.3 Welcome to the Real World

Defining the Correlation Function

Having established the increased probability of measuring two-particles with momenta $\vec{p}_1$, $\vec{p}_2$ we must now find the appropriate normalization for the data which will allow us to compare to this simple form for the correlation (ie. one plus the square of the F.T. of the source density). One might consider[3] normalizing by the product of the individual single particle distributions,

$$C_2(\vec{p}_1,\vec{p}_2) = \frac{1}{\sigma}\frac{d^6\sigma}{d^3\vec{p}_1 d^3\vec{p}_2}\Big/\frac{d^3\sigma}{d^3\vec{p}_1}\frac{d^3\sigma}{d^3\vec{p}_1}. \tag{1.4}$$

However, this definition does not properly account for the fact that the total two-particle inclusive cross-section integrates over a different set of events than the total one-particle inclusive cross-

[3]If one were a theorist.

section. What we seek instead is a distribution similar in all respects to the measured two-particle distribution but which does not contain the Bose-Einstein effect. There are several different prescriptions for forming such a background or reference distribution; these will be discussed in Ch. 2 and Sec. 4.4.1. The definition of the correlation function in terms of the ratio of the measured *Actual* distribution to the generated *Background* distribution is given by,

$$C_2(\vec{p}_1, \vec{p}_2) = A(\vec{p}_1, \vec{p}_2) \Big/ B(\vec{p}_1, \vec{p}_2) . \tag{1.5}$$

The Choice of Variables

Retaining the assumptions which led to Eq. 1.3, the correlation can be expressed as a function of only the *relative* momentum of the particles. Thus we rewrite Eq. 1.5 as,

$$C_2(\vec{q}) = A(\vec{q}) \Big/ B(\vec{q}) \qquad ; \qquad \vec{q} = \vec{p}_1 - \vec{p}_2. \tag{1.6}$$

This relation can be further developed if our model distribution for the source is separable into different orthogonal components. In that case, we can express the correlation function as a product of separate functions of the canonically conjugate relative momentum components. This is equivalent to saying that each pion pair provides a measure of the source in the direction along the relative momentum vector.[4] A number of different functional forms of the source distribution have been adopted for Bose-Einstein correlation studies. These parameterizations will be presented and discussed at length in both Ch. 2 and Sec. 5.1. We present here instead the definitions of all the relative momentum variables used in this thesis (Table 1.2), along with a clarification of what they are presumed to measure. In this table $\hat{\beta}_{\pi\pi}$ refers to the direction of the pion pair momentum (velocity). The definitions of longitudinal and transverse in Table 1.2 depend upon the variable and the particular analysis at hand. As a general rule Q_L is parallel to the pair momentum, $\vec{q}_L$ is parallel to the beam, and the transverse direction follows from the definition of longitudinal. q_{Tout} is always transverse to the beam, while q_{Tside} is always perpendicular to both the beam and to $\hat{\beta}_{\pi\pi}$.

[4] A non-zero lifetime appears as an elongation of the source along the direction of the total pair momentum, or as an energy difference, depending upon the choice of variable.

Variable	Definition		Measurement
Q	$\sqrt{(\vec{p}_1 - \vec{p}_2)^2 - (E_1 - E_2)^2}$	R_Q,	separation of pions in their co-moving frame
Q_L	$\sqrt{(\vec{p}_{z1} - \vec{p}_{z2})^2 - (E_1 - E_2)^2}$	R_{QL},	longitudinal (along $\hat{\beta}_{\pi\pi}$) separation of pions in their co-moving frame
q	$\lvert\vec{p}_1 - \vec{p}_2\rvert$	R,	assuming spherical symmetry
q_0	$\lvert E_1 - E_2\rvert$	τ,	duration of pion emission
q_L	$\lvert\vec{p}_{z1} - \vec{p}_{z2}\rvert$	R_L,	longitudinal dimension (usually chosen parallel to beam)
q_T	$\sqrt{(\vec{p}_{x1} - \vec{p}_{x2})^2 + (\vec{p}_{y1} - \vec{p}_{y2})^2}$	R_T,	transverse dimension
q_{Tside}	$\lvert\vec{q}_T \times \hat{\beta}_{\pi\pi}\rvert$	R_{Tside},	transverse dimension *without* contribution from lifetime
q_{Tout}	$\lvert\vec{q}_T \cdot \hat{\beta}_{\pi\pi}\rvert$	R_{Tout},	transverse dimension *with* contribution from lifetime

Table 1.2: Definition of Relative Momentum Variables.

Laundry List of Caveats

We now briefly consider other effects which can distort the pure Bose-Einstein relative momentum distribution or otherwise muddle the interpretation of the correlation as the strict Fourier transform of a source distribution. We reserve a thorough discussion of such effects until the next chapter. Table 1.3 contains of list of these effects. Many of them are negligible, but some will require further consideration both in this and future correlation analyses. The aim here is to present the reader with enough reason to be generally suspicious of a correlation analysis so that he will appreciate the need to conduct a careful study of the technique and its application to heavy ion physics.

Effect	Section Reference
Di-pion strong interaction	2.1
Di-pion coulomb repulsion	2.1
Pion-nucleus coulomb interaction	2.1
Coherent pion production	2.1
Two-particle detection inefficiencies	4.3.3, 4.4.2
Resonance Production	2.1
Energy Conservation	4.4.1
Relative Momentum Resolution	3.3.1, 5.6
Multi-particle Correlations	2.2
Dynamical Correlations	6

Table 1.3: Caveats for the application of Bose-Einstein interferometry to heavy ion physics.

1.2.4 Experiment E802

The first two-pion correlation measurement for heavy ion collisions at the AGS was performed by experiment E802 [Mor90, A+92a]. Correlation functions were formed from the inclusive two-pion distributions for pions of both signs produced in the Si+Au and Si+Al systems. The data were compared to fit functions corresponding to Gaussian distributions in space and time,

$$\rho(r,t) \sim \exp\left(-\frac{r^2}{2R^2} - \frac{t^2}{2\tau^2}\right). \tag{1.7}$$

For each system the extracted parameters are consistent within two standard deviations to a radius of 2 fm and a lifetime of 2 fm/c (see contours in Fig. 1-2). The RMS radius for such a distribution is $R_{rms}=\sqrt{3}R=3.5$ fm, which is slightly larger than the R_{rms} charge distribution for the Si projectile (3.04 fm) [PB75, p 99].

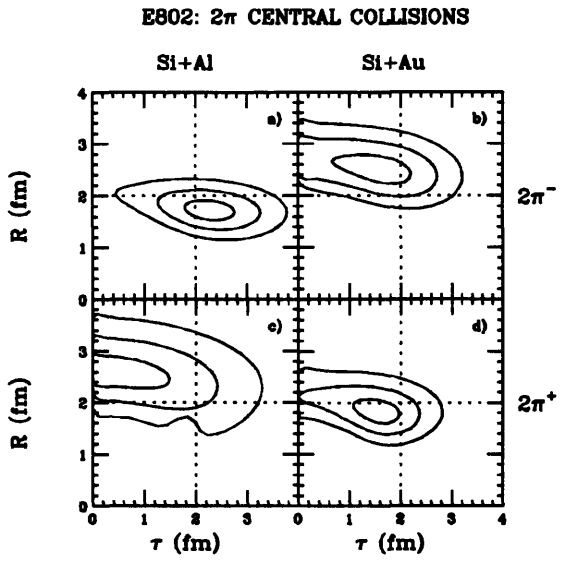

Figure 1-2: E802 Pion correlation results [A+92a]. The contours mark the 1, 2 and 3 sigma confidence limits. The dotted lines correspond to a 2 fm radius and 2 fm/c lifetime.

That the source looks like a Si nucleus fits well with the notion of a pion source which resides within the geometric overlap of the two colliding nuclei. In fact, results from other heavy ion experiments at other energies [Bar86] lend support to this simple picture. However, one must be careful when comparing results between experiments since there are examples of large variations among measurements of identical systems made by different experiments (Sec. 2.2.3). Given the large list of effects which may alter the interpretation of the correlation radius as a true measure of the pion source, we can expect that different experimental acceptances, cuts, and analysis procedures may contribute to this variation. The most useful comparisons are those that can be made between

measurements made by a single experiment, providing a self-consistent check on the interpretation of the Bose-Einstein effect in relativistic heavy ion collisions.

1.2.5 Research Goals

The primary aim of this thesis is to conduct such an investigation by measuring the Bose-Einstein correlation as a function of the centrality of the collision within and between different systems. This study is undertaken partly to enrich our understanding of the technique of Bose-Einstein interferometry, and partly to improve our understanding of the space-time evolution of relativistic heavy ion collisions. Barring some truly extraordinary new physics, we expect the pion source size to decrease for increasing impact parameter. We have no direct measure of the collision impact parameter, and therefore gate on two measured quantities, total charged particle multiplicity and forward energy deposition, which are each related to the impact parameter.

The low multiplicity peripheral collisions also produce fewer pions in the spectrometer. Thus, obtaining an adequate two-pion data set for peripheral collisions is difficult. Experiment E859, with its smart trigger, is capable of preferentially selecting events with two pions in the spectrometer. It is therefore well equipped to make such a measurement. In this thesis we present correlation results for the Si+Au and Si+Al systems as a function of both multiplicity and forward energy of the collision. As an added bonus, we also present a correlation analysis for the Au+Au central system, made by experiment E866. The analysis of these data is guided by three basic questions:

1. Does the source size vary with collision centrality and system?
2. If so, how can this variation best be characterized?
3. What do 1 and 2 above tell us about what Bose-Einstein correlations actually measure and the processes that occur during these collisions?

The next chapter sets the stage for this investigation with a review of theoretical and experimental work in the application of Bose-Einstein correlations to measuring collision sources. This is followed by a description of the experimental apparatus used to collect the data. Chapters 4 and 5 present the analysis and results. To aid in answering the last question we make limited use of the RQMD cascade model. Chapter 6 contains all discussion of this model and its predictions. Conclusions are given in Chapter 7.

Chapter 2

A Brief Review of Bose-Einstein Correlations

Since the work of Goldhaber, Goldhaber, Lee and Pais (GGLP) there have been many other experimental applications of the technique of Bose-Einstein interferometry to study a wide range of accelerator produced collisions, and many theoretical contributions to our understanding of the underlying physical processes involved. Because the research to be presented in this thesis is as much an attempt to learn about the technique as it is a quest to uncover the secrets of heavy ion collisions, a short review of theoretical and experimental contributions is included to provide context. Despite the author's best intentions, the following review is incomplete, and those interested in learning more about the field should consult the published review articles [Boa90, Lor89, Zaj88].

We start with a review of the theoretical contributions, organized by author rather than by topic. Though unusual, this organizational scheme follows the development of the field chronologically, and gives appropriate credit to the principal authors. This is followed by a synopsis of what has been learned from Bose-Einstein correlations between pions from lepton-lepton and lepton-hadron collisions. The application of Bose-Einstein interferometry to e^+e^- annihilations is included partly because this environment is so different from heavy ion collisions, and partly because the development of this field in many ways parallels the more recent developments in heavy ion physics. We then discuss experimental advances made in the study of hadron-hadron collisions which followed the work of GGLP. Finally, the results for different pA and AA systems are reviewed and compared.

2.1 Theoretical Development

Kopylov

As stated in Sec. 1.2.2, Kopylov and co-authors provided the language for the technique of Bose-Einstein interferometry, though it was initially proposed for use in the study of widths of resonances emitted by excited nuclei [Gri71]. The application of the technique to pion production in relativistic heavy ion collisions is first suggested by Kopylov and Podgoretskiĭ [Kop72]. The interference of pions radiated from a spherical shell are considered, yielding a correlation function (one plus the square of the F.T.) of the following form:

$$C_2 = 1 + 2\left[\frac{J_1(q_T R)}{q_T R}\right]^2 \Big/ \left[1 + (q_0 \tau)^2\right] \tag{2.1}$$

Here $\vec{q}_T$ is defined to be transverse to the pion pair velocity, $\vec{\beta}_{\pi\pi}$. In this article the authors provide a rough estimate of the effect of the pion-nucleus Coulomb interaction by taking the ratio of the angular deflection of a pion emitted tangentially from a spherical shell to the opening angle between the pions in the region of interference. For relativistic pions this ratio takes the form,

$$\begin{aligned} \theta/\phi &= Ze^2/(2\hbar c\beta) \\ &\approx Z/240. \end{aligned} \tag{2.2}$$

The dimension parallel to the pair velocity has been neglected under the assumption [KP74a] that there is a long lifetime which masks this component of the source distribution. A later article [KP74b] presents a more general approach and considers the different interference exhibited by coherent and incoherent pion emission. Their contributions are summarized in an article by Kopylov [Kop74], in which the correlation function is formally defined in terms of the ratio of the two-pion relative momentum distribution in which the Bose-Einstein interference is switched on, to a distribution that has the interference switched off. It is suggested that mixing pions from different events is a convenient way to generate the latter distribution. Furthermore, Kopylov suggests making directional cuts in the pair momentum (and thus the relative momentum which is perpendicular) to measure the shape of the collision region.

Koonin

Author of the seminal paper on proton-proton correlations [Koo77], Koonin co-authored a paper with Yano [YK78] which presents an invariant Gaussian source distribution, and the corresponding invariant correlation function (Sec. 5.1.3). In this paper, they demonstrate the relative insensitivity to the lifetime, τ, of the enhancement in $\vec{q}$. They recommend performing cuts in the angle between the relative and total momentum of the pion pair as a means of obtaining information on the lifetime.

Gyulassy

Together with numerous co-authors, Gyulassy has made many contributions to the application of two-particle intensity interferometry to nuclear physics as well as to the field of relativistic heavy ion collisions in general. In [GKW79] the authors note that that it is natural to apply the technique of pion interferometry to such collisions, where classical geometric concepts play a significant role. In this paper a new language is introduced, the density matrix formalism, to accommodate some of the shortcomings of the plane wave treatment of Kopylov. This formalism allows for the inclusion of coherent and chaotic pion production, final state interactions and pion production dynamics. The authors show that pions produced coherently do not exhibit Bose-Einstein interference[1] and suggest that the intercept (λ parameter) can be used to measure the degree of coherent pion production in the source. The Gamow factor [Gam28] is introduced to correct for the Coulomb final state interaction between the pions (Sec. 4.4.2). The π-nucleus Coulomb interaction is treated in a later article [GK81]. Also in a later article [Gyu82] Gyulassy presents two analytic models of dynamical correlations, pion shadowing and coherent jet production, to illustrate how severely the two-pion correlation can be distorted by dynamics.

Pratt

A major advancement in the study of the dynamics was made by Scott Pratt, who re-formulated the two-pion probability density matrix using Wigner functions [Pra84]. The correlation function then becomes,

$$C\left(\vec{p}_1,\vec{p}_2\right) = 1 + \frac{\int d^4x_1 d^4x_2 g\left(x_1,\vec{K}/2\right) g\left(x_2,\vec{K}/2\right) e^{ik\cdot(x_1-x_2)}}{\int d^4x_1 d^4x_2 g\left(x_1,\vec{p}_1\right) g\left(x_2,\vec{p}_2\right)}. \tag{2.3}$$

[1] There will still be a two-particle correlation, however, resulting from the first-order interference [Bus94].

Here $\vec{K} = \vec{p}_1 - \vec{p}_2$, $k = (\vec{p}_1 - \vec{p}_2, E_1 - E_2)$, and $g(x, \vec{p})$ is the probability for emitting a pion at the space-time point x, with momentum $\vec{p}$. The derivation of Eq. 2.3 is contained in the article [Pra84]; a more recent article by Zajc [Zaj93] provides a general introduction to Wigner functions and their use in Bose-Einstein interferometry. In applying this to transport models, the integral in the numerator is replaced by a sum over the phase space points which are the output of the models. The weight term $(e^{ik\cdot(x_1-x_2)})$ is simply the square of symmetrized plane waves of Eq. 1.2. This can be replaced by the square of the wave-functions (Coulomb plus strong interaction). The full procedure developed by Pratt is described in [Pra94] and the code can be delivered upon request over the Internet.

The above prescription is only valid if the source distribution does not violate the uncertainty principle. The momentum range we measure for 14.6 A · GeV/c ^{28}Si+Au collisions extends over roughly 1 GeV/c and the source produced by the RQMD cascade code (Sec. 6.1) extends over several fermi. Thus, the product $\Delta R \Delta P$ is an order of magnitude larger than $\hbar$. However, this test is not enough, we must also be certain that the source distributions do not exhibit substructure (through dynamical correlations) which violate uncertainty. There is no simple way to test for this. Gyulassy [PGG90] recommends smearing the phase space points via Gaussian wave packets. Then, if the correlation function is sensitive to this smearing, it is because the transport model is violating quantum mechanics.

Pratt applies Eq. 2.3 to a rapidly expanding source [Pra84] and arrives at measured source sizes which decrease with increasing pair momentum. This trend has been observed in a number of experiments [B$^+$86, C$^+$93] including E859 [Cia94]. However, this trend can also be understood as higher energy pions escaping from an earlier stage in the collision (smaller π-N cross-section) when the source was smaller. Scott also discusses in detail methods for using pion interferometry to detect the deconfinement phase transition [Pra86]. The central argument in this article is that long lived sources can be detected by comparing the correlation measured along the pair momentum to the correlation measured perpendicular to it (see Sec. 5.1.3 for further discussion regarding this technique).

Bowler

Bowler has calculated the effect of the di-pion strong interaction on the two-pion correlation function for both heavy ion collisions and e^+e^- annihilations [Bow88]. His calculation follows the work of Suzuki [Suz87]: the experimental I=2 s-wave phase shifts are parameterized with a scattering

length. However, rather than evaluating the square of the scattering amplitude at the origin, Bowler integrates the symmetrized wave-functions over an extended exponential source ($\sim$4 fm for heavy ions, $\sim$1 fm for e^+e^-) to arrive at a correlation function modified by the presence of the strong interaction. The reason given for integrating over a finite source for the strong interaction while assuming a point source for the Coulomb interaction is that the short range strong interaction varies considerably over the source whereas the long range Coulomb interaction does not. For heavy ion collisions this treatment of the di-pion strong interaction results in a small reduction in λ with no change in radius. For e^+e^- annihilations the effect is far more significant, causing the correlation function to dip below one just beyond the enhancement. This modified correlation function is shown [Bow88] to adequately describe the TPC data taken at the PEP storage ring [A$^+$85a].

Emboldened by his success[2] with the di-pion strong interaction, Bowler sought to provide a complete picture of pion interferometry in e^+e^- annihilations by incorporating resonance decays as well as the effects of the strong interaction [Bow90]. To accomplish this, these two effects were applied to the pion source distributions of the string model [AH86], with reasonable success in matching the data. The application of the string model to Bose-Einstein correlations in e^+e^- annihilations is discussed further in Sec. 2.2.1.

2.2 Review of the Data

The review of the data begins with a few examples from lepton-lepton and lepton-hadron collisions which are relevant to the present situation in relativistic heavy ion collisions. Then we proceed to discuss some of the advances that have been made in the field through the study of hadron-hadron collisions. We pay particular attention to evidence for multiplicity dependence in the radius parameters. This is followed by a chronological survey of nucleus-nucleus collisions. Again, we are primarily concerned with reporting what has been learned from attempts to gate on different impact parameters using multiplicity and forward energy cuts.

There are two topics which have been investigated in the literature that are not covered in the following review: shape analysis and multi-particle correlations — both topics are beyond the scope of the analysis for this thesis. Sec. 5.1 discusses some of the complications for performing such an analysis with the E859 data. Calculations of the effects of higher-order correlations have been performed by Zajc [Zaj78] and Pratt [Pra93]. Many experiments have formed a three-particle

[2]Some poetic license has been taken here to keep the reader entertained.

correlation function to search for these effects. To date, all such three-particle analyses have been consistent with the observed two-particle effects.

2.2.1 Bose-Einstein Correlations in e^+e^- Annihilations.

It is worth noting that the GGLP effect was first observed in e^+e^- annihilations by the MARK II collaboration and reported by Goldhaber [Gol82, J+89]. Since then, Bose-Einstein correlations have been observed in jet events by many different experiments stationed at many different accelerator facilities. These measurements all have in common that they are measuring the interference of pions produced from a string fragment. The study of this process through pion interferometry has led to two significant results which are relevant to the present study of heavy ion collisions. These are the determination of the appropriate parameterization for the correlation functions, and the success that has been achieved in using models to reproduce the features of the data.

The Right Variable

Most e^+e^- and lepton-hadron experiments have chosen to parameterize the correlation function with the variables Q_{inv} and Q_L (see Table 1.2) where the longitudinal axis is defined to be parallel to the pion pair momentum. These choices contrast with the Kopylov (Eq. 2.1) and Gaussian (Eq. 1.7) source parameterizations used for heavy ion physics. Correlation functions in Q_{inv} and Q_L are invariant (Q_L is invariant to boosts along the pair momentum) and measure the extent of the source in the rest frame of the pion pair (see Sec. 5.1.1 for further discussion). It is for this reason that Q_{inv} (Q_L) is both appropriate for the study of string fragmentation and inappropriate for the study of heavy ion collisions.[3] While the heavy ion community has been slowly convinced of the truth of this statement, the correctness of the invariant parameterizations for string fragmentation has been directly observed in the data!

The TASSO Collaboration [A+86] (e^+e^- with $\sqrt{s}$=34 GeV) fit their data to Eq. 2.1 (with additional terms to account for the high-q rise seen in e^+e^- annihilations). The best fits to the data were for values of r^2 that were negative. This prompted them to fit to the following functional form,

$$C_2(q, q_0) = N\left(1 + \delta q^2 + \epsilon q_0^2\right)\left[1 + \lambda e^{-q^2R^2 + q_0^2t^2}\right]. \tag{2.4}$$

Fits to this function produced values of t^2 that were positive and approximately equal in magnitude

[3] If one is comparing to data to models, then any parameterization will do.

to R^2. In other words, when given additional degrees of freedom, the fits converge to values which are consistent with a Q_{inv} parameterization.

This observation is not limited to Bose-Einstein correlations in e^+e^- annihilation. Experiment E665 has also performed such an analysis for μ-nucleon collisions at 490 GeV and reached similar conclusions. Fig. 2-1a shows the enhancement in q^2 and q_0^2 for these data. The function plotted is the correlation function (here defined to be $R(q^2, q_0^2)$) minus one. The lengths of the sides of the boxes are proportional to the value of the function, R-1, and the negative values are suppressed. The data demonstrate a clear enhancement along the diagonal, consistent with an enhancement in Q_{inv}.[4] This feature of Fig. 2-1a is to be contrasted to the distribution shown to the right (Fig. 2-1b) for the central Si+Au $\rightarrow 2\pi^-$ system measured by experiment E859. Here the sides of the boxes plotted are proportional to log $(R(q, q_0) - 1)$. The enhancement exists for small values of q *and* q_0 only, as one would expect for a source that is Gaussian in space and time, always in the same reference frame.

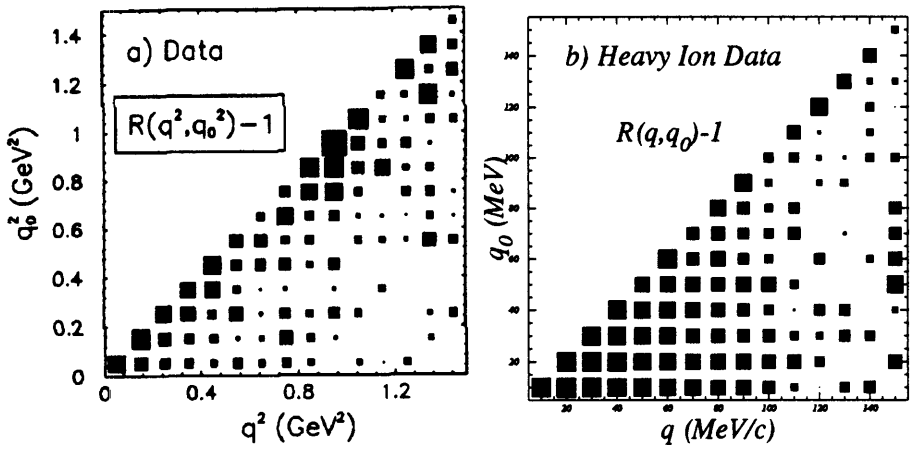

Figure 2-1: Comparison of Bose-Einstein enhancement in e^+e^- annihilations [A+93a] vs. heavy ion collisions. See text for details.

Lessons from the Models

That production of pions occurs in a local frame is readily understood in terms of the Lund string model [AH86] (and references therein), where hadronization of the string occurs over the proper

[4]Note that the enhancement along the diagonal is not enough, by itself, to indicate that the correlation is a function of Q_{inv}. Similar behavior would be seen for a Kopylov source for which the variables are calculated far from the rest frame (see Fig. 5-10).

time, $\tau = t^2 - x^2$. The Bose-Einstein interference effects are incorporated into the string model through a sum over possible histories of identical particle production [AH86]. A discussion of this process is well beyond the scope of this review. However, we note that Bowler achieves a similar result by taking the Fourier Transform of the spatial distribution for particle production from the string.

The string model predicts an elongation of the source along the jet axis and a increase in the source with $\sqrt{s}$. Both TASSO [A+86] and the MARK II experiment [J+89] have measured a spherical source, and so far the Bose-Einstein radius seems to be independent of energy [A+91]. The similarity to the present situation in heavy ion physics is in the strong dynamical correlations between particle production points and momenta. Andersson and Hofmann [AH86] point out that the length scale for Bose-Einstein correlations is not the entire region of hadronization, but a length scale over which two pions with low relative momentum are likely to be produced. Thus far string model predictions for Bose-Einstein correlations show good, but not perfect agreement with the data [Bow91]. Yet, there are those who are not comfortable with a picture that calls for Bose-Einstein interference to occur over only a part of the string. Osborne [Osb88] presents an alternate approach which preserves uncertainty in the spatial location of the string break. This "excited quark" model preserves the elongation of the source along the jet axis that is destroyed by dynamical correlations in the Lund model.

This point will certainly be resolved by the data sometime in the future, and is not of particular relevance to the analysis of heavy ion collisions which is to follow. In e^+e^- annihilations (and other jet events) we are learning about the process of hadronization on a string, and thus attempts to understand Bose-Einstein correlations in this environment are bound to a particular model of hadronization. In heavy ion physics we are just now reaching a point where the models have matured, and we have available statistics in the data to permit detailed comparisons between the two. If we find that the dynamical correlations are weak and do not change our analysis, then so be it. Otherwise, we can at least revel in the fact that we are not alone.

2.2.2 Bose-Einstein Correlations in Hadron-Hadron Collisions

High statistics measurements of the correlation function for pions from hadronic collisions provided the test-bed for refining the application of the formalism developed by Kopylov. The large data sets produced in pp and $\bar{p}p$ collisions enabled one to make systematic studies of the energy and multiplicity dependence of the fit parameters, and to search for directional dependence as well. We

do not present any numbers for the radii measured by these experiments, most of the radii measured are consistent with a Gaussian radius of 0.8 to 1.0 fm.

Deutschmann *et al.* [D$^+$82] were the first to acquire enough statistics to show that the correlation functions (in this case for the systems π^+K, K$^-$p, and $\bar{\text{p}}$p) do not approach a value of 2 in the $q \rightarrow 0$ limit. To account for this empirical observation they introduced the parameter λ,

$$C_2 = N\left[1 + \lambda \frac{2\left(J_1(q_T R)/(q_T R)\right)^2}{1 + (q_0 \tau)^2}\right] \tag{2.5}$$

This group also performed a study of three different background distributions:

1. Unlike — the distribution of unlike-sign pions.

2. Shuffled — the distribution of unlike-sign pions with the transverse components switched at random.

3. Mixed — the distribution of like-sign pions taken from different events.

Fits to the functional form of Eq. 2.5 gave consistent results when the second and third distributions were used, while the radii for the first background were consistently higher for all three systems, despite attempts to mitigate the contribution of resonance decays by restricting the region of the fit.

The Axial Field Spectrometer Collaboration has measured the two-pion correlation for pp, $\bar{\text{p}}$p ($\sqrt{s}$=53,63 GeV) and $\alpha\alpha$ ($\sqrt{s}$=126 GeV) systems [A$^+$83, A$^+$87b, A$^+$87a]. For all systems the parameters R and τ from Eq. 2.5 were observed to increase with increasing the charged particle multiplicity of the event. The authors perform directional cuts in the angle between the relative momentum vector and the beam axis to find a steady increase in the radius of the pp and $\bar{\text{p}}$p systems as this angle approaches zero [A$^+$87a]. The authors note that this contrasts with the work of De Marzo *et al.* [M$^+$84] who determine the pp source ($\sqrt{s}$=19.4) to be oblate, using a different set of angle cuts.

The UA1 Collaboration has demonstrated the independence of the radius parameters (fit to Eq. 2.5 without the τ dependence and to Eq. 2.6) by taking two-pion data during a ramping run at the SPS $\bar{\text{p}}$p collider.

$$C_2(q_T) = N\left[1 + \lambda e^{-q_T^2 R_T^2}\right]. \tag{2.6}$$

The data sets span $\sqrt{s}$=200 to 900 GeV [A$^+$89]. R_T increases and λ decreases with increasing charged particle density ($\delta n/\delta\eta$). The decrease in λ is consistent with the increase in τ seen by the

AFS Collaboration. For a narrow range in $\delta n/\delta\eta$ both R_T and τ are constant across the entire range of beam energies.

Experiment Na23 [B$^+$89a] measured the one-dimensional correlation function of Q_{inv} for pp ($\sqrt{s}$=36 GeV) and found no multiplicity dependence. However, aside from the different variable used, the lower beam energies do not provide the same range in multiplicity available to the UA1 and AFS Collaborations.

More recently experiment E735 has measured the two-pion correlation for $\bar{p}p$ collisions at the Tevatron ($\sqrt{s}$=1.8 TeV). Rather than performing a two-dimension form, they fit to separate slices in q_T and q_0,

$$\begin{aligned} C_2(q_T) &= N\left(1+\lambda e^{-q_T^2 R_T^2}\right) && ; q_0 < 200\text{MeV} \\ C_2(q_0) &= N\left(1+\lambda e^{-q_0^2 \tau^2}\right) && ; q_T < 200\text{MeV}. \end{aligned}$$

Both the radius and lifetime increase with increasing charged particle density while both λ parameters decrease, even when corrected (through Monte Carlo) for the effects of averaging over the other dimension.

2.2.3 Bose-Einstein Correlations for Collisions Involving Nuclei

As stated, the review of nucleus-nucleus data is organized chronologically. We pay attention to both the refinement of the correlation analysis and progress in studying impact parameter dependence of the radius parameters. Where possible, comparisons are made between the results of different experiments that have studied the same systems.

pA

De Marzo *et al.* measured the two-pion correlation function for proton and antiproton beams at 200 GeV on H and Xe targets [M$^+$84] . It is interesting to note that one of the motivations for this study was to search for the deconfinement phase transition! All measured radii are roughly equal to 0.9 fm. The authors do not see a difference in the pXe radii when the events are restricted to a charged particle multiplicity of 20 or greater. However, such a result is obviously less significant than experiments which compare radii from non-overlapping ranges in multiplicity.

AA

The first observation of the two-pion correlation were made for 1.8 A·GeV Ar+BaI_2 and Ar+Pb_3O_4 systems by Fung *et al.* [F+78] at the LBL Bevalac streamer chamber. The enhancement at low-q is unmistakable, however the results are intended primarily to stimulate further work: the statistics are limited, no Coulomb corrections are applied, and the τ parameter is fixed in two of the three fits. This initial work is followed by a trilogy of Rapid Communications by Beavis *et al.* [B+83b, B+83a, B+86]. These papers study the Ar+KCl and Ar+Pb systems. The second of these obtained enough statistics to permit a fit of τ (see Table 2.2 for parameters) for a two-dimensional Gaussian parameterization. The final article contains the first notable observation of multiplicity dependence of the source parameters. Radius parameters for a one-dimensional Gaussian are measured for three bins in negative pion multiplicity (Table 2.1).[5] The Gamow correction has been applied to these data. All radii are barely consistent with a radius of 3.50 fm to within two standard deviations for these one-dimensional fits. Nevertheless, the trend is clear and expected. The authors also observe a decrease in the radius with increasing pair momentum (at about the same level of statistical significance as the multiplicity dependence).

$N_{\pi-}$	R	λ
2–7	2.54±0.50	0.56±0.21
8–10	3.61±0.42	1.04±0.24
11–20	4.22±0.36	1.01±0.18

Table 2.1: Multiplicity dependence of parameters.

Systems of Ar+KCl and Ne+NaF at incident beam energy of 1.8 A·GeV were analyzed by Zajc *et al.* [Zaj82, Z+84]. This work introduces to the field a number of significant refinements to the technique of measuring source sizes through Bose-Einstein correlations. In particular Zajc notes the existence of, and presents a procedure for removing the residual correlations introduced into the background through event mixing (Sec. 4.4.1 and [Cia94]). He also presents the first study of the statistics of event-mixed backgrounds (Appendix C). Both Gamow (π-π) and π-N Coulomb corrections are successively applied to the correlation functions. The parameters for the $2\pi^-$ correlations for the Ar+KCl system are given in Table 2.2 along with the results from the streamer chamber [B+83a]. The results of Zajc are shown with only the Gamow correction to be

[5] The value of R has been divided by $\sqrt{2}$ to match the standard form $C_2(q) = 1 + \lambda e^{-q^2R^2}$.

more consistent with the Gamow corrected streamer chamber results. Also, there are fundamental differences between the data sets of the two experiments; these differences are given[6] in the table. We present this comparison to illustrate the difficulty in relating measurements made by different experiments. Nevertheless, the parameters from the two measurements are consistent to within the sum their errors.

Experiment	Acceptance	Beam Energy	Trigger	λ	R	τ
Janus Spectrometer	-5<y<0	1.2 A·GeV	min. bias	0.63±0.04	$2.04^{+0.4}_{-0.6}$	$2.33^{+1.0}_{-1.1}$
Streamer Chamber	4π	1.8 A·GeV	30% central	0.74±0.17	2.69±0.4	3.8±1.27

Table 2.2: Comparison of two $2\pi^-$ measurements for Ar+KCl system.

A measurement of the Fe+Fe system (1.7 A · GeV) was made by Chacon *et al.* using the same spectrometer [C+88]. Using a fit to a three-dimensional Gaussian in R_T, R_L, and τ (transverse and longitudinal components are defined relative to the beam axis) they determine the source to be oblate for both forward and central rapidity regions. This paper also presents fit parameters for correlation functions generated from a cascade model. The agreement between model and data is rough at best; the authors discuss some possible sources of dynamics which may be responsible and call for more careful study.

At about this time, Bartke published a compilation of most of the world's Bose-Einstein results for nucleus-nucleus collisions [Bar86]. The thrust of this paper is reproduced in Fig. 2-2, which shows the equivalent RMS radii plotted vs. the atomic number of the projectile raised to the 1/3 power.[7] We have not distinguished between minimum bias and centrally triggered data since this distinction is arbitrary unless more details about the experiment are also known. The dotted line shows the scaling of the *effective* nuclear radius ($R_I = 1.2A_p^{1/3}$), determined from fits to the interaction cross-section for various combinations of projectiles and targets [Tan85]. The rough agreement between the data and this simple scaling law illustrate the expected trend one would get from a simple geometric picture. However, there a few points worth noting:

1. The plot combines central and minimum bias data. However, as will be demonstrated for experiment E859, in most cases there is a strong bias towards central events when the condition of detecting two identical pions is imposed.

2. This scaling indicates that the measured radii are *larger* than the projectile. The plot compares

[6]Minimum bias for two-pion data in the Janus Spectrometer is roughly equivalent to a 6% central [Zaj82, pp 96-100].
[7]Note that for all systems the target is larger than the projectile.

RMS radii of the collisions to the interaction radius of the projectile. The equivalent RMS scaling of nuclear sizes is $R_{RMS} = 0.82A^{1/3} + 0.58$ fm [PB75, p 100].

3. The measurements of pp collisions made by the AFS Collaboration would fall slightly below the scaling line. These results were not included due to the limited acceptance of this experiment, however this selection criteria is not applied to the data from heavy ion collisions.

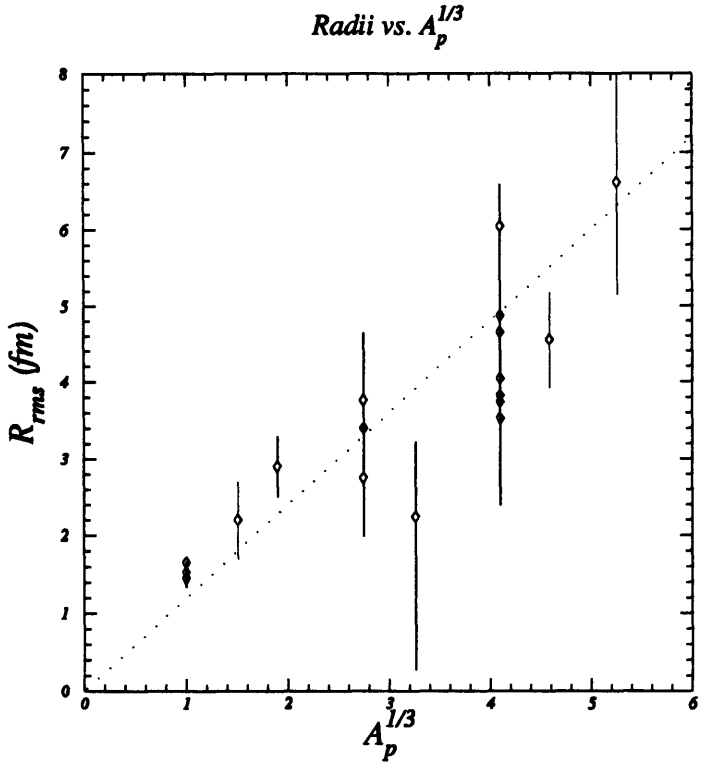

Figure 2-2: RMS radii vs. $A_p^{(1/3)}$. Reproduced from [Bar86].

Following these initial measurements and the compilation by Bartke, many experiments continued measurements at the Bevalac with heavier systems. Bock *et al.* has measured the radius for Au+Au and Nb+Nb with 650 A·MeV incident beam energy. They report [B$^+$89c] a Gaussian radius parameter 3.4±0.4 fm. The authors report two-dimensional fits results (R and τ) from a different publication in which they also claim evidence for radii that are independent of multiplicity [B$^+$88].

Bossy *et al.* searched for a centrality dependence in La+La collisions (1.26 AEGeV) [B$^+$93] and found none. Here the centrality of the collisions is defined by a scintillator array placed downstream to detect forward charged particles. However, the inverse relationship between centrality and forward multiplicity was established from a Monte Carlo GEANT simulation, and only existed

when the additional requirement of having two like-sign pions in the spectrometer was imposed. It may be that this condition dominates the small variation provided by the multiplicity cuts (see previous footnote regarding analysis by Zajc).

The two-pion correlation function for the 1.2 A · GeV La+La system was also measured using the HISS spectrometer (Christie *et al.* [C+93]) along with 1.8 A · GeV Ar+KCl/La and 1.2 A · GeV Xe+La systems [C+92]. The correlation functions in these papers are corrected for close-pair detection inefficiencies and the π-π Coulomb interaction (Gamow). For the Ar+KCl and La+La systems the centrality dependence was investigated by cutting on the energy deposited in a forward TOF scintillator. The Gaussian fit parameters, shown in Table 2.3 are suggestive, but not conclusive. For each system the lifetime is fit to or consistent with zero — this and the anti-correlation between R and τ may be the reason that the central (peripheral also) Ar+KCl radius given here is larger than both the values given in Table 2.2 above.

System	TOF ADC cut	λ	R	τ
Ar+KCl	Peripheral	0.68±0.14	3.04±0.34	0.0±2.0
	Central	0.70±0.15	3.42±0.34	0.0±2.0
La+La	Peripheral	0.62±0.10	3.57±0.35	$1.1^{+1.8}_{-1.1}$
	Central	0.83±0.09	4.68±0.28	0.0±2.3

Table 2.3: Fit parameters for different cuts in forward energy.

Recently Bose-Einstein correlations have been measured at much higher energies (incident beams of 14.6 A · GeV/c at the BNL AGS and 200 A · GeV at the CERN SPS). As mentioned, The E802 collaboration has measured 14.6 A · GeV/c Si+Al/Au systems [Mor90, A+92a], and (as E859) has measured the two-kaon correlation [A+93b, Cia94, Vos94]. NA44 has also measured both the two-kaon and two-pion correlation for 200 A · GeV Si+Pb and 450 A · GeV p+Pb and compared these measurements with what has been seen by E859 [Hum94]. NA35 has studied the rapidity and p_T dependence for Si+S/Ag/Au [R+94], and WA80 has investigated the variation of two-pion correlation measured in the target rapidity for several targets using beams of ^{16}O at 200 A · GeV/c. All of the heavy ion experiments have begun comparing the data to cascade codes and have presented their results in the most recent Quark Matter Conference Proceedings: E859 [V+94], NA44[S+93, S+94], NA35[R+94], WA80[P+94], and E814 [X+94].

The only study of centrality dependence at high energy was done by Morse [Mor92] using the NA35 data. The cuts were made in the energy deposited in a forward (veto) calorimeter; statistics only permitted a fit to the one-dimensional Gaussian in Q_{inv}. Fig. 2-3 shows the veto calorimeter

energy spectrum for minimum bias events, and the radius parameters fit to data sets for two cuts on calorimeter energy. The variation in the radii follow the expected trend.

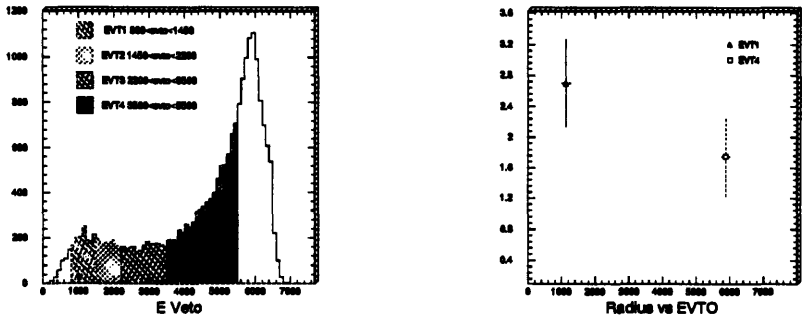

Figure 2-3: NA35 dependence of R_Q on forward energy [Mor92].

Given the simple projectile scaling observed early on in the study of Bose-Einstein correlations in nucleus-nucleus collisions, it is surprising that conclusive evidence for a centrality dependence has not been observed. The most dramatic variation was obtained by Beavis *et al.* [B$^+$86]. However, these data are fit with τ fixed at zero, the errors on R and λ are large by present standards, and the correlation functions for the data sets cut on multiplicity are not shown. Later studies have all been consistent with no variation, despite the fact that most of the results exhibit the expected trend.

Chapter 3

Experimental Overview

3.1 Experiment History

3.1.1 The AGS Accelerator

The Alternating Gradient Synchrotron (AGS) at Brookhaven (see Fig. 3-1) has been accelerating high energy protons at 30 GeV/c since 1970. With the addition of a 680 m Heavy Ion Transfer Line (HITL) connecting it to the three-stage tandem Van de Graaff accelerator, it has been used to accelerate ^{16}O and ^{28}Si ions to 14.6 A · GeV/c for relativistic heavy ion collisions since 1986. In 1992, the HITL was extended to reach the newly constructed AGS booster facility. With the booster, ions as heavy as Au can be accelerated in the AGS. The acceleration process described below is adapted from an article by Thieberger *et al.* [T+88].

The acceleration of ^{28}Si ions begins with pulsed Cs^- ions striking a silicon sputter target at one end of the MP6 injector, held at -8 MV potential (see Fig. 3-2). The emerging Si^- ions reach 0.78 A · MeV/c at ground and then enter the MP7 two-stage tandem. Here a series of two carbon stripping foils placed at the 14.8 MV potential and one quarter of the way back to ground, respectively, strip all but two electrons with 25% efficiency. The Si^{+12} ions, now at 6.6 A · MeV/c, are fully stripped (50% efficiency) within the HITL and transferred to the AGS. Once in the AGS, the 300 μsec pulses are stacked nine deep and then accelerated by two RF systems. The first RF system accelerates the beam up to the 200 A · MeV/c proton injection energy and then hands-off to the second, which provides the remaining beam energy. The maximum beam energy is a function of the charge to mass ratio. Thus, the 30 GeV synchrotron can accommodate $\sim$ 15 A · GeV/c beams of ^{28}Si and $\sim$ 12 A · GeV/c beams of ^{197}Au. The mass of the ion species is limited by the

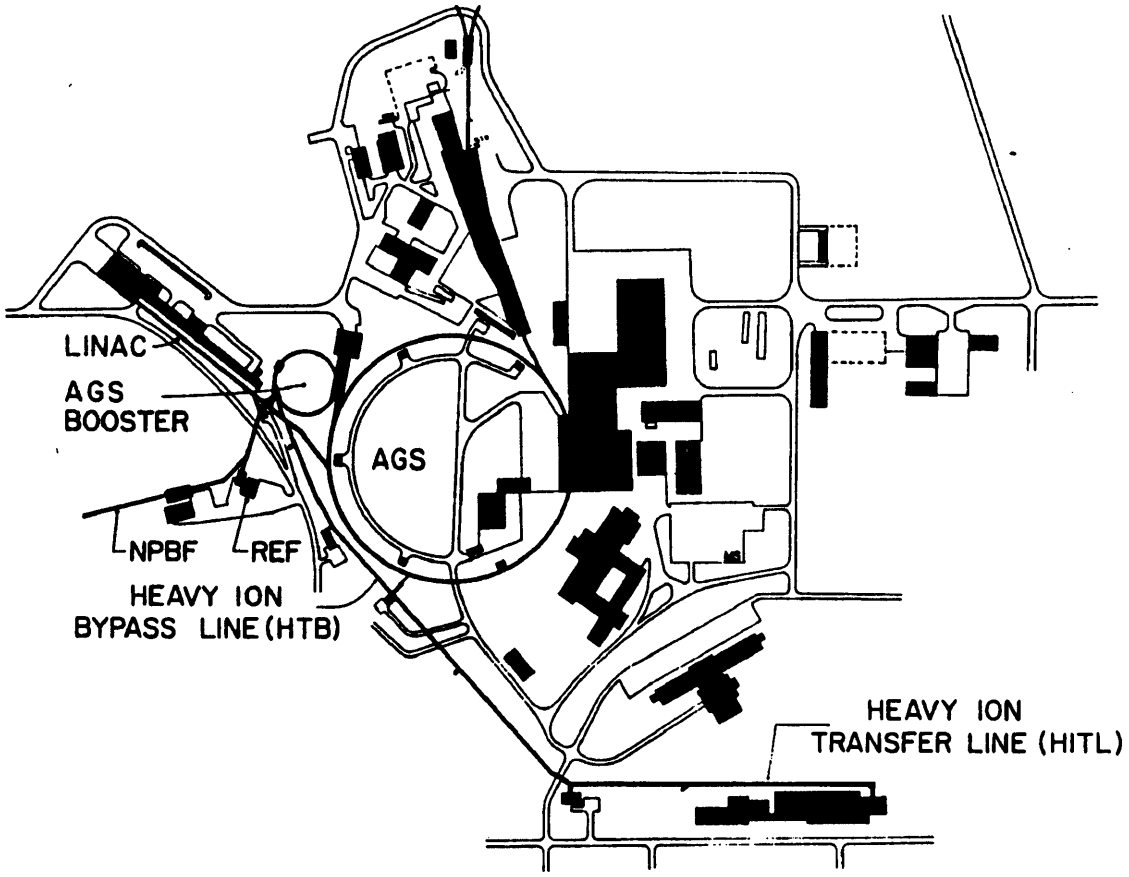

Figure 3-1: AGS acceleration complex

stability of the accelerated charge state within the AGS vacuum of 10^{-7} torr. Ions must be nearly fully stripped upon injection to the AGS and must have sufficient energy to prevent a substantial rate of electron capture from the residual gas. For this reason, the booster facility was constructed to allow acceleration of ^{197}Au beams within the AGS.

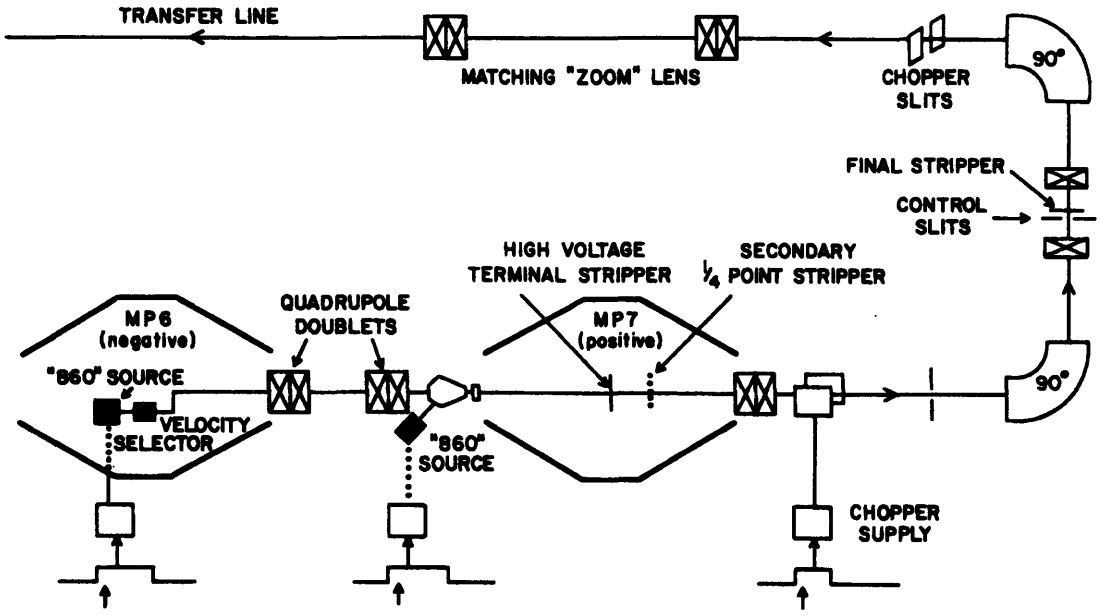

Figure 3-2: Schematic of three-stage Tandem acceleration

During the 1992 heavy ion run, beams of ^{28}Si and ^{197}Au were both pre-accelerated in the booster prior to injection into the AGS. For silicon, the final Tandem stripper was removed, yielding a higher intensity beam. The charge states going into the booster were Si^{+8} and Au^{+33} [$A^{+}92b$], with the final stripping occurring before the AGS injection. The Si ion is easily stripped, but the Au entering the Booster-to-AGS transfer line consists of roughly equal parts of the (+78) and (+79) states. This transfer line was initially setup to select the fully stripped ion. However, after a power dip, the line was inadvertently retuned to pick up the (+78) charge state, which was subsequently accelerated by the AGS for most of the E866 running. Thus the beam momentum was 11.6 A · GeV/c and not 11.7 A · GeV/c. The lone Au electron managed to hang on for dear life (there was no significant loss of beam intensity) during the AGS acceleration, and was probably stripped off by one of the vacuum windows [Ree94] on the way to the experimental floor. The booster circumference is 1/4 that of the AGS. Four turns of three buckets each are injected into the AGS for each spill. The twelve buckets are then de-bunched prior to extraction into the AGS. For the E859 booster run, there

was still a significant remnant of this twelve bucket structure in the ^{28}Si beam that was extracted to the experiment. This problem has since been fixed, by de-bunching both before and after the AGS acceleration [Ree94]. However, the E859 Si data from 1992 contain an unusually high percentage of follow events.

3.2 Development of the Experiment

The data to be presented were collected using two experiments, E859 and E866. These two experiments were in fact the young descendants of an earlier experiment, E802. While both E859 and E866 were significantly different from E802 in terms of the physics which they were able to address, much of the experimental apparatus has remained from one generation to the next; they have all successively occupied the experimental floor of the B1 beam line at the AGS. All three experiments are described below in chronological order.

Experiment E802 was designed to study collisions of ^{16}O and ^{28}Si at 14.6 A $\cdot$ GeV/c with a fixed target. As a first generation experiment in a new field, its aim was to provide a "first look" at heavy ion collisions at AGS energies [HS98]. This was achieved through an ambitious program which measured particle spectra with a rotating 25 msr single arm magnetic spectrometer (see Fig. 3-3). Through a series of five overlapping rotation settings the spectrometer covered a region of $\theta \in (5°, 58°)$. Behind it sat a 1 msr rotating Çerenkov complex to extend the particle identification to higher momentum. In addition, various detectors were used for triggering and event characterization. For purposes of defining triggers, and assigning tasks in offline data analysis, each detector or set of detectors was assigned a given partition name. Table 3.1 lists each of the detectors, their assigned partition name, the experiment for which they were installed, and their function.

Experiment E802 was enormously successful in satisfying its objectives, and made tremendous strides towards the characterization and understanding of relativistic heavy ion collisions. The data collection rate, however, imposed restrictions on the measurements of rare events (for example, those with an antiproton or two kaons in the spectrometer). Given that the AGS is capable of delivering much more beam than E802 was able to handle, this led naturally to a second generation experiment with a more sophisticated trigger. Besides the addition of a second level trigger, an array of phoswich detectors were added to measure baryons from the target rapidity region. Thus equipped, E859 set out to measure the following [LR88] in comparison to the E802 results:

1. Increased statistics and Y-p_T coverage for charged kaons

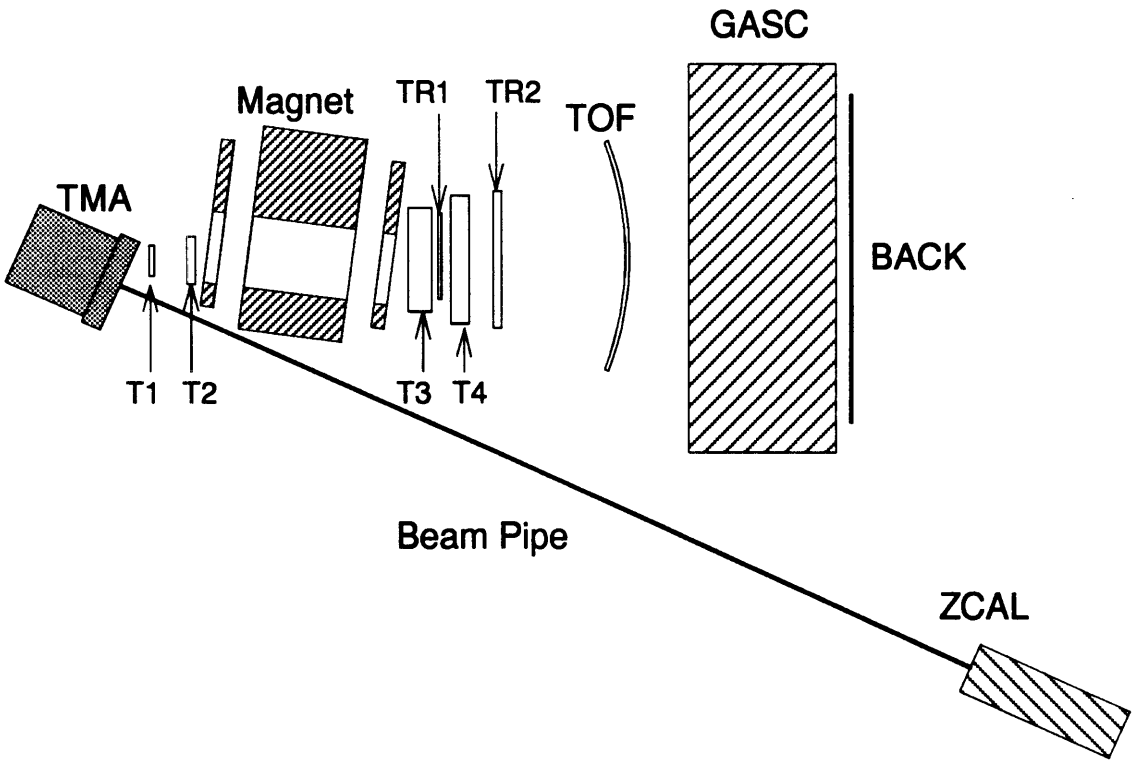

Figure 3-3: Schematic Drawing of E859 Spectrometer. Courtesy of D. Morrison

Detector(s)	Partition	Installed	Function
event characterization . . .			
beam counter assembly	BC	E802	Valid beam particles and interactions
target mult. array	TMA	E802	Total charged particle multiplicity
zero-degree calorimeter	ZCAL	E802	Kinetic energy of projectile spectators
lead-glass array	PBGL	E802	Transverse neutral energy
phoswich array	PHOS	E859	Protons from target rapidity
25 msr spectrometer . . .			
F0	F0	E802	Background generation
T1–T4 drift chambers	TRCK	E802	Tracking through magnet
time of flight wall	TOF	E802	Time-of-flight for PID
gas Çerenkov	GASC	E802	Extended PID separation
back counter	GCBC	E802	Verification for GASC
TR1,TR2 MWPC's	LVL2	E859	Online tracking for lvl2 trigger
1 msr extension . . .			
Çerenkov complex	CC	E802	Super-extended PID separation

Table 3.1: Detector elements and partitions for E802 and E859

2. Increased antiproton statistics

3. The $2K^+$ correlation and extended correlation measurements for 2p and 2π

4. Baryon spectra in the target rapidity region

5. Extended measurements of high P_T particles

In retrospect, the complete E859 data set is more than sufficient for meeting these objectives. The data have additionally provided a measurement of the ϕ mass, width and yield [Wan94], yields of Λ [Sun94] and $\bar{\Lambda}$ [Rot94] and a measurement of several non-identical particle correlations [Vos94]. All ^{28}Si data to be presented were collected by experiment E859, using the second level trigger. Data from the ^{197}Au beam were collected by E866. This experiment is more difficult to characterize because it was still being commissioned when these data were taken. At that time the experiment was identical to E859 with two important exceptions. The Target Multiplicity Array (TMA) had not been designed with sufficient segmentation to handle the larger event multiplicities of central ^{197}Au+Au collisions and was removed. Also, the Zero-degree Calorimeter (ZCAL) electronics were improved to provide the primary centrality trigger for the experiment. The full experiment is not yet completed and will incorporate many upgrades [CC99], including a second, 5 msr spectrometer to complete the proton and kaon measurements in the high multiplicity forward region.

The individual detector elements will now be described in detail. Please note that the lead glass array, phoswich array, F0 scintillator, gas Çerenkov, back counter and Çerenkov complex were not used in this analysis and have been excluded from the following description. Also, an aerogel Çerenkov counter and a TPC were both part of the spectrometer at one time, but were removed because they did not perform as expected under actual run conditions.

3.3 Event Characterization

3.3.1 Beam Counters

The beam counters serve two primary functions. They define the quality of the beam for triggering purposes, and also provide a common start time for the other detectors. They consist of a series of plastic scintillator counters with photo-multiplier tube readouts laid along the path of the beam as shown in Fig. 3-4. Proceeding downstream they are UDEW, BTOT, BTOF, BVETO and BE. All of the beam counters are read out by a pair of Hamamatasu 2083 PMT's placed on opposing sides of

the scintillator. UDEW consists of two pair of scintillators, which set the vertical (east/west) and horizontal (up/down) tolerance for the beam particles. The logic signal, also known as UDEW, is taken from the OR of the discriminated signals. The BVETO counter serves a similar function by defining an aperture 1 cm in diameter just before the target. The BTOT signal defines the initial charge state of the beam. The logic signal of the same name is formed from the AND of both an upper and lower threshold discrimination, thereby setting a narrow window on the allowed Z of the projectile. A smaller and thinner scintillator, BTOF, provides the timing start for the experiment. Finally the Bull's-eye counter (BE) defines the final charge state of the beam, after it has passed through the target, and is used to determine an interaction in the target.

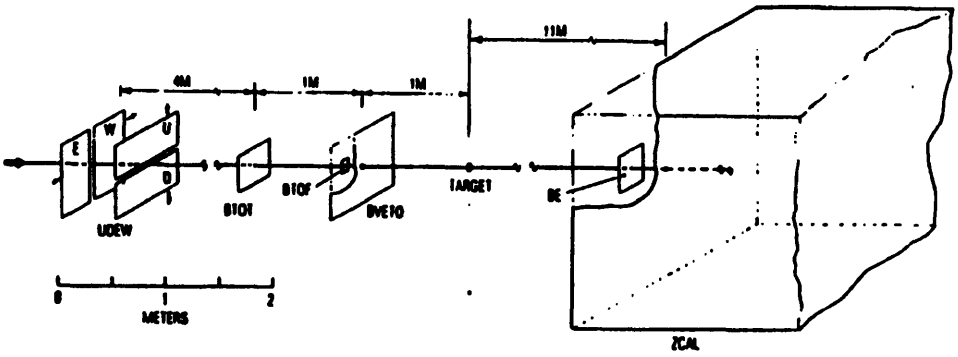

Figure 3-4: A schematic of the E802/E859 beam line and its beam counter scintillators.

There is one additional logical signal, PRE, used to define a valid beam event. It is the discriminated (lower threshold only) BTOT signal displaced by its width and extended to cover a specified period of time, and it indicates that a potential beam event was preceded too closely by another beam particle. For E859 running this period was set to be 200 nsec.[1] A valid beam event is then defined to be,

$$\text{BEAM} = \text{BTOT} \cap \text{BTOF} \cap \overline{\text{PRE}} \cap \overline{\text{UDEW}} \cap \overline{\text{BVETO}}. \tag{3.1}$$

Similarly a delayed BTOT signal in coincidence with the next BTOT particle is used to define FOLLOW, in order to reject events which were followed too closely by another beam particle. However, since this is known only after the event has been formed, the FOLLOW bit is read out as part of the event, and included in cuts made offline.

[1]The minimum value is set by the 200 nsec drift time of the TMA streamer tubes.

An interaction is defined as a good beam event for which the charge state of the projectile has been reduced by ~ 1.5.

$$\text{INT} = \text{BEAM} \cap \overline{\text{BE}}. \tag{3.2}$$

The BE distribution for INT and BEAM events is shown in Fig. 3-5. Sometime in the latter part of the E859 running an INTFOL bit was formed to indicate when the beam particle responsible for the FOLLOW also satisfied the INT condition.

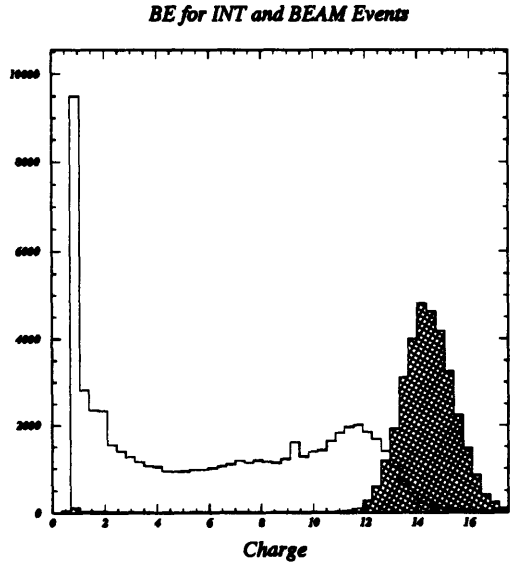

Figure 3-5: BE signal, in units of charge, for Si+Au INT and BEAM (hatched) events.

Target

The targets are supported by an aluminum frame that has a 22 mm hole for the beam. The metal foil targets are rotated into position remotely, and the entire assembly is maintained in a vacuum which extends downstream to the Bulls-Eye detector. The choice of target thickness is dictated by the conflicting needs for high interaction rates for the beam and low multiple scattering for the pions. The RMS scattering angle is given approximately by [Gro90],

$$\theta_0 = \frac{13.6\,\text{MeV}}{\beta \text{cp}} \sqrt{\frac{x}{X}}. \tag{3.3}$$

Here β, and p are the velocity and momentum of the particle traversing a distance, x, through the target. The radiation length, X, is given by,

$$\mathrm{X} = \frac{716.4\ \mathrm{g/cm^2} A}{Z(Z+1)\ln(287/\sqrt{Z})}. \tag{3.4}$$

A and Z are the atomic weight and charge of the target. Monte Carlo simulations have shown multiple scattering in the target to be the dominant contribution to the uncertainty in momentum (see Sec. 4.1.3). Using the mean momentum (800 MeV/c) for pions which contribute to the region of low relative momentum (Q_{inv}<50 MeV/c) , and multiplying by a factor of two to convert to the uncertainty in the *relative*[2] momentum, we arrive at the following relation for the uncertainty in the relative momentum,

$$\delta q = 27 \times \sqrt{\frac{x}{\mathrm{X}}}. \tag{3.5}$$

This leads to the values given in Table 3.2. A 4 fm source will produce an enhancement in the relative momentum that extends to $\Delta q = \hbar/\Delta R = 50$ MeV/c. Thus, the choice of targets permits the observation of source sizes as large as 10 fm.

target	Au 1%	Al 6%
density (g/cm^2)	0.944	1.63
δq_{rms} (MeV/c)	11	7

Table 3.2: Target thickness and contribution to relative momentum resolution. Interaction percentages quoted are for the Si beam; for the Au beam the Au target has a 1.6% interaction length.

3.3.2 TMA

The target multiplicity array (TMA) provides information on the total number of charged particles emitted from the collision, their approximate position of intersection with the detector, and a fast analog signal for use in the first level trigger. The basic detector element is a rectangular resistive plastic tube with copper wire anode mounted on copper-clad fiberglass sheets. The tubes contain a 70/30 mix of Argon-Isobutane and are run in the proportional mode. The ionization avalanche collected on the anode induces a signal on the copper surface which is amplified and then discriminated. The pads are arranged serially in panels, which in turn are assembled into two configurations known as the barrel and the wall (see Fig. 3-6). The barrel covers the region

[2]This factor comes from calculating the width of a difference distribution for a Gaussian in two dimensions.

$\theta \in (30°, 140°)$, and the wall covers the region $\theta \in (6°, 40°)$. As can be seen in Fig. 3-6, two panels on the left side of the wall have been removed to provide a clear path to the spectrometer. Additional panels were removed from the barrel during E859 (not shown in Fig. 3-6) to make way for the phoswich detectors. The phoswich array required that the two panels above and below the x-z plane on the non-spectrometer side be taken out. To prevent any biasing (of the TMA trigger) in directions to or from the spectrometer, the corresponding panels on the spectrometer-side were also removed. This gives the TMA a range of $\phi \in (15°, 165°) \cup (195°, 345°)$ at backward angles. The first level trigger is formed by taking the analog sum of the individual discriminated

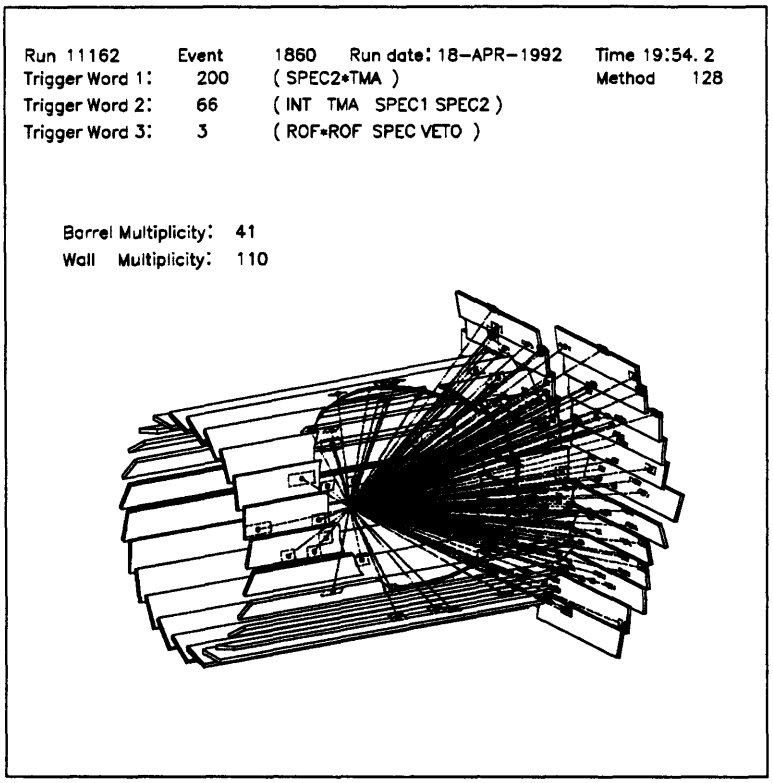

Figure 3-6: The Target Multiplicity Array

pad signals. Usually, a high multiplicity (central) trigger is desired, and this analog sum must exceed a discriminator threshold to satisfy the LVL1 trigger condition. However, a low multiplicity (peripheral) trigger is obtained by logically inverting the discriminator output level. The effect of the peripheral trigger is shown clearly in Fig. 4-6.

The procedure which translates the number of struck pads per event into a "true" multiplicity comprises two steps. Each step occurs during a given pass over the data. There are a total of three passes, **pass0**, **pass12**, and **pass3**, during which collaboration-wide analysis takes place. They are

each described in greater detail in Sec. 4.1.1. During **pass0** *dead* pads and *hot* pads are recorded in the appropriate entry in a relational database[3], and are effectively removed from the TMA acceptance. Then, in **pass12**, the active pads are grouped into clusters of adjacent struck pads. Even clusters of N pads count as N/2 hits. Odd clusters of N pads count as (N+1)/2 hits. This counting convention is an attempt to correct for two competing effects. An over-counting of particles occurs when a single track strikes multiple pads. A compensating under-counting occurs when several tracks pass through a single pad, or when isolated tracks fail to record a hit at all. Monte Carlo simulations verify that the above counting convention provides a close approximation to the actual number of particles striking the TMA [Abb90]. Finally, hits which occur in overlapping regions of the wall and barrel are counted only once. Further details on the TMA hardware and data analysis are found in Tony Abbott's thesis [Abb90].

3.3.3 ZCAL

The zero degree calorimeter provides a measure of the forward energy. It is important to the analysis in this thesis that this quantity can be taken as a count of the number of spectator (non-interacting) nucleons in the projectile times the kinetic energy per beam particle. The detector is situated 11.7 m downstream from the target, and presents a 60 x 60 cm front face to the beam. The fundamental detector element is a 3 mm thick sheet of scintillator preceded by a 10 mm thick steel plate absorber. The detector is divided into two sections (H1 and H2), which contain 32 and 106 of these elements, respectively, providing for a total depth of 8.9 interaction lengths. The use of two hadronic sections [4] was motivated by the desire to have some control over the separate processes of large fragment breakup and absorption. Each section has 8 wave length shifter guides (two per side) coupled to photo-multiplier tubes.

The ZCAL response has been studied as a function of the number of nucleons in the projectile fragment [B+ 89b]. It was discovered that the optimal response (minimal variance in the beam peak) was achieved by summing the signals from H1 and H2 (after pedestal subtraction) with weights of 0.57 and 0.43 respectively. There is an overall normalization factor which is adjusted to match the expected energy of the beam peak. The results of this study showed the signal (without this overall normalization factor) to be linear in the number of nucleons, as can be seen in Fig. 3-7. The number

[3]The collaboration standard is RDB, provided by Digital Equipment Corp.

[4]The ZDC calorimeter of WA80, after which ZCAL was modelled, is divided into electromagnetic and hadronic sections.

of nucleons in the fragment was determined from the charge ($A = 2Z$) as measured by the BTOT, BTOF and BE. The ZCAL energy plotted is the centroid of a Gaussian fit to the energy distribution. The resolution was determined to be $0.73 \times \sqrt{E}$ for ^{28}Si, and showed no dependence on the number of nucleons in the projectile. The ZCAL resolution has degraded in time due to the high beam rates used by E859[5] (Sec. 5.3.2). The approximate resolution for E859 is $1.5 \times \sqrt{E}$

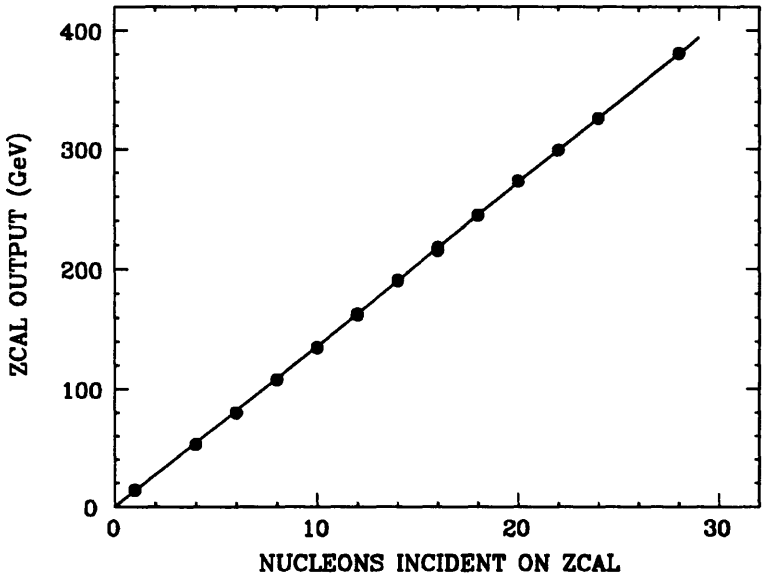

Figure 3-7: ZCAL output as a function of number of incident 13.6 GeV (kinetic energy) nucleons

3.4 Main Spectrometer

3.4.1 The Magnet

The Henry Higgins magnet was initially used (and named) at the Cambridge Electron Accelerator. The magnet uses two sets of coils to provide the dipole field (in y) and correct for inhomogeneities. The magnet can operate at field settings of 0.4, 0.6, 0.8, and 1.0 Tesla; however only the 0.4 Tesla setting was used for the data presented in this thesis. The magnet has been mapped along the y=0 mid-plane [DW87] with a Hall probe and a Taylor series approximation for the field [Vut88] shows

[5]Both radiation damage to the scintillator and noise in the electronics have contributed to this degradation

the z-integrated field to be roughly constant over the inner air gap of 85 cm in x, and 40 cm in y. The integrated field used for track reconstruction is 0.585 T·m for the 0.4 Tesla setting.

3.4.2 Drift Chambers

The drift chambers provide four sets of two-dimensional hit positions ($\hat{z}$ and a projection in a plane perpendicular to $\hat{z}$) along the path through the spectrometer. Two chambers, T1 and T2, are placed approximately 100 cm and 50 cm before the start of the B-field. The other drift chambers, T3 and T4, are approximately 75 and 100 cm after the end of the field. Each chamber comprises a set of alternating cathode and sense planes, with wires oriented along a chosen direction. The sense planes are effectively subdivided into drift cells, centered about the sense anode wires, and bounded in z by the surrounding cathode planes and on the left and right (in directions perpendicular to the wires) by negatively biased field wires. The field is shaped to be roughly constant far from the anode, and assumes the nominal $|\vec{E}| \sim V/r$ at distances comparable to the diameter of the sense wire. The ionized electrons drift at a roughly constant velocity (50 μm/nsec) towards the high field region, where the ensuing avalanche amplifies the signal by a factor of $\sim 10^5$. Those left unsatisfied by this cursory explanation should consult the CERN report by Sauli [Sau77] for an excellent discussion of the physics of wire chambers.

The specifications for the chambers and their planes are given in Table 3.3. Given that the construction and maintenance of the T2–T4 chambers were the primary responsibility of the E802 MIT graduate students, they are extensively described within the students' theses. In particular, the thesis of Brian Cole [Col92] is the most thorough in its treatment of the tracking chambers. However, there were two important modifications to the tracking chamber configuration for E859 which are not described elsewhere. T2 has been redesigned to better handle the higher beam rates. It now possesses a smaller drift cell, reducing the required voltage. Unfortunately, during its construction there was a machining error when the wire-holes for the UV module were being drilled. This led to a wire-by-wire angle deviation for the UV wires. This deviation is slight and was not noticed until after the chamber was installed, when the chamber's geometry parameters were being fine tuned. The effect is greatest in the corners of the chambers, where the acceptance is small. Since the discovery of the error, the geometry parameters have been accordingly modified to account for a shift in angle for individual wires. The second modification was the addition of a new module consisting of a series of three X-planes and one resistive wire plane. This module has been positioned immediately behind T3, and is sensibly called T3.5. The addition of three x-z

space points has proven enormously helpful in reconstructing tracks. However, the experimental resistive wire plane has not yielded the expected 3-D space-point information.

Chamber	Angle	Planes	Wires	Drift Length (mm)
T1	x (0)	2	32	4
	v (-45)	2	32	4
	y (-90)	2	16	4
	u (45)	2	32	4
	w (-26)	2	32	4
T2	x (0)	3	28/27/27	7
	y (-90)	3	13/13/14	7
	u (45)	3	28	7
	v (-45)	3	28	7
T3	u (45)	2	36	16.1
	x (0)	3	36	15.3
	y (-90)	3	16	15.3
	v (-45)	2	36	16.1
	x (0)	3	36	15.3
T4	u (45)	2	44	16.1
	x (0)	3	40	15.3
	y (-90)	3	16	15.3
	v (-45)	2	44	16.1
TR1	x (0)	1	160	3.5
TR2	x (0)	1	256	3.5

Table 3.3: Specifications for the E859 tracking chambers. The wire angles are measured clockwise from vertical as viewed from the target.

The wire signals are read from the wires with preamps and discriminators designed by Vassili Vutsadakis and Chuck Parsons and were built at MIT. The discriminated drift times are digitized in LeCroy 1879 TDCs, with a 2 nsec clock. Multiple hits are recorded, provided that the leading time of the second pulse arrives after the trailing edge of the initial pulse. The hit times are converted to distances during **pass12** using predetermined calibrations for the timing offset and the non-linearities in the drift velocity that typically occur near the anode and near the edges of a drift cell. The left-right ambiguity inherent in perpendicular distances to a wire is resolved during the track reconstruction, also performed in this pass.

3.4.3 Trigger Chambers

Two multi-wire proportional chambers, TR1 and TR2, were added to the spectrometer as part of the LVL2 trigger for E859. They are positioned behind T3 and T4 respectively. Together with the x information from the TOF wall, they provide three x-z space points behind the magnet for the online tracking performed by the trigger. The specifications are given in Table 3.3. The electronic readout for these chambers is an integral part of the LVL2 trigger operation and will be described in Section 3.6.

3.4.4 Time-of-Flight Wall

The fundamental detector unit in the time-of-flight (TOF) wall is a 78 x 1.6 x 1.6 cm plastic scintillator (BC 404) referred to as a *slat*. The slats are arranged 16 to a panel, with the 16^{th} slat made from SCSN-38 and having double the width of the others. There are 10 such panels arranged in a semi-circle that is approximately equidistant from the center of the magnet. The slats are read out from top and bottom with Hamamatasu R2083 photo-multiplier tubes. A study of the timing resolution of several photo-tubes and scintillators can be found in [S+86].

The signal coming out of the photo-multipliers is immediately split. One copy is sent to a FASTBUS ADC to record pulse height; the other copy is discriminated before and after travelling to the counting house, where it provides a stop to 50 psec per channel LeCroy CAMAC TDC's. Optimal timing resolution is achieved only after a slewing correction is applied to compensate for the fact that larger signals cross the discriminator threshold sooner. This correction assumes that the pulse shape is initially quadratic in time, and does not depend on signal height. This correction thus takes the following form,

$$t_{slew} = a + b\frac{t}{\sqrt{ADC}}. \tag{3.6}$$

Here, the ADC value corresponds to the geometric mean of the top and bottom signals. The actual time of flight for the particles is then taken to be the difference between the slew corrected TOF signal and the BTOF time, plus a constant. This constant must be calibrated and is discussed further in Section 4.1.4. A timing resolution of 120 psec was achieved for E859. This is sufficient to provide 3σ $\pi - K$ separation up to a momentum of 1.82 GeV/c.

3.5 Data Acquisition and Triggering

An important aspect of the E802 (and accordingly E859) triggering is the 75 meters distance between the counting house (where the first level triggers are made) and the target. A direct consequence of the decision to form the triggers in the counting house was that all those working on trigger electronics were required to endure the sub-zero temperatures of the counting house electronics room. An additional consequence was to form the BEAM (scaled down) and INT triggers on the floor to provide the TDC starts for some of the detectors. The trigger supervisor then accepts various trigger bits from each of the detector *partitions*. It also issues the BUSY signal for the partitions. If, after a specified scaledown, no enabled trigger condition is satisfied, the supervisor issues a fast clear to the detectors on the floor. The actual LVL1 decision takes only about 500 nsec in the trigger supervisor; however the total elapsed dead time is about 6 μsec. An additional feature of the trigger supervisor is the veto input. This allows a second (more restrictive) decision to be made (see Section 3.6) about whether to accept an event.

Once the final decision to accept an event is made, the data acquisition begins the event readout. It consists of two main elements, a VAX 11/785 host computer and a Motorola 68020 based VME chairman. The chairman collects the event fragments from the FASTBUS and CAMAC crates. These are formatted, translated (FASTBUS only), and transmitted to the VAX for logging to disk or 9-track tape. The speed of the data acquisition is limited by the DR11W link, which connects the master VME crate to the VAX, and transmits data at a rate of $\sim$ 600 kbytes/sec. Further information on the both the trigger supervisor and data acquisition can be found in [Abb90] and [Col92] and references therein.

3.6 Second Level Trigger

3.6.1 Motivation

As stated previously, the main distinction between the experimental results of E802 and those of its upgrade, E859, is the enhanced data set that E859 was able to collect with its second level trigger.[6] The improved rate of data collection is a function of many things, including beam rate, live time,

[6] Apologies to the able builders of the Phoswich array who were foolish enough to hire the author.

and event size. This can be seen in the following expression for the dead time during a spill.

$$t_s\,(1 - l/n) = l\,(f_i + f_b)\,[t_1 + f_1\,(t_2 + f_2 t_e)] \tag{3.7}$$

Variable	Typical Value	Definition
n	10^6	total beam per spill
l	$3 \cdot 10^5$	live beam per spill
t_s	1 sec	time per spill
t_1	6 μsec	time for LVL1 decision
t_2	50 μsec	time for LVL2 decision
t_e	10 msec	time for data acquisition to read one event
f_i	1%	interaction fraction
f_b	0.3%	beam floor scaledown fraction
f_1	15%	LVL1 fraction (of INT+BEAM after floor)
f_2	15%	LVL2 fraction (of LVL1)

Table 3.4: Definition of variables for Eq. 3.7.

Here, the total dead time is the sum of times for three processes: the LVL1 decision, the LVL2 decision, and the readout of the data. The quoted times, t_1 and t_2, are valid for all E859 runs. The cited event time, t_e, and fractions are for ^{28}Si+Au with 1% target, and a non-central LVL2 and $2\pi^-$ LVL2 trigger. In this case the combined contribution of the LVL1 and LVL2 decision times is a negligible part (about one msec) of the dead time incurred for each accepted event. For most data sets this contribution is even smaller. Equation 3.7 can then be simplified to

$$t_s\,(1 - l/n) = l f_i\,(f_1 f_2 t_e)\,. \tag{3.8}$$

Using the the values specified above, one can calculate the event rate per spill. For the non-central ^{28}Si+Au data set, there is a 10% abundance of real $2\pi^-$ events (as determined offline). This leads to the following rate of collection.

$$\begin{aligned} 2\pi^-\ per spill &= 10\% \times (f_i f_1 f_2 l) \\ &= 10\% \times f_i f_1 f_2 \frac{t_s}{f_i f_1 f_2 t_e + t_s/n} \qquad (3.9) \\ & \qquad (3.10) \end{aligned}$$

A beam rate of 10^6 events per spill leads to a collection rate of seven $2\pi^-$ per spill. To achieve good two-dimensional correlation functions in two regions of low multiplicity, approximately 100K pion pairs are needed [LR88]. The required beam time is given by,

$$100 \text{ Kpairs} \times \frac{1 \text{ spill}}{7 \text{ pairs}} \times \frac{1 \text{ AGS hrs}}{900 \text{ spills}} \times \frac{1.6 \text{ human hrs}}{1 \text{ AGS hrs}} = 25 \text{ human hrs.} \tag{3.11}$$

Without the use of the LVL2 trigger, the event rate remains roughly constant, but the abundance of valid $2\pi^-$ events decreases by a rejection factor of seven ($1/f_2$) or more.[7] A one day measurement now takes one week! Other measurements such as the $2K^+$correlation, or the single K^- spectra at backward rapidities, are simply no longer feasible. The complete case for the trigger is, of course, made in the E859 proposal [LR88]. For a review of the LVL2 rejection factors achieved for other run conditions, see the LVL2 N.I.M. article to be published.

3.6.2 Hardware

The charge of the trigger is to identify, if possible, all particles passing through the spectrometer from the three sets of x-z space points behind the magnet given by the TR1, TR2 and TOF hits and a corresponding set of flight times matched to the TOF hits. If it is determined that an event does not contain a specific particle or combination of two particles, then a signal is sent to the veto-input of the trigger supervisor. The trigger supervisor then issues a fast clear to the various partitions, if no other (unvetoed) LVL1 triggers have been satisfied.

The trigger functions in two stages. The hit positions and slat times must first be encoded and stored. In the second stage the trigger loops over all combinations of TR1 and TOF hits in search of the specified particle candidate(s). Each of these tasks is performed using LeCroy CAMAC modules. ECL ribbon and twisted pair cables transport the data words and control signals between modules. Figure 3-8 is a complete schematic diagram of the trigger, including all modules and control logic.

Loading and Encoding

The process by which hits and times are digitized and stored is illustrated in the upper portion of figure 3-8. This loading procedure works differently for the trigger chamber hits than for the

[7] If one takes the expression "without the LVL2 trigger" to imply removing the trigger chambers, then the abundance suffers from a weakened LVL1 condition as well.

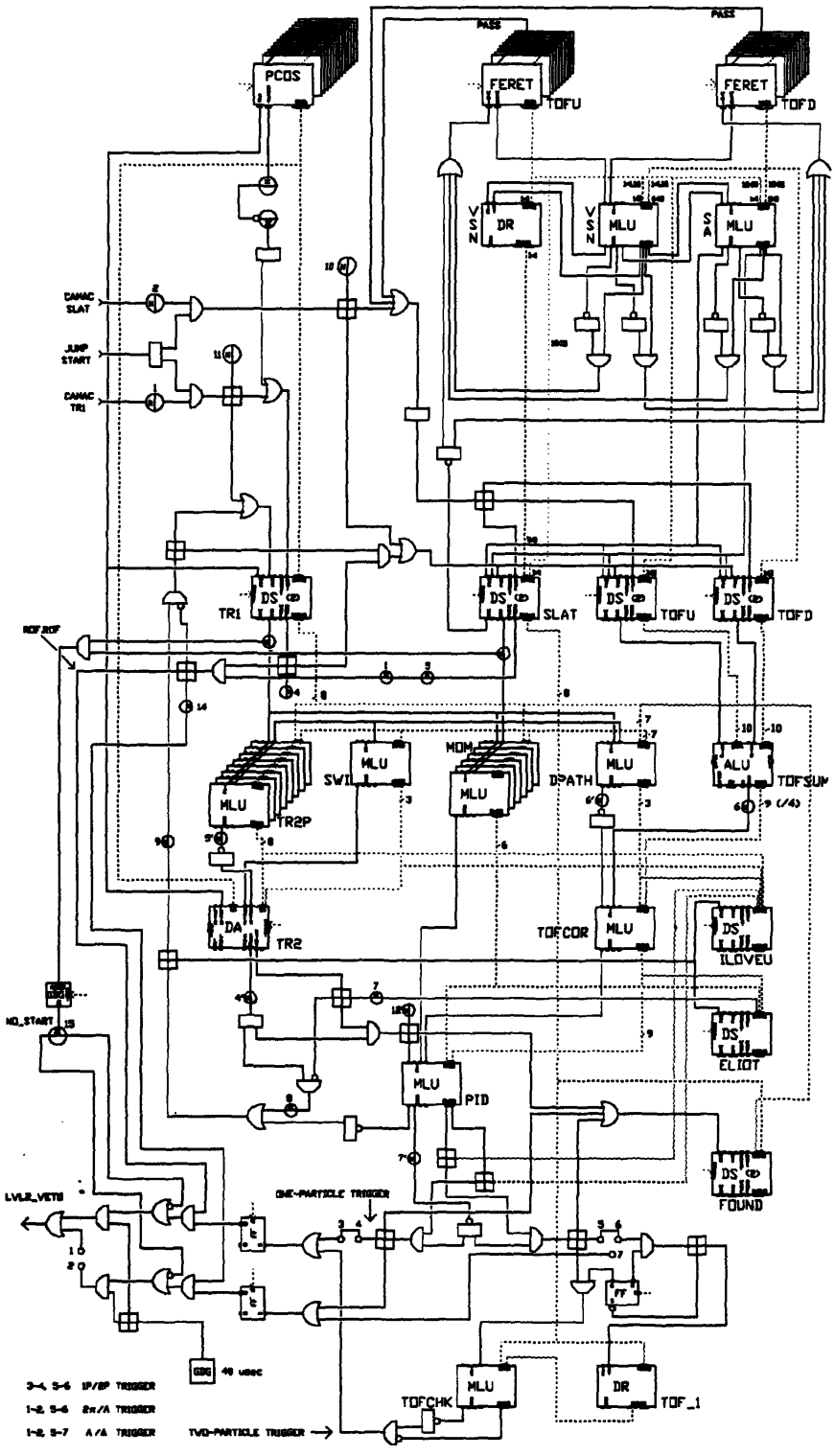

Figure 3-8: Complete diagram of the LVL2 trigger. Courtesy of L. Remsberg.

Module	Abbrev.	Description
Arithmetic Logic Unit	ALU	Addition (16 bits), calculates average of up and down TOF TDC's.
Memory Lookup Unit	MLU	Memory (4096 words), operates in one of five modes depending on number of input and output bits.
Data Stacks	DS	Sequential Storage (256 words), records TR1 wire hits and TOF slat hits and times.
Data Register	DR	Storage (1 word), saves one word for FERET slat matching.
Data Array	DA	Indexed Storage (256 words), records TR2 wire hits and responds (Y/N) to queries on stored hits.
Flip-Flop	FF	Switch, used to count up to two particles and to set veto condition.

Table 3.5: Description of LeCroy CAMAC modules used in the LVL2 trigger.

TOF slat hits and times. The trigger chamber hits are handled by the LeCroy Proportional Counter Operating System or PCOS. A complete description of this system and how it was incorporated into the E859 trigger can be found in [CL91]. The main feature of PCOS is its adjustable ripple-thru delay. This permits hits on the wire chamber to read out continually. These hits are *latched* by the event strobe signal, and subsequently written into the TR1 Data Stack and TR2 Data Array.

The loading path for time of flight slats is more complicated. A second NIM output from the TOF discriminators is used for the LVL2 purposes. The digitization is a three-step process (ie. three modules). The NIM discriminator signals are first converted to ECL output with a Brookhaven build CAMAC unit. The ECL signal then serves as a stop to the LeCroy FERET module which in turn feeds its integrated charge to a LeCroy FERA ADC. Each FERA ADC stores one set of up or down photo-tube times for 16 slats with 1024 50 psec channels and provides a 256 channel pedestal range. The slat hits are formed via a matching process that is carried out by two FERA driver modules, two MLU's, and a Data Register (see upper right corner of 3-8). This matching process is described elsewhere [Zaj92]. When two FERA times from opposing up and down photo-tubes of the same slat are matched, the slat number is loaded into the TOF data stack, and the up and down times (after pedestal subtraction) are loaded into the TOFU and TOFD data stacks.

Looping

Once the loading of hits and times has been initiated, the trigger begins searching for particles. Akin to the multi-stage offline analysis effort, this search can be divided into two phases: tracking

and particle identification. An article by Zajc [Zaj92] contains a detailed description of the tracking and PID aspects of the trigger which follow explicitly the control and information lines of Fig. 3-8. Rather than duplicate the technical description referred to above, a simplified explanation is presented.

The trigger performs online tracking by examining, one at a time, all combinations of TR1 and TOF hits, and checking for the presence of the appropriate TR2 hit. The TR1 and TOF data stacks present their first data words to the TR2P MLU's. If the particular TR1/TOF hit could have been made by a track, originating from the target and traveling through the spectrometer,[8] then this set of MLU's present the appropriate prediction for the corresponding TR2 wire hit. Otherwise, a zero is given as the output data word. Concurrently the first TOF data word arrives at the SWI MLU, which returns a data array search width. This TOF-dependent search-width is needed to accommodate the double-wide slats. The data array returns a .true. ECL logic signal if it stores a TR2 hit within the search width of the TR2 prediction. Failure results in a loop-kick signal which instructs the TR1 data stack to present its next data word, in concert with the same TOF data. When the TR1 data stack has exhausted all of its entries, it cycles back to the first entry and sends a signal to the TOF data stack telling it to present its next data word.

Once a track is found, the corresponding particle is identified the old-fashioned way, with momentum and beta. Similar to track-finding, particle identification proceeds through a series of lookup tables, constructed in advance and entered into LeCroy Memory Lookup Units. Simultaneous with the track-finding the TR1 and TOF data words are presented to the MOM and DPATH MLU's. The DPATH and average of TOFU and TOFD data stack entries are presented to the TOFCOR MLU, which "looks-up" the value of beta. Then, provided that the track-finder was successful, the momentum and beta data words are presented to the PID MLU. The PID MLU produces two bits of output, for one and two-particle selection. The one-particle bit simply sets a flip-flop. The two-particle bit must first set one flip-flop, thereby lifting a logic gate that permits a second flip-flop to be set. Additionally, the second particle can be required to have struck a different TOF slat than the first. During the Feb'91 running period, the trigger was run in one of either the one or two-particle modes, and the veto signal was inhibited if the appropriate flip-flop was set. However, by the time March'92 rolled around, we were bold enough to operate both modes independently, combining the final veto decisions in strange and wonderful ways. Sec 4.2 describes the different triggers modes used to collect the various two pion data sets.

[8]What constitutes a valid track depends upon the magnet polarity, field setting and particle charge(s).

3.6.3 Software

The above description points the way to a number of important tasks that must be accomplished in software. The look-up tables which provide the trigger with most of its computational proficiency must first be created; and once generated they are downloaded to the individual units through a KUIP-based interface known affectionately as INTER. Finally, we have written routines which permit us to recreate artificial LVL2 events to test various aspects of the hardware. Each of these tasks will now be described in more detail.

Table Generation

The generation of MLU tables proceeds in three stages. First, the actual physical values associated with particles (p, K, π) traversing the spectrometer are determined from a Monte Carlo simulation. The simulation includes only the relevant detectors (TR1, TR2 and TOF), incorporates no physical processes, and uses an effective edge approximation for the magnetic field. Possible combinations of hits on chambers are stored in an output file along with their momentum, path-length, and velocity. The output file is a function of the magnetic field and polarity.

During the second stage, these values are binned according to the specifications of the desired tables. Minimum and maximum values for momentum, path-length and velocity are required as input. In addition, there is a separate maximum momentum value for particle identification. All particles with a momentum above such a cut-off are treated as overflow. They are given a bit pattern corresponding to the highest momentum bin and are uniformly rejected or accepted by the PID table, depending on the physics measurement. This additional overflow bin prevents bins from being wasted in a region where unique particle identification is prohibited by the time-of-flight resolution. Another important input at this stage is the timing offset or *tzero*. This is the value that must be added to the FERA times to arrive at the absolute time-of-flight. It is incorporated into the TOFCOR table which calculates β.

In the final stage, the table entries are translated into the bizarre bit spliced format required by the hardware. The exact translation algorithm depends upon the number of input and output bits needed. In the case of the TR2P and MOM MLU's, we used several in parallel, each reporting one bit of the final predicted TR2 wire number or signed momentum bin. More details on this aspect of the MLU's can be found in the LeCroy Manual [LeC89]. The table loading is handled through the INTER program, described next.

CAMAC Interface and Database

INTER is based on the KUIP command-parser from CERN. It is menu-driven and handles almost all of the communication with the trigger CAMAC modules. It is also the primary means of interacting with the LVL2 database, which is used to store a hardware map of the modules, the FERA pedestal values, and the MLU tables. The database is built upon the CERN ZEBRA routines. Both the database and the INTER template were the work of Dave Morrison, and more details can be found in [Mor90] and [Mor94].

FERA Calibration

The TOFCOR MLU output is of course useless without proper calibration of the pedestals [Sak92b] for each slat. The initial calibration proceeds as follows: The pedestals are initially set to their median value of 128. Then, the FERA start signal (taken from event strobe) is delayed such that the fastest pions arrive approximately 40 μsec after the start.[9] Next, several runs from both polarities are taken and reconstructed, and a $t_{exp} - t_{calc}$ distribution for pions is histogrammed for each slat. The average shift for all slats determines the tzero value for the tables, and the relative shifts determine the new pedestal values. These distributions are then monitored closely during the entire running period to account for drifts that may occur.

Loop tests

All of the LeCroy modules are equipped with both front panel ECL and rear panel CAMAC inputs and outputs. Thus it is possible to test various subcomponents of the trigger with software. These tests are mostly stand-alone programs which load fake hits into the data stacks and data array and then start the trigger by generating an output signal (*kick start*) via a CAMAC I/O register. These programs provide the option to loop repeatedly over the same sequence of fake data. This is an important feature which allows one to test the control logic in real time with an oscilloscope. One such program which tests the track finding function of the trigger is described in detail in [Sol91]. These loop tests are the principal method for diagnosing problems that arise during the early stages of building and modifying. When problems arise during the run, the loop tests are frequently used to trouble-shoot and diagnose errors.

[9] This marks the start of linear response of the FERA's.

3.6.4 Performance

In assessing the performance of the LVL2 trigger, the high quality of the E859 data that are soon to be published speaks for itself. However, there are also more direct means available for monitoring the performance of the trigger during and after data taking. Immediate feedback is provided by the E859 scalers. They display the number of beam particles, interactions, LVL1 spec triggers, LVL2 vetoes, etc., for each spill, as well as other information in the number of counts per spill. The most common LVL2 error is the failure to properly initialize the trigger for data taking. This is detected immediately via the scalers, which show that all LVL1 spec events are being vetoed. Also, during the experiment a few thousand events are logged to disk every run for online monitoring. Periodically an entire run is taken with the veto bit disabled. The LVL2 trigger decision is recorded, but it does not influence the final decision of the trigger supervisor to accept an event. These runs are then analyzed offline to search for any bias in the data that may have been introduced by the trigger. The results of a bias study carried out for the two-pion correlation data are to be found in Appendix B.

As our understanding of what constitutes useful diagnostic information has evolved from run to run, and so has the functioning of the LVL2 online monitor. In its most recent incarnation it serves three primary purposes. First, it plots hit distributions for the two trigger chambers as well as the TOF-hit distribution after digitization in the FERA's. Second, the monitor provides a check of the FERA pedestals. It makes use of an independent determination of particle-id[10] using an effective edge approximation for magnetic field, and projecting backwards to the target given the TR1 and TOF space points behind the magnet. From this one can compare the expected and recorded flight times for pions. When required, the pedestals can be adjusted to compensate for timing drifts. Finally, the monitor provides a check on the entire trigger calculation using a software emulator. Before going into further detail, it is necessary to describe the contents of the LVL2 data banks. Each of the data stacks (and TR2 data array) has a clone data stack stationed in a CAMAC crate to which the host computer has access. In addition, there are two diagnostic data stacks which contain the values of all MLU output bits, and the FND track decision. The contents of each data stack are then read out as part of the total event stream. The monitor contains in software a duplicate of the entire chain of trigger logic and reads from the database each of the MLU table contents. Using the initial hits and times collected from the data bank, it can check the final veto decision as well as the

[10]It is independent in the sense that there is no binning as with the tables, otherwise the same experiment geometry and field approximations used to generate the tables are employed.

progression of each TR1-TOF combination as it proceeds through the sequence of look-up tables.

Chapter 4

Correlation Analysis

This chapter begins with an overview of the general analysis procedures used to obtain the Bose-Einstein correlation from the data. These include the collaboration-wide software that enables us to identify particles in the spectrometer and determine their momenta, and also the software and data structures used to generate the correlation function. A summary of the two-pion data set follows, including a description of the different triggering conditions that were used to collect the data. The next section addresses the means of selecting the pion pairs that are used in the correlation analysis. This is followed by a discussion of the procedures by which the correlation function is formed: generating the background, correcting for Coloumb repulsion and detector inefficiencies, and fitting.

4.1 Description of General Procedures

4.1.1 Data Passes

The initial phase of the analysis proceeds through a set of collaboration passes. Each of these passes maintains the YBOS bank structure of the initial event stream when generating output (to be used as input by the next pass in the series). The end result of running these passes is a final set of YBOS data files, one per run, which contain the calibrated measurements made by each detector — or set of detectors in the case of the spectrometer — for each event. Each pass consists of a set of subroutines assembled by the ANALYSIS_CONTROL software package, developed by the CDF collaboration at Fermilab. In general, the members of each partition are responsible for writing and maintaining the code which handles the data from their detector(s). In addition to any YBOS

output, all of the passes produce diagnostic information using the CERN HBOOK4 histograming package. Each of the passes is administered by some lucky soul, whose job is to ensure that the data runs are all processed without error. The general procedure outlined above and the breakdown of pass tasks presented below are common to all three experiments: E802, E859, and E866.

The first pass, **pass0**, accomplishes two tasks. First, the data are copied from 9-track tapes to 8 mm video tapes, thereby reducing by an order of magnitude the number of tapes in the analysis chain. The ANALYSIS_CONTROL shell is run during the second part, however it does not produce any output other than diagnostic histograms and text files. In addition to providing feedback on the performance of the detectors and electronics, these are used to determine hot and dead regions of detectors, ADC gains and pedestals, and TDC timing offsets. These quantities are ultimately stored in the RDB, for retrieval during later stages in the analysis.

Pass12 derives its name from passes **1** and **2** which are run simultaneously. During **pass1** the calibration constants determined from **pass0** are used to calculate the detector physics quantities, which are then added to the YBOS data stream. For example, the TMA struck pads are used to determine the event multiplicity at this time, and the drift chamber hit times are converted into distances from the wires, assuming $\beta = 1$ particles. The reconstruction of tracks in the spectrometer occurs during **pass2**. For E859, two codes were developed for this task, AUSCON [Rot94] and TRCK3[Sak92a, Sak92b]. Although they utilize different algorithms, comparisons of the tracks found by each have shown them to achieve remarkably similar results. For this analysis, AUSCON was chosen. It has a simpler algorithm than TRCK3, performs a cleaner reconstruction of close tracks and was written and maintained locally (here at MIT).

The tracks reconstructed in **pass2** are identified as particles in **pass3**. The software to perform this task was developed primarily by Shige Hayashi, and is known informally as PICD, named for the YBOS data bank that it produces. However, before tracks can be reconstructed and particles identified, the tracking chamber positions must be established, and the timing calibrations for the TOF wall must be determined. The wire, plane, and chamber positions are specified for each spectrometer setting using a combination of zero field tracks, surveyed distances, and common sense. The TOF wall calibration constants are determined for selected sets of runs using an iterative procedure which uses all identified particles (π, K, p) to calculate the TDC clock and offset for each TOF slat. The tracking code, timing calibration procedure and particle identification scheme are unique to experiment E859 and have a significant bearing on the quality of the two-pion correlation. They are described in more detail in the following sections.

4.1.2 Tracking

The following description of the tracking code provides only a rough guide to the algorithm used. A more detailed description including a list of the exact cuts used can be found in the appendix of Peter Rothschild's PhD thesis [Rot94].

AUSCON employs a macroscopic approach to finding tracks. It searches for track candidates *before* collecting the hits from the drift chambers, in contrast to its predecessor, RECONSTRUCT, the standard track reconstruction code for E802 written by Martin Sarabura [Sar89] and Huan Huang [Hua90]. This approach has become more viable since the installation of TR1 and TR2. The LVL2 trigger has already demonstrated the ability to find suitable track candidates using only information from the TOF wall and the two trigger chambers. AUSCON begins its search by collecting hits on the TOF wall; this is a logical place to begin the search for two reasons:

- All tracks must be uniquely identified with a TOF hit in order to be identified as a particle.
- The TOF wall provides 3-D space points.

Like the trigger hardware, the AUSCON code combines TOF and TR1 hits to form XZ-track candidates. These track candidates are also formed from TOF and TR2 hit combinations, in case the TR1 hit is missing. If a particle fails to register a hit in both TR1 and TR2, it will not be found by AUSCON. The raw XZ-tracks are then used to define appropriate search ranges in X on each of the drift chambers behind the magnet. If enough X-hits are collected on each module, the X-track is fit to the hits, and the TOF Y-position is used to define a search range for the Y, U, and V modules (still behind the magnet). Again, hits are collected on these modules and the T3T4 track is fit and projected *back* to the TOF wall to select the best TOF hit.

The T3T4 tracks are then projected forwards through the magnet using a spline fit, assuming the target position. A thin lens approximation is also used, to account for vertical focusing of tracks in the fringe fields. A T1T2 XZ-track is formed from selected X-hits within a search range about the projected track; then hits from the Y, U, V, and W modules are added to form the complete track in front of the magnet. The full T1T2 and T3T4 tracks are fit independently, and are used to form a complete track only if they pass slope and position matching criteria. The final momentum is determined from the bend angle through the magnet, according to an effective edge approximation for the magnetic field.

AUSCON's efficiency for detecting particles has been studied both with a GEANT Monte Carlo simulation of the experiment and by scanning real events using an event display [Rot94, Mor94].

However, the single particle reconstruction efficiency ($\approx$ 90%) is not particularly relevant to the two-particle analysis, since these efficiencies will be present in both the data and the reference sample. Of greater concern is the two-particle reconstruction efficiency as a function of their relative momentum. The underlying source of this inefficiency is the inability of the drift chamber electronics to resolve signals that are closer than 40 nsec in time (see Fig. 4-1), which would occur for tracks that pass simultaneously through a drift cell with a separation of less than 2 mm. This is a problem for the two-particle analysis because we lose information in precisely the low-relative momentum region where we expect to see the greatest enhancement. How this loss of information effects the correlation function depends upon the reconstruction code, and the number of hits that adjacent tracks are permitted to share. If two tracks are not allowed to share any hits, then too many tracks with low relative momentum are lost. Conversely, if two tracks are allowed to have almost of all their hits in common, then there will be a large number of ghosts, and the q-distribution will have an artificial spike at zero. This is a particular problem in a high-multiplicity environment, where one is always likely to find a few adjacent hits that can complete an artificial pair of tracks. The strategy

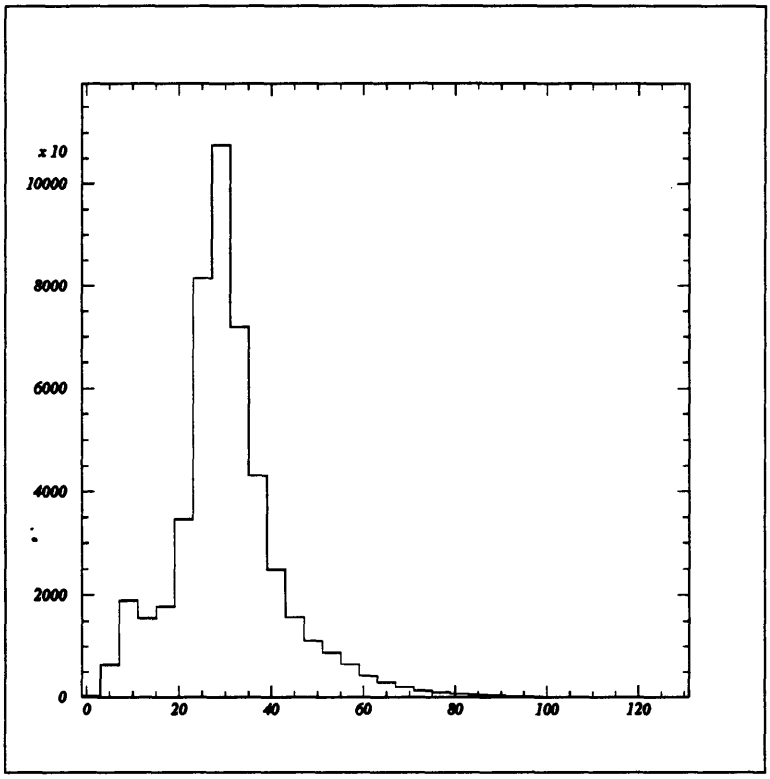

Figure 4-1: T2 Pulse Width Distribution. The x-axis units are nsec.

adopted by AUSCON is to eliminate all ghosts, while preserving as many of the real two-track pairs

as possible. This is achieved by limiting the number of shared hits per view. AUSCON's two-track efficiency has been studied using the Monte Carlo, and also using real data. The results of these studies are presented in Sec. 4.3.3 and 4.4.2.

4.1.3 Particle Identification

As stated previously, the collaboration particle identification scheme is known as PICD [HT93]. PICD possesses two outstanding qualities which make it suitable as a particle identification standard for the collaboration.

- It correctly accounts for the uncertainty in the mass calculation by propagating the errors from the measured time-of-flight and momentum.
- It produces a status word which contains the result of each of the decisions made during the identification.

The output status word provides a large degree of flexibility, by permitting one to easily study the impact of a particular aspect of the overall PID decision. For example, the pion definition used for this analysis differs from the strict PICD definition. The implications of this are discussed in Section 4.3.2, and a comparison of one data set analyzed both ways is presented in Appendix D. The accuracy and flexibility of PICD are most clearly illustrated by Fig. 4-2, which shows the particle decision as a function of $1/\beta$ and p and the logical conditions used to separate particles in ambiguous regions.

Pairs of lines in Fig. 4-2 delineate the $\pm 3\sigma$ cuts in $1/\beta$ for identifying a given particle. Areas filled in black are regions for which the particle identification is unique for a given value of the momentum.[1] Hatched regions indicate that information from the GASC, BACK counter, and TOF ADC's may have been used in the identification process. These additional selection criteria introduce many subtleties into the particle identification process, and overall efficiencies must be studied carefully. This analysis includes only pions with momentum below [2] 1.82 GeV/c, where a pion is defined as any particle with Z$\geq$1 (TOF ADC cut) that satisfies the $\pm 3\sigma$ pion cuts. Thus, a relevant concern is electron contamination (see Sec. 4.3.2). It is worth noting that the PICD code often adds the photoelectrons from adjacent cells when determining whether a given particle

[1] The e/π region above the GASC threshold for pions is also filled in black because we have no ability to distinguish between them; these particles are assumed to be pions.

[2] This is the momentum for which the pion and kaon 3σ limits cross, using a value of 120 psec for σ_t.

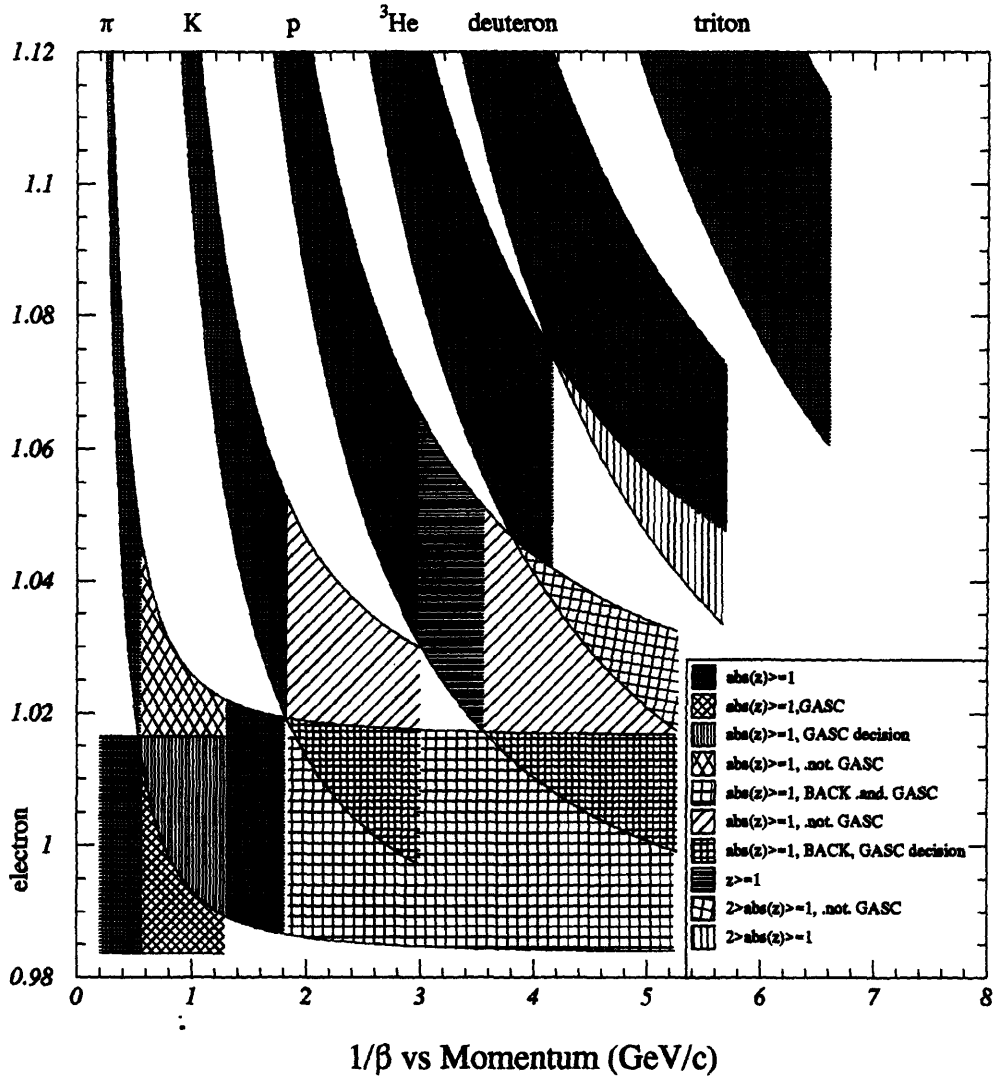

Figure 4-2: PICD particle identification (see text for details), courtesy of V. Cianciolo and D. Morrison

exceeds the GASC threshold (i.e. fires the GASC). This is appropriate when a particle crosses more than one GASC cell in a low multiplicity environment (spectrometer setting of 44°), but presents problems when there are many tracks in the spectrometer. This is especially troublesome for measuring the enhancement of close pairs. For this reason, the GASC information is not used for pion identification in this analysis.

The uncertainty in the mass calculation is most easily derived in terms of the difference between expected and measured values for $1/\beta$ [HT93]; the uncertainty in the measured value comes directly from the time-of-flight, and the uncertainty in the expected value is due to the errors in the determination of the bend angle (momentum) caused by multiple scattering and spatial resolution of the drift chambers.

$$\begin{aligned} \beta_{meas}^{-1} &= \frac{c}{l}t \\ \beta_{calc}^{-1} &= \sqrt{p^2+m^2}/p \\ \sigma^2\left(\beta_{meas}^{-1}-\beta_{calc}^{-1}\right) &= \left[\frac{m^2}{p^2\sqrt{p^2+m^2}}\right]^2\sigma_p^2+\left(\frac{c}{l}\right)^2\sigma_t^2 \end{aligned} \tag{4.1}$$

The uncertainty in the momentum is parameterized in the following manner, according to [Sak92a],

$$\begin{aligned} \sigma_p^2 &= \left(\sigma_{sr}p_{GeV/c}^2\right)^2+\left(\frac{\sigma_{ms}p_{GeV/c}}{\beta}\right)^2. \\ \sigma_{sr} &= 0.006\frac{0.4}{B_{tesla}} \\ \sigma_{ms} &= 0.012\frac{0.4}{B_{tesla}} \end{aligned}$$

The values for the spatial resolution (σ_{sr}) and the multiple scattering through the spectrometer (σ_{ms}) were determined using both a Monte Carlo simulation and fits to the data, assuming a predetermined time-of-flight resolution, although the proportionality constants above (used in **pass3**) are slightly larger than those determined in [Sak92a]. The canonical value for E859 was chosen to be 120 psec, corresponding to the largest of the timing resolutions among the entire range of TOF slats. On average (see Fig. 4-3), the resolution is somewhat better.

4.1.4 Timing Calibrations

Proper calibration of the timing constants for the TOF wall is crucial for accurate particle identification. In the past, timing calibrations have been performed during three different stages of the

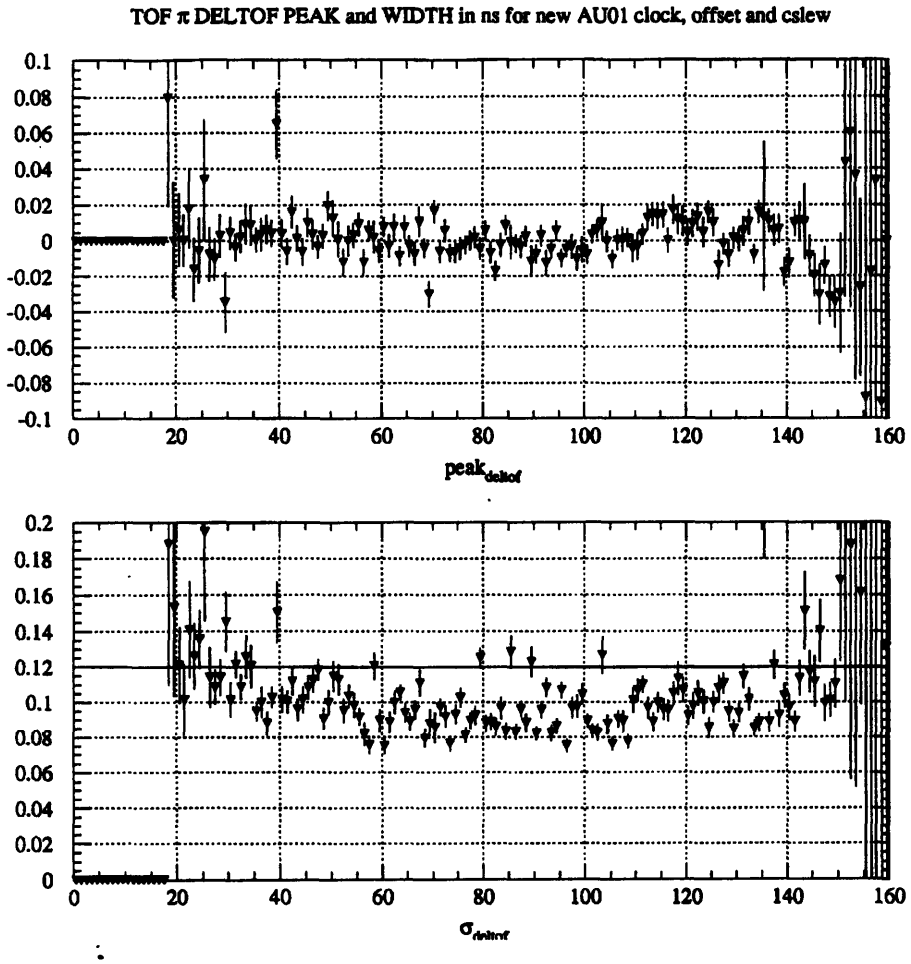

Figure 4-3: Distribution of σ_{TOF} for different slats.

collaboration analysis chain.

The reconstruction codes require that the TOF wall times be calibrated to give reasonable values for the particle transit times, and semi-accurate Y-positions. In practice, the tracking codes are not that sensitive to the accuracy of these calibrations. A timing resolution of 500 psec introduces a spatial jitter of only 25 μm. Thus, an initial set of approximate calibration constants are determined prior to the running of **pass12**.

Then, prior to **pass3**, a more thorough set of calibration constants are derived. A new program written for E859, primarily the work of Ole Vossnack,[3] performs a linear regression fit for pions, kaons and protons to fit the timing offset, clock time, and slew correction for each slat. Several sets of runs are chosen, in an attempt to maintain a fairly accurate set of calibrations over the course of an entire running period. The selection of these runs and the command procedure to run Ole's executable are described in [Sol93].

A final calibration, run as a pre-burner to **pass3**, serves to correct for global shifts in the entire TOF wall for each run. A small number of events (500) are analyzed and the t_0 offset is fit using only pions. Such shifts are often caused by a sagging BTOF signal, or daily temperature cycles. The quality of the calibrations are monitored closely during the running of **pass3** through a bevy of diagnostic histograms [Cia93].

4.1.5 HBT Machinery

This section briefly describes the software used to carry the **pass3** output data stream into the actual and background histograms that define the correlation function. The HBT analysis routines used to accomplish this were developed by Vince Cianciolo and myself, and were based initially upon the work of Richard Morse. While the details of the programs and choice of data structures should not (one hopes) have any bearing on the physics results, the HBT software chain exhibits such a high level of organization (thanks to Vince) that I present here an introduction to the basic software elements we use to manipulate the data.

The correlation data set for E859 spans well over one hundred 8 mm tapes. The first goal is to produce a reduced data structure which contains all of the potentially useful information. This structure must be flexible enough to permit the following:

- projection of event, single, and two-particle distributions,

[3] with a little help from his friends

- examination of cuts in event, single and two-particle variables,
- generation of a mixed-event background possessing a similar structure.

These criteria led us to develop the HBT *Stream*. The *stream* is a brain child of Chuck Parsons and Brian Cole. It is a modification of the CERN HBOOK ntuple structure that allows for additional data compression through bit packing and a hierarchy of ntuple-word entries. The different entry levels enable one to make cuts on information from upper level entries (event variables) when plotting lower level entries (track variables). Many of innovations of the stream have since been incorporated into the new column-wise ntuples maintained by CERN. An entire data set for one correlation measurement is stored in a single stream file (the ACT Stream, named for the Actual distribution) containing one stream ntuple for every run in the data set. We developed two separate schemes for accessing and manipulating the information for all of the runs within the ACT Stream. One, HBT_LOOP, resides within a modified[4] version of the Physics Analysis Workstation (PAW) from CERN. The other, is a stand-alone shell program, HBT_USER, which runs more quickly. Taken together, they provide a convenient format for viewing the data, selecting the cuts, and generating a background (the BCK Stream).

After gaining some experience as correlators, one of us, Vince, began to yearn for something simpler. This thing is the Qtuple, which is a regular, old-fashioned CERN-style ntuple containing only the momentum variables for each member of an identical particle pair. This simplifies the task of projecting the pair momenta onto the relative momentum coordinates once the essential event and single particle cuts have been decided upon. Then, the other of us, myself, realized that the event-mixed background is most efficiently constructed after all cuts have been chosen and irrelevant information has been removed. Thus the background can be generated from the ACT stream (10 CPU *hours*)[5] and then projected into a Qtuple, or projection to the Qtuple can be done first, and then the background can be generated much more quickly (10 CPU *minutes*). The various paths that the data can take are shown in Fig. 4-4. The histogram projection and correlation function fitting are both performed using commands within the HBT shareable image version of PAW. The fitting makes use of the MINUIT fitting routines to minimize two versions of log-likelihood fitting functions. Details of these functions are presented in Section 4.4.3. A more thorough description of the HBT code can be found in [CSed], which also contains a list of the HBT Stream and Qtuple

[4]This modification takes the form of a shareable image of PAW, enabling the user to link in additional routines relatively quickly. It is another creation from the ubiquitous Chuck Parsons.

[5]on a DEC model 4000-60

contents, as well as more information on running and maintaining the HBT software.

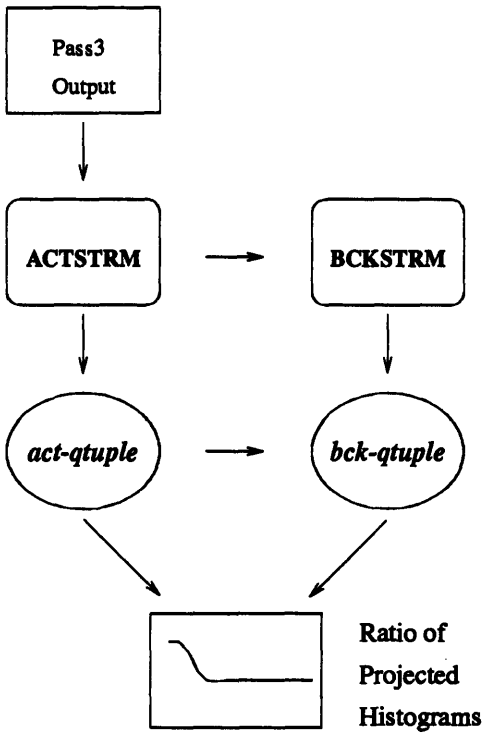

Figure 4-4: The Correlation Machinery Flowchart.

4.2 The Data

The two-pion data sets taken by E859 and E866[6] are listed in Table 4.1. Data using the Si beam were taken with the spectrometer positioned at 14° which encompasses the nucleon-nucleon center-of-mass rapidity of 1.72 (see Fig. 4-5). The Au beam data were taken with the spectrometer at 21° because Y_{nn} for this beam is 1.60, and partly because there was some concern over whether the drift chambers would handle the higher track densities at the 14° setting.

All of the two-pion data sets incorporate some form of the SPEC trigger, and of course, the LVL2 trigger. The non-central Si+Au $\rightarrow 2\pi^-$ data set was taken using only the tracking part of the LVL2 trigger. In order to obtain an even distribution in multiplicity for the non-central region, the $\overline{\text{TMA}}$ trigger was run with two different thresholds. The minimum bias multiplicity distribution for Feb'91, the distribution for those events for which there are $2\pi^-$ in the spectrometer, and the scaled

[6]There is one additional Si+Au $\rightarrow 2\pi^+$ central measurement taken at a spectrometer setting of 19° for comparison with the two-kaon measurement.

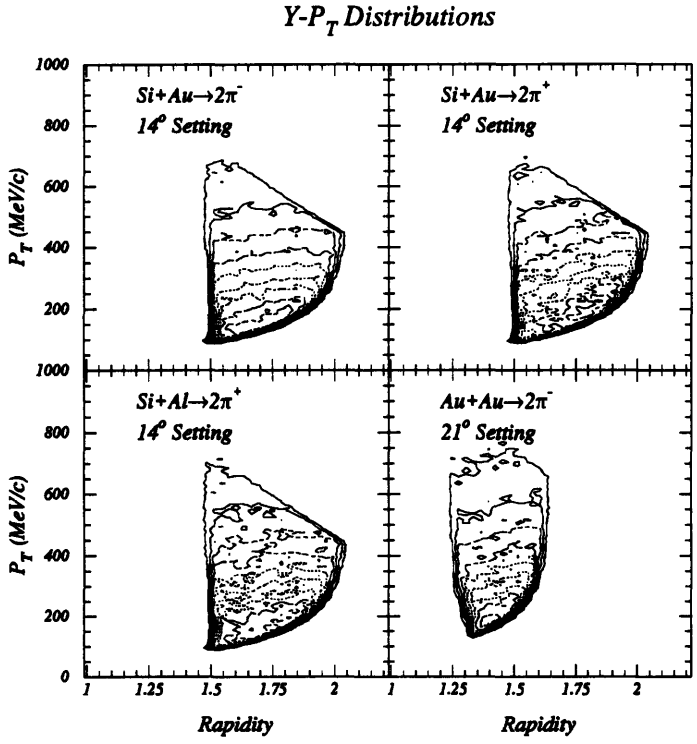

Figure 4-5: Phase space distributions (Y-p_T) for the pions used in this analysis.

distributions for the two different TMA thresholds are shown in Fig 4-6a. These data have been scaled to show

- the absence of any bias in the multiplicity distribution (the LVL2-triggered data follow the untriggered distributions),
- the difficulty of obtaining good 2π statistics in the low multiplicity region.

The latter point is why two-pion measurements in the peripheral region are beyond the ability of most heavy ion experiments, E802 included. The multiplicity distributions for the Mar'92 Si+Au $\rightarrow 2\pi^-$ and Si+Au $\rightarrow 2\pi^+$ central data sets are shown separately (Fig. 4-6b) because the multiplicity distribution differs for the two E859 running periods (Feb'91 and Mar'92) due to the increase in the number of dead pads over time. In Fig. 4-6b, the stars show the minimum bias distribution for events with $2\pi^+$ in the spectrometer. The cross-hatched region is actually the triggered $2\pi^-$ distribution (vertical hatch marks) superimposed with the triggered $2\pi^+$ (horizontal hatch marks). Both of these 2π distributions have been scaled to agree with the minimum bias distribution. For the Si+Au $\rightarrow 2\pi^-$ data set, a $2\pi^-$ trigger was combined with a Λ trigger, such that one π^- candidate and a second π^- or a proton candidate were required. Here, an upper mass cut of 300 MeV/c^2 was used for the pion definition and an upper momentum cut of 3 GeV/c was used for LVL2 particle identification. The exotica trigger used for the $2\pi^+$ data used similar mass cuts for pion identification and required the following: two of $\pi^+/K^+/K^-/\bar{p}$, with at least one of π^+/K^+.

The initial proposal to measure Bose-Einstein correlations for Si+Al collisions as a function of multiplicity called for a $2\pi^-$ data set, akin to the Si+Au $\rightarrow 2\pi^-$ measurement. However, there is strong motivation for measuring high p_T pions and protons (using the CC) for the Si+Al system. Since neither of these two measurements exhausts the data collection rate, we were able to combine them. However, the spectrometer acceptances (Henry Higgins and CC) are optimized for collecting particles of one sign for a given magnetic field polarity. By opting for a Si+Al $\rightarrow 2\pi^+$ data set instead, we were able to collect both data sets in parallel. In all, two LVL2 veto conditions were applied to four LVL1 triggers. The SPEC and SPEC·$\overline{\text{TMA}}$ LVL1 triggers were vetoed by the absence of two π^+ candidates, while the CC·SPEC and CC·SPEC·$\overline{\text{TMA}}$ LVL2 triggers were vetoed by the absence of a positive track with momentum less than 3 GeV/c. The scaled multiplicity distributions for the $2\pi^+$ events are shown in Fig. 4-7.

The TMA detector was removed for E866 because it did not have sufficient segmentation to handle the high multiplicity Au+Au collisions. At this time the ZCAL electronics were upgraded

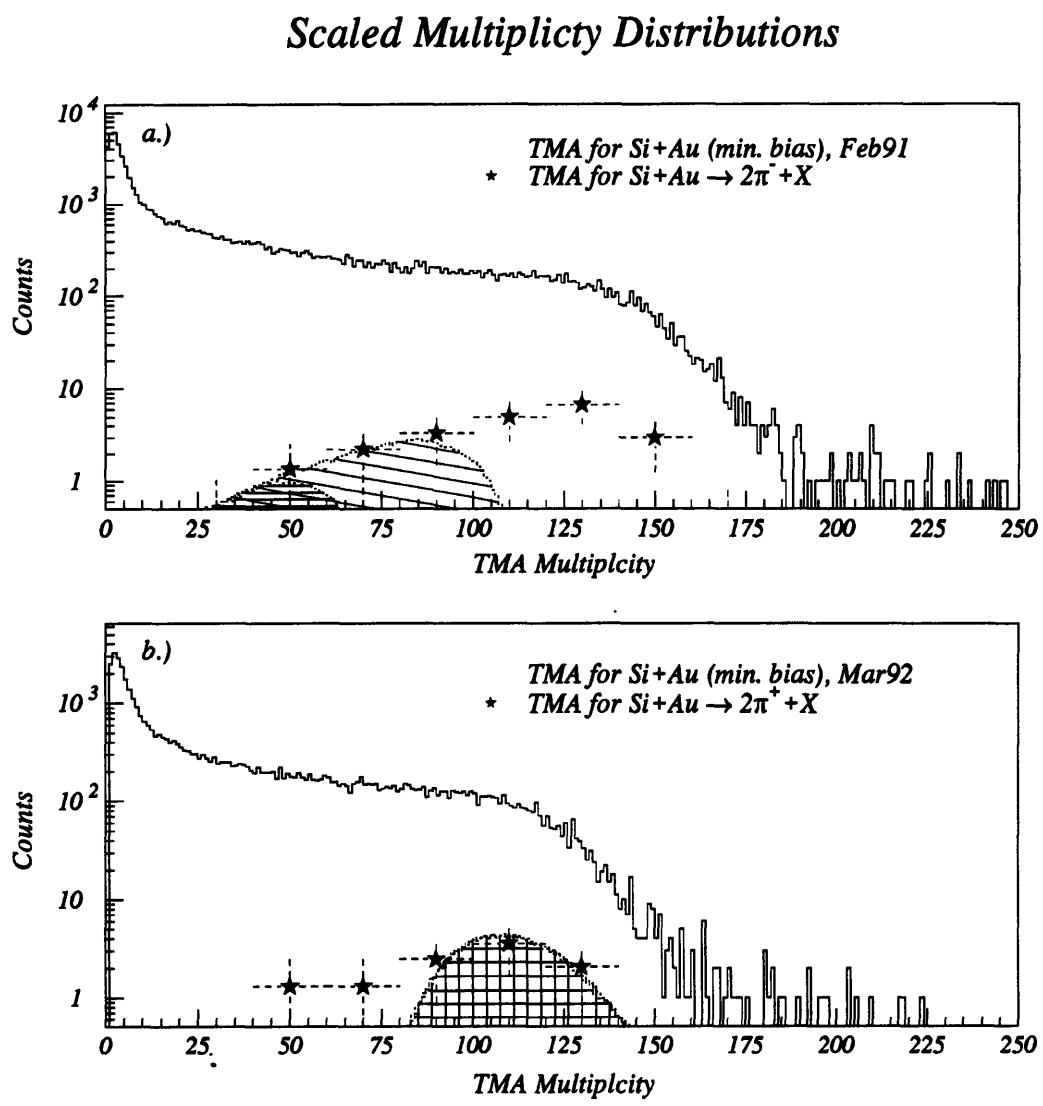

Figure 4-6: Multiplicity distributions for Si+Au with and without $2\pi^{\pm}$. Hatched regions show data distributions for events with $2\pi^{\pm}$taken with different TMA hardware cuts.

System	LVL1	LVL2	Runs	Date	Comments
Si+Au $\rightarrow 2\pi^-$	$\overline{\text{TMA}}$	2 neg. track	10193–10222	*feb'91*	includes two non-central regions
Si+Au $\rightarrow 2\pi^-$	TMA	$2\pi^-/\pi^-$ p	11120–11168	*mar'92*	central (10%), $2\pi^-$ or Λ
Si+Au $\rightarrow 2\pi^+$	TMA	$2\pi^+$/exotica	11170–11187	*mar'92*	central (10%), see text
Si+Al $\rightarrow 2\pi^+$	$\overline{\text{TMA}}$, INT	$2\pi^+$/CC	10826–10878	*mar'92*	non-central, minimum bias
Au+Au $\rightarrow 2\pi^-$	$\overline{\text{ZCAL}}$	$2\pi^-$	11358–11377	*mar'92*	central (5%)

Table 4.1: Summary of Data Sets

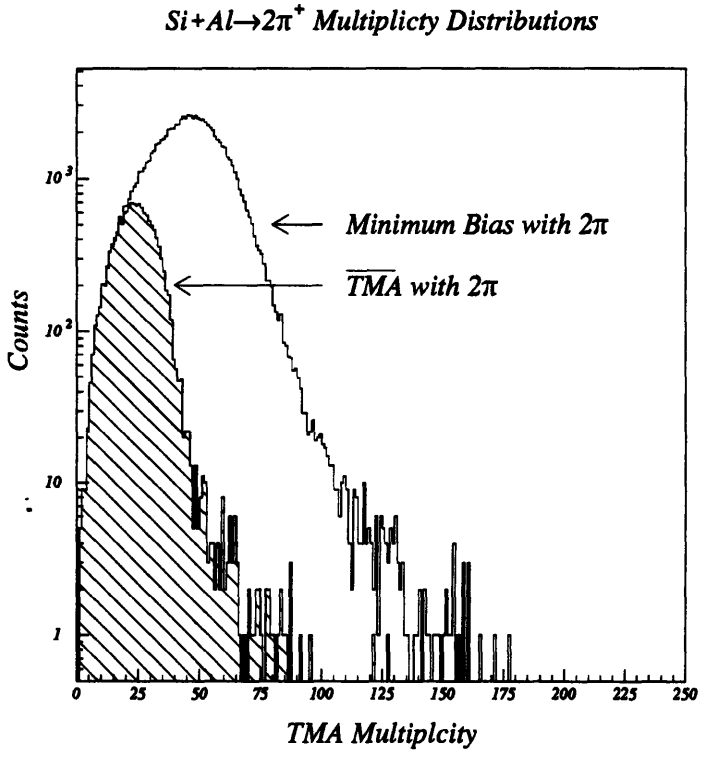

Figure 4-7: Multiplicity distributions for Si+Al for the two trigger conditions: Minimum Bias with $2\pi^+$ and Peripheral TMA trigger with $2\pi^+$.

to enable a LVL1 trigger to be formed. The $2\pi^-$ data set for Au+Au was centrally triggered with $\overline{\text{ZCAL}}$ (see Fig. 5-30). An upper mass cut of 300 MeV/c^2 and an upper momentum cut of 3 GeV/c were used in the LVL2 trigger decision.

4.3 Specification of Pion Pairs

The overall aim of this analysis — to measure the Bose-Einstein interference between like-sign pions as a function of global event observables — places strict requirements on the types of particles and events which can be used. For measurements in which the dependent variable is the total charged multiplicity or the forward energy, one is limited to events for which these quantities are measured faithfully. The accurate identification of the pions is also an important concern. Finally, the measured relative momenta of the pion pairs must be free from the influence of experimental procedures, such as an inefficient detection and reconstruction of low-momentum pairs. Once the events and particles to be used in the analysis have been determined, additional cuts are applied to the pion pairs to insure that this condition is met.

4.3.1 Event Selection

BTOT and FOLLOW cuts

The primary source of distortion for both the multiplicity and forward energy distributions is pile-up. As described in Section 3.3.1, the FOLLOW bit is set when the next beam particle arrives within a 200 nsec gate. However, there is a window of 5-10 nsec during which another particle can sneak by without setting the FOLLOW bit.[7] This is illustrated in Fig. 4-8, which shows a clearly discernible second peak in the BTOT signal even when the FOLLOW cut has been applied. These events are potentially a problem for the analysis of spectrometer data, though perhaps not a severe one for the correlation analysis. For example, Peter Rothschild found that false antiproton events artificially heightened the secondary peak; these events often contained pions that were mistakenly identified as antiprotons.[8] Cutting on BTOT helps mitigate the effects of pile-up not covered by FOLLOW and helps insure the purity of the 2π sample. The primary peak in the BTOT distribution has a resolution of approximately one charge unit (see Fig. 4-8). Requiring the BTOT signal to be less

[7] A similar window also exists in setting the PRE logic signal. These windows establish a safety margin, which prevents a beam particle from becoming it's own PRE/FOLLOW

[8] A previous beam particle starts the clock early leading to a longer time of flight for the pion, giving it the apparent mass of an antiproton.

than 18 is roughly equivalent to a 3σ cut and cleanly removes the second peak. For some of the Feb'91 and E866 Au-beam runs, the BTOT signal has a very poor resolution. It appears that some of the signal from one ADC was lost during these runs. In this case, a cut is made on the BTOF signal instead, which is nearly the equivalent of BTOT. The BTOT/BTOF cut is applied to all of the data sets. Furthermore, FOLLOW events are eliminated from all distributions that are gated on ZCAL, either in hardware or in software. This cut is too restrictive for distributions gated on the multiplicity. Unlike the ZCAL, only beam particles that interact will produce a signal in the multiplicity array.[9] The INTFOLLOW signal was formed during the Mar'92 run (when the beam microstructure led to a high percentage of FOLLOW events) specifically for this reason. Thus, for Mar'92 data gated on and binned in multiplicity, the INTFOLLOW cut is used. For the Feb'91 this signal was not available. Since the FOLLOW cut is overly restrictive and results in a 20% loss in statistics when combined with the BTOT cut, we do not use it for the multiplicity analysis. It is worth noting that adjacent beam particles can only *increase* the recorded multiplicity of an event. Events in the lowest multiplicity bin would remain in this bin if it were possible to subtract out the effect of the FOLLOW particle. The BTOT/BTOF cut is retained, however, as a precaution for particle identification and because the reduction in statistics is tolerable (13%).

Multiplicity cuts

The choice of multiplicity cuts are dictated by the following concerns:

- to achieve good statistics in as many multiplicity bins as the data permit,
- to *clean up* the hardware multiplicity cuts with more restrictive cuts in software.

The first item is a rather subjective criteria. Ultimately it can be reduced to the puerile, "It's my thesis, and I'll place the cuts where I like." However, a more quantitative argument also exists. Having established that the one-dimensional Q_{inv} parameterization is inappropriate for fitting a heavy ion source, it is desirable to obtain enough pion pairs to achieve accurate two-dimensional fits. There is no magic number. The accuracy of the fit depends upon the statistics in the low-q region, and this depends upon both the source size and the experimental acceptance. Included in the E859 proposal [LR88] is a Monte Carlo calculation for the E859 acceptance. The study concludes that approximately 50,000 pairs are needed to achieve 10% relative errors for a three parameter fit

[9]Note that "interact" here includes interactions that occur outside the target.

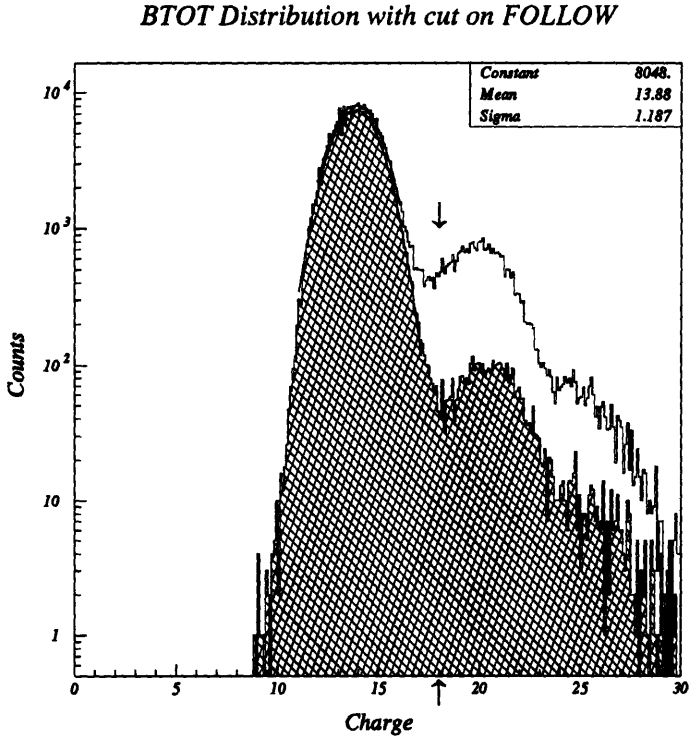

Figure 4-8: BTOT distribution for Si+Au → $2\pi^-$ data set of Mar'92. The hatched region results when FOLLOW events are eliminated.

to an R_L=R_T=τ=4 fm source. However, the E802 correlation analysis [Mor90, A$^+$92a] shows this estimate to be optimistic. For E802, with a similar acceptance to E859, a data sample of this many pairs yields roughly 10% errors for a two-dimensional parameterization of an R=τ=2 fm source. These cuts are chosen to yield 50,000 pairs per multiplicity bin when possible.

The second item above refers to the slow roll-over of the multiplicity distribution near the TMA threshold. This is caused by slow particles that hit the TMA after the analog trigger sum has been formed. INTFOLLOW events also contribute to a long tail above the threshold. In a world of infinite statistics, one would cut in software exactly at the point where the gated multiplicity distribution begins to deviate from the ungated distribution. This would insure that event multiplicity is the only characteristic of the event used to separate the pions in one multiplicity bin from those in another. However, to do so would compromise our ability to satisfy the first criteria established above. This deviation occurs precisely at the peak of each of the multiplicity gated distributions. Instead, to enhance statistics the software cuts are applied at the multiplicity for which the gated distribution falls to 80% of the ungated distribution. This rule defines the two Si+Au $\rightarrow 2\pi^-$ peripheral regions, the Si+Al $\rightarrow 2\pi^+$ peripheral cut, and the lower multiplicity cut for the Si+Au $\rightarrow 2\pi^{\pm}$+X central systems. In all, eight bins in multiplicity were formed. The number of pion pairs in each of these bins is given in Table 4.2. The final multiplicity distributions are shown in Fig. 4-9.

System	Multiplicity range	Event cuts	Final statistics
Si+Au $\rightarrow 2\pi^-$	TMA<51	BTOT<18	52,696
Si+Au $\rightarrow 2\pi^-$	51<TMA<89	BTOT<18	58,437
Si+Au $\rightarrow 2\pi^-$	100<TMA<114	BTOT<18$\cap\overline{\text{INTFOL}}$	90,087
Si+Au $\rightarrow 2\pi^-$	114<TMA	BTOT<18$\cap\overline{\text{INTFOL}}$	88,629
Si+Au $\rightarrow 2\pi^+$	100<TMA	BTOT<18$\cap\overline{\text{INTFOL}}$	57,612
Si+Al $\rightarrow 2\pi^+$	TMA<23	BTOT<18$\cap\overline{\text{INTFOL}}$	43,285
Si+Al $\rightarrow 2\pi^+$	23<TMA<47	BTOT<18$\cap\overline{\text{INTFOL}}$	45,466
Si+Al $\rightarrow 2\pi^+$	47<TMA	BTOT<18$\cap\overline{\text{INTFOL}}$	43,496

Table 4.2: The multiplicity data sets. Final statistics refer to the total number of pairs after all cuts have been made.

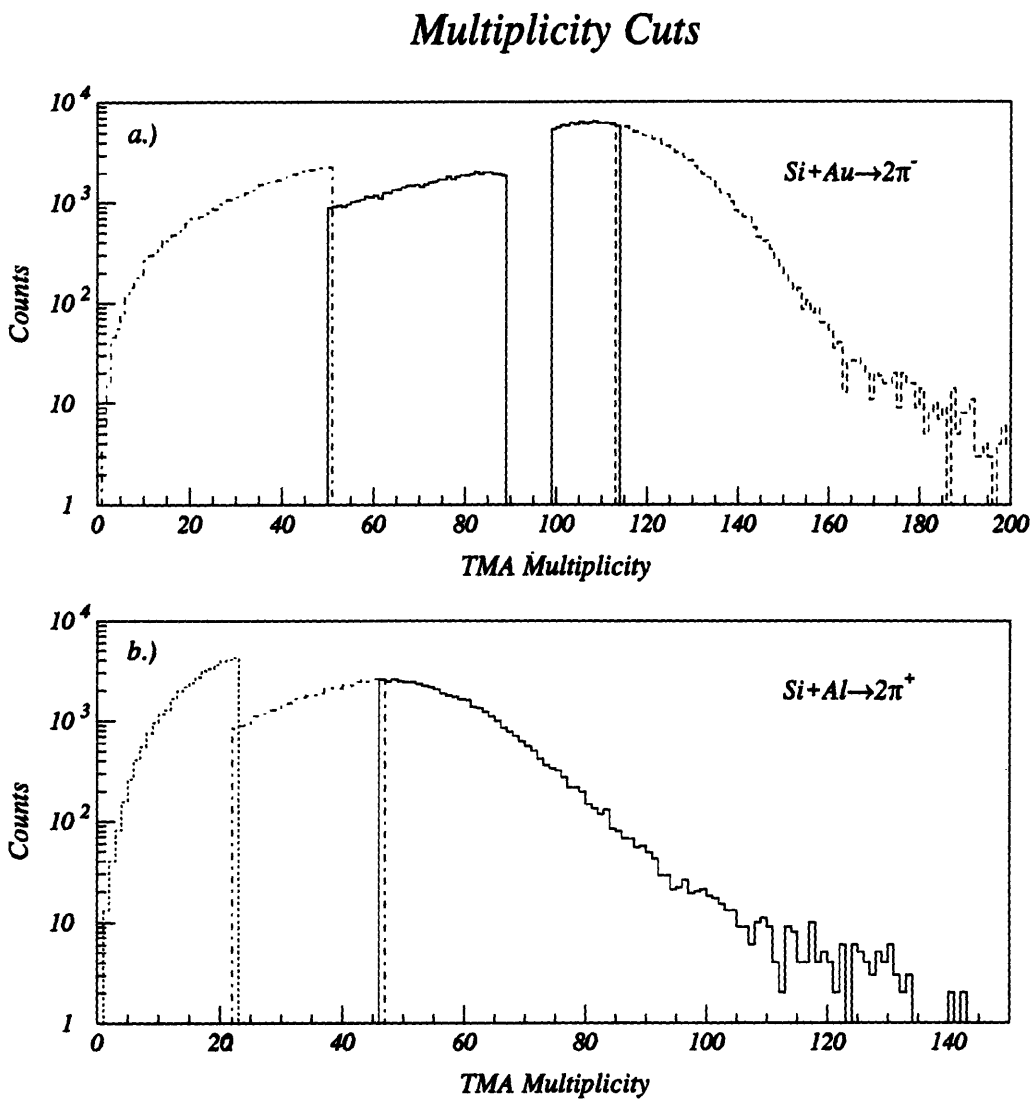

Figure 4-9: Multiplicity distributions after software cuts.

Forward Energy cuts

The study of the Bose-Einstein interference as a function of forward energy deposition proves to be more difficult for a number of reasons. That the Si+X systems were gated on multiplicity makes this variable a more natural choice for continuing to pursue software cuts. Yet, the forward energy measured by ZCAL is more easily interpreted in terms of the collision geometry; it provides a count of the number of projectile spectators. Unfortunately, obtaining this information from the ZCAL for E859 has proven to be a formidable task. During each of the running periods, the ZCAL was plagued by a different problem.

feb91 The high rates of E859 lead to a rate dependent offset in the measured forward energy.

mar92 The rate dependence is fixed, but this introduces a rate dependent noise problem.

Examples of each of these effects are given in Sec. 5.3, where an attempt is made to correct for them in calculating the number of projectile spectators.

These problems are avoided for the central Si+Au systems. Fig. 4-10 shows the relation between a healthy ZCAL signal and the Multiplicity. For high multiplicity events, the ZCAL signal remains essentially fixed at zero. These events correspond to a picture in which the projectile is completely occluded by the target. Thus, for the centrally gated TMA data sets, no further cuts in forward energy are necessary. The usual BTOT and INTFOL cuts are made to insure the accuracy of the hardware multiplicity selection.

For peripheral Si+Au collisions, Fig. 4-10 shows a broad range in forward energy for a given band in multiplicity, and a forward energy cut is needed. As with the software TMA cuts, the ZCAL cut was placed where the forward energy distribution for the $\overline{\text{TMA}}$ gated data (higher threshold) falls to 80% of the ungated value. The more peripheral $\overline{\text{TMA}}$ data set (lower threshold) was similarly cut in ZCAL; however, there were only enough pairs to perform a one-dimensional analysis. The 80% rule was modified for the Si+Al $\rightarrow 2\pi^+$ $\overline{\text{TMA}}$ data set, for which the ZCAL distribution did not match the INT distribution because of the poor ZCAL resolution for high rate events. In this case the distribution was scaled to match the INT distribution before the 80% cut was applied. For the Si+Al $\rightarrow 2\pi^+$ central data set the ZCAL cut was deliberately chosen away from the ZCAL central peak to improve the accuracy of the projectile spectator calculation. The Au+Au $\rightarrow 2\pi^-$ data set was taken using a 5% $\overline{\text{ZCAL}}$ hardware trigger. Since the ZCAL distribution for this system falls quite sharply, no further software cut was applied.

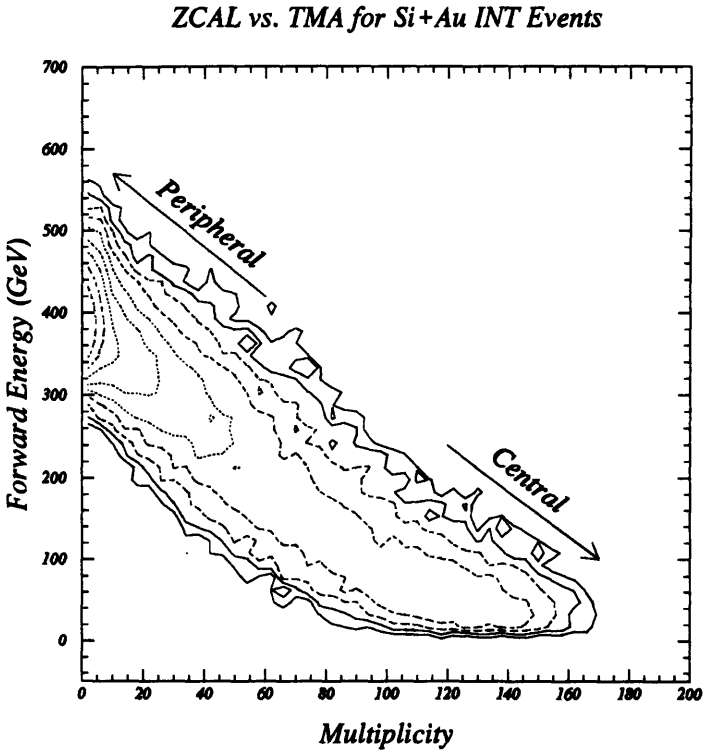

Figure 4-10: TMA Multiplicity vs. ZCAL Forward Energy.

System	ZCAL	Event cuts	Final statistics
Si+Au $\rightarrow 2\pi^-$	160<ZCAL	BTOF< 18$\cap\overline{\text{FOLLOW}}$	37,076
Si+Au $\rightarrow 2\pi^-$	270<ZCAL	BTOF< 18$\cap\overline{\text{FOLLOW}}$	15,089
Si+Au $\rightarrow 2\pi^-$	central TMA	BTOT< 18$\cap\overline{\text{INTFOL}}$	232,296
Si+Au $\rightarrow 2\pi^+$	central TMA	BTOT< 18$\cap\overline{\text{INTFOL}}$	76,661
$\vdots$			
Si+Al $\rightarrow 2\pi^+$	330<ZCAL	BTOT< 18$\cap\overline{\text{FOLLOW}}$	28,558
Si+Al $\rightarrow 2\pi^+$	ZCAL<200	BTOT< 18$\cap\overline{\text{FOLLOW}}$	57,435
Au+Au $\rightarrow 2\pi^-$	ZCAL central	$\overline{\text{FOLLOW}}$	85,573

Table 4.3: The forward energy data sets. Not all central cuts used ZCAL; see text for details. Final statistics refers to the total number of pairs after all cuts have been made.

4.3.2 Pion Selection

As stated in Section 4.1.3, particles were identified as pions using time-of-flight and momentum, up to a momentum of 1.82 GeV/c. This definition is different from that of the *straight-ahead* PICD scheme for two regions in $1/\beta$ vs. p:

I From the beginning of the $e - \pi$ overlap up to the π GASC threshold (0.54<p<1.3 GeV/c). All particles that fall within this region are identified as pions in this analysis.

II From the beginning of the $\pi - K$ overlap up to the K GASC threshold (1.82<p<5.0 GeV/c). These particles are not used in this analysis.

In short, the GASC information is ignored because of a suspected q-dependent bias. Two particles with low-Q_{inv} are more likely to pass through the same or adjacent GASC cells. As stated in Section 4.1.3, the PICD algorithm often adds the photoelectrons from adjacent cells when deciding whether the GASC fired. These particles are thus more likely to be identified as electrons in region I, and pions in region II. In principle, one could eliminate this bias by excluding from the analysis all pion pairs striking the same or adjacent GASC cells, as is done for two pions striking the same TOF slat, but to apply this to the entire data set would all but eliminate the pairs with low relative momentum. The GASC has a much lower segmentation — 40 GASC cells compared to 144 usable TOF slats.

The consequences of the decision to ignore the GASC information vary according to the region. Excluding the pions in region II has negligible effect upon the correlation function. In the E859 acceptance these pions contribute to a Q_{inv} above 70 MeV/c (see Fig. 4-11), beyond the principal region of enhancement for a 4 fm source. The additional high-Q statistics would serve to better define the normalization for the multidimensional fits; however, one would first have to verify that GASC identification does not introduce a systematic Q-dependent offset in this region.

The treatment of particles in region I has a greater bearing on the final shape of the correlation function. The effect on Q_{inv} of heeding the GASC identification in region I is shown in Fig. 4-12. As seen in Fig. 4-2, from a momentum of 0.54 GeV/c (the beginning of the $e - \pi$ overlap) up until 1.3 GeV/c (the GASC π threshold) PICD requires that all pions not fire the GASC. This will remove some of the electron contamination, but will also remove some actual pions from the data stream. By separating this region into the pion only region (I.A) and electron/pion overlap region (I.B), one can estimate the fraction of particles in I.B that are actually electrons. Fig. 4-13 shows the particles in each of these subregions, and the number of those which fire the GASC. A total of 11.5% of

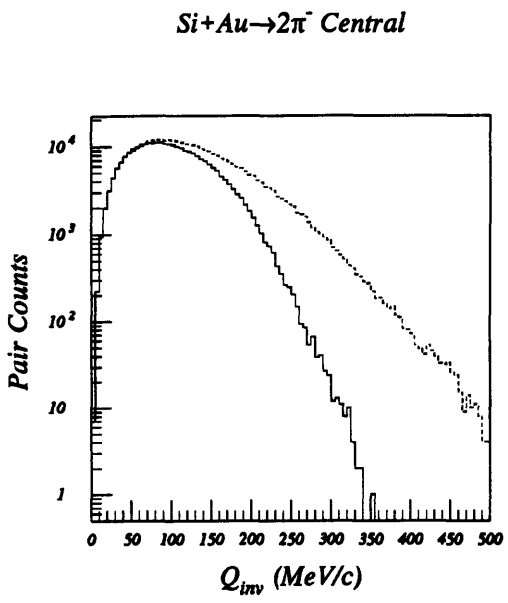

Figure 4-11: Q_{inv} distribution for Si+Au $\rightarrow 2\pi^-$ using TOF identification only (solid) and extending the momentum coverage to 5.0 GeV/c by adding the PICD pions from region II (dashed).

the particles in region I.B are not identified as pions by PICD because they are determined to have fired the GASC. However, in the region where there are no electrons, the GASC still fires 5.5% of the time. If one assumes that this fraction of real pions in the overlap region also fires the GASC, and that all of the electrons in this region fire the GASC, this leads to an electron contamination of approximately 6.3% of region I.B, or 3.8% of all of region I. The numbers and percentages quoted are specific for the Si+Au $\rightarrow 2\pi^-$ system and can be expected to change slightly for other systems. This is, of course, only a crude estimate of the actual electron contamination. An accurate analysis of the electron spectra for E859 is presently being performed by Kevin Rathbun [Rat94].

One estimate of the systematic errors has been obtained by fitting the correlation function for the Si+Au $\rightarrow 2\pi^-$ central system, using both the present pion definition, and also the standard PICD with GASC electron rejection, still keeping the high momentum cutoff at 1.82 GeV/c. A comparison of the correlation functions and fitted parameters obtained from both methods of pion identification is presented in Appendix D .

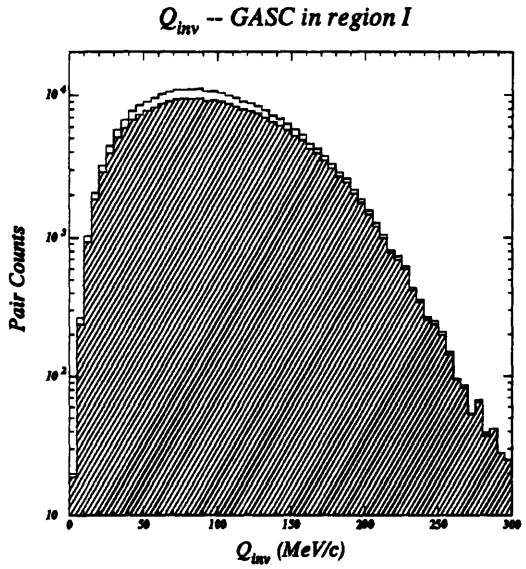

Figure 4-12: Q_{inv} distribution with and without PICD GASC electron rejection

4.3.3 Two-Pion Selection

The final cuts are applied to the pion pairs; they correct for two-particle detection inefficiencies in the drift chambers and TOF wall.

An individual TOF slat is incapable of recording a time for more than one particle per event. In general, slats which suffer multiple hits will lead to some fraction of particle misidentification for all particles. This effect is particularly important for the two-particle analysis when one considers the possibility of two pions striking the same slat. Many of these pion pairs will not be identified properly, and many that are identified as such may be combinations of other particles. To avoid biasing the low relative momentum region (two pions of the same sign that strike the same slat are very likely to have similar momenta) such pairs are eliminated from both the Actual and Background distributions.

Unlike the TOF slats, individual drift cells have multi-hit capability. However, as demonstrated in Fig. 4-1, the drift chambers cannot resolve chamber hits that are closer than 2 mm (assuming similar transit times – usually a good assumption for pions). We can look for these inefficiencies by comparing the data to an event mixed background, which will have the same relative chamber position distribution without the close hit inefficiency, (Fig 4-14). The figure shows a clear hole in the relative position on T1, which extends roughly 1 cm in δx and 2.5 cm in δy. It is not immediately obvious why the depleted region should extend further in y than in x. The timing resolution is the

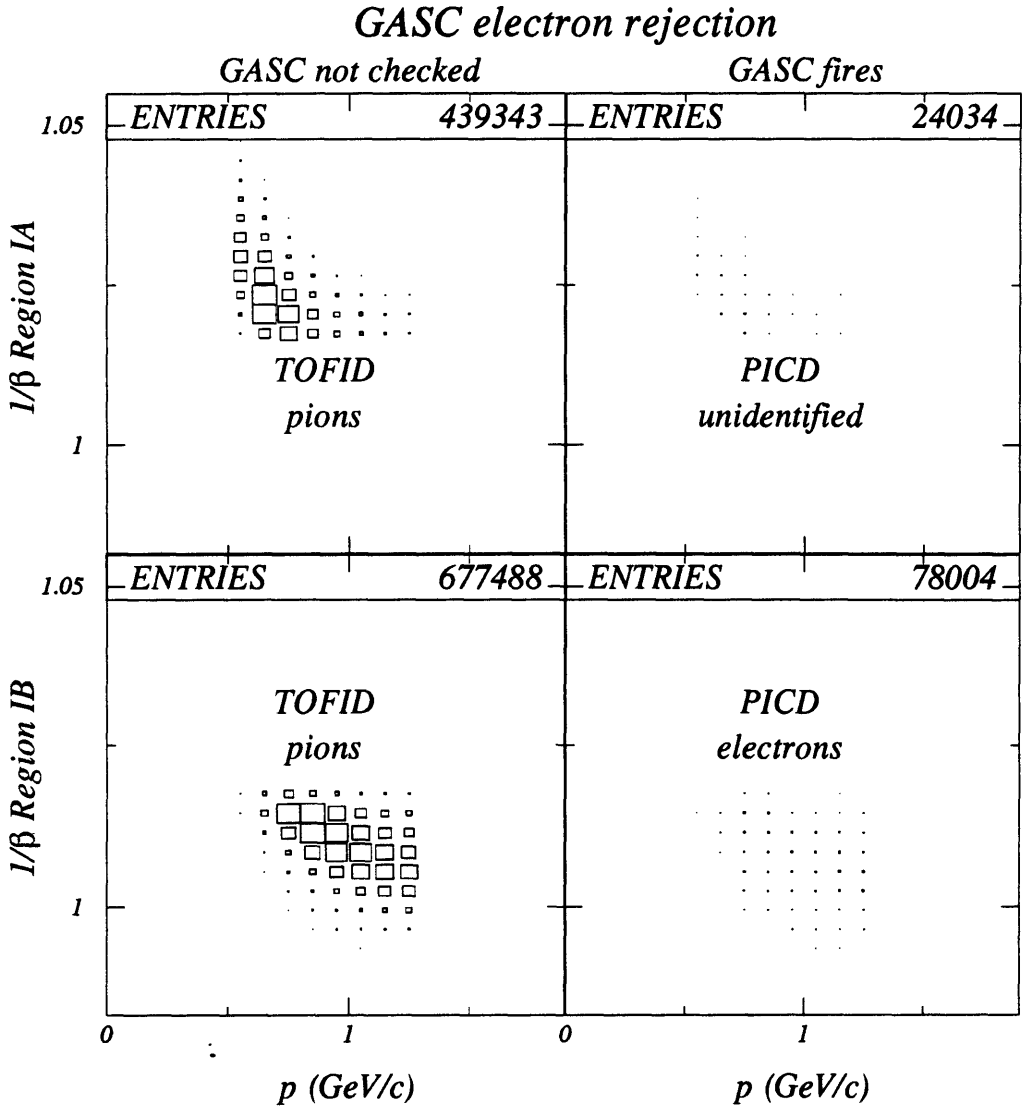

Figure 4-13: Si+Au $\rightarrow 2\pi^-$ $1/\beta$ vs. momentum for the particles in the pion only region (I.A) and the $e - \pi$ overlap region (I.B) and the subset in each region which register in the GASC

same regardless of the wire orientation. However, along a track in front of the magnet, the u, v, and w planes provide more information for the projection in x than for the projection in y. This particular problem is not seen behind the magnet, where a small separation on one chamber does not imply a small separation on another.

We correct for this inefficiency by eliminating pairs from the region for which the efficiency is less than 50% (see Fig. 4-15) and assigning a correction factor (the inverse of the efficiency) to the rest of the pairs. The cut is applied to pairs which satisfy,

$$(2.75)^2(p_{x1}/p_{z1} - p_{x2}/p_{z2})^2 + (p_{y1}/p_{z1} - p_{y2}/p_{z2})^2 < (0.011)^2. \tag{4.2}$$

This corresponds roughly to an ellipse on T1, with a semi-major y-axis of 11 mm and a semi-minor x-axis of 4 mm. The factor of 2.75 was obtained from a two-dimensional Gaussian fit to the depleted region, used to obtain the correction factor. Details of the fit and corresponding correction are given in Section 4.4.2. The exact placement of the cut boundary is somewhat arbitrary. Although AUSCON does not show any obvious signs of ghost tracks,[10] we still do not trust pairs of tracks which have a projected separation of less than 4 mm. Also, there is little to be gained by applying a large correction to a set of pairs that have very poor statistics. On the other hand if the cut were extended far enough to eliminate the need for a correction, this would severely limit the low-Q statistics. Sec. 5.6 presents the results of analyzing the data under these conditions.

4.4 Extraction of the Correlation Function

4.4.1 Background Generation

The ideal background, or reference distribution, contains all of the features of the data except for the correlation in relative momenta induced by Bose-Einstein statistics. As demonstrated by the different experiments reviewed in Ch. 2, there are a number of different prescriptions for forming backgrounds which strive towards this ideal. For many of the experiments, a comparison of the fitted parameters obtained with different background techniques is used to estimate the systematic error — often larger than the statistical error. However, in such cases, we can conclude that at most one of the prescriptions used is correct, although the means to choose between them may not be available.

[10]Ghost track refers to one of a pair of close tracks that are reconstructed when only one track actually exists.

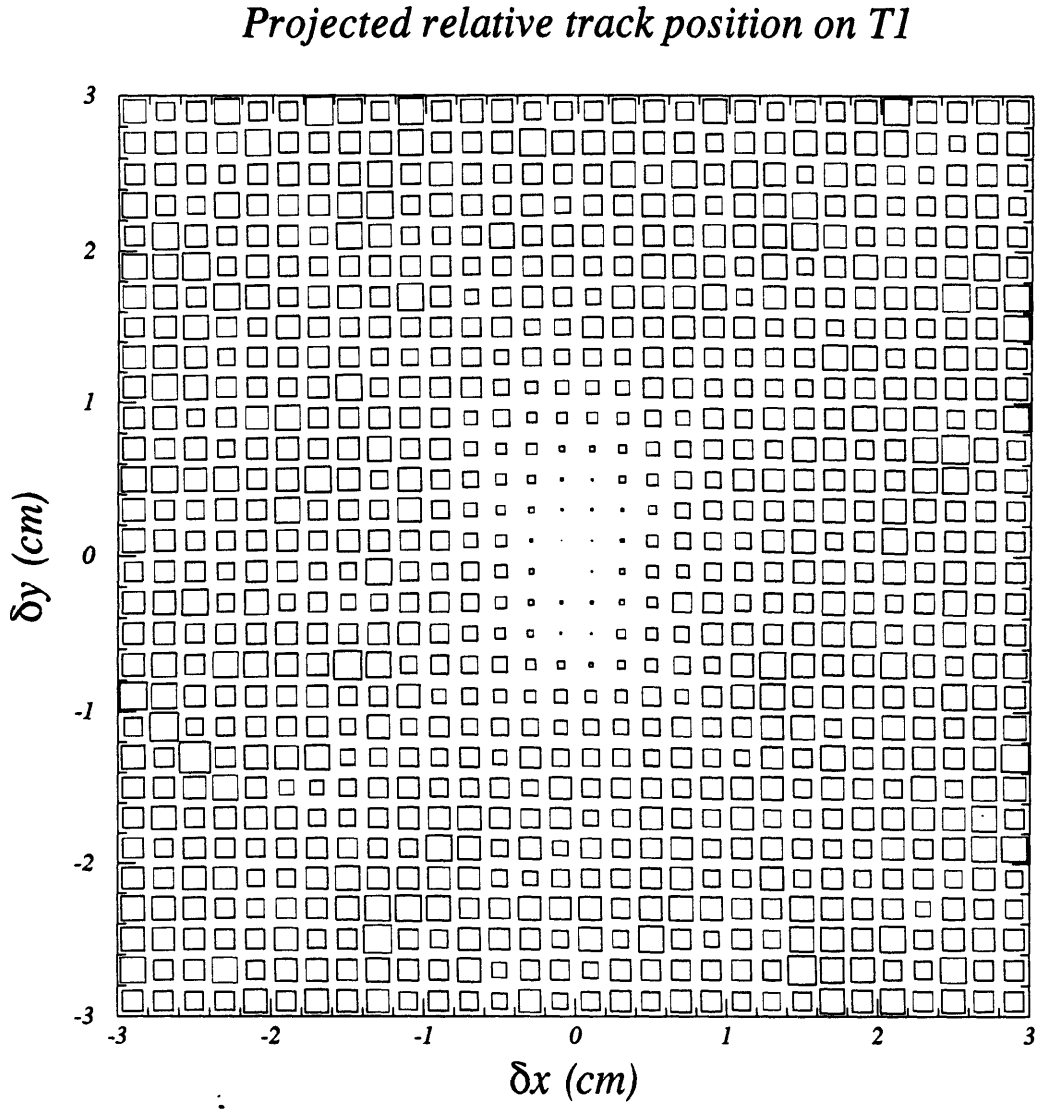

Figure 4-14: Projected relative position on T1 for the Si+Au $\rightarrow 2\pi^-$ central system. The projected distribution has been divided by an event mixed background. All tracks are assumed to come from a single target position at the origin. Also, the sign of the separations have been randomized to correct for ordering asymmetries.

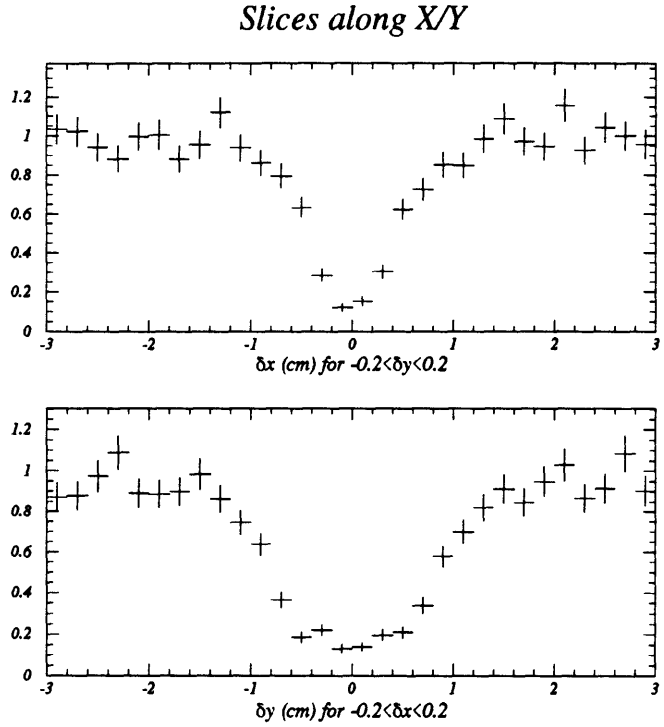

Figure 4-15: Two center slices of Fig. 4-14 in x and y.

For E859 the choice of background prescription is not difficult. The purist's definition of the correlation function as the ratio of the double differential cross-section to product of the singles (Eq. 1.4) is not appropriate for these data. Zajc [Zaj82] and Gyulassy [GKW79] have pointed out that the class of two-particle events is different from the class of one-particle events. Even if one were to compensate for this discrepancy by appropriately weighting the one-particle distributions, one would still have to contend with possible differences between the one- and two-particle acceptance parameterizations. A background made from unlike sign pions is also inappropriate for E859 because the spectrometer does not have equal acceptances for positive and negative particles. Furthermore, one has to either eliminate or correct for the regions in the $\pi^+\pi^-$ spectrum that are affected strongly[11] by the ρ, ω, and η resonance decays. While we have the Monte Carlo simulation and event generator tools needed to correct for these effects, it is much simpler to form a background from pions taken from different events as proposed by Kopylov [Kop74]. In heavy ion physics at AGS energies we are blessed with a large energy reservoir — two pions, each with 1.82 GeV/c, traveling perpendicular to the beam carry away only 3% of the available center of mass kinetic energy of a Si+Al collision. Also, we need not concern ourselves with relating the momenta to a jet axis[12] (a limiting factor for the CLEO experiment [A$^+$85b]).

The prescription for creating the event-mixed background is very simple. After all the previously mentioned cuts have been applied to the data (now in the form of a Qtuple) we select two events at random, checking to verify that a single event is not matched with itself. Then one pion from each event is chosen to form a background pair. These pairs must then pass the same two-particle cuts that have been applied to the data (delta slat and relative x-y momentum cuts). Multiple use of the same pair of events is permitted, although unlikely. If there are 50K pair events, and ten times that many background pairs are formed, multiple pairs will account for approximately 0.04% of the background. One must be careful in assigning errors to an event-mixed distribution, however. Zajc [Zaj82, Z$^+$84] uses a toy model to demonstrate that the errors for such a distribution are not Poisson. For his model, the analog of forming all possible background pairs leads to a relative error that goes as $(\frac{1}{B})^{\frac{1}{4}}$ instead of $(\frac{1}{B})^{\frac{1}{2}}$, where B is the number of background pairs formed. In Appendix C, we extend this model to apply to our situation, where we form only a random subset of all possible pairs. This model predicts that the errors will be approximately Poisson, provided

[11] no pun intended

[12] It can be argued that mixing particles from events with different reaction planes will bias the background. However, at this time there does not exist any strong evidence to link the reaction plane to measured particle spectra for collisions at these energies.

that one does not *over-mix* the background. For our data sets, this corresponds to a background that is not more than ten times the number of actual pairs. An empirical study of the data (also in Appendix C) shows that this model provides a conservative estimate of the true errors, which depend upon both the binning and the relative momentum distributions. For this analysis they are well approximated by Poisson errors at almost all levels of mixing.

As stated above, the ideal background should be devoid of any effects from the Bose-Einstein correlation. Yet by selecting pions from two particle events we introduce a residual Bose-Einstein correlation into the background through the distortion of the single pion momentum spectrum that exists for events with two identical pions [Zaj82, Z+84]. The single pion momentum spectrum that we use to generate the background is

$$\begin{aligned} \rho_m(p_1) &= \int \rho(p_1, p_2) dp_2 \\ &= \int C_2 \rho(p_1)\rho(p_2) dp_2. \end{aligned} \tag{4.3}$$

Here the region of integration is the spectrometer acceptance. Thus, the background will be more distorted for a very small aperture experiment for which the enhanced region will consume a greater fraction of the two-particle acceptance.[13] From Equation 4.3 we see that if the value of C_2 is known, one can correct for this residual correlation in the background. An iterative procedure is often used [Zaj82, Z+84], whereby a final corrected correlation function is calculated. This procedure was applied to the E859 data by Cianciolo [Cia94] in the following manner:

1. An initial correlation is formed with the uncorrected ratio (A/B).
2. A weight is calculated for each pion in the background. This weight is determined by taking a random sample of partners and calculating the average value of the correlation for these pairs.
3. The background is re-projected, each pair being weighted by the inverse of the product of the individual weights of each particle in the pair.
4. A new correlation is formed, and we return to step 2 above.

Fig. 4-16 shows the effect of performing six iterations on the Q_{inv} correlation for the Si+Au $\rightarrow$ 2K$^+$ system.

[13] In the absurd limit of an acceptance which measures only pairs in the enhanced region (q $\rightarrow$ 0), use of an event-mixed background will lead to a correlation function which is a constant ($1/C_2(q = 0)$).

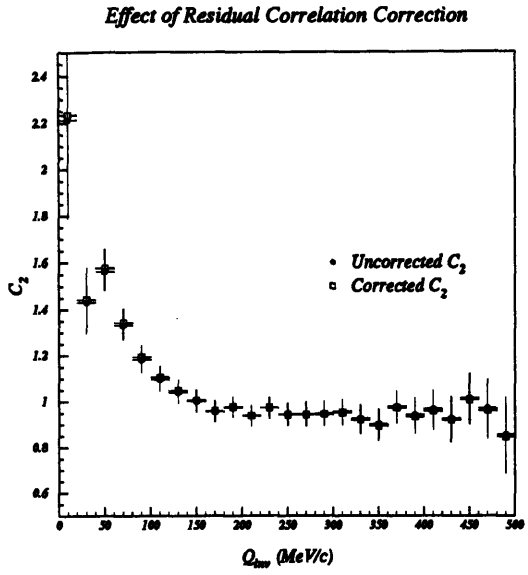

Figure 4-16: The Si+Au $\rightarrow$ 2K$^+$ Q_{inv}correlation function with no correction for residual correlations and after a six-iteration correction.

For this figure the weights have been calculated using the correlation function parameterized in Q_{inv}. However, there is no reason why this must be so. In fact, using a higher dimension parameterization of the correlation function to ascribe weights to the background is likely to be a better approximation to the *true* correlation. Fig. 4-17 shows the percent change in the fit parameters for three different parameterizations of the correlation function. Iterations one through six refer to the percent change with respect to the uncorrected fits; the weights are determined using the same parameterization used to fit the data. The last two data points in each plot refer to the percent change in the parameters for the sixth iteration in which two other parameterizations are used to determine the residual correlation correction weights. The errors in Fig. 4-17 represent the relative errors between the plotted points. They were obtained by multiplying the absolute errors of the fit parameters by the error in the weights used in a given bin divided by the square-root of the number of counts in a bin. All of the corrections lead to a 2–5% increase in λ and a comparable decrease in the radii and lifetimes, consistent with the E802 results for pions [A$^+$92a]. None of the data presented in this thesis have been corrected in this fashion.

4.4.2 Correction Weights

Two sets of correction weights are applied at the time of filling the actual and background histograms. The weights applied to the actual distribution are inversely proportional to the inefficiency for

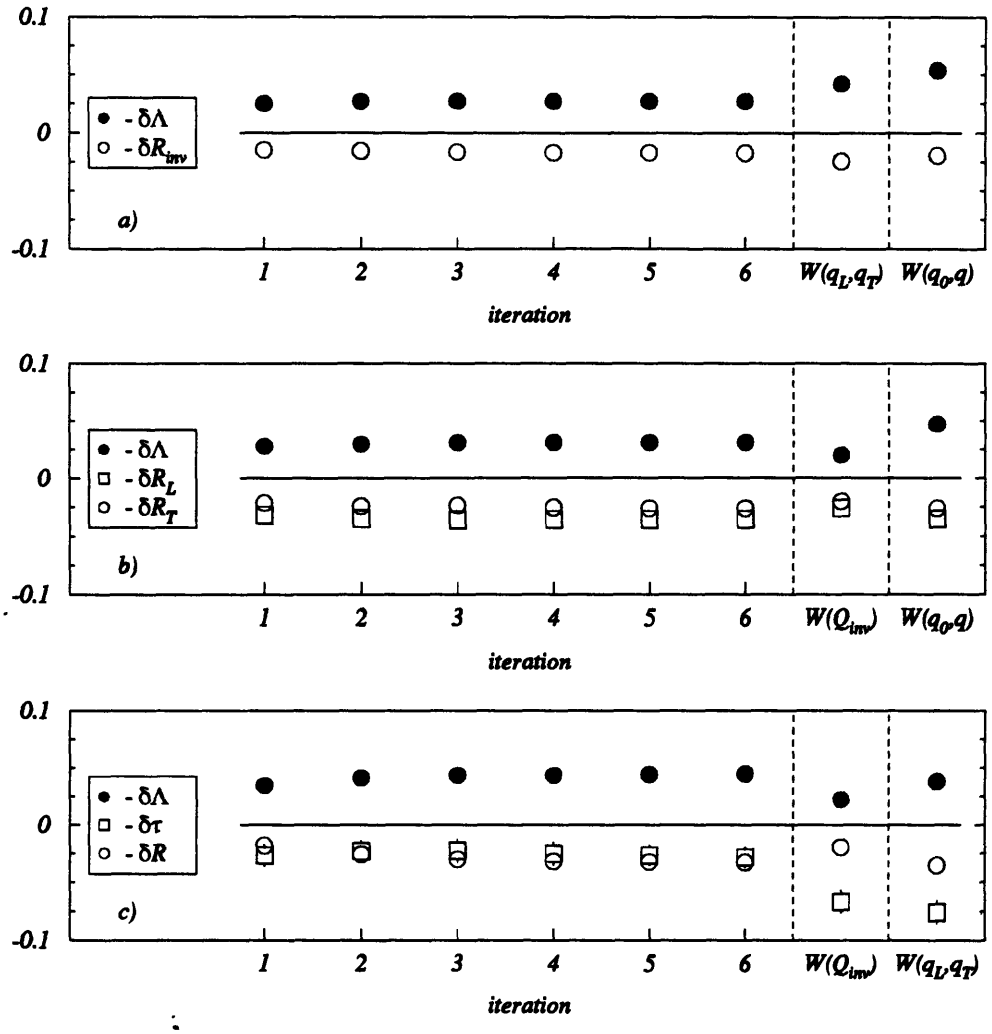

Figure 4-17: The relative change in fit parameters for iterations one through six using the same identical parameterizations for the correlation fit and for the calculation of the weights. The results of the sixth iteration are plotted for the case when a different parameterization was used to calculate the weights. Courtesy of V. Cianciolo.

detecting close pairs. Those applied to the background are the Gamow correction weights, which simulate the Coulomb repulsion for the event-mixed pion pairs.

Close-pair

The close pair correction weights were derived using the same method used to select the close pair cuts; the relative x and y momentum were projected onto T1 for both the data and an event-mixed background. The Si+Au $\rightarrow 2\pi^-$ HBT *Stream* was used for this, which contains the set of all triggered events that contain one TOF-identified pion and at least one other full status reconstructed track. The following cuts were applied:

1. Identical pion pairs (for pions meeting the definitions set in Sec. 4.3.2) were excluded.

2. A close-pairs cut of 0.005 using equation 4.2 was applied.

3. Pairs striking the same TOF slat were excluded.

The first cut was applied to prevent the Bose-Einstein enhancement from biasing the result. To include such pairs would lead to a slight underestimate of the real inefficiency. These pairs account for 20% of the data set. Other pairs of identical particles account for a much smaller fraction of the data set and were not excluded. No attempt was made to remove the effects of the Coulomb repulsion/attraction that affects all particles. However, since both sign particles were included, we expect the net effect to be negligible. That the important correlations (if indeed there are any) have been removed from the data is supported by the remarkably similar fit parameters obtained from fits to real data and fits to the Monte Carlo data. The cut on close pairs was applied to prevent pairs which we knew would not be included in the analysis from influencing the 2-D Gaussian fit. We deliberately set this cut to be smaller than the expected final value to allow for some flexibility in our final choice. The same-slat cut was applied as well, although we do not expect this cut to noticeably affect this correction procedure.

The Monte Carlo data consists of a set of two pion events, with pion momentum distributions chosen according to the rapidity yields and m_T fits determined by C. Parsons for the E802 data [Par93]. These particles are propagated through a simulation of the spectrometer using GEANT, with all physics processes turned on, then reconstructed and identified using the same PASS12 and PASS3 executables used to process the real data. The pion pairs are free from statistical correlations and Coulomb interactions. Cuts 2 and 3 above are applied to these data, as well as to an event-mixed

background. Both the real and simulated ratios are then fit to a two-dimensional Gaussian of the following form,

$$A/B = N\left[1 - \lambda \exp\left(-\frac{\delta x^2}{2\sigma_x^2} - \frac{\delta y^2}{2\sigma_y^2}\right)\right] \tag{4.4}$$

(4.5)

$$\delta x \equiv \mathrm{T1}_z(p_{x1}/p_{z1} - p_{x2}/p_{z2})$$

$$\delta y \equiv \mathrm{T1}_z(p_{y1}/p_{z1} - p_{y2}/p_{z2}).$$

As can be seen in Table 4.4, the values of σ_x and σ_y produced from fits to the data and the Monte Carlo are identical within errors. The only difference between the two-particle reconstruction efficiency is that for the data, roughly 10% of the pairs with nearly identical x and y momenta are still reconstructed, whereas none of these pairs are found in the Monte Carlo event sample ($\lambda \approx 1$). We attribute this to the presence of background chamber hits, and other particles in the real data, that are missing in the Monte Carlo. In fact, it is not possible to have a cleaner or lower multiplicity environment and still have two particles, short of turning off all the physics processes. That the parameters are very similar indicates that the inefficiency depends primarily on how the reconstruction algorithm handles the hit sharing and not on the minor aspects of drift chamber resolution which are difficult to simulate exactly. Slices of the T1 separations for both the data and Monte Carlo, along with the fitted functions are shown in Fig. 4-18

Parameter	Data	Monte Carlo
σ_x	0.46 ± 0.01	0.45 ± 0.02
σ_y	1.26 ± 0.03	1.30 ± 0.06
λ	0.89 ± 0.02	1.00 ± 0.01

Table 4.4: Fit parameters for close pair weighting function.

Gamow

The Gamow correction [Dav65, pp 401–404] is the square of the two-pion Coulomb wave-function at the origin normalized to its asymptotic value.

$$G = \frac{|\psi(r=0,k)|^2}{|\psi(r\to\infty,k)|^2} = \frac{2\pi\eta}{e^{2\pi\eta}-1} \quad ; \quad \eta = \frac{m_\pi e^2}{\hbar Q_{inv}} \tag{4.6}$$

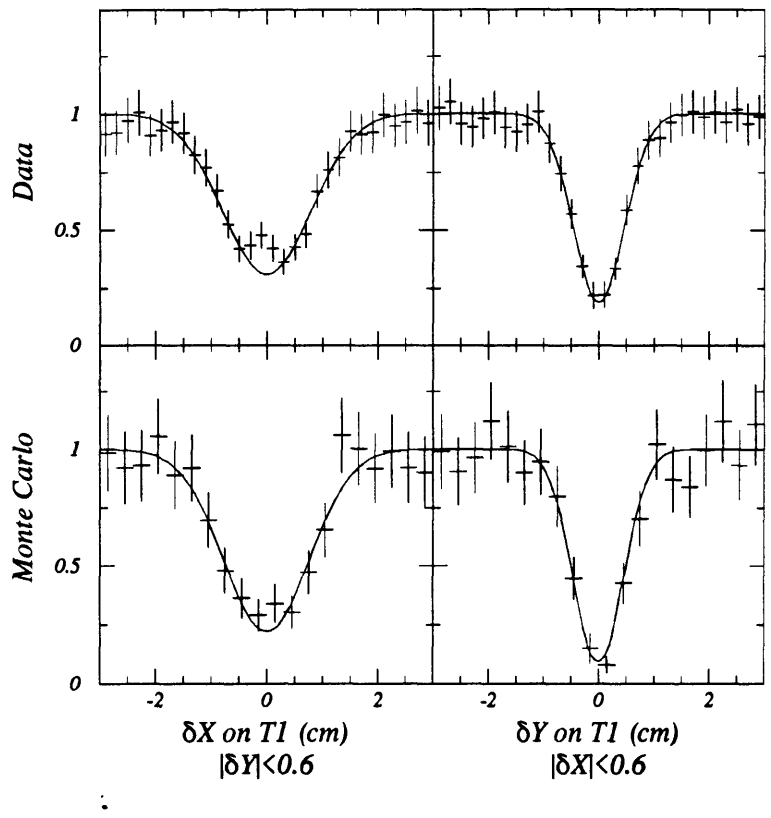

Figure 4-18: Slices for the T1 hole and fitted function for both the data and the Monte Carlo.

Thus, it is a function of Q_{inv}. Unlike the close-pair weights, which are applied as a correction to the Actual, the Gamow correction is applied to each pair in the Background. Integrating this quantity over a finite source leads to correction terms (in the low Q_{inv} region) on the order of the radius over the Bohr radius [Zaj82, pp 108-112]. For pions the Bohr radius is $\sim$194 fm, and these corrections are negligible.

4.4.3 Fitting Procedures

As stated in Sec. 4.1.5, we have two different minimization functions which we can use to find the most likely correlation function to fit the data. Both follow the treatment in [Zaj82, pp 56–59] in that they are log-likelihood functions generalized to match a chi-squared statistic in the limit of large counts. The first of them is a likelihood-chi-squared function to which a background errors term has been added. It was put forth by Zajc [Zaj91] and has been used extensively for the E802 analysis and for most of the analysis presented here. The second method, developed recently, introduces background errors in a more natural way, but has not yet been sufficiently tested. Thus far, both minimization functions have produced almost identical fit results. A later update on the status of this fitting technique exists in V. Cianciolo's PhD thesis [Cia94].

Augmented Likelihood-χ^2

We begin with the Poisson probability for observing A counts in the actual distribution, and define the likelihood-χ^2 to be twice the negative logarithm making use of Stirling's approximation, but without the additional $\sqrt{2\pi A}$ term. This definition comes from the analogous definition of the standard χ^2 statistic which is just the logarithm of a Gaussian probability distribution. In the limit of large counts, the Poisson distribution is well approximated by a Gaussian. For now we will treat all distributions as if they contain only one bin — the generalization to n bins is simply a product of the individual probabilities (ie. a sum over the log of the probabilities).

$$\begin{aligned} P(A|\mu) &= \frac{\mu^A}{A!}e^{-\mu} \\ \chi^2_{PML} &= -2\ln P(A|\mu) - \ln(2\pi A) \\ &= -2\left[(\mu - A) - A\ln\frac{\mu}{A}\right] \end{aligned} \tag{4.7}$$

The mean, μ, is the expected value of the actual distribution, C_2B. In the limit of large counts,

$$\begin{aligned}
\lim_{A\to\infty} \chi^2_{PML} &= -2\left[(\mu - A) - A\ln\left(\frac{\mu - A}{A} + \frac{A}{A}\right)\right] \\
&= -2\left\{(\mu - A) - A\left[\left(\frac{\mu - A}{A}\right) - \frac{1}{2}\left(\frac{\mu - A}{A}\right)^2 + O\left(\left(\frac{\mu - A}{A}\right)^3\right)\right]\right\} \\
&= \frac{(\mu - A)^2}{A} \\
&= \frac{(\mu - A)^2}{\sigma_A^2}
\end{aligned} \tag{4.8}$$

We thus recover χ^2. However, the χ^2_{PML} presumes that for a particular guess of the value of the correlation, C_2, we know the mean of the background distribution exactly. It is only accurate when the errors in the background are negligible compared to those in the actual. Since we generate a background which contains at most a factor of ten times the number of pairs in the actual distribution, this assumption is not valid here. In order to extend the likelihood-chi-squared formula, Zajc identified the A terms in Eq. 4.8 which lead to the final σ_A^2 term and replaced them with $\sigma_A^2 + \sigma_{C_2B}^2$. If we also substitute C_2B for μ we arrive at Eq. 7 of [Zaj91],

$$\chi^2_{PMLA} = -2\left[(C_2B - A) - \left(\sigma_A^2 + \sigma_{C_2B}^2\right)\ln\frac{(C_2B - A) + \left(\sigma_A^2 + \sigma_{C_2B}^2\right)}{\left(\sigma_A^2 + \sigma_{C_2B}^2\right)}\right]. \tag{4.9}$$

In the limit of large counts this augmented likelihood-χ^2 reduces to the standard χ^2 for the difference of two distributions, each exhibiting Gaussian fluctuations,

$$\lim_{A,B\to=\infty} \chi^2_{PMLA} = \frac{(C_2B - A)^2}{\sigma_A^2 + \sigma_{C_2B}^2}. \tag{4.10}$$

However, as noted by Zajc, that the χ^2_{PMLA} has such a limiting form is the only justification for such a statistic. If one extrapolates backwards, one obtains a probability distribution which is neither Poisson, nor Gaussian,

$$P(A,B) = \frac{\left[C_2B - A + \left(\sigma_A^2 + \sigma_{C_2B}^2\right)\right]^{\left(\sigma_A^2 + \sigma_{C_2B}^2\right)}}{\left(\sigma_A^2 + \sigma_{C_2B}^2\right)!} e^{-\left[C_2B - A + \left(\sigma_A^2 + \sigma_{C_2B}^2\right)\right]}. \tag{4.11}$$

χ^2-Poisson

There is a more general way to introduce fluctuations in background which explicitly accounts for the fact that both the actual and background distributions are Poisson. However, this derivation rests upon the Bayes' Posulate [FSf79, pp 24–29].[14] This is to say that before we have obtained a measurement for the Actual, A, we assume all values of the mean, μ, to have equal probability. Assuming that A is Poisson distributed, this leads to the following probability distribution for μ once A has been measured,

$$F(\mu|A) = \frac{\mu^A}{A!}e^{-\mu}, \tag{4.12}$$

We now apply this to the measurement of A and B, both assumed to be Poisson distributed, with the additional constraint that the ratio of their means, μ/ν, be equal to C_2. The probability distribution for C_2 is given by,

$$\begin{aligned} P(C_2|A,B) &= \iint \frac{\mu^A}{A!}e^{-\mu}\frac{\nu^B}{B!}e^{-\nu}\delta\left(C_2 - \frac{\mu}{\nu}\right)d\mu d\nu \\ &= \int \frac{C_2\nu^A}{A!}e^{-C_2\nu}\frac{\nu^{B+1}}{B!}e^{-\nu}d\nu \\ &= \frac{{C_2}^A}{A!B!}\int \nu^{A+B+1}e^{-(C_2+1)\nu}d\nu \\ &= \frac{(A+B+1)!}{A!B!}\frac{{C_2}^A}{(C_2+1)^{A+B+2}}. \end{aligned}$$

Again we take twice negative logarithm and subtract out the additional square-root terms,

$$\begin{aligned} \chi^2_{Poisson} &= -2\ln P(C_2|A,B) - \ln(2\pi A) - \ln(2\pi B) + \ln\left[2\pi(A+B+1)\right] \\ &= \ln[(A+B+1)!] - \ln(A!) - (B!) + A\ln C_2 \\ &\quad -(A+B+2)\ln(C_2+1)\,. \end{aligned} \tag{4.13}$$

Minimizing this distribution by taking the derivative with respect to C_2 leads to the relation,

$$C_2 = \frac{A}{B+2}. \tag{4.14}$$

This may seem a rather curious result, but keep in mind that we have defined C_2 in terms of the ratio of the means of the Poisson distributions for A and B, which is different from the ratio of their

[14] The author wishes to thank Bill Zajc for bringing Bayes' Theorem and this reference to his attention.

most probable values. In the limit of large counts,

$$\lim_{A,B\to\infty} \chi^2_{Poisson} = \frac{(C_2 B - A)^2}{AB\,(C_2+1)^2\,/\,(A+B)} \tag{4.15}$$

Setting $C_2 = A/B$ the term in the denominator simplifies to $A + C_2^2 B$, which is identical to the χ^2 errors term one would use for the ratio of two Poisson distributions, A and B.

This minimization function properly incorporates the Poisson fluctuations in both the actual and background distributions. It is also well founded in a probability distribution.

Chapter 5

Results

This chapter begins with a discussion of the various parameterizations employed in fitting the correlation function. Specifically, we show the actual and background distributions for each and discuss the interpretation of the fit parameters, paying special attention to the role of the experimental acceptance. This is followed by a presentation of the two-dimensional correlation functions (data and fits) for the multiplicity and forward energy data sets. For each of the data sets we first demonstrate the quality of the fits to the data, and then examine trends among the fit parameters within and between different collision systems. Next, the fits to the three-dimensional correlation functions are presented. Finally we evaluate the systematic errors by varying some of the analysis procedures for a small subset of the data.

5.1 Parameterizations

In all, six parameterizations of the correlation function are used in fitting the data; they are listed in Table 5.1. All of the correlation functions assume Gaussian source distributions. We adopt this convention because it has become a standard by which results of different experiments can be compared. Other functional forms, such as the Kopylov spherical shell [KP74a] or an exponential have also been proposed, and applications of them can be found in the literature (see Chap. 2). To date, the data from heavy ion collisions have not shown a strong preference for one particular source distribution function. However, for high energy elementary particle collisions there is some evidence [A^+93a, B^+89a] that a double-Gaussian and exponential forms of the correlation function both provide a better description of the data than does a single-Gaussian fit.

Each of the parameterizations given in Table 5.1 is discussed at length in the remainder of this

Dimension	Source Distribution	Correlation Function
1-D	$\sim \exp\left(-\frac{r^2-t^2}{2R_Q^2}\right)$	$N\left[1+\lambda e^{-Q_{inv}^2 R_Q^2}\right]$
2-D	$\sim \exp\left(-\frac{r_T^2}{2R_T^2}-\frac{r_L^2}{2R_L^2}\right)$	$N\left[1+\lambda e^{-q_T^2 R_T^2 - q_L^2 R_L^2}\right]$
2-D	$\sim \exp\left(-\frac{r^2}{2R^2}-\frac{t^2}{2\tau^2}\right)$	$N\left[1+\lambda e^{-q^2 R^2 - q_0^2 \tau^2}\right]$
3-D	$\sim \exp\left(-\frac{r_L^2}{2R_L^2}-\frac{r_{Tside}^2}{2R_{Tside}^2}-\frac{r_{Tout}^2}{2R_{Tout}^2}\right)$	$N\left[1+\lambda e^{-q_L^2 R_L^2 - q_{Tside}^2 R_{Tside}^2 - q_{Tout}^2 R_{Tout}^2}\right]$
3-D	$\sim \exp\left(-\frac{r_L^2}{2R_L^2}-\frac{r_T^2}{2R_T^2}-\frac{t^2}{2\tau^2}\right)$	$N\left[1+\lambda e^{-q_L^2 R_L^2 - q_T^2 R_T^2 - q_0^2 \tau^2}\right]$
3-D	$\sim \exp\left(-\frac{r^2}{2R^2}-\frac{t^2}{2\tau^2}\right)_{\text{source frame}}$	$N\left[1+\lambda e^{-(R^2+\tau^2)(\mathbf{q}\cdot\mathbf{U_s})^2+\mathbf{q}^2 R^2}\right]$

Table 5.1: Correlation fit functions and their corresponding source distributions. $\mathbf{U_s}$ is the source velocity four vector. See text for an explanation of the different q variables.

section. Before beginning this discussion, it is interesting to note that much of the difficulty in interpreting the radius parameters comes about through the simple relation between $\vec{q}$ and q_0,

$$q_0 = \vec{q} \cdot \vec{\beta}_{\pi\pi}. \tag{5.1}$$

Here $\vec{\beta}_{\pi\pi} = (\vec{p}_1 + \vec{p}_2) / (E_1 + E_2)$ is the pion pair velocity. Thus, even if all of our simplifying assumptions regarding the nature of the collision ring true, and each dimension of the source leads to an enhanced region in the canonically conjugate relative momentum variable, if $\vec{\beta}_{\pi\pi}$does not vary we have only three independent relative momentum variables with which to characterize a four-dimensional source. This has several important concerns for the meaning of the fit parameters. These concerns are discussed below within the context of the various functional forms used to model the correlation.

5.1.1 One Dimension (Q_{inv})

R_Q, the extent of the Q_{inv} enhancement, measures the relative separation of pions within their rest frame at the time the second pion is emitted. While this is the appropriate reference frame in which to measure the pion source for pions produced by the fragmentation of a single $q\bar{q}$ string (see Fig. 2-1), one must be mindful of the Lorentz transformation properties of the fit parameters when using this *invariant* parameterization to study collisions between relativistic heavy ions. If we

assume for the moment that the true source is well described by a spherically symmetric Gaussian distribution with Gaussian lifetime, then we can relate the two-dimensional Gaussian exponent to the invariant parameterization using Eq. 5.1. We first define Q_{inv} in terms of $\vec{q}$,

$$Q_{inv}^2 = \vec{q}^2 - q_0^2 = \vec{q}^2 \left(1 - \vec{\beta}_{\pi\pi}^2 \cos^2\theta\right),$$

Substituting for both $\vec{q}$ and q_0,

$$\vec{q}^2 R^2 + q_0^2 \tau^2 = Q_{inv}^2 \underbrace{\left[\frac{R^2 + \vec{\beta}_{\pi\pi}^2 \tau^2 \cos^2\theta}{1 - \vec{\beta}_{\pi\pi}^2 \cos^2\theta}\right]}_{R_Q^2}. \tag{5.2}$$

Here θ is the angle between $\vec{q}$ and $\vec{\beta}_{\pi\pi}$. If we furthermore assume τ is zero and that $\vec{q}$ is parallel to $\vec{\beta}_{\pi\pi}$ we come to an expression for R_Q which shows this parameter to measure a Lorentz *extended* source, $R_Q = R\gamma_{\pi\pi}$. This is what we expect for a length measurement in a moving lab frame which is simultaneous in the rest frame of the object — the interference occurs when the second pion is emitted[1] from the source. This extension is different for each pion pair in the ensemble, making it difficult to calculate the dimensions of the source except with Monte Carlo techniques. See [Cia94, Zaj93] for an explanation of how this has been applied to the kaon correlation analysis.

Because of the ambiguity in the interpretation of R_Q, we avoid using the Q_{inv} correlation function to study the dependence of the source size on multiplicity and forward energy. Nevertheless, it is convenient to use the one-dimensional form to show the effects of the Gamow and two-particle inefficiency corrections. Fig. 5-1 shows the actual and background distributions for the Si+Au $\rightarrow 2\pi^-$ central data set before and after these corrections are applied. The two-particle correction multiplies the Actual, whereas the Gamow correction multiplies the Background. The successively corrected correlation function is given in Fig. 5-2.

5.1.2 Two Dimensions

The two-dimensional parameterizations have an obvious advantage over the Q_{inv} parameterization; the extra dimension means that we are integrating over fewer degrees of freedom in our projection of the two-pion correlation function. In addition, the two-dimensional parameterizations do not suffer from the same reference frame ambiguities as does the one-dimensional parameterization in

[1] when the last pion to appear or interact does so.

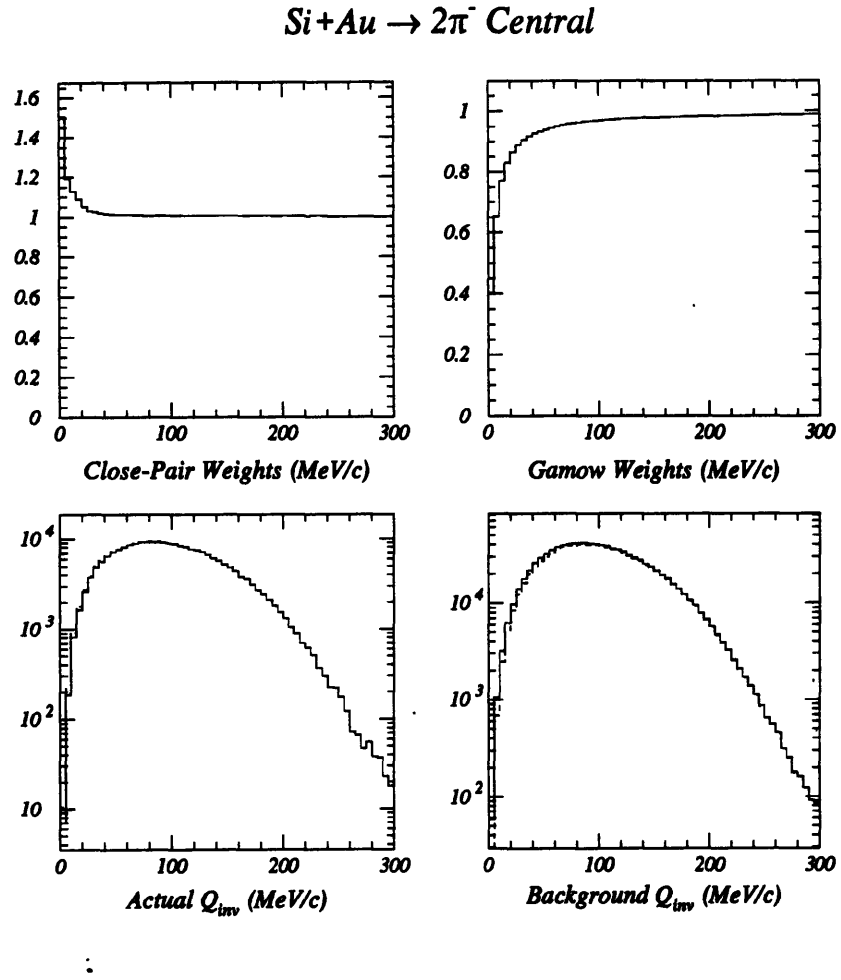

Figure 5-1: Raw (solid) and Corrected (dashed) Actual and Background distributions in Q_{inv}.

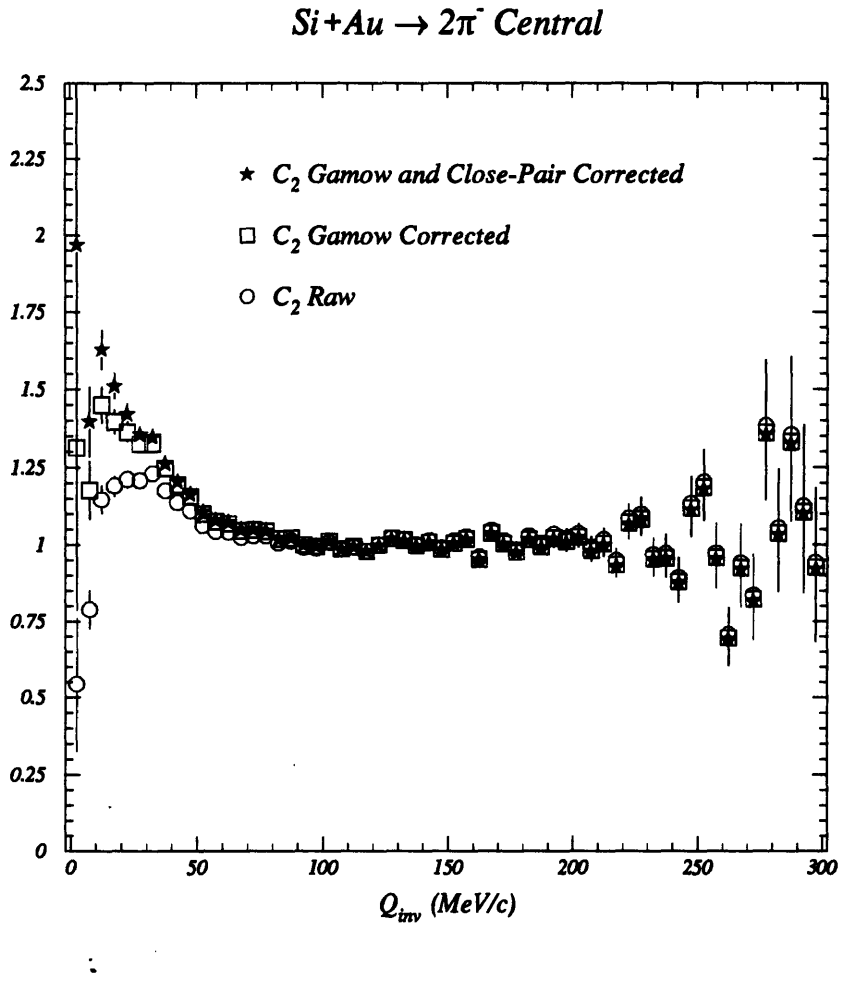

Figure 5-2: Raw (solid) and Corrected (dashed) Correlation Functions in Q_{inv}.

Q_{inv}. Instead, the 2-D fit parameters have their own interpretational difficulties.

q_0-q and the trouble with τ

As shown in figure Fig. 2-1, q_0 and q are a more natural set of variables with which to study the correlation. We now allow for and determine the lifetime (duration) of the pion emission. However, there are several effects intertwined in the interpretation of the τ parameter:

- We cannot distinguish between τ and the component of R parallel to $\vec{\beta}_{\pi\pi}$.
- τ is sensitive to the dynamics of $\vec{\beta}_{\pi\pi}$.
- Mother Nature gives us only a limited window to view the influence of τ.

The first of these effects follows once again from Eq.5.1,

$$\begin{aligned} C_2(q_0,q) &= 1+\lambda\exp\left[-\vec{q}^2R^2-q_0^2\tau^2\right] \\ &= 1+\lambda\exp\left[-\vec{q}^2R^2-\left(\vec{q}\cdot\vec{\beta}_{\pi\pi}\right)^2\tau^2\right] \\ &= 1+\lambda\exp\left[-\frac{\left(\vec{q}\times\vec{\beta}_{\pi\pi}\right)^2}{\vec{\beta}_{\pi\pi}^2}R^2-\left(\vec{q}\cdot\vec{\beta}_{\pi\pi}\right)^2\left(\frac{R^2}{\vec{\beta}_{\pi\pi}^2}+\tau^2\right)\right]. \end{aligned} \tag{5.3}$$

If the source distribution is spherically symmetric, and $\vec{q}$, R, and τ are all insensitive to the direction and magnitude of $\vec{\beta}_{\pi\pi}$, then the component of $\vec{q}$ perpendicular to $\vec{\beta}_{\pi\pi}$ will determine the value of R, and τ will also be fit correctly. However, any difference between components of the source perpendicular to and parallel to $\vec{\beta}_{\pi\pi}$ will result in a modification of the fitted values of τ and R. $\vec{\beta}_{\pi\pi}$ for the detected pions depends upon the experimental acceptance; we discuss $\vec{\beta}_{\pi\pi}$ for E859 below.

The second item above requires some clarification regarding what is meant by "the dynamics of $\vec{\beta}_{\pi\pi}$". Any dynamics which introduce a correlation between the position and momentum distributions of the pions will affect our interpretation of all the fitted parameters. Here we refer specifically to an expanding spherical shell [Pra84] for which pions emitted at different times will have different distributions in $\vec{\beta}_{\pi\pi}$ and the meaning of τ becomes unclear.[2]

Eq. 5.1 illustrates the final difficulty in determining the lifetime through the q_0-q correlation function — that the distribution in q_0-q is limited by the condition: $|\vec{q}| > q_0$. This is seen clearly

[2]We are indebted to Scott Pratt for explaining this point, *repeatedly*

in Fig. 5-3, which shows the actual, the normalized ratio of actual to background, and the fitted function for the Si+Au $\rightarrow 2\pi^-$ central data set.

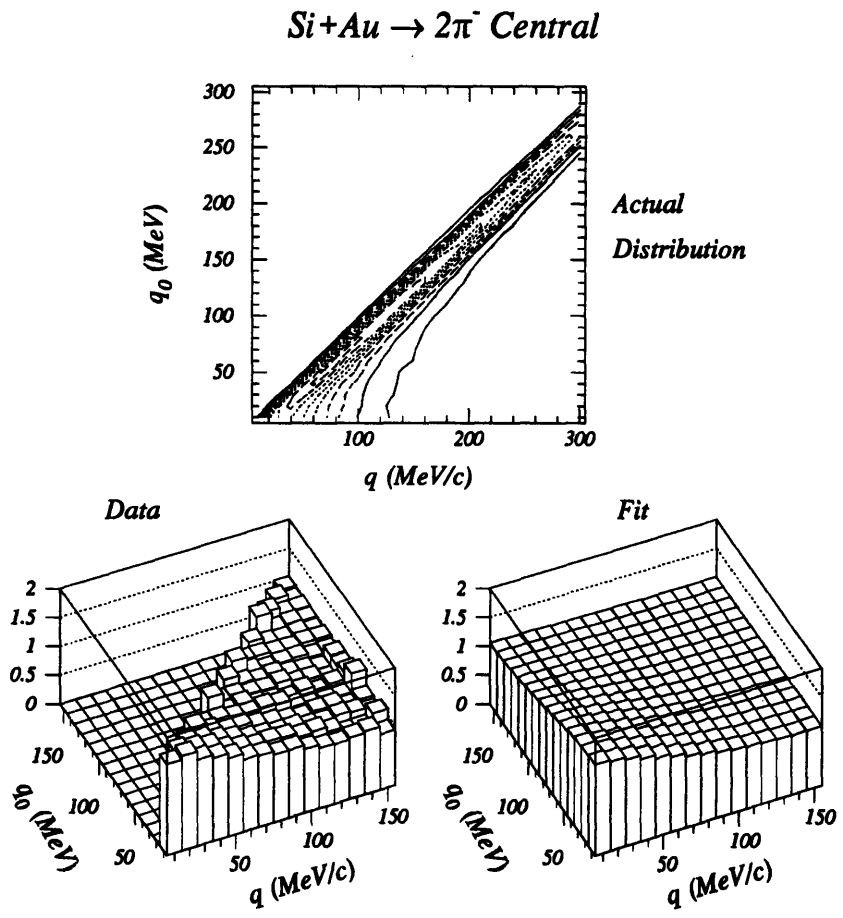

Figure 5-3: Distributions and correlation functions in q_0-q (data and fit) for the Si+Au $\rightarrow 2\pi^-$ central data set.

We have avoided the Lorentz effects of the Q_{inv} correlation function by calculating the variables q and q_0 in the presumed rest frame of the source. Naturally, if this is different from the true rest frame of the source, or if we are dealing with a source distribution with a velocity component, we need to understand how the fit parameters transform under Lorentz boosts. For symmetric systems and for peripheral Si+Au collisions, we use the nucleon-nucleon center of mass rapidity. We use the participant center of mass rapidity (participants are calculated with a Glauber model assuming b=0) for Si+Au central collisions. The reference frames used for the different systems for all fits are summarized in Table 5.2.

System	Rapidity
Si+Al	1.72
Si+Au non-central	1.72
Si+Au central	1.25
Au+Au	1.60

Table 5.2: Summary of reference frames used.

To understand the Lorentz transformation properties of R and τ we start with the Lorentz invariant parameterization of Yano and Koonin [YK78], which reduces to the R-τ fit when the source velocity (β_s) is zero. Evaluating the four-vector dot products leads to,

$$C_2(\mathbf{q}) = 1 + \lambda \exp\left[-\gamma_s^2 \left(\vec{q}\cdot\left(\vec{\beta}_{\pi\pi} - \vec{\beta}_s\right)\right)^2 \left(R^2 + \tau^2\right) + \left(\left(\vec{q}\cdot\vec{\beta}_{\pi\pi}\right)^2 - \vec{q}\cdot\vec{q}\right) R^2\right]. \quad (5.4)$$

To see how this can affect the measured value of R for non-zero β_s, we limit ourselves to one spatial dimension (along $\vec{\beta}_{\pi\pi}$) and examine the argument of the exponent in Eq 5.4 two special cases:

1.) $\beta_{\pi\pi} \to 0$

$$\begin{aligned} -\gamma_s^2 (q\beta_s)^2 \left(R^2 + \tau^2\right) - q^2 R^2 &= -\left(\gamma_s^2\beta_s^2 + 1\right) q^2 R^2 - \gamma_s^2\beta_s^2 q^2\tau^2 \\ &= -\gamma_s^2 q^2 R^2 - \gamma_s^2\beta_s^2 q^2\tau^2 \end{aligned}$$

In this case the measured source is Lorentz extended. This result is not surprising, since our limit of $\beta_{\pi\pi} \to 0$ measures R in the rest frame of the pion pair, as does the Q_{inv} parameterization.

2.) $\beta_{\pi\pi} = \beta_s$

$$-\left(1 - \beta_{\pi\pi}^2\right) q^2 R^2 = -\frac{1}{\gamma_s^2} q^2 R^2$$

This corresponds to emitted pions which are co-moving with the source, and leads to a measurement that is Lorentz contracted.

$q_L - q_T$ and the trouble with R_T

This parameterization has the advantage that $\vec{q}_T$ is invariant under boosts along the the beam (longitudinal) axis. Also, it presumes to measure the oblateness of the source, although it does not directly account for the effects of a non-zero lifetime. As shown in Eq. 5.3, the value of τ

will enter into the component of R which is parallel to $\vec{\beta}_{\pi\pi}$. Fig. 5-4 shows that for the E859 spectrometer positioned at the 14° setting, $\vec{\beta}_{\pi\pi}$ is predominantly transverse to the beam. The normalized projection of $\vec{\beta}_{\pi\pi}$ onto the transverse axes is strongly peaked near unity. This is no accident, since we have deliberately placed the spectrometer at this setting to collect pions emitted at 90° in the center of mass frame. Allowing for a non-zero lifetime and assuming that $\vec{\beta}_{\pi\pi}$

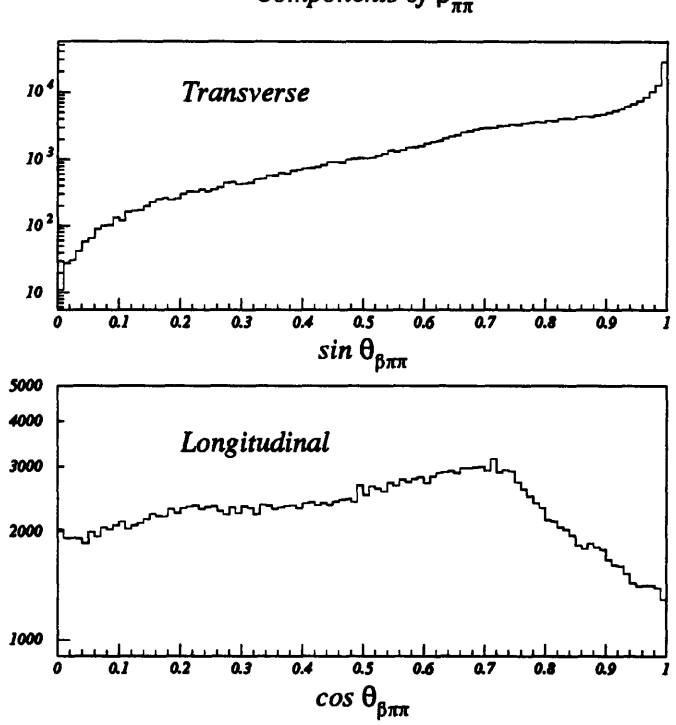

Figure 5-4: Normalized projection of $\vec{\beta}_{\pi\pi}$ onto $\vec{q}_T$ and $\vec{q}_L$ axis for a 14° Si+Au $\rightarrow 2\pi^-$ measurement. $\vec{\beta}_{\pi\pi}$ is calculated relative to a source rapidity of Y=1.25.

lies exclusively in the transverse plane leads to the following expression for the q_L-q_T correlation function,

$$C_2(q_L, q_T) = 1 + \lambda \exp\left[-q_L^2 R_L^2 - q_T^2\left(R_T^2 + \vec{\beta}_{\pi\pi}^2 \tau^2\right)\right]. \tag{5.5}$$

Fitted values of R_T and R_L which satisfy $R_T^2 = R_L^2 + \vec{\beta}_{\pi\pi}^2 \tau^2$ are thus consistent with a spherically symmetric source [A+92a]. The q_L-q_T distributions and correlation functions (data and fit) are shown in Fig. 5-5.

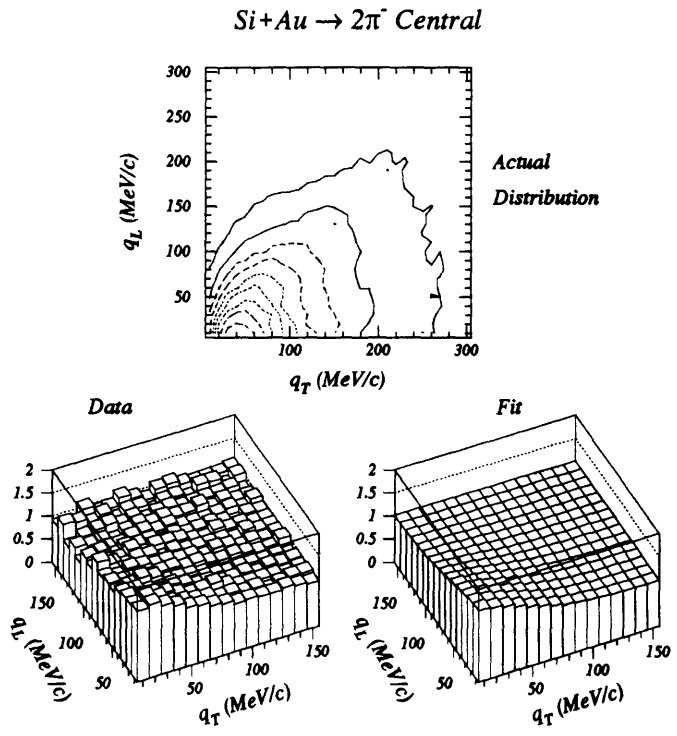

Figure 5-5: Distributions and correlation functions in q_L-q_T (data and functional fit) for the Si+Au $\rightarrow 2\pi^-$ central data set.

5.1.3 Three Dimensions

The three-dimensional fit functions have the capacity to provide a more accurate description of the source. Two of these parameterizations (Bertsch and q_0-q_L-q_T) attempt a better separation of time and space components. The third, the Koonin fit described above, enables one to fit, rather than assume, the source rest frame. Yet, there are few experiments to date (including E859) which have the available statistics to accurately determine three or more source parameters.

$q_0 - q_L - q_T$

This fit function is an augmented version of the two-dimensional functions; it allows for a source with different longitudinal and transverse dimensions and non-zero lifetime. It does not remove the ambiguity between τ and the component of R parallel to $\vec{\beta}_{\pi\pi}$, however. Another problem with the 3-D projections is visualizing them in black & white in two dimensions. Fig. 5-6 shows layered two-dimensional slices of the actual distribution. The actual distributions (left) are shown for three slices in q_0. They show the strong correlation between q_T and q_0 implied by Fig. 5-4. As with the R-τ parameterization the value of q_0 is constrained by q_L and q_T. The separation of q into transverse and longitudinal provides some addition leverage on τ, but there are fits, such as this one, for which τ is undetermined. See Table 5.5 for a listing of the fit parameters.

Bertsch

The Bertsch fit explicitly removes the contribution of τ to one of the parameters by setting one component of the transverse relative momentum, $\vec{q}_{Tside}$, perpendicular to $\vec{\beta}_{\pi\pi}$. The remaining component, $\vec{q}_{Tout}$, is parallel to $\vec{\beta}_{\pi\pi}$. The separation of the relative momentum into components along and perpendicular to $\vec{\beta}_{\pi\pi}$ was first suggested by Kopylov [Kop74] and later expanded upon by Pratt [Pra86] as a way of exploring the long pion emission times expected for a plasma freeze-out. Bertsch [Ber89] applied this separation specifically to the transverse component of the relative momentum, to take advantage of the azimuthal symmetry.[3] The q_{Tside}-q_{Tout}-q_L variables are defined with respect to the $\vec{p}_{beam}$ and $\vec{\beta}_{\pi\pi}$ vectors according to Fig 5-7. Bertsch suggests that one can use the condition $R_{Tout} \gg R_{Tside}$ as a test for the long pion emission times for a decaying plasma. The Bertsch fit function is frequently used to calculate a lifetime via the relation $\tau = R_{Tout} - R_{Tside}$.

[3]While an ensemble of truly central collisions should possess azimuthal symmetry, this may not be explicitly true for the central collision sources seen by our spectrometer or for peripheral collisions in general.

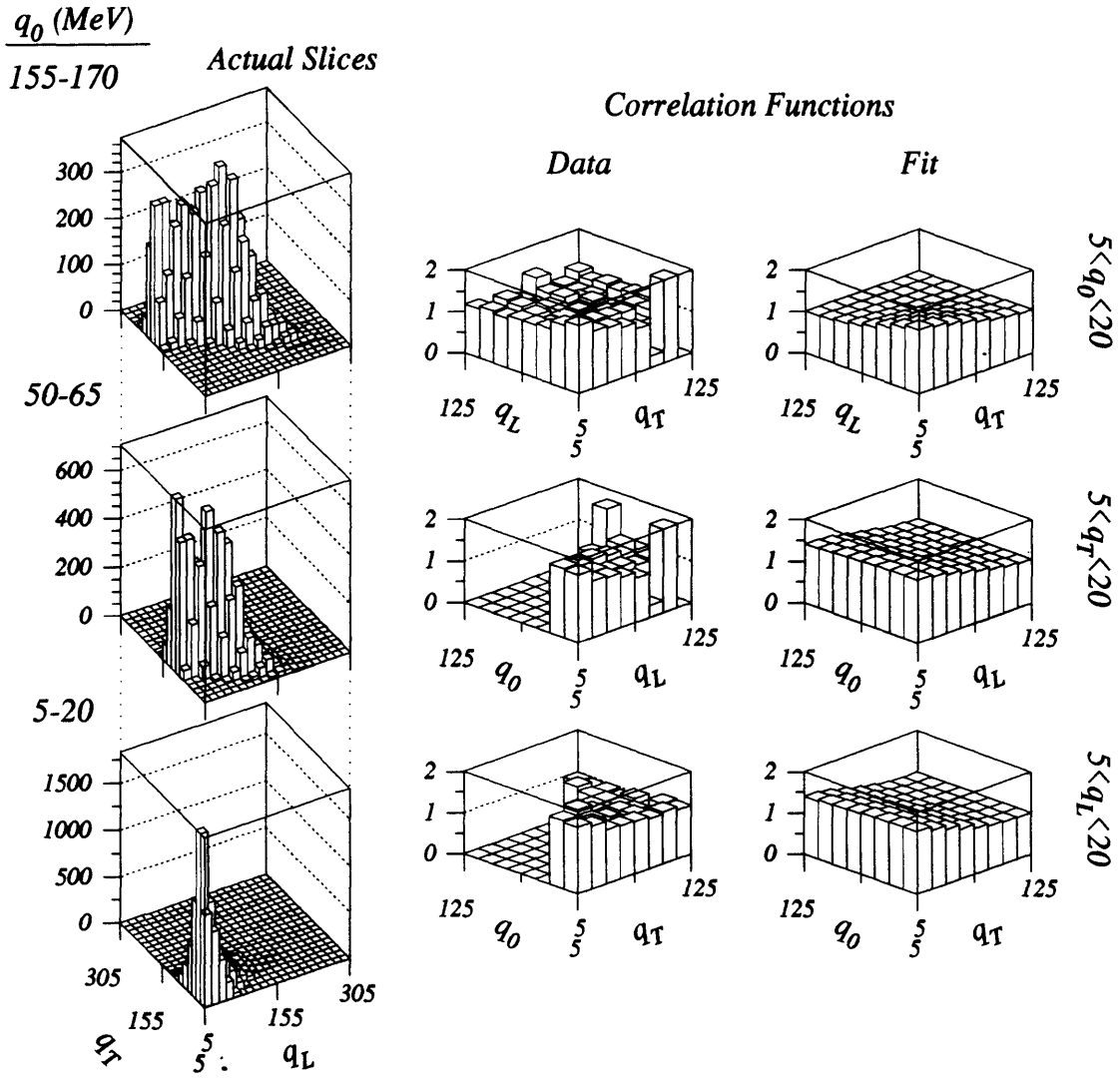

Figure 5-6: Actual Distributions (slices in q_0) and correlation functions for q_0-q_L-q_T (data and fit slices) for the Si+Au $\rightarrow 2\pi^-$ central data set.

This is only true in the approximation $\vec{q}_L \cdot \vec{\beta}_{\pi\pi} = 0$. The actual distributions and correlation functions for the Si+Au $\rightarrow 2\pi^-$ central system are shown in Fig. 5-8. The distributions show nearly full coverage in all variables, except that the distribution in q_{Tside} does not extend much beyond the region of the enhancement. For this reason the R_{Tside} parameter has, on average, a larger error than the other two radii.

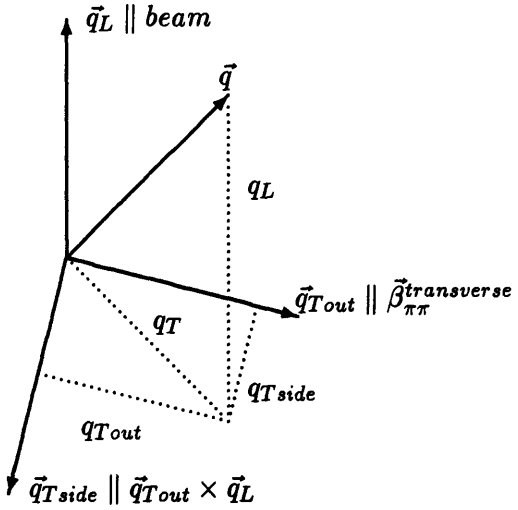

Figure 5-7: Diagram of the q_{Tside}-q_{Tout}-q_L variables. Courtesy of V. Cianciolo.

Koonin

The Lorentz invariant form of the correlation function of Yano and Koonin [YK78] has already been discussed above. We will use this function to test our assumptions regarding the reference frame of the source. The distributions are shown in Figs. 5-9 and 5-10 for a rapidity of 1.25 and 0.0 respectively. Note that the distribution in q_0 and q_L becomes constricted and extended along the diagonal as the reference frame moves further from the source rest frame. Ideally, the Koonin fit should give the same results regardless of the reference frame chosen for the variables. However, we find that this is not the case. The behavior of the Koonin fits for different reference frames will be discussed further in Sec. 5.5.

We can extend this formula to allow for different longitudinal and transverse source components and still preserve invariance under boosts along the beam axis. We make no attempt to fit our data

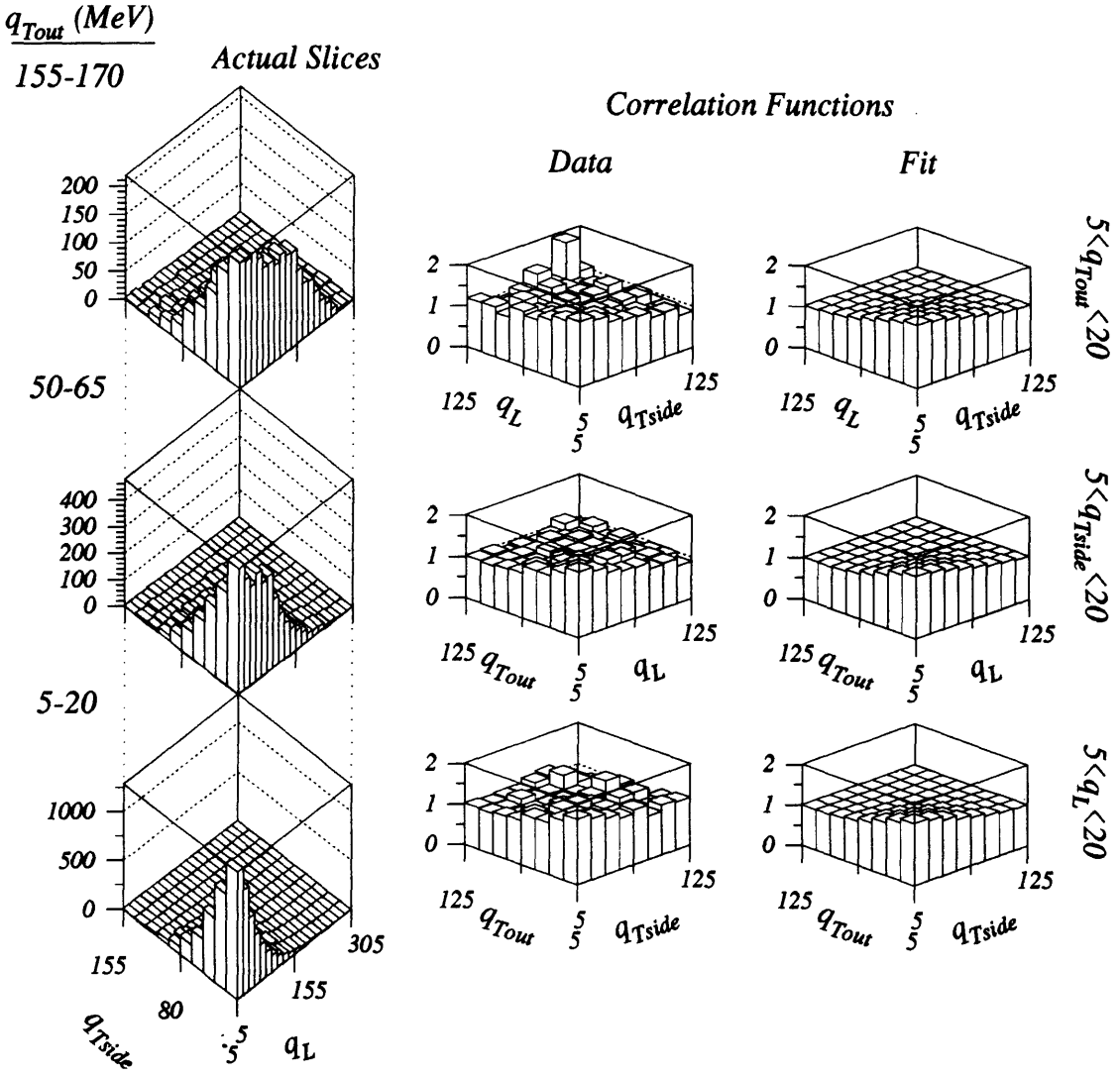

Figure 5-8: Actual distributions (slices in q_{Tout}) and correlation functions for q_{Tside}-q_{Tout}-q_L (data and fit slices) for the Si+Au $\rightarrow 2\pi^-$ central data set.

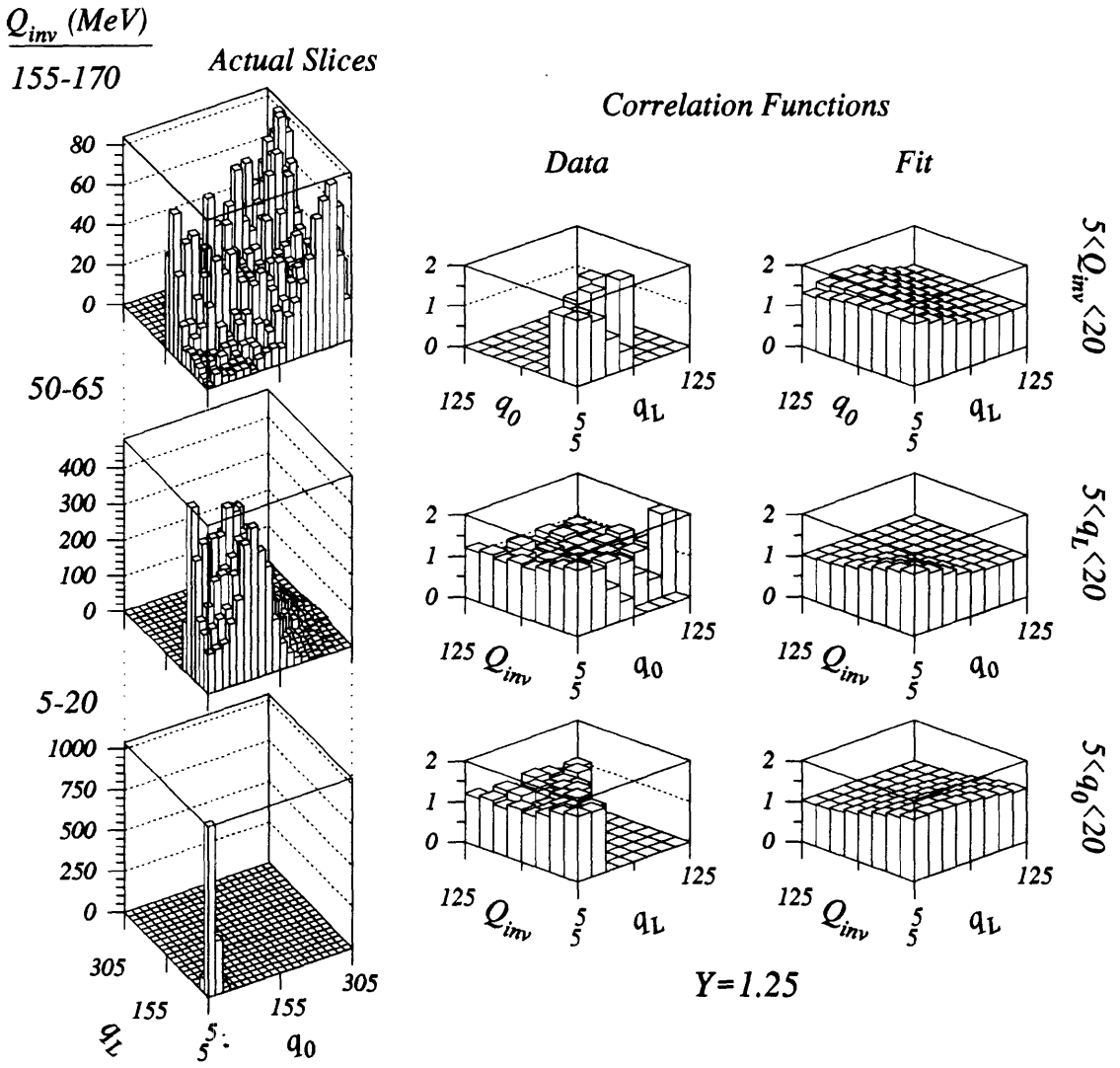

Figure 5-9: Actual distributions (slices in Q_{inv}) and correlation functions for the Koonin (data and fit) for the Si+Au → $2\pi^-$ central data set. All distributions are in the Y=1.25 frame.

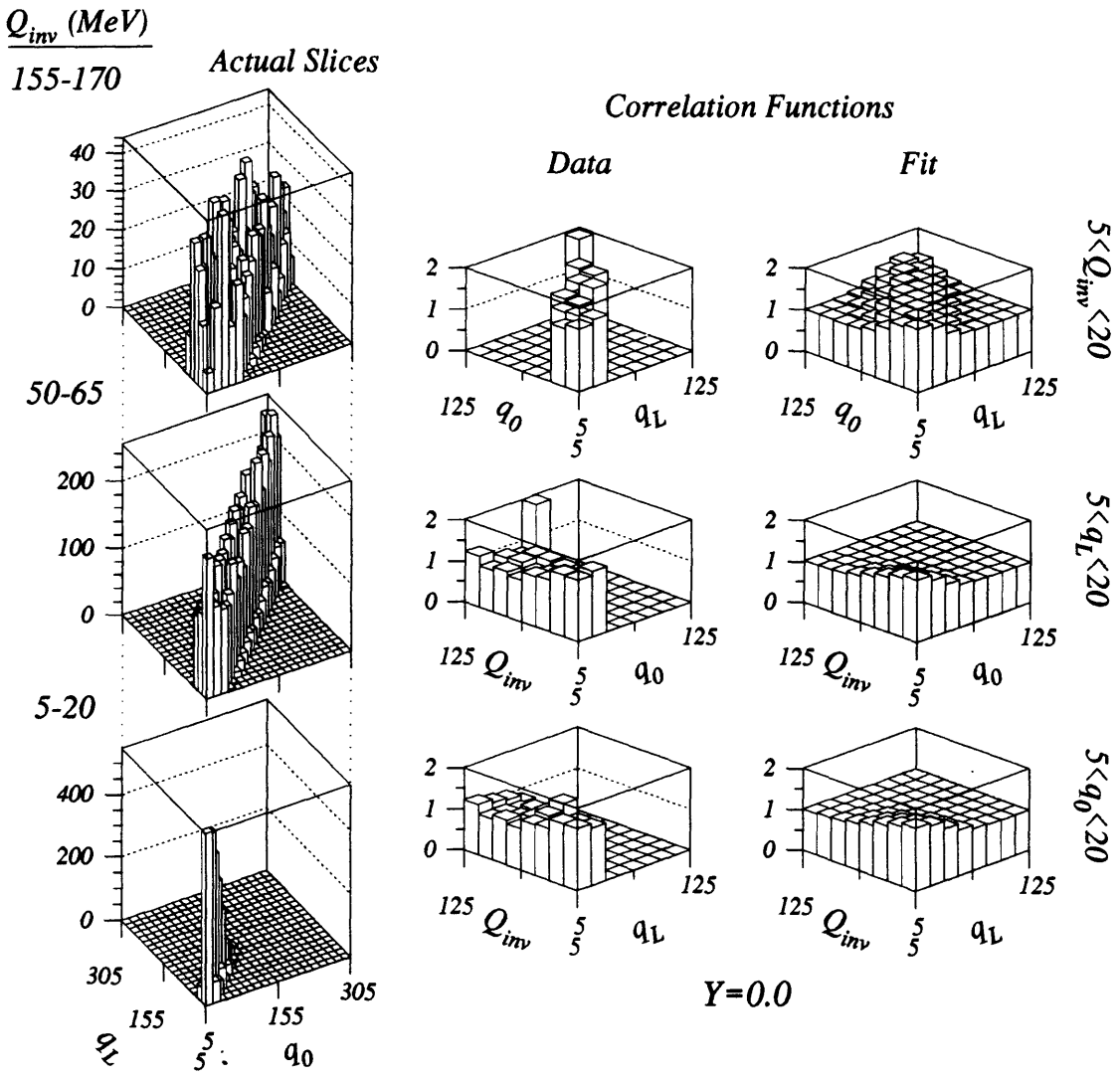

Figure 5-10: Actual distributions (slices in Q_{inv}) and correlation functions for the Koonin (data and fit) for the Si+Au $\rightarrow 2\pi^-$ central data set. All distributions are in the lab (Y=0.0) frame.

to this four-dimensional beast.

$$C_2(\mathbf{q}) = 1 + \lambda \exp\left[-\left(R_L^2 + \tau^2\right)(\mathbf{q}\cdot\mathbf{U_s})^2 - Q_L^2 R^2 - q_T^2 R_T^2\right]. \tag{5.6}$$

5.2 Multiplicity Fit Results

Here we present the correlation fit results for the data sets listed in Tab. 4.2 of Section 4.3.1. The data are fit using the R-τ and R_T-R_L two-dimensional parameterizations. We first inspect the quality of fits to the data for the Si+Au and Si+Al systems. After comparing the E859 measurements to those made by E802 we search for trends in the fit parameters for each system.

Because it is difficult to show on one plot the full two-dimensional distributions for the data and fit function we elect to show slices of the data (with errors) in one dimension, with the appropriate slice of the fit function superimposed. Figs. 5-11 and 5-12 show the R-τ correlation functions for the eight data sets. Each successive slice in q_0 is missing an additional bin due to the restricted q_0-q phase space. Overall, the data are well fit by these parameterizations of the correlation function.

Figs. 5-13 and 5-14 show the slices of the R_T-R_L data and fit functions. Again the data are well fit, and there is no evidence for any systematic deviations from the fit. This claim is supported by the distributions of the deviation (data *minus* fit divided by uncertainty) per bin, shown in Fig. 5-15 for the distributions with the most and least number of pairs. For Gaussian errors on the correlation function, these distributions should follow the Gaussian curves shown in Fig. 5-15. This will only be true for bins which have large numbers of counts in both the Actual and Background distributions. We suspect that the distributions are slightly skewed to the right because there are fewer counts in the Actual than in the Background and bins with zero counts (Actual more often than Background) are excluded from our fitting procedure.

We compare the E859 R-τ results with the E802 published results in Fig. 5-16. There are several distinctions between the two data sets. Both the reconstruction algorithms and particle identification schemes used for E802 and E859 are different. Furthermore, the E802 data have been corrected for residual correlations in the background (a $\sim$ 5% reduction in R and τ), whereas the E859 have not been corrected in this way. The E859 data sets for the Si+Au system are taken from the three-dimensional fit distributions (Sec. 5.5) which used a centrality cut of 10%, similar to the 12% cut of E802. The Si+Al fits shown for E859 correspond to a 20% centrality cut. The higher statistics E859 measurements for Si+Au $\rightarrow 2\pi^-$ and Si+Al $\rightarrow 2\pi^+$ provide a better determination

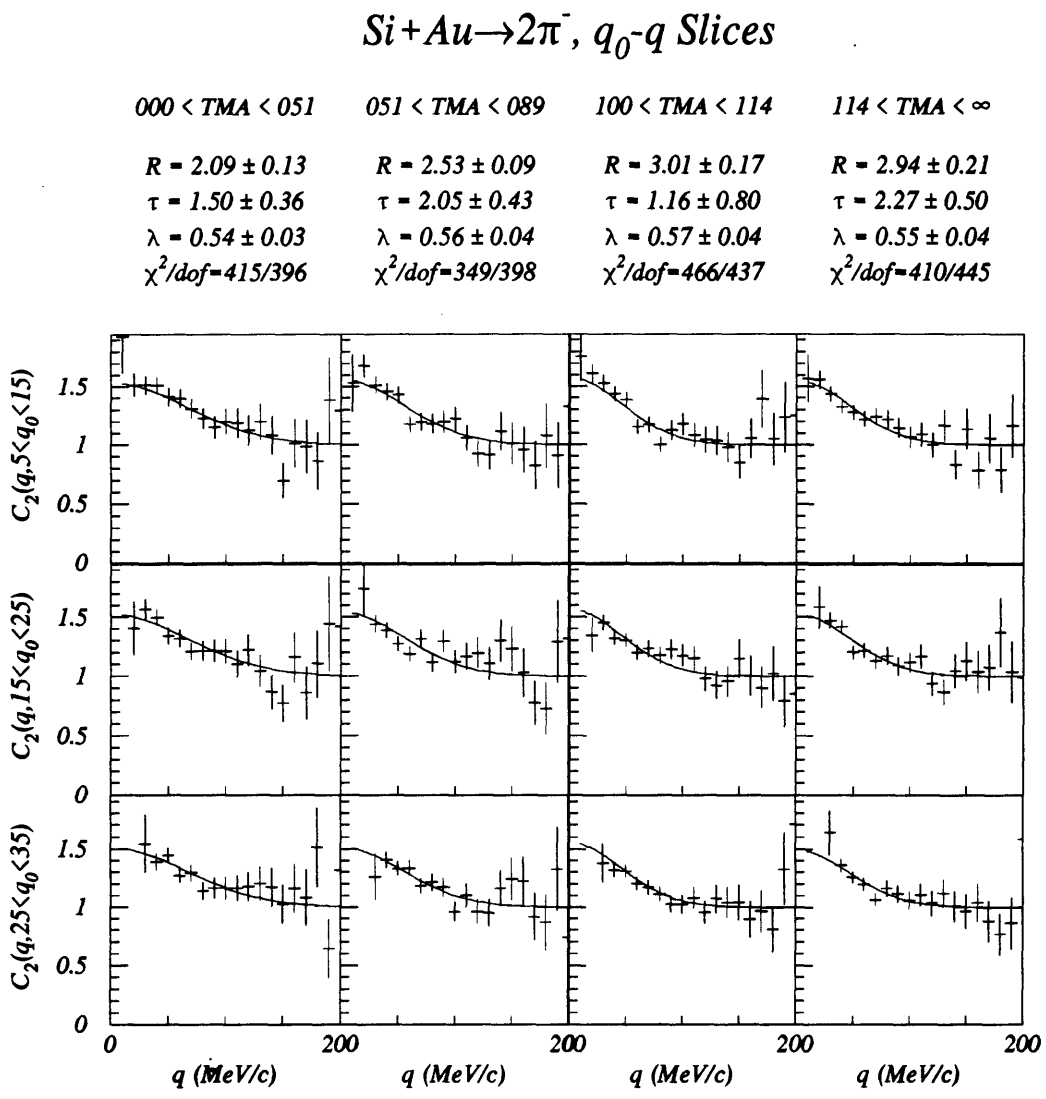

Figure 5-11: Slices (q_0-q) for Si+Au $\rightarrow 2\pi^-$ multiplicity data sets.

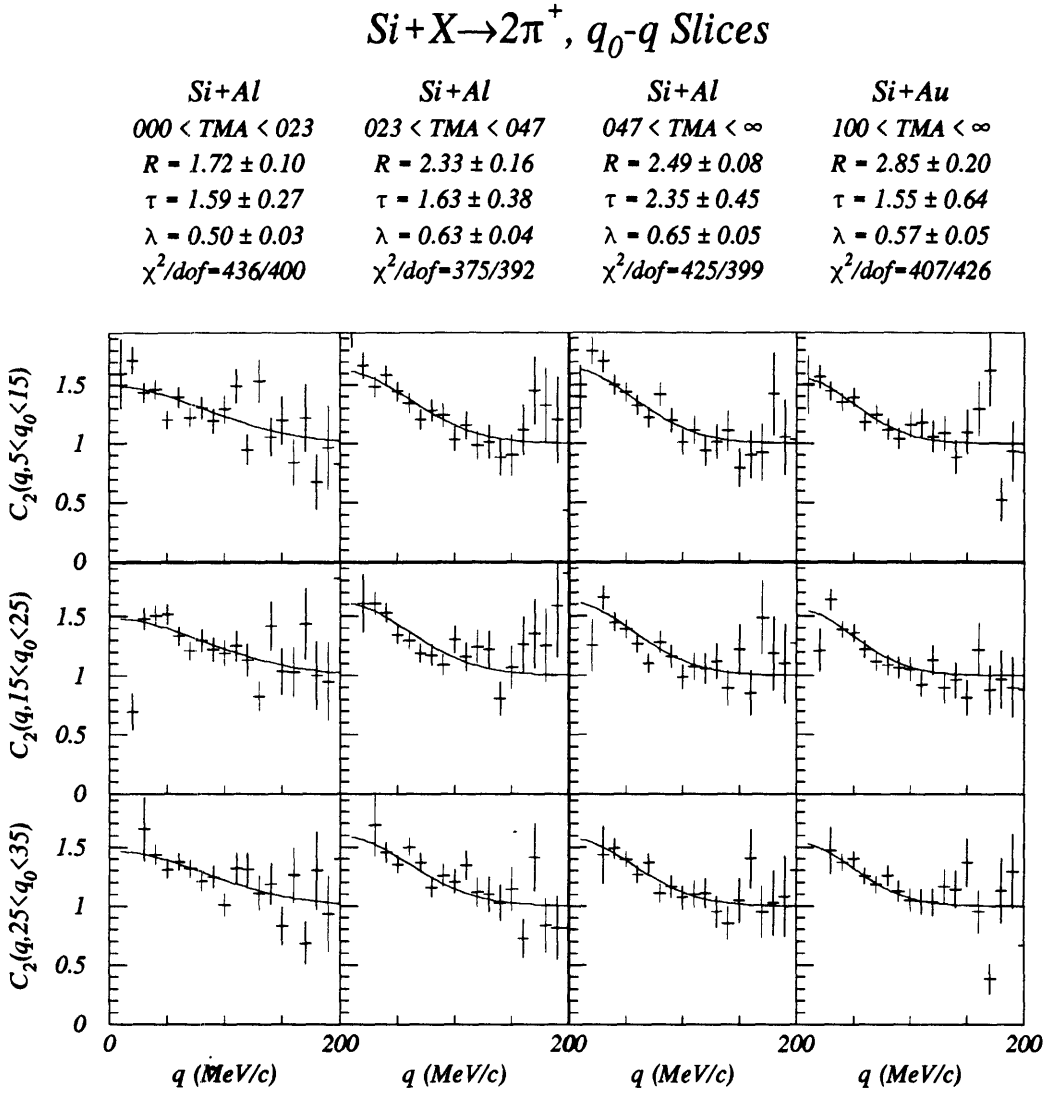

Figure 5-12: Slices (q_0-q) for Si+Al → $2\pi^+$ and Si+Au → $2\pi^+$ multiplicity data sets.

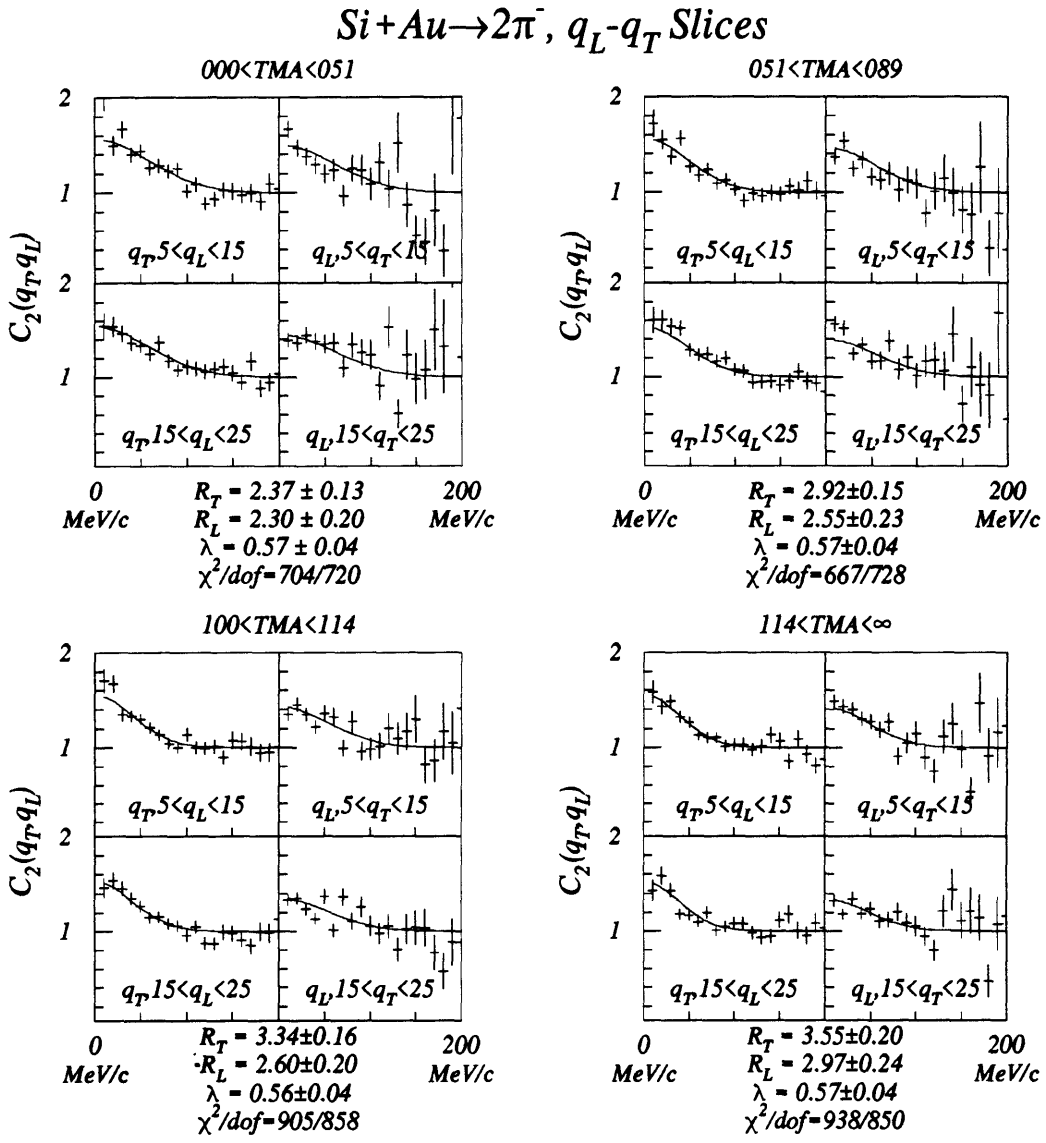

Figure 5-13: Slices (q_L-q_T) for Si+Au → $2\pi^-$ multiplicity data sets.

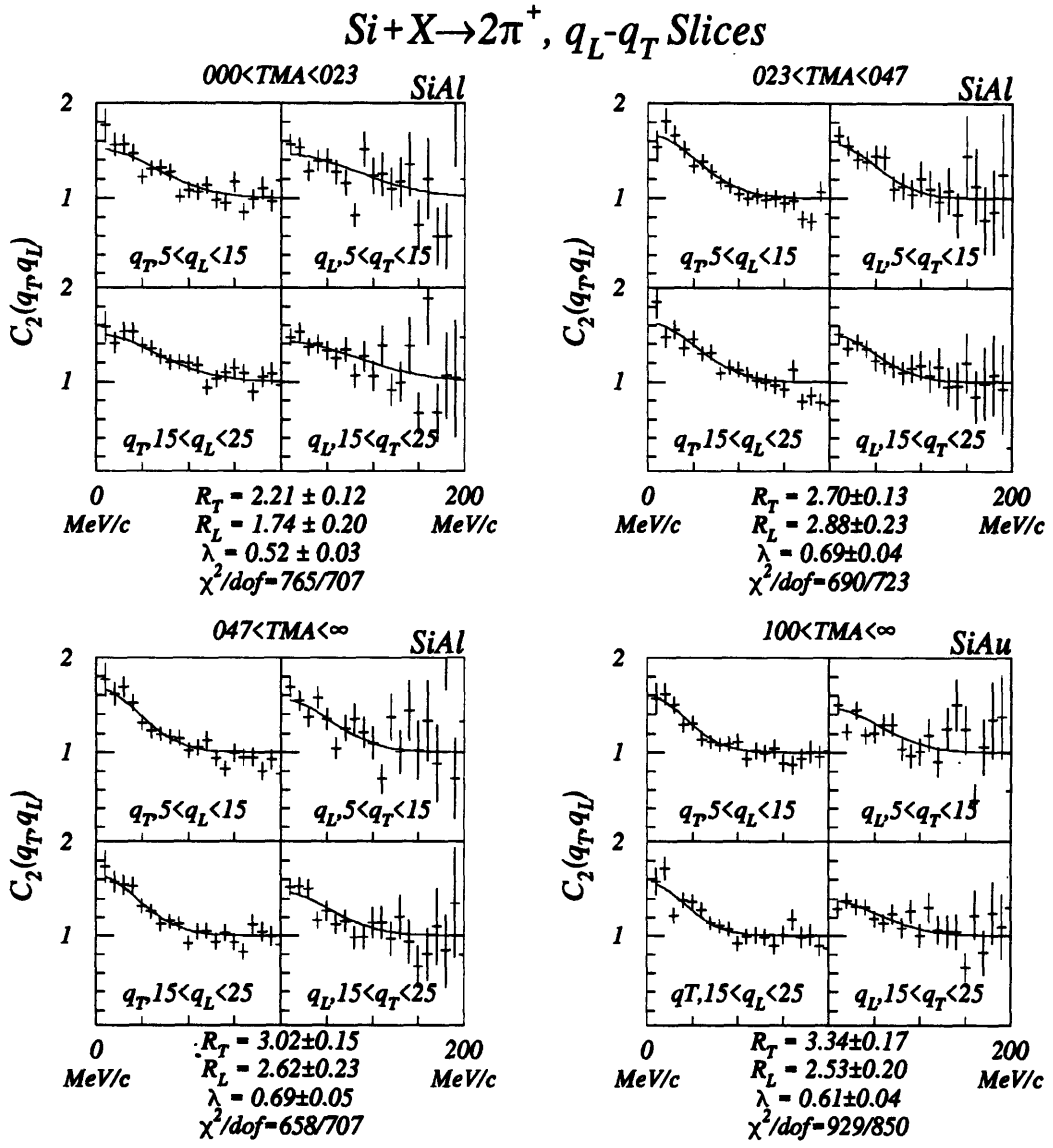

Figure 5-14: Slices (q_L-q_T) for Si+Al → $2\pi^+$ and Si+Au → $2\pi^+$ multiplicity data sets.

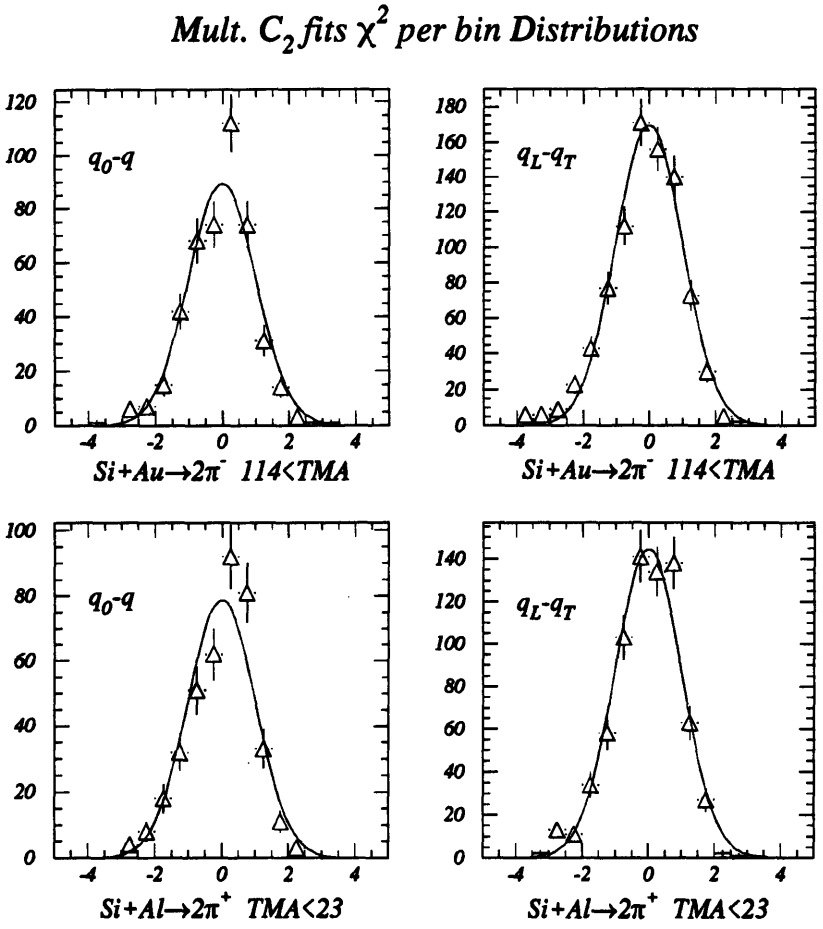

Figure 5-15: Deviation per bin distributions for the Si+Au $\rightarrow 2\pi^-$ most central and Si+Al $\rightarrow 2\pi^+$ peripheral q_0-q and q_L-q_T correlation fits. The curves are Gaussians ($\sigma = 1$).

of R and τ, but are still within two standard deviations of the E802 results. The Si+Au $\rightarrow 2\pi^+$ radius has increased significantly, and it now exceeds that of the Si+Al $\rightarrow 2\pi^+$ system.

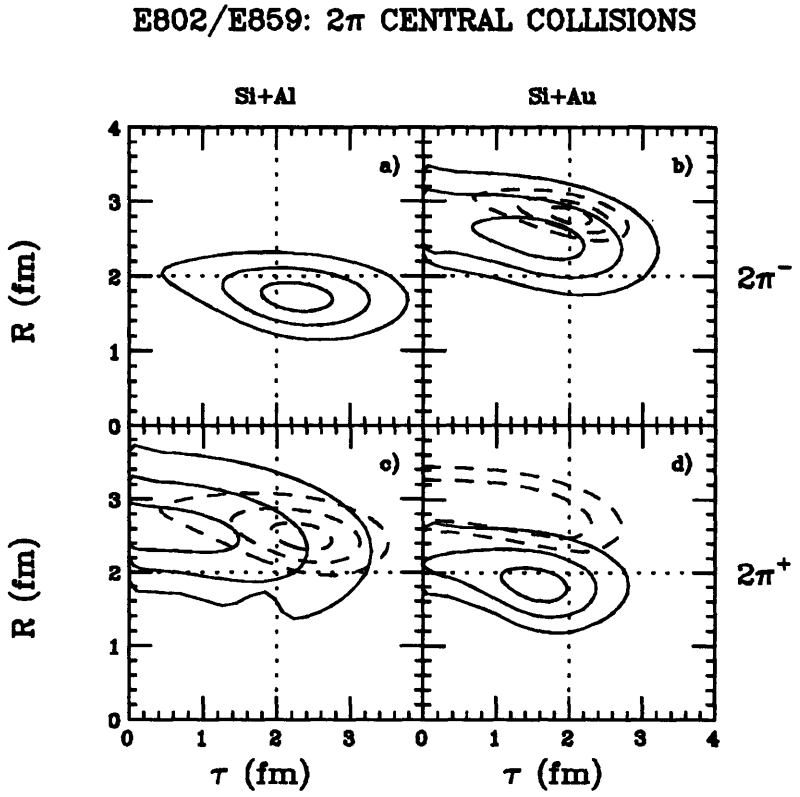

Figure 5-16: Contours of E802 (solid) and E859 (dash) fitted parameters. The Si+Au $\rightarrow 2\pi^+$ 1σ E859 contour is not shown.

Examination of the fit parameters reveals (Table 5.3) that the radius parameters increase with multiplicity for each system. For the Si+Au system this is shown clearly in Fig. 5-17. Each of the parameters are plotted as a function of the mean value of the multiplicity for the events which

produced the pion pairs in the fit. Both R and R_T increase significantly with multiplicity. For R_L the increase is less strong, and for τ the large errors overwhelm any trend which may be present in the data. The value of λ remains constant at 0.55–0.60. The behavior of λ contrasts with the Si+Al $\rightarrow 2\pi^+$ system (Fig. 5-18), where it appears to increase with multiplicity. Otherwise, the same observations regarding the Si+Au data are also applicable to this system. For each fit function we have one parameter which increases significantly while the other shows at most a slight increase. The R-τ and R_T-R_L contours for the highest and lowest multiplicity bin for each system are shown in Fig. 5-19. We note that each of the contours are separated by roughly two to three standard deviations.

System	Mult.	$\lambda_{R-\tau}$	R	τ	$\lambda_{R_T-R_L}$	R_T	R_L
Si+Au $\rightarrow 2\pi^-$	0–51	0.54±0.03	2.09±0.13	1.50±0.36	0.57±0.04	2.37±0.13	2.30±0.20
Si+Au $\rightarrow 2\pi^-$	51–89	0.56±0.04	2.53±0.09	2.05±0.43	0.57±0.04	2.92±0.15	2.55±0.23
Si+Au $\rightarrow 2\pi^-$	100–114	0.57±0.04	3.01±0.17	1.16±0.80	0.56±0.04	3.34±0.16	2.60±0.20
Si+Au $\rightarrow 2\pi^+$	100+	0.57±0.05	2.85±0.20	1.55±0.64	0.61±0.04	3.34±0.17	2.53±0.20
Si+Au $\rightarrow 2\pi^-$	114+	0.55±0.04	2.94±0.21	2.27±0.50	0.57±0.04	3.55±0.20	2.97±0.24
Si+Al $\rightarrow 2\pi^+$	0–23	0.50±0.03	1.72±0.10	1.59±0.27	0.52±0.03	2.21±0.12	1.74±0.20
Si+Al $\rightarrow 2\pi^+$	23–47	0.63±0.04	2.33±0.16	1.63±0.38	0.64±0.04	2.68±0.13	2.26±0.18
Si+Al $\rightarrow 2\pi^+$	47+	0.65±0.05	2.49±0.08	2.35±0.45	0.66±0.05	2.99±0.16	2.07±0.19

Table 5.3: Fit parameters for multiplicity data sets.

5.3 Forward Energy Fit Results

5.3.1 The Correlation Functions and Parameters

We now present the fit results for the data sets listed in Table 4.3 of Sec. 4.3.1. The quality of the fits is illustrated in the q_0-q and q_L-q_T slices of Figs. 5-20 to 5-23. The correlation fits are presented in order of increasing system size. The fit parameters for each system (given with the figures) are also listed in Table 5.4 below.

The contours for the highest and lowest ZCAL distributions are shown in Fig. 5-24. As observed with the multiplicity data sets, these contours are separated by roughly three standard deviations. Occasionally the fitting program has difficulty finding a contour, and the contour cannot be shown.[4]

[4] Alternating minimization functions (we have two) or calling MINUIT with a higher fitting strategy does the trick, but this is rather time consuming.

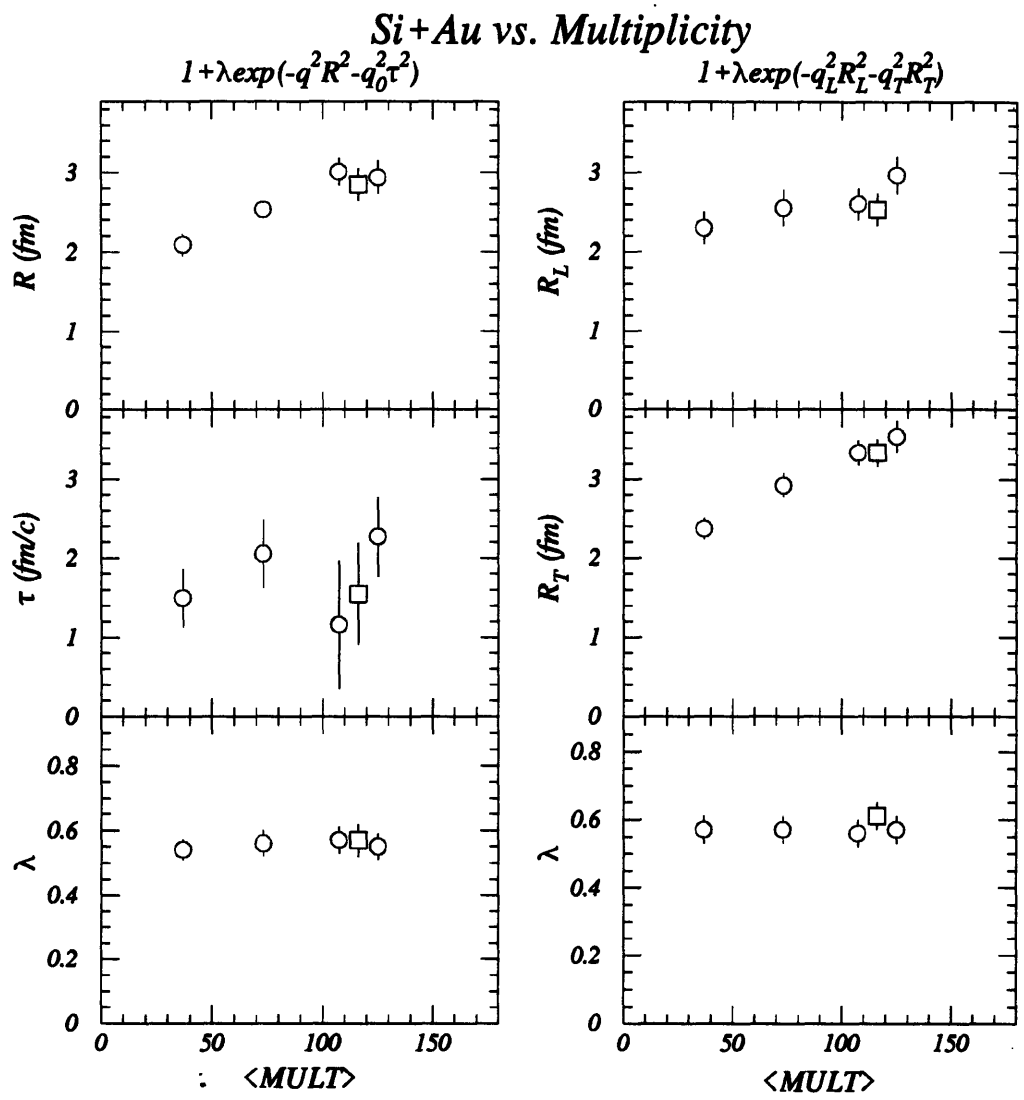

Figure 5-17: Multiplicity dependence of fitted parameters. The circles are for Si+Au $\rightarrow 2\pi^-$, the squares are for Si+Au $\rightarrow 2\pi^+$.

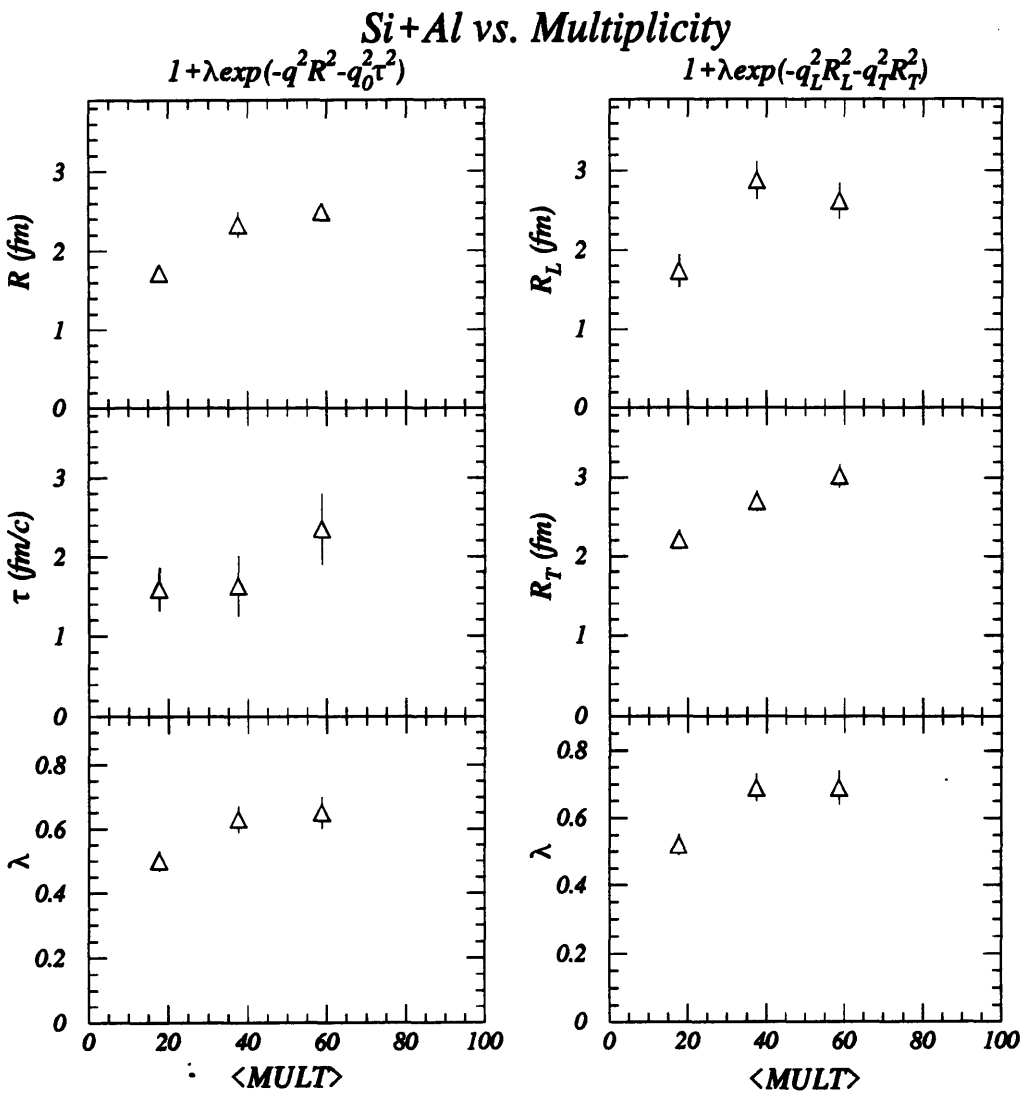

Figure 5-18: Multiplicity dependence of the fitted parameters for Si+Al $\rightarrow 2\pi^+$.

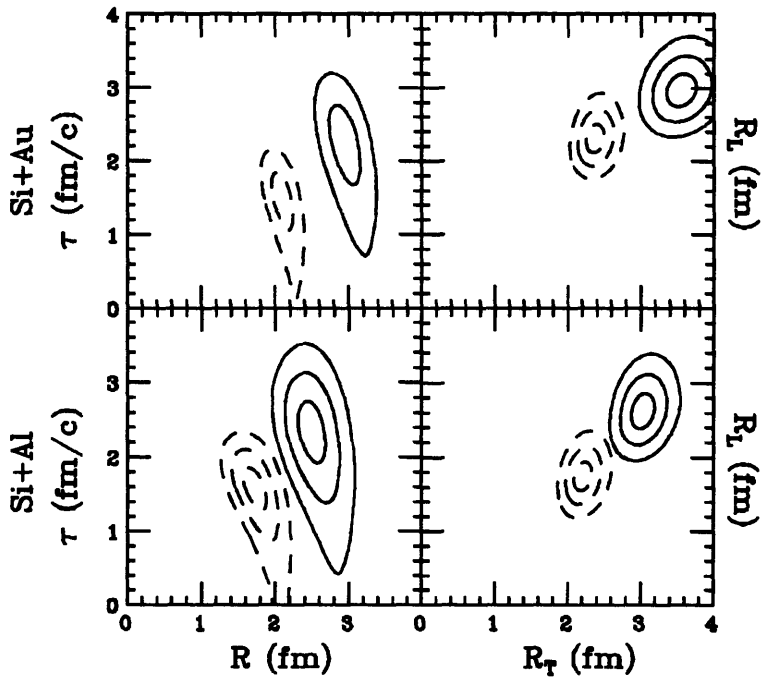

Figure 5-19: Si+Au $\rightarrow 2\pi^-$ and Si+Al $\rightarrow 2\pi^+$ contours for the highest and lowest multiplicity bins. The Si+Au $\rightarrow 2\pi^-$ R-τ contours show only the 1σ and 2σ limits.

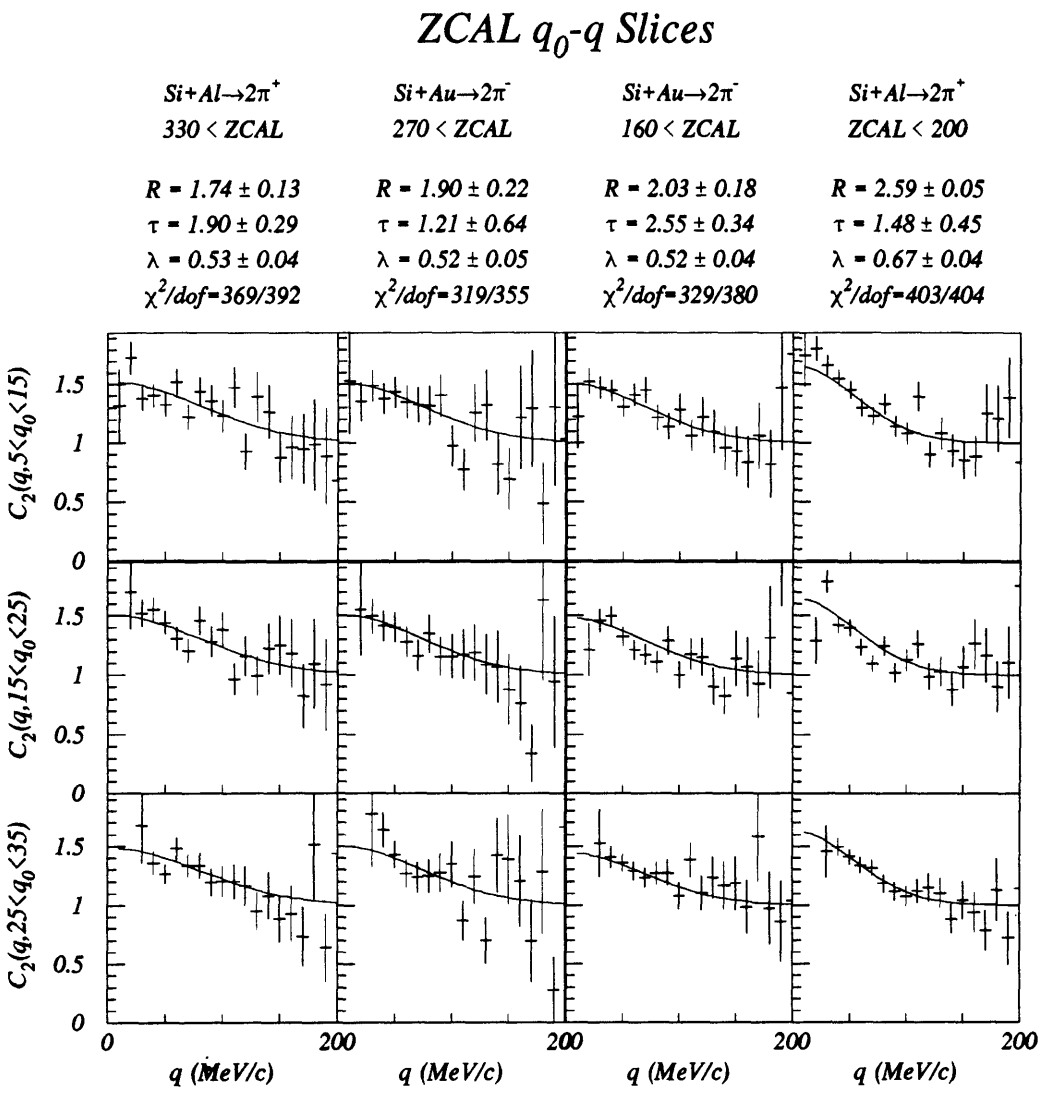

Figure 5-20: Slices (q_0-q) for forward energy data sets.

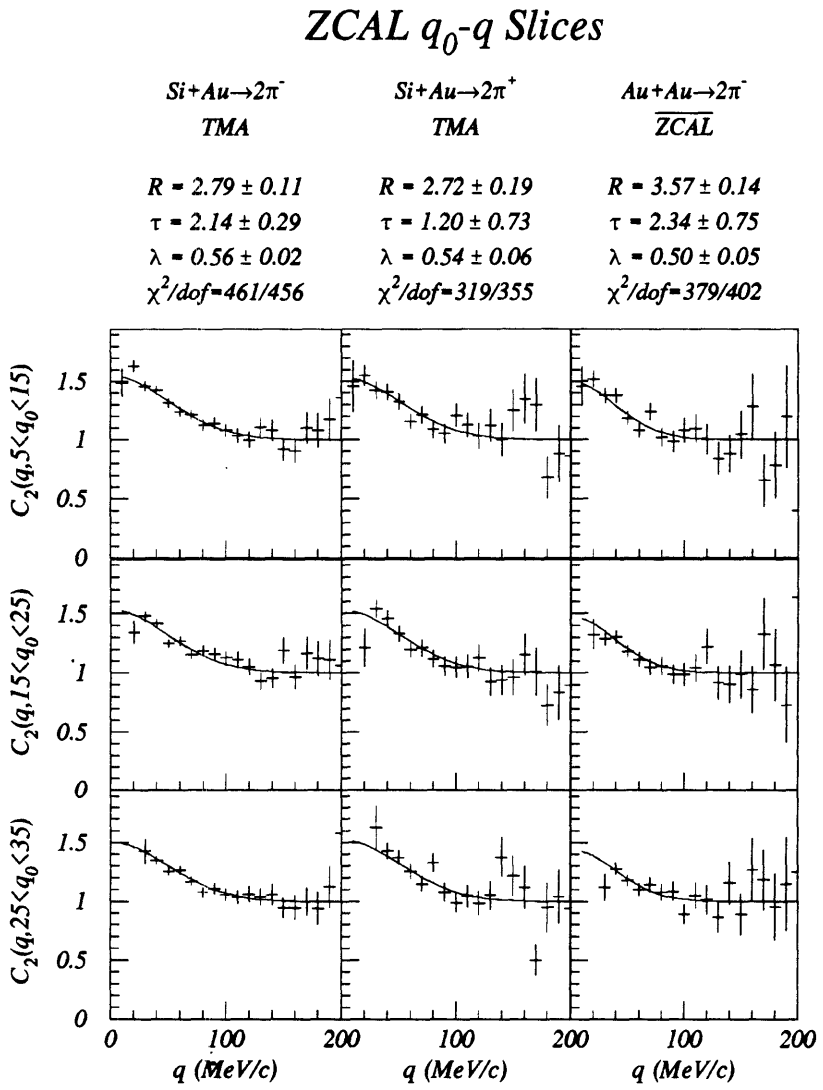

Figure 5-21: Slices (q_0-q) for forward energy data sets.

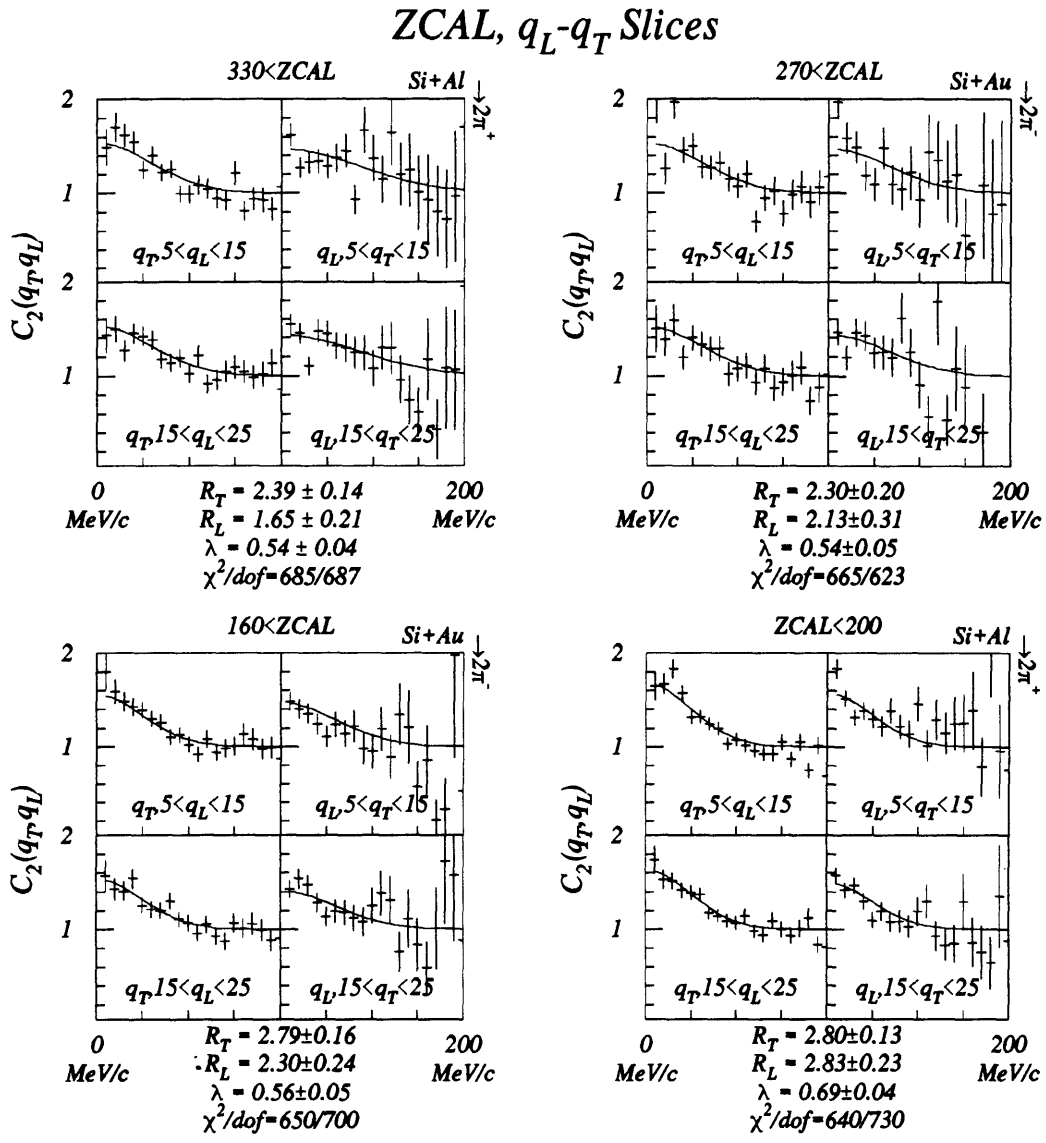

Figure 5-22: Slices (q_L-q_T) for forward energy data sets.

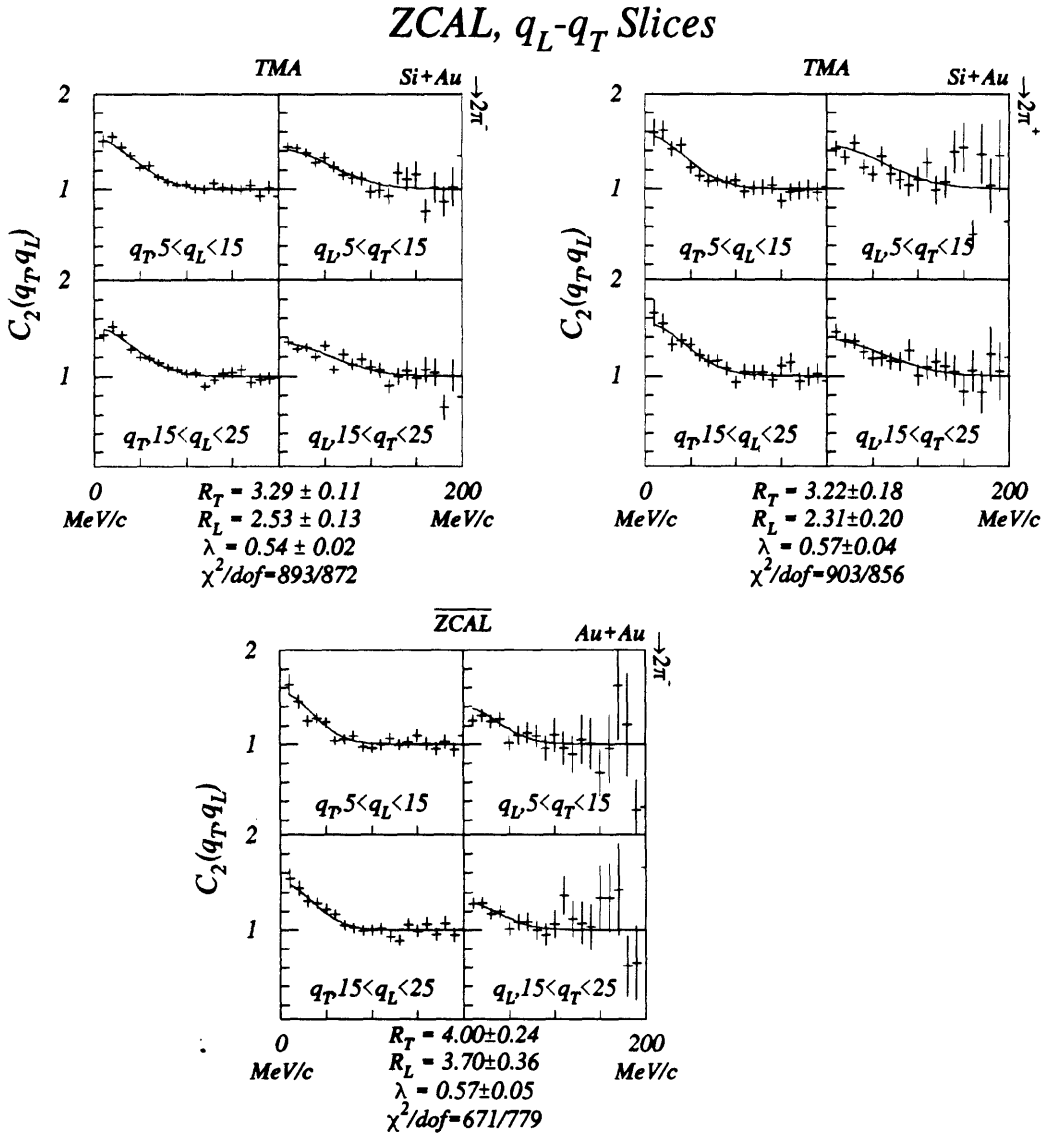

Figure 5-23: Slices (q_L-q_T) for forward energy data sets.

System	Cut	$\lambda_{R-\tau}$	R	τ	$\lambda_{R_T-R_L}$	R_T	R_L
Si+Al $\rightarrow 2\pi^+$	ZCAL>330	0.53±0.04	1.74±0.13	1.90±0.29	0.54±0.04	2.39±0.14	1.65±0.21
Si+Au $\rightarrow 2\pi^-$	ZCAL>270	0.52±0.05	1.90±0.22	1.21±0.64	0.54±0.05	2.30±0.20	2.13±0.31
Si+Au $\rightarrow 2\pi^-$	ZCAL>160	0.52±0.04	2.03±0.18	2.55±0.34	0.56±0.05	2.79±0.16	2.30±0.24
Si+Al $\rightarrow 2\pi^+$	ZCAL<200	0.67±0.04	2.59±0.05	1.48±0.45	0.69±0.04	2.80±0.13	2.83±0.23
Si+Au $\rightarrow 2\pi^-$	TMA	0.56±0.02	2.79±0.11	2.14±0.29	0.54±0.02	3.29±0.11	2.53±0.13
Si+Au $\rightarrow 2\pi^+$	TMA	0.54±0.06	2.72±0.19	1.20±0.73	0.57±0.04	3.22±0.18	2.31±0.20
Au+Au $\rightarrow 2\pi^-$	$\overline{\text{ZCAL}}$	0.50±0.05	3.57±0.14	2.34±0.75	0.57±0.05	4.00±0.24	3.70±0.36

Table 5.4: Fit parameters for forward energy data sets.

We see the same trend towards higher radii as the collisions become more central. The main advantage of the ZCAL cuts, however, is that we now have the ability to compare the fit parameters from different systems, using the number of projectile participants. Normally, this would involve dividing the mean ZCAL forward energy by the kinetic energy per projectile nucleon and subtracting this quantity from the atomic number of the projectile,

$$A_{pp} = A - \frac{< E_{ZCAL} >}{E_{beam}}. \tag{5.7}$$

Given the problems of the ZCAL during the 1991 and 1992 heavy ion runs, the determination of the mean forward energy to be used in Eq. 5.7 requires special attention. The following section specifically addresses how we obtain <ZCAL> from the correlation data sets.

5.3.2 The ZCAL Corrections

The problem with the ZCAL is not the result of a defect in the calorimeter but a lack of photomultiplier signal clipping needed to handle the high rates of E859. The ADC readout of ZCAL was designed to accommodate typical E802 beam rates of 50,000 particles per second. The more than tenfold increase in rate for E859 led to an overall offset in the recorded ZCAL ADC values due to the long signal tails. The following year, double delay amplifiers were installed to provide such clipping by adding a reflected delayed signal. This cancelled the overall rate dependence, but introduced large fluctuations in a small fraction of the events. The fraction and range of the fluctuations increased significantly for higher beam rates. Each of these effects is seen clearly in Fig. 5-25, which shows that the ZCAL BEAM and INT distributions are distorted as the rate increases. The lines are drawn at zero (dashed) and at full beam energy (solid). The distributions for

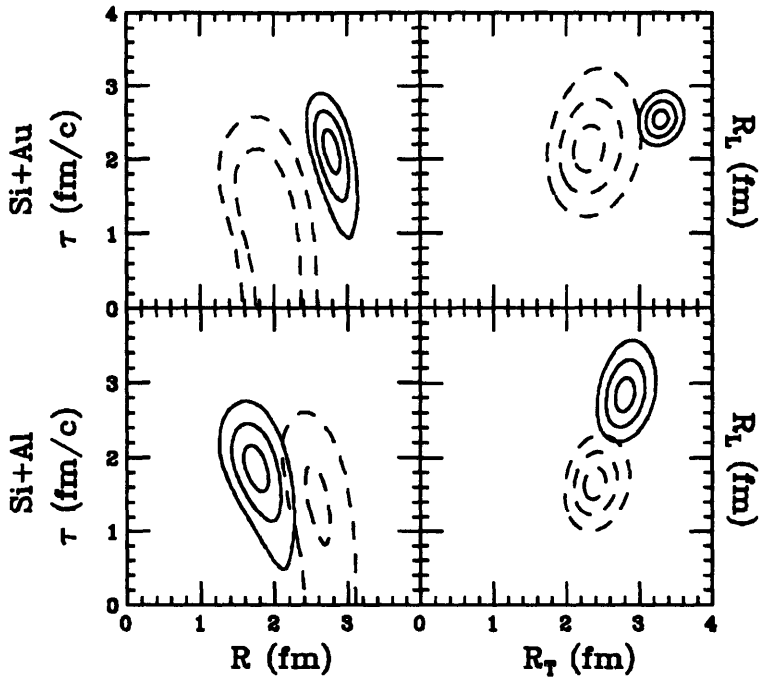

Figure 5-24: Contours for Si+Au $\rightarrow 2\pi^-$ and Si+Al $\rightarrow 2\pi^+$ central (solid) and peripheral (dash) systems. The R-τ contours (1σ for Si+Au $\rightarrow 2\pi^-$ and 2σ for Si+Al $\rightarrow 2\pi^+$ are missing) were obtained with the $\chi^2_{Poisson}$ minimization function.

Feb'91 appear to increase linearly with rate whereas for Mar'92 the resolution degrades at the higher rates though the mean of the distributions appear to be independent of rate. The calculated rate is the average rate since the last recorded event. The minimum elapsed time between two recorded events is roughly 1 μsec. The time scale appropriate for studying the ZCAL rate dependence is not precisely known, but is probably somewhat shorter. The corrections we apply rest on the assumption that the recorded ZCAL signal is most accurate for the low-rate events.

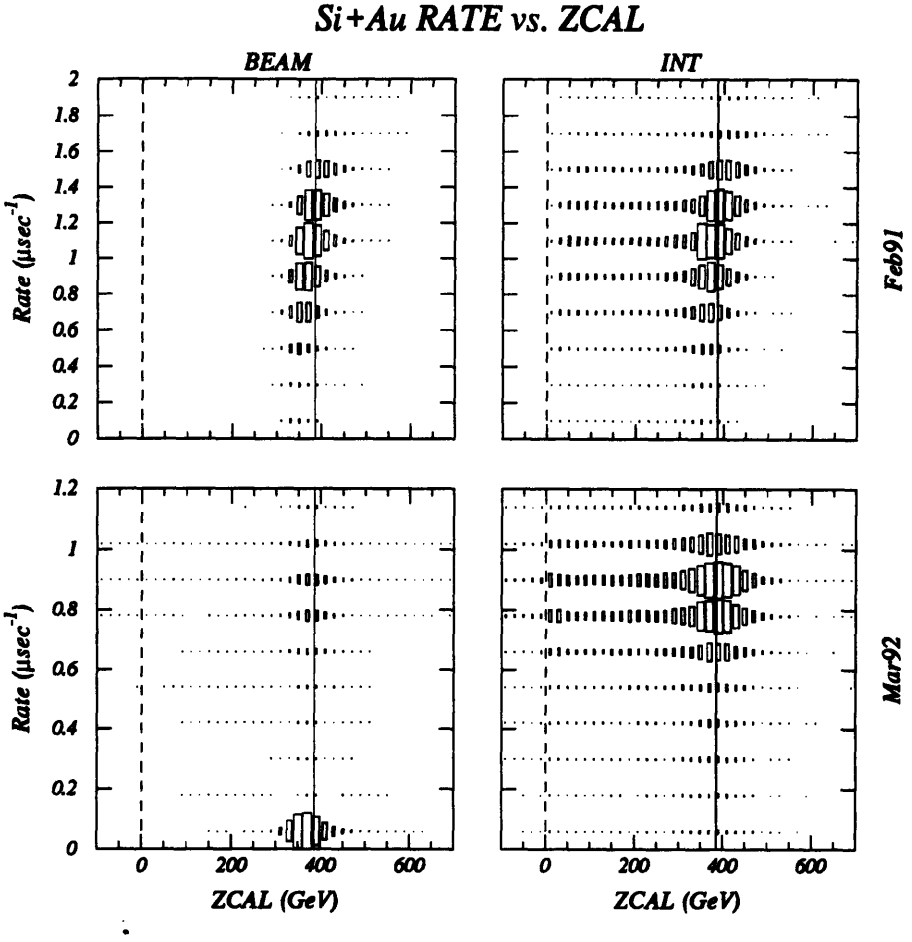

Figure 5-25: ZCAL BEAM and INT distributions for different rates (plotted as rate vs. ZCAL). Lines are drawn at zero (dashed) and beam energy (solid).

ZCAL Feb'91

We show the ZCAL rate dependence for beam events and events containing two pions in Fig. 5-26. The two-pion data sets are those gated on the hardware $\overline{\text{TMA}}$ value for the two different thresholds.

A similar study of the TMA has shown both the multiplicity and hardware TMA trigger to be independent of rate. It appears that the ZCAL energy is constant below a rate of ≈0.4 MHz, and above that the mean ZCAL energy is a linear function of the beam rate. This behavior is also seen in the two-pion events, however, the slopes are not identical. That the rate dependence varies for different event classes demonstrates that this dependence is not just an offset, but that the overall effect is more complicated. We cannot determine the exact rate dependent slope for the two peripheral Si+Au $\rightarrow 2\pi^-$ ZCAL data sets because the peripheral ZCAL cuts for these data sets are themselves rate dependent. Instead, we use the corresponding TMA-gated distributions of Fig. 5-26 to estimate the slope. The correction is performed as follows:

1. All distributions are fit to a horizontal line below a rate of 0.3 MHz. This determines the rate independent value, and for beam events it is used to re-calibrate the beam peak.

2. The TMA-gated distributions are assumed to depend linearly on rate above a certain rate value. They are fit with a straight line starting at a rate of 0.5 MHz.

3. The intersection of the two line segments determines where the rate correction begins.

In the following formula R is the rate, R_i is the point of intersection, m is the rate-dependent slope and G_C is the low rate beam peak calibration correction factor.

$$\text{Corrected ZCAL} = \left\{ \begin{array}{ll} G_C \cdot \text{ ZCAL} & ; R \leq R_i \\ G_C \cdot [\text{ZCAL} - m\,(R - R_i)] & ; R > R_i \end{array} \right\} \tag{5.8}$$

$$G_C = A_{beam} \cdot E_{beam}/\text{ZCAL}_{beam}; R \leq R_i$$

The corrected ZCAL distributions are given in Fig. 5-27. We use the mean value of ZCAL to calculate the number of projectile participants (Eq. 5.7), and take the RMS deviation about the mean as an estimate of the spread.

ZCAL Mar'91

The Mar'91 data cannot be corrected in the same way since the problem is one of resolution. Here we calculate the mean ZCAL from the low-rate events. It is rather straightforward to deal with the central, high multiplicity Si+Au events, for which the projectile is almost always fully occluded by the target. A healthy ZCAL distribution varies little in this region. To eliminate any bias from

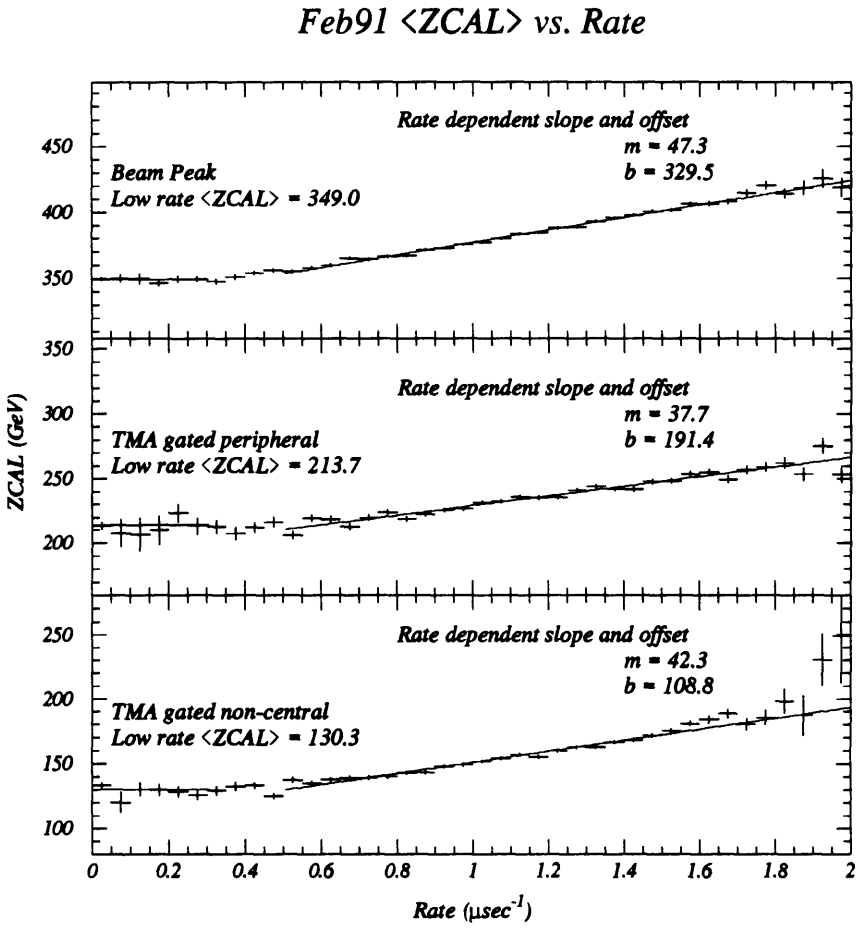

Figure 5-26: Rate dependence of <ZCAL> for BEAM events and the two $\overline{\text{TMA}}$ two-pion distributions.

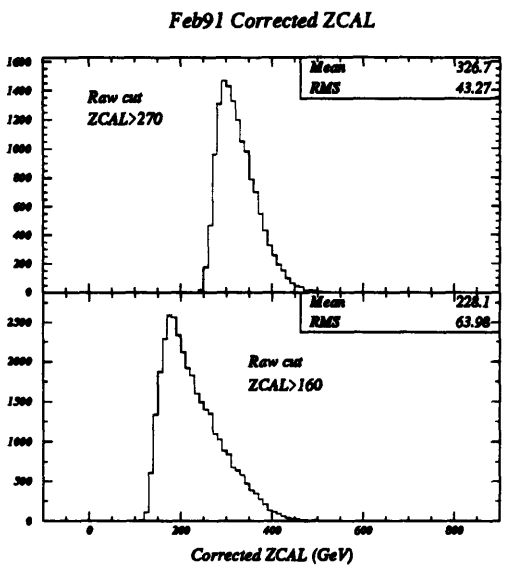

Figure 5-27: Rate corrected ZCAL distributions for the two Si+Au $\rightarrow 2\pi^-$ peripheral distributions.

the small fraction of events with extremely poor resolution we integrate inwards from the tails and remove the outermost 5% of the low-rate (<0.1 MHz) distribution. This is shown in Fig. 5-28. Also shown in this figure is the full ZCAL distribution without a rate cut for comparison.

The Si+Al $\rightarrow 2\pi^+$ distributions present more of a problem because they are cut on ZCAL, and for some small fraction of events this cut is unreliable. Here we apply the 5% tail subtraction to the low-rate events away from the cut. These distributions are shown in Fig. 5-29.

ZCAL Au beam

For the Au+Au $\rightarrow 2\pi^-$ data set, also taken in Mar'92, the electronics were improved to enable the ZCAL signal to be used in the LVL1 trigger, and the scintillator in the first hadronic section was replaced. Finally, radiation safety considerations require that beam rates not exceed approximately 100K beam particles per spill, close to beam rates used for E802, although the energy per beam particle represents a five-fold increase. The ZCAL BEAM and $\overline{\text{ZCAL}}$ with $2\pi^-$ distributions are shown in Fig. 5-30. Also shown in the inset of Fig. 5-30 is the mean forward energy for BEAM events for different values of the rate. Note that neither the mean ZCAL, nor the RMS spread (dashes) is affected by the rate.

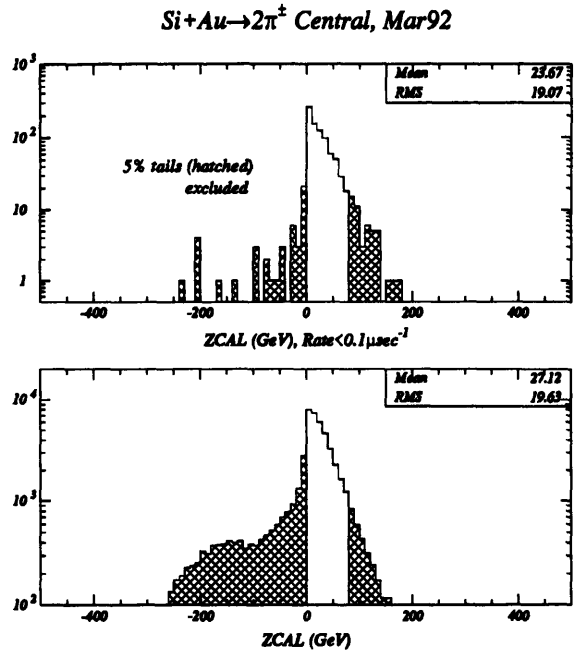

Figure 5-28: ZCAL distribution for low-rate central Si+Au events, and for all central Si+Au events. For the low-rate distribution the hatched region corresponds to the 5% tails, integrating inwards from each side. For the full distribution the same region is hatched, but it now contributes more than 5%. For both distributions the hatched regions are not included in the mean and RMS values quoted.

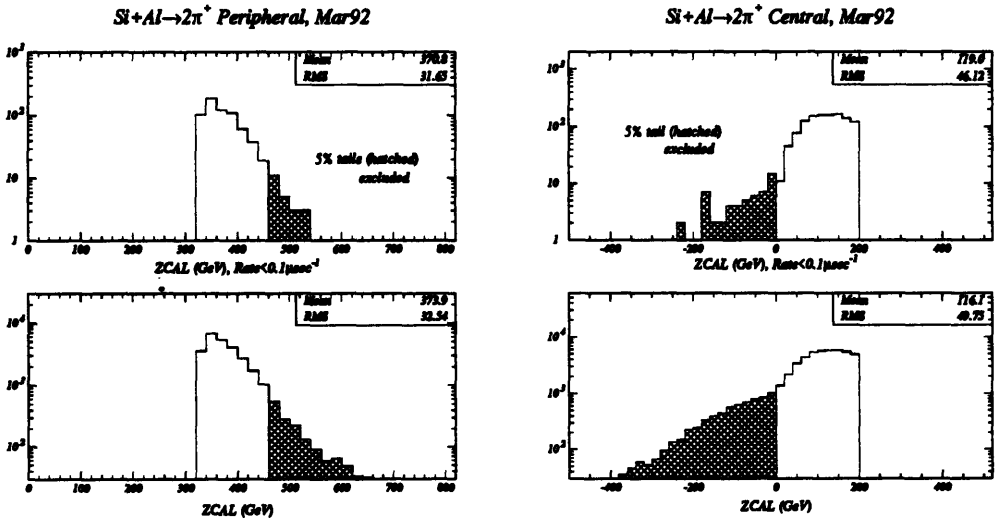

Figure 5-29: ZCAL distribution for low-rate peripheral Si+Al $\rightarrow 2\pi^+$ events and for all peripheral Si+Al $\rightarrow 2\pi^+$ events. The hatched regions represent the 5% tails in the low-rate distributions, and are not included in the mean and RMS quoted.

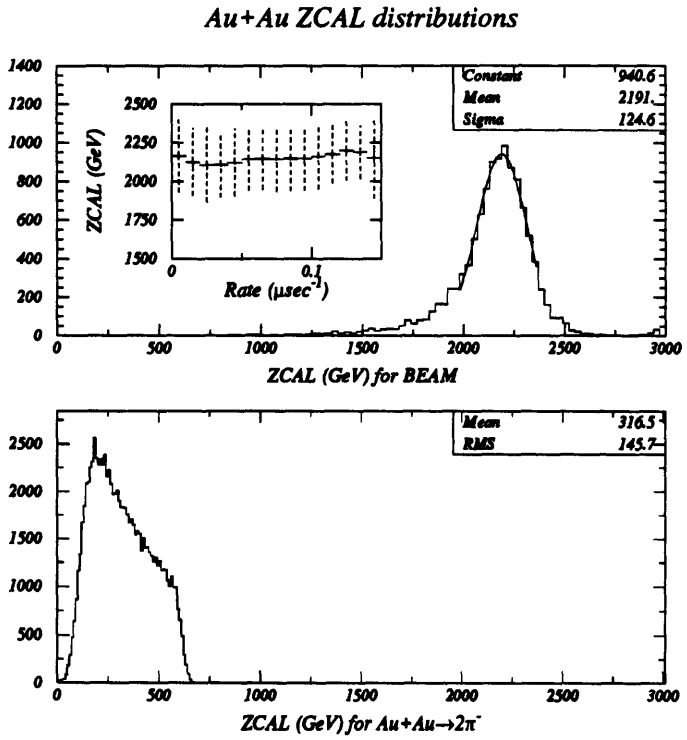

Figure 5-30: ZCAL distributions for the Au beam. The inset is <ZCAL> vs. rate, dashes indicate the RMS spread. The lower plot shows the ZCAL distribution with a 5% central $\overline{\text{ZCAL}}$ trigger.

5.3.3 Scaling with Projectile Participants

With the corrected mean forward energy, we can now plot the radius parameters for all systems as a function of projectile participants to the 1/3 power. All of the radii scale roughly linearly with this quantity. Once again the lifetime parameter remains constant (within errors) with a value of 2 fm/c.

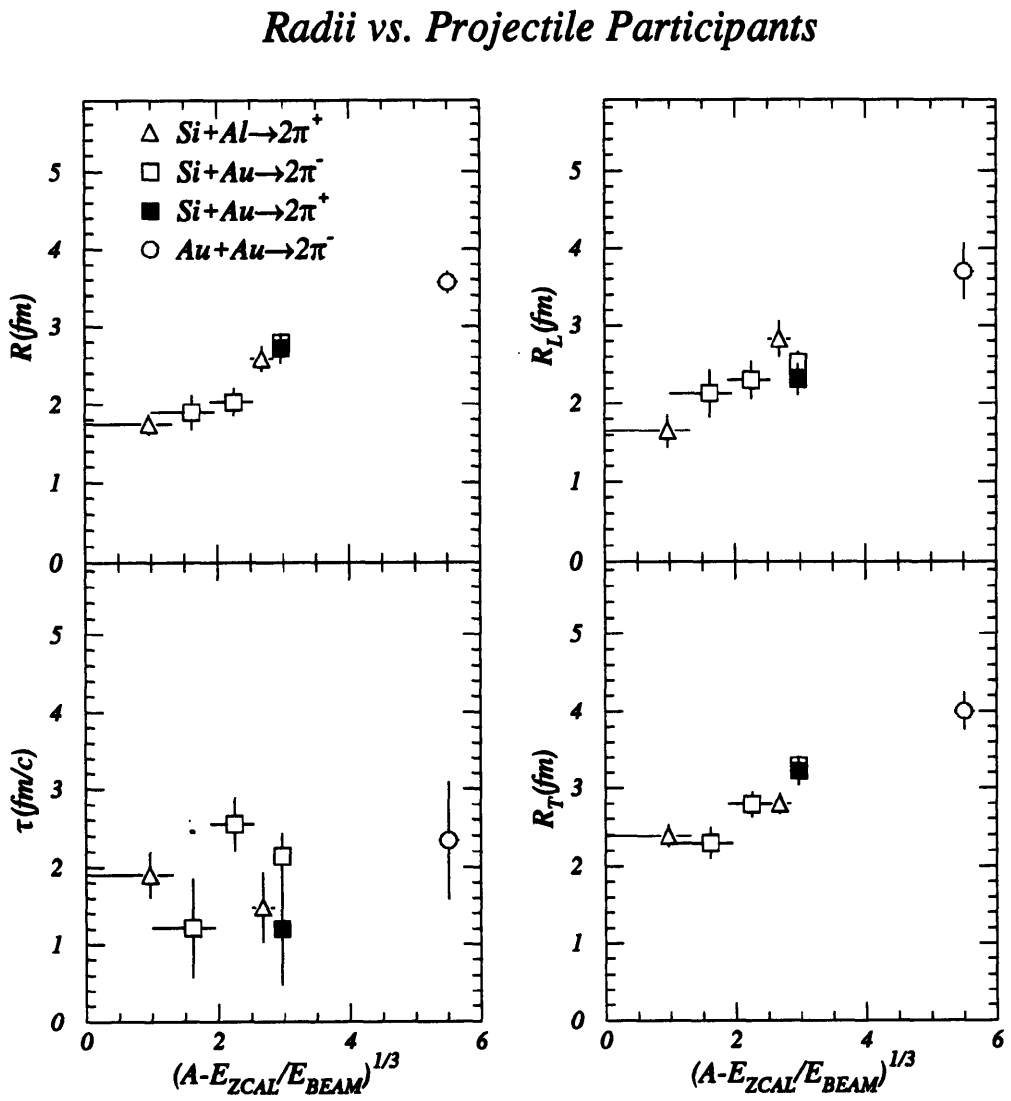

Figure 5-31: Radius parameters vs. projectile participants to the 1/3 power.

5.4 Multiplicity Dependence in the Central Region

We have thus far established that the correlation radii vary as a function of both the multiplicity and the forward energy. Each is related to impact parameter, but the two event observables are not equivalent. The forward energy is directly related to the geometry and therefore seems more natural choice for comparison. However, in the past the multiplicity dependence has been incorporated into various freeze-out arguments. In an attempt to distinguish between the two scenarios we subdivide the most central Si+Au data sets into data sets of 50K pairs each. The expectation is that for the most central events, the forward energy would remain constant. Thus if the dependence were simply geometric, there would be no further increase in the radius parameters. The results, shown in Fig. 5-32, are inconclusive. We cannot differentiate between a continued increase and a plateau at very high multiplicities.

5.5 Three-Dimensional Fit Results

At this time the three-dimensional fit results should be regarded as preliminary. They are included here as a check on the two-dimensional fit results. In particular we are interested in testing our understanding of the relationship between R_L and R_T, making independent observations of the τ parameter, and checking our assumptions regarding the reference frame of the source.

Fig. 5-33 shows slices in each variable for the peripheral and central Si+Au $\rightarrow 2\pi^-$ data sets. It appears that there is not enough of a range in q_{Tside} to cover the tail of the correlation function for small radii. Otherwise there is good agreement between the data and the fit slices. Due to the restricted regions of the actual distributions neither q_0-q_L-q_T nor Koonin correlations can be viewed easily with slices. The parameters for all three-dimensional fits are given in Tables 5.5, 5.6, and 5.7 along with their two dimensional counterparts.

5.5.1 The Radius Parameters

Here we discuss the parameters given in the bottom half of the listings for each system. The consistency of the fit values for R_L across the different parameterizations is striking. With one exception any pairing of the R_L parameters within a given system differ by less than the sum of their errors. The one exception to this is the Si+Al $\rightarrow 2\pi^+$ central system, which is also the only system to have a value of R_T which does not exceed R_L in the two-dimensional R_T-R_L fit. This

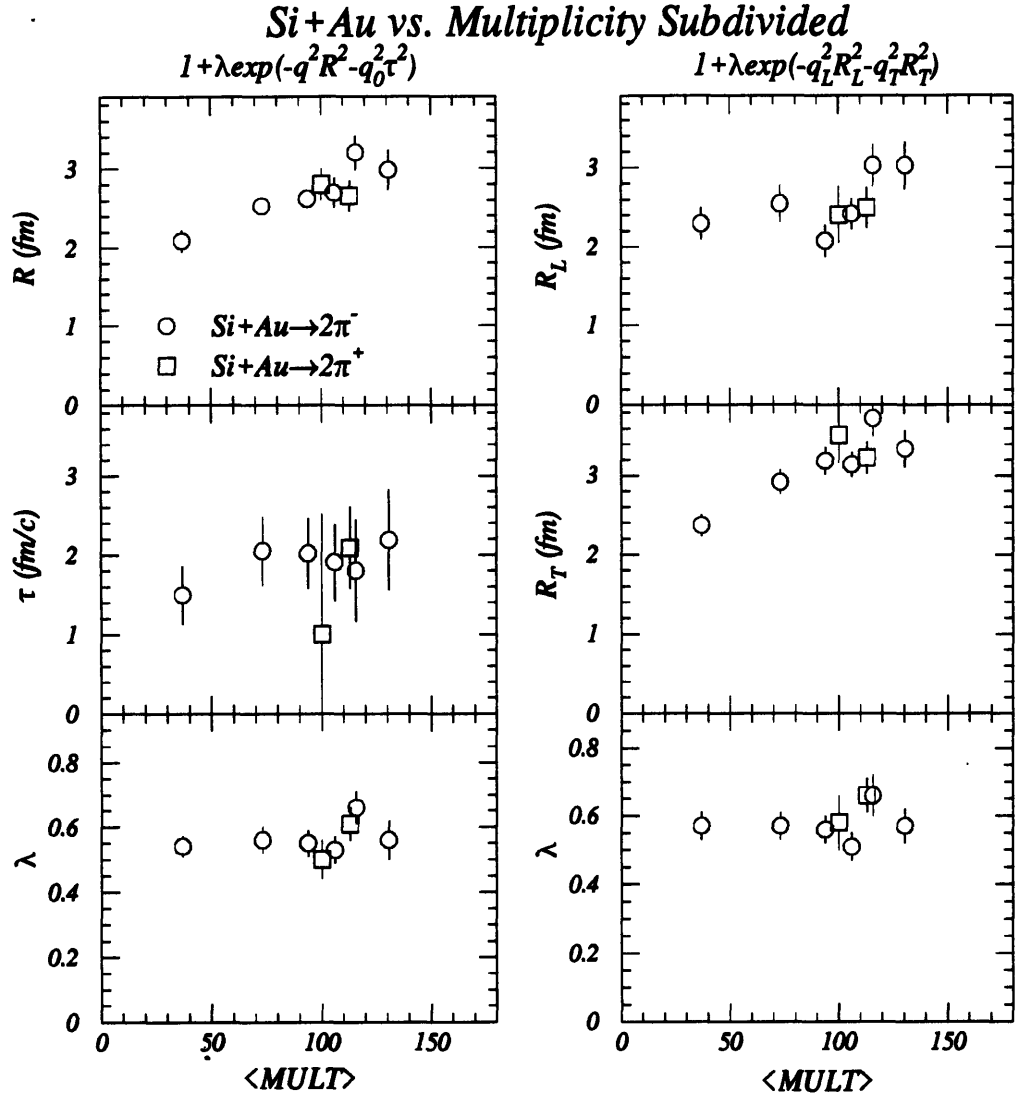

Figure 5-32: Radius parameters as a function of multiplicity with further subdivision of the most central multiplicity bins.

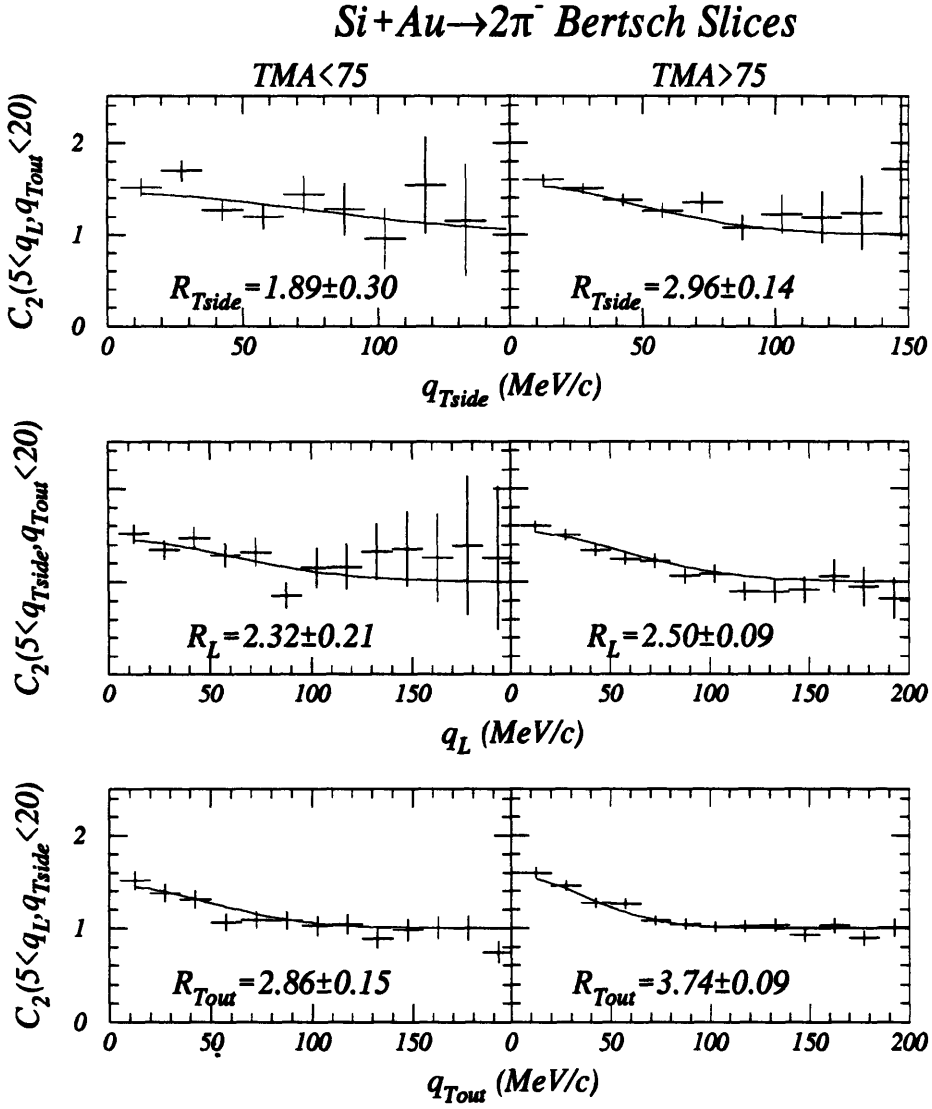

Figure 5-33: Bertsch slices for peripheral and central Si+Au → $2\pi^-$ data sets.

Si+Au → $2\pi^-$ 0<TMA<075

Koonin		R-τ	
λ	0.49±0.02	λ	0.50±0.03
R	2.36±0.09	R	1.99±0.12
τ	2.19±0.38	τ	1.99±0.30
Y	$1.74^{+0.11}_{-0.09}$	Y=1.72	

Bertsch		R_L-R_T-τ		R_L-R_T	
λ	0.48±0.04	λ	0.50±0.04	λ	0.53±0.04
R_L	2.32±0.21	R_L	2.02±0.14	R_L	1.97±0.18
R_{Tside}	1.89±0.30	R_T	2.24±0.29	R_T	2.54±0.15
R_{Tout}	2.86±0.15	τ	1.82±0.30		

Si+Au → $2\pi^-$ 0<TMA<115

Koonin		R-τ	
λ	0.53±0.03	λ	0.54±0.03
R	2.74±0.14	R	2.27±0.14
τ	2.00±0.18	τ	2.39±0.27
Y	$1.76^{+0.09}_{-0.08}$	Y=1.72	

Bertsch		R_L-R_T-τ		R_L-R_T	
λ	0.55±0.02	λ	0.53±0.03	λ	0.58±0.03
R_L	2.56±0.14	R_L	2.32±0.17	R_L	2.44±0.16
R_{Tside}	2.17±0.21	R_T	2.33±0.16	R_T	2.88±0.11
R_{Tout}	3.27±0.12	τ	2.36±0.21		

Si+Au → $2\pi^-$ 75<TMA

Koonin		R-τ	
λ	0.55±0.01	λ	0.57±0.24
R	3.08±0.07	R	2.80±0.11
τ	2.53±0.24	τ	2.00±0.29
Y	1.62±0.06	Y=1.25	

Bertsch		R_L-R_T-τ		R_L-R_T	
λ	0.60±0.02	λ	0.57±0.05	λ	0.56±0.02
R_L	2.50±0.09	R_L	2.52±0.14	R_L	2.52±0.12
R_{Tside}	2.96±0.14	R_T	3.34±0.11	R_T	3.30±0.11
R_{Tout}	3.74±0.09	τ	0.87±1.29		

Table 5.5: Part I of 3-D fit results. Rapidity (Y) under Koonin refers to the fit value, while the value of Y given in the large box to the right is the assumed reference frame used for the non-invariant parameterizations.

Si+Au → $2\pi^+$ 75<TMA

Koonin		R-τ	
λ	0.59±0.05	λ	0.57±0.04
R	3.21±0.25	R	2.87±0.18
τ	2.56±0.55	τ	1.21±0.69
Y	$1.56^{+0.18}_{-0.15}$	Y=1.25	

Bertsch		R_L-R_T-τ		R_L-R_T	
λ	0.66±0.03	λ	0.57±0.03	λ	0.61±0.05
R_L	2.62±0.17	R_L	2.58±0.25	R_L	2.53±0.23
R_{Tside}	3.38±0.25	R_T	3.41±0.12	R_T	3.30±0.19
R_{Tout}	3.87±0.17	τ	0.19±0.96		

Si+Al → $2\pi^+$ 0<TMA<045

Koonin		R-τ	
λ	0.45±0.02	λ	0.51±0.02
R	1.88±0.15	R	1.72±0.11
τ	1.78±0.27	τ	1.75±0.18
Y	1.71±0.08	Y=1.72	

Bertsch		R_L-R_T-τ		R_L-R_T	
λ	0.47±0.02	λ	0.49±0.03	λ	0.53±0.02
R_L	2.06±0.16	R_L	1.76±0.15	R_L	1.78±0.14
R_{Tside}	0.94±0.04	R_T	1.68±0.25	R_T	2.17±0.09
R_{Tout}	2.47±0.12	τ	1.87±0.30		

Si+Al → $2\pi^+$ 30<TMA

Koonin		R-τ	
λ	0.66±0.05	λ	0.68±0.03
R	2.86±0.11	R	2.52±0.11
τ	1.84±0.41	τ	1.85±0.34
Y	$1.73^{+0.09}_{-0.08}$	Y=1.72	

Bertsch		R_L-R_T-τ		R_L-R_T	
λ	0.82±0.03	λ	0.71±0.02	λ	0.73±0.0.
R_L	3.47±0.15	R_L	3.02±0.14	R_L	2.88±0.17
R_{Tside}	2.58±0.17	R_T	2.38±0.09	R_T	2.88±0.10
R_{Tout}	3.53±0.11	τ	2.41±0.19		

Table 5.6: Part II of 3-D fit results. Rapidity (Y) under Koonin refers to the fit value, while the value of Y given in the large box to the right is the assumed reference frame used for the non-invariant parameterizations.

Au+Au → $2\pi^-$ 0<ZCAL<700

Koonin		R-τ	
λ	0.51±0.06	λ	0.51±0.05
R	4.05±0.15	R	3.46±0.25
τ	2.34±0.06	τ	2.73±0.66
Y	$1.69^{+0.10}_{-0.09}$	Y=1.60	

Bertsch		R_L-R_T-τ		R_L-R_T	
λ	0.56±0.07	λ	0.51±0.03	λ	0.57±0.05
R_L	3.43±0.40	R_L	3.45±0.27	R_L	3.37±0.33
R_{Tside}	3.57±0.52	R_T	3.14±0.19	R_T	4.00±0.24
R_{Tout}	4.53±0.33	τ	3.57±0.40		

Table 5.7: Part III of 3-D fit results. Rapidity (Y) under Koonin refers to the fit value, while the value of Y given in the large box to the right is the assumed reference frame used for the non-invariant parameterizations.

contradicts the expectation that τ will contribute more to R_T than to R_L (see Sec. 5.1). These fits also show an anomalously large value for λ. We also find the trend $R_{Tside} < R_{T_{3D}} < R_{T_{2D}} < R_{Tout}$ to be generally true. The few cases where this trend is not explicitly followed are still consistent with the trend to within one standard deviation. The difference, $R_{Tout} - R_{Tside}$ is roughly 1 fm for all systems, and therefore consistent with the observation of non-zero lifetimes in the two-dimensional fits. The lifetime values tell a peculiar story. In most cases the value of τ is approximately 2 fm, and consistent between different fits. However, there are certain fits for which the τ parameter is simply undetermined (i.e. τ is small or zero, but with a large error). This behavior seems to be random, and occurs for two of the large statistics data sets, the Si+Au → $2\pi^-$ and Si+Au → $2\pi^+$ central measurements. We expect that this is due primarily to the kinematic restrictions on the range of q_0. Finally, the R parameters in the Koonin and R-τ fits are consistent for all systems.

5.5.2 Fitting the Rapidity

The Koonin fit results are intriguing. The measured rapidities are consistent with Y_{nn} for all systems except for the central Si+Au → $2\pi^-$ and Si+Au → $2\pi^+$ systems, which are both slightly backwards of Y_{nn}, as expected. However, the central Si+Au fits give a rapidity $Y \approx 1.6$ that is forwards of the center-of-mass rapidity, $Y_{cm} = 1.25$, that were used for each of the non-invariant parameterizations. If this is indeed correct, we expect no more than a 10% variation in the radius parameters (see Sec. 5.1.2). That the symmetric systems each give a rapidity of Y_{nn} lends confidence to the measured source velocities for Si+Au central collisions. Yet, there is still reason to be doubtful:

the Lorentz-invariant Koonin parameterization is not so Lorentz-invariant. All of the Koonin fit results shown in Tables 5.5, etc. were performed in the $Y = 1.0$ frame. A second round of fits performed in the expected source frame for the each system also gave consistent rapidities, but fits performed with variables defined in the lab frames gave rapidities which were systematically lower by $\Delta Y = 0.3$.[5] This may be due to difficulties in binning the variables in a reference frame that is far from that of the source, (see Sec. 5.1.3) until this is understood the present results must be regarded as inconclusive.

5.6 Systematics

Here we examine the fit parameters as the two-particle cuts, corrections, and fit regions are varied. We also attempt to understand the effect of the choice of rest frame by fitting the data in different reference frames for a few select systems. Finally, we derive a rough estimate for the systematic errors for the different parameters.

5.6.1 Two-Particle Cuts and Weights

The high statistics Si+Au $\rightarrow 2\pi^-$ and Si+Au $\rightarrow 2\pi^+$ central data sets used for the three-dimensional fits were chosen to study the systematic errors. The variation in fit parameters is shown clearly in Fig. 5-34. A variety of cuts were applied to test assumptions regarding the appropriate close pair cuts and weighting function:

std Standard. These are the fit parameters presented in Sec. 5.5.

Cut 20 Instead of the 11 mrad scaled angle cut (roughly equal to the Gaussian width of the two-dimensional correction weight function) a cut of 20 mrad was used.

Cut 30 The scaled angle cut was set at 30 mrad.

Bin 2 Eliminate from the fit one row of bins along each axis. For the q_0-q histograms, one row along the q-axis and one row along the diagonal are eliminated.

Bin 3 Eliminate two rows of bins as above.

NW Eliminate the close-pair weight function. These fit parameters are separated by the dotted line to demonstrate that here we are removing a correction rather than increasing the cuts.

[5] A study performed by V. Cianciolo produced a very similar trend over a different set of reference frames.

We see from the figure that the q_L-q_T fit parameters are extremely stable. Eliminating close-pairs and those with low relative momentum has little effect upon the measured radii. Furthermore the radii are not sensitive to the efficiency correction. The q_0-q parameters are not so stable; however, the radius parameters do not vary by more than their statistical errors. Any motion in τ is always accompanied by an opposite, lesser motion in R. This anti-correlation is consistent with the fit contours, and these errors are included in the estimation of the errors on the correlated parameter (in this case R). Removing the close-pair correction leads to a sizable increase (decrease) in τ (R) for each system.

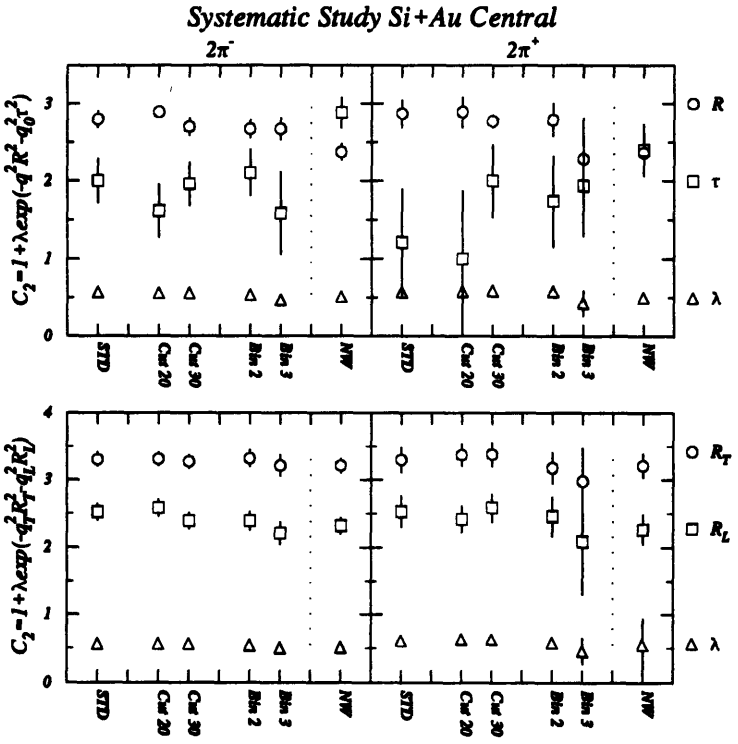

Figure 5-34: Fit parameters for Si+Au → $2\pi^-$ and Si+Au → $2\pi^+$ central systems under varying fit conditions. See text for explanation of x-axis labels.

5.6.2 The Reference Frame

The fit parameters for Si+Au → $2\pi^-$ and Si+Au → $2\pi^+$ central systems (for different source rapidities) are given in Table 5.8. As anticipated, R_T is unchanged under longitudinal Lorentz boosts. It is also not too surprising that R does not vary either, since two of its components are transverse to the boost. As usual, the errors on τ are too large to permit any meaningful observation.

For each system, R_L increases 15–20% for the rapidities away from Y_{nn}. However, depending on the value of $\vec{\beta}_{\pi\pi}$ this can be due to a source rest frame of Y_{nn} which is contracted when observed at Y_{cm}, or source at rest at Y_{cm} which is extended when viewed from Y_{nn}. This dilemma is perhaps resolved by the fact that two of the Si+Al $\rightarrow 2\pi^+$ systems show identical behavior (Table 5.9). This leads to the following conclusions:

1. In agreement with the Koonin Lorentz invariant fit results, the source rest frame for central Si+Au collisions lies closer to Y_{nn} than to Y_{cm}.

2. The longitudinal component of $\vec{\beta}_{\pi\pi}$ is zero (on average) when viewed in the Y_{nn} frame for both Si+Au and Si+Al collisions.

The latter conclusion is necessary to have a value of $\beta_{\pi\pi}$ equal to the source velocity when viewed in another frame — this provides the Lorentz contraction (see Sec. 5.1.2). Fig. 5-35 shows that for the 14° setting, the pions have a mean rapidity of 1.7, in support of item 2 above. In any case, it is clear that a more thorough study will be necessary to understand all of the rapidity dependent behavior that has been seen.

Sign	Y	$\lambda_{R-\tau}$	R	τ	$\lambda_{R_T-R_L}$	R_T	R_L
$2\pi^-$	1.25	0.57±0.02	2.80±0.11	2.00±0.29	0.56±0.02	3.30±0.11	2.52±0.12
	1.72	0.57±0.02	2.85±0.10	2.63±0.25	0.58±0.02	3.39±0.10	2.92±0.14
	2.19	0.55±0.02	3.14±0.08	0.00±0.59	0.55±0.02	3.46±0.11	2.39±0.13
$2\pi^+$	1.25	0.57±0.04	2.87±0.18	1.21±0.69	0.61±0.05	3.30±0.19	2.53±0.23
	1.72	0.59±0.04	2.91±0.18	2.16±0.51	0.60±0.04	3.32±0.16	2.83±0.22
	2.19	0.55±0.04	2.93±0.13	0.00±0.89	0.57±0.04	3.48±0.20	2.09±0.20

Table 5.8: Two-dimensional fit parameters for Si+Au $\rightarrow 2\pi^-$ and Si+Au $\rightarrow 2\pi^+$ central collisions for different rapidities: Y_{cm}, Y_{nn}, and $Y = 2.19$.

Mult.	Y	λ	R_T	R_L
23–47	1.25	0.64±0.04	2.68±0.13	2.26±0.18
	1.72	0.69±0.04	2.70±0.13	2.88±0.23
47+	1.25	0.66±0.05	2.99±0.16	2.07±0.19
	1.72	0.69±0.05	3.02±0.15	2.62±0.05

Table 5.9: R_T-R_L fit parameters for Si+Al $\rightarrow 2\pi^+$ central and semi-peripheral collisions for Y_{cm} and Y_{nn}

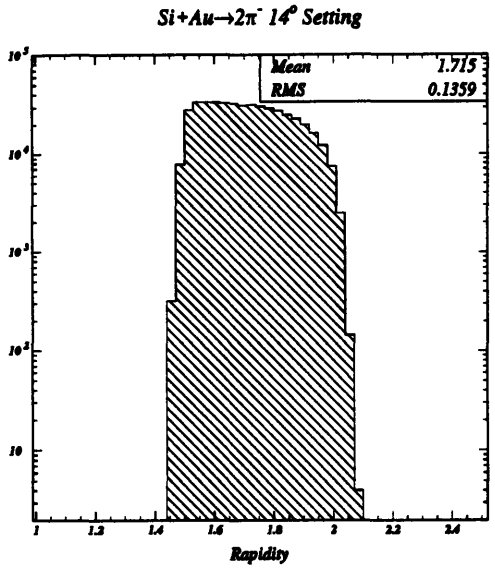

Figure 5-35: Rapidity of pions for Si+Au $\rightarrow 2\pi^-$ data set.

5.6.3 Estimate of Systematic Errors.

As an estimate of systematic errors we recommend a value of 20% for the longitudinal radii for the central Si+Au systems. The fits shown here do not show any strong systematic trends introduced by the weight correction or low-q cutoff. From the PID study shown in Sec. D a value of 10% is appropriate for R and R_T. It is not obvious that a systematic error for τ would be meaningful, due to the inconsistent nature of the fits. It remains to be seen whether this is simply a difficulty in the minimization process or whether this behavior has a physical origin. Further study may shed light on the issue.

Chapter 6

Model Comparisons

Comparisons of single particle spectra for relativistic heavy ion collisions to predictions of various cascade models have become commonplace over the past several years. Only recently have we been able to make similar comparisons for the two-particle correlations data. One should always treat such predictions with skepticism — the models are only reliable in as much as they are able to predict the data. However, when used with care, we can hope to learn something about the relevant particle production processes.

One of the much heralded features of the correlation analysis has been the ability to provide a model independent measure of the spatial and temporal extent of the particle production region. Recent results cast doubt on this assumption for the simple reason that the pions detected in our spectrometer are not produced isotropically throughout the source (ie. dynamical correlations exist).

In this chapter we present a cursory treatment of the fundamental effects which have been observed in the models. We start with a description of the RQMD cascade model. This is followed by an examination of the dynamical correlations which it exhibits. We study the relevance of these correlations to the present analysis by measuring the source sizes directly as a function of forward energy.

6.1 Description of RQMD

RQMD is one of two cascade codes (the other being ARC [Kah93]) which are capable of reproducing the general features of A+A collisions measured at the AGS and CERN [Sor93]. At AGS energies both codes operate primarily as hadronic cascades: collision probabilities between particles are calculated according to their cross-sections, the collisions are ordered in the Y_{nn} frame, the produced

excited states decay through various channels, the list of collisions is periodically updated and re-ordered. RQMD decays the excited states two ways. States with a mass less than 2 GeV/c^2decay through resonances, whereas states with masses above this threshold become strings which then fragment. Strings which overlap longitudinally form ropes (a kind of color capacitor). Although rope formation is enabled in the version of RQMD run for this analysis (version 1.08), the string density is not high enough for ropes to play a significant role in Si+X collisions at AGS energies. In addition, RQMD propagates particles through a mean field. At AGS energies the presence of the mean field also makes very little difference. For the results presented here it has been turned off through one of the switches which can be set at run time. RQMD version 1.08 contains a number of these switches; a list of those used for this analysis (we ran in the default mode) is given in Appendix E.

At the end of the collision, RQMD prints out a particle list with particle id, momenta, and position at the point of last interaction. These positions and momenta are not interpreted literally, because this violates the uncertainty principle. Instead, we view the particle collision lists as having sampled a distribution. Then we must address the question of whether these distributions obey the uncertainty principle. The transverse source distributions for particles entering the E859 spectrometer are Gaussians with a width of roughly 2 fm, and the transverse momentum distribution covers a range of about 0.5 GeV/c. Thus, the product of the two widths exceeds $\hbar/2$ by an order of magnitude. It is conceivable that strong dynamical correlations could lead to trouble, but it appears the primary effect of the dynamics is the constraint imposed by the experimental acceptance, and the dynamics beyond this constraint are minimal.

6.2 RQMD Sources

Neither ARC nor RQMD accounts for the pair-wise correlations between particles. To incorporate these effects Scott Pratt has written a code which calculates the square of the symmetrized two-particle wave-functions and applies this as a weight to pairs of identical particles [Pra94]. Comparisons of the E859 data to ARC [Pra94] and RQMD [Cia94] have shown both codes to give approximate agreement with the data. A detailed comparison of the correlation functions as a function of centrality will be an important test for the models, but this is a task for the future. Here we examine the source distributions directly to understand the role the dynamics play in limiting our view of the source and to see if the models predict a different dependence on forward energy

with or without the constraint of an experimental acceptance.

6.2.1 Dynamical Correlations in RQMD

While we only recently have had the privilege of using reliable models to estimate the effect of the dynamical correlations, the reasons for the effects are quite simple. Given a πN cross-section of $\sim$ 100 mb (near the Δ resonance), and taking the density of normal nuclear matter, we obtain a pion mean free path,

$$\lambda = \frac{1}{\sigma_{\pi N}\rho_o} = 10 \times 0.16^{-1} = 0.6\,\text{fm}.$$

Thus, a pion with momentum anti-parallel to its position[1] is unlikely to survive. However, most pions ($\gamma = 5$) will be carried in the direction of their momentum through a finite formation time ($\tau \approx 1$ fm/c,) and resonances ($\tau_\Delta = 1.7$ fm/c). Thus the final positions of these pions will be shifted along the direction in which they are traveling. The alignment of the momentum and position vectors for pions produced in RQMD is shown clearly in Fig. 6-1.

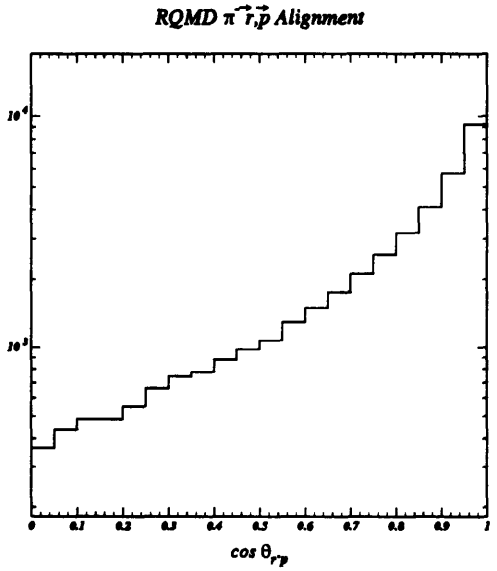

Figure 6-1: RQMD Si+Au central π^- alignment of position and momentum.

Since the E859 experimental acceptance selects only a limited range of momentum directions, we measure (according to RQMD) only a limited region of the source (see Fig. 6-2). There is also a concern that even with no acceptance cuts RQMD would still predict a reduction in the measured

[1] relative to the center of the source region

source due to strong correlations between the magnitude of Δr and Δp. One expects this to follow from Fig. 6-1, however, the dynamical correlations between *relative* position and momentum is much weaker. Fig. 6-3 shows the Gaussian widths (fit to a range of 10 fm) of Δx and Δy as a function of q_x and q_y, respectively. The source widths are reduced by $\sim$10% in the regions of low relative momentum. Thus the primary effect is due to the limitations imposed by the acceptance.

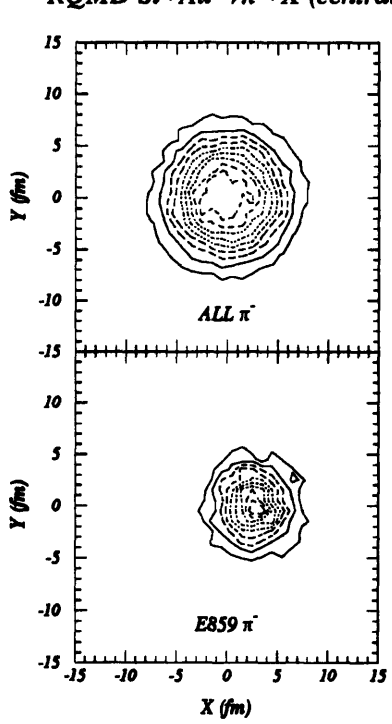

Figure 6-2: Y vs. X for π^- emission points in Si+Au central collisions for all pions (above) and those that fall within the E859 acceptance (below).

6.2.2 Forward Energy Dependence of RQMD Sources

We now study the relative emission points for two pions as a function of forward energy deposition. In choosing to look directly at the source production points we are not attempting to test the models. Instead we wish to gain some understanding of how the dynamics affect our interpretation of the fit parameters for the data. Specifically we want to know if the predictions of RQMD dramatically alter the observed scaling with projectile participants. Unfortunately it is not obvious how best to measure the RQMD sources, which extend well beyond what can be "seen" in the data due to finite momentum resolution. We have chosen to fit the distributions with the sum of two Gaussians

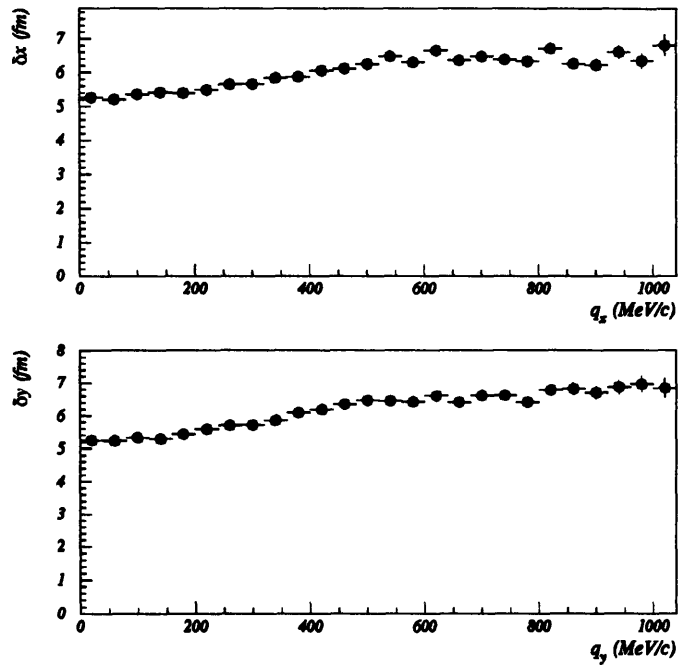

Figure 6-3: Gaussian widths of Δx and Δy distributions as a function of their conjugate momentum variables q_x and q_y. Courtesy of V. Cianciolo.

(Fig. 6-4). The Gaussian with the larger width accounts for the long lived resonances which decay to pions and leads to correlations in momentum that are too narrow for the spectrometer to resolve.[2] The smaller width is taken to be the relative separation that leads to the observed correlation function in the data. Fig. 6-4 shows the distributions in ΔR and with the double Gaussian fits superimposed. To study the dependence on forward energy (with and without acceptance cuts) the data are shown for three separate regions of a simulated ZCAL signal. This signal is calculated by summing the kinetic energy of baryons (plus twice the mass for anti-baryons) and total energy of mesons that fall within the ZCAL acceptance and then smearing with an appropriate resolution.

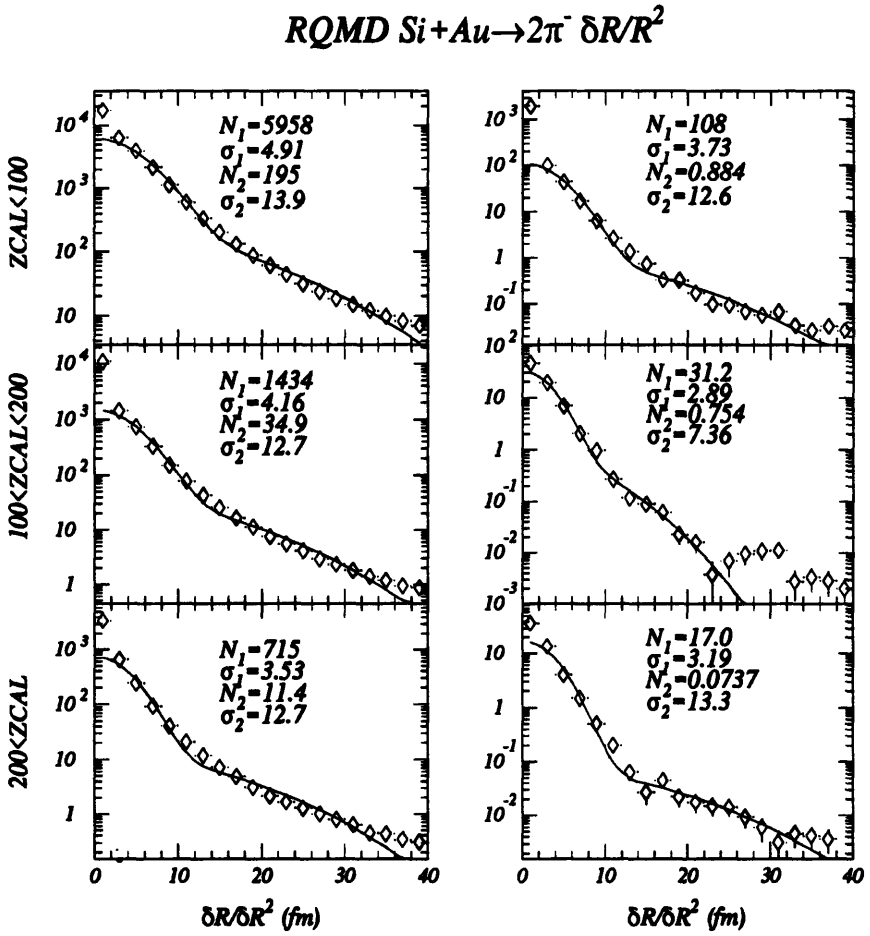

Figure 6-4: Double Gaussian fits to RQMD Si+Au → $2\pi^-$ with and without E859 acceptance cuts for three regions of simulated ZCAL energy.

Fig. 6-5 shows the smaller of the two Gaussian widths as a function of projectile participants

[2]It is the inclusions of these resonances which enables RQMD to match the value of λ observed in the data.

to the 1/3 power for both Si+Au $\rightarrow 2\pi^-$ and Si+Al $\rightarrow 2\pi^+$ RQMD data sets. To compare to the data (also shown in the figure) the ΔR parameters have been divided by the appropriate conversion factor,$\sqrt{2}$, for Gaussian distributions. To reiterate, this is not a true test of the models,[3] but we see that the general trend is reproduced in the RQMD Gaussian widths when the E859 acceptance is imposed. A careful comparison of RQMD correlation functions to the data for similar cuts in multiplicity and forward energy will be performed in the future.

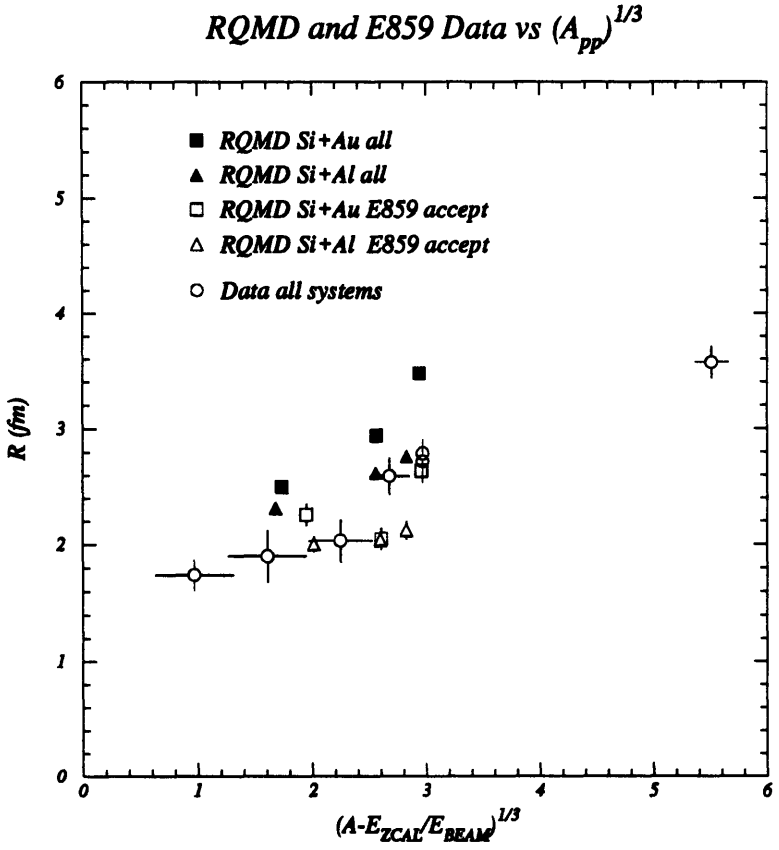

Figure 6-5: RQMD Gaussian widths and E859 Radius parameters versus projectile participants.

[3]The data points are the apples; the RQMD points are the oranges.

Chapter 7

Conclusions

Before addressing the questions that were put forth in the introduction, we return briefly to the topic of plasma formation. Detecting this phase transition was not part of the initial objective of studying the variation of the radius with impact parameter in heavy ion collisions. Nevertheless there was some chance that we might have observed the onset of QGP formation in one of the following ways:

- An unusually large radius or lifetime in the most central (2%) Si+Au collisions.
- An unusually large radius or lifetime in central (5%) Au+Au collisions.
- Indications of a long-lived emission (lifetime) from comparison of the Bertsch fit parameters for either one of the above systems.
- Any deviation from the observed trend in radius parameters as a function of system size.

The data do not show any of these signs. It is, of course, possible for the QGP to have been formed in some events, but we see no evidence for it in this analysis.

7.1 Answers

We now address the questions of Sec. 1.2.5.

1. Does the source size vary with collision centrality?

Yes, it does. We see distinct trends within each system when the data are cut in either multiplicity or forward energy. The contour plots of the most peripheral and most central cuts in each variable show clearly that the radii we have measured for these extremes are indeed significantly different.

While other experiments have performed measurements which suggest this dependence [F+78, L+81, B+86], and an analysis of the La+La system has shown a significant difference for one parameterization [C+93], this is the first time that such a stark contrast has been observed.

2. How is this variation best characterized?

The linear scaling of the radii with $A_{pp}^{1/3}$ makes a strong argument for the use of projectile participants to describe this variation. The number of projectile participants, A_{pp}, has a natural geometric interpretation in terms of system size and therefore can be applied to describe the observed variation between different systems as well. However, the fact that multiplicity and forward energy deposition are related makes it difficult to argue forcefully that the number of projectile participants is the true dependent variable. Attempts to observe a plateau in the radii for the most central multiplicities were inconclusive.

In the past, it has been argued that the multiplicity variation can be understood in terms of a pion freeze-out radius. This requires further assumptions regarding the nature of the collisions (thermalization, etc.). The appropriate variable is then the pion multiplicity per unit rapidity. The TMA does not provide us with the ability to distinguish between the pions and protons. This variable, dn_π/dy, is more easily calculated for experiments which cover 4π in solid angle than for a small aperture spectrometer experiment. For these reasons we have made no attempt to explain the data in terms of dn_π/dy, but this may be a consideration for future analysis.

3. What do Bose-Einstein correlations actually measure?

If, for the moment, we ignore the model results and consider only the data, then the observed trend in the measured radii is reassuring. The fact that this result is consistent with a simple geometric picture of the collision (pion production in the region of overlap) lends support to the belief that the pion correlation function yields an accurate measure of the size of the pion source. One would conclude that despite the many subtleties involved in its application and interpretation, pion interferometry provides reliable source measurements for heavy ion collisions.

The models, however, point to a non-subtle effect which substantially alters this conclusion. Results from two cascade models indicate that the E859 spectrometer does not detect particles emitted isotropically throughout the collision source. That these models both provide an adequate description of the single particle distributions and show some agreement with the correlation results as well means that this prediction cannot be ignored. Thus, despite the success of our self-consistent

check of the two-pion correlation, there is still reason for much caution. This is not to say that our result is in doubt, only that we do not yet have an interpretation of the Bose-Einstein radius parameters which can be translated into a measure of the full source. In closing, we return to the context of e^+e^- annihilations and the lessons learned there. In a talk given to the heavy ion community on the topic of Bose-Einstein correlations in jets [Bow91], M.G. Bowler had these words of advice, "Be very very careful."

7.2 Recommendations

The Herculean task facing the next generation of students who choose to study Bose-Einstein correlations at the AGS is to find a measurement which will confirm or disprove the presence of the strong dynamical correlations predicted by the cascade models. Experiment E866 is now outfitted with a beam fragment hodoscope in addition to the ZCAL, and will soon have a new multiplicity array for use with the Au beam. The same dynamical correlations observed in the two-particle predictions also lead to strong dependence of particle production on the collision axis (reaction plane). The combination of these three detectors may measure this axis with enough precision to study this dependence in the data, provided that this data set extends to target and projectile rapidities. A two-particle analysis can also be performed in this fashion to search for shadowing of the source region by spectator nucleons. While measurements such as these have the potential to clearly illustrate the dynamics, they are also very difficult to perform for collisions at relativistic energies, and are just as likely to prove inconclusive.

Without an independent means to verify the dynamics, the two-particle correlation measurements themselves become a constraint on the dynamics contained in the models. While this may signify the end of attempts to obtain a model-independent yardstick (of the collision) through Bose-Einstein correlations, it is not the end of the physical usefulness of correlation studies. In this scenario, for better or worse, the correlation data are married to the dynamics. But this is perhaps nothing new. It is very likely that the two have been married — though always seen apart — for some time, and only now do we see how much we have missed.

Appendix A

Bose-Einstein Statistics

We start with the commutation relations between the creation and annihilation operators,

$$\{a_{\mathbf{p}}, a^{\dagger}_{\mathbf{p}'}\} = (2\pi)^3\delta(\mathbf{p}-\mathbf{p}'); \qquad \{a_{\mathbf{p}}, a_{\mathbf{p}'}\} = \{a^{\dagger}_{\mathbf{p}}, a^{\dagger}_{\mathbf{p}'}\} = 0.$$

The corresponding field operators are constructed from superpositions of momentum operators multiplied by the proper phase,

$$\begin{aligned}\psi^{\dagger}(x) &= \int \frac{d\mathbf{p}^3}{(2\pi)^3} a^{\dagger}_{\mathbf{p}} e^{+ix\cdot p} \\ \psi(x) &= \int \frac{d\mathbf{p}^3}{(2\pi)^3} a_{\mathbf{p}} e^{-ix\cdot p}.\end{aligned}$$

The density operator is defined by,

$$\rho(\mathbf{p}) = a^{\dagger}_{\mathbf{p}} a_{\mathbf{p}} \tag{A.1}$$

The remainder of this derivation of the pair correlation function is essentially identical to that found in the quantum mechanics text by Baym [Bay69, pp 427–431] except that it has been generalized for a continuum normalization.[1] We wish to evaluate the two-particle momentum density,

$$\begin{aligned}P(\mathbf{p}_1, \mathbf{p}_2) &= \frac{\langle N|\rho(\mathbf{p}_1)\rho(\mathbf{p}_2)|N\rangle}{\langle N|N\rangle} \\ &= \frac{\langle N|a^{\dagger}_{\mathbf{p}_1} a_{\mathbf{p}_1} a^{\dagger}_{\mathbf{p}_2} a_{\mathbf{p}_2}|N\rangle}{\langle N|N\rangle}\end{aligned}$$

[1] The author wishes to thank Xiandong Ji for help in making this generalization.

$$= \frac{\langle N| \int d\mathbf{x_1}^3 d\mathbf{x_2}^3 d\mathbf{x_3}^3 d\mathbf{x_4}^3 e^{i\mathbf{p_1}\cdot(\mathbf{x_1}-\mathbf{x_2})+\mathbf{p_2}\cdot(\mathbf{x_3}-\mathbf{x_4})} \psi^\dagger(x_1)\psi(x_2)\psi^\dagger(x_3)\psi(x_4)|N\rangle}{\langle N|N\rangle}$$

The integrand above is non-zero for only two cases, which we will project out by multiplying the integrand by the appropriate normalized delta functions. These delta functions are normalized by the volume: $(2\pi)^3\delta^3(0) = V$.

1. $\mathbf{x_1} = \mathbf{x_2}, \mathbf{x_3} = \mathbf{x_4} \rightarrow \delta^3(\mathbf{x_1} - \mathbf{x_2})\delta^3(\mathbf{x_3} - \mathbf{x_4})/[\delta^3(0)]^2$

2. $\mathbf{x_1} = \mathbf{x_4}, \mathbf{x_2} = \mathbf{x_3} \rightarrow \delta^3(\mathbf{x_1} - \mathbf{x_4})\delta^3(\mathbf{x_2} - \mathbf{x_3})/[\delta^3(0)]^2$

These two cases are not mutually exclusive so we must subtract their intersection,

1. ∩ 2. $\mathbf{x_1} = \mathbf{x_2} = \mathbf{x_3} = \mathbf{x_4} \rightarrow -\delta^3(\mathbf{x_1} - \mathbf{x_2})\delta^3(\mathbf{x_2} - \mathbf{x_3})\delta^3(\mathbf{x_3} - \mathbf{x_4})/[\delta^3(0)]^3$.

Performing the integration over the delta functions,

$$\begin{aligned} P(\mathbf{p_1}, \mathbf{p_2}) &= \int \frac{d\mathbf{x_1}^3 d\mathbf{x_3}^3}{[\delta^3(0)]^2} \frac{\langle N|\psi^\dagger(x_1)\psi(x_1)\psi^\dagger(x_3)\psi(x_3)|N\rangle}{\langle N|N\rangle} \\ &+ \int \frac{d\mathbf{x_1}^3 d\mathbf{x_2}^3}{[\delta^3(0)]^2} \frac{\langle N|\psi^\dagger(x_1)\psi(x_2)\psi^\dagger(x_2)\psi(x_1)|N\rangle}{\langle N|N\rangle} e^{i(\mathbf{p_1}-\mathbf{p_2})\cdot(\mathbf{x_1}-\mathbf{x_2})} \\ &- \int \frac{d\mathbf{x_1}^3}{[\delta^3(0)]^3} \frac{\langle N|\psi^\dagger(x_1)\psi(x_1)\psi^\dagger(x_1)\psi(x_1)|N\rangle}{\langle N|N\rangle}. \end{aligned}$$

Substituting the volume for the $\delta^3(0)$ terms, we see that the third term is proportional to $1/V^2$ and therefore vanishes in the continuum limit. The first two terms are equivalent to the square of the single particle field density and the square of the F.T. of the single particle density, respectively. Thus,

$$\begin{aligned} P(\mathbf{p_1}, \mathbf{p_2}) &= \left\{ \int \frac{d\mathbf{x}^3}{\delta^3(0)} \frac{\langle N|\rho(\mathbf{x})|N\rangle}{\langle N|N\rangle} \right\}^2 \\ &+ \left\{ \int \frac{d\mathbf{x}^3}{\delta^3(0)} \frac{\langle N|\rho(\mathbf{x})|N\rangle}{\langle N|N\rangle} e^{i(\mathbf{p_1}-\mathbf{p_2})\cdot\mathbf{x}} \right\}^2. \end{aligned} \tag{A.2}$$

Given a suitable form for the single particle density distribution we can gain some measure of the extent of this distribution by comparing its F.T. to a measured relative momentum distribution. This is the essence of the use of Bose-Einstein statistics in measuring source sizes.

Appendix B

LVL2 Bias Study

The final search for trigger errors is performed with a thorough examination of each of the runs taken with the veto disabled. The focus of such a *veto-out* study is to collect valid events for which the LVL2 veto bit was set and to ascertain the exact reason why LVL2 did not accept these events. Such a study depends on the final definition of a good event, and the conclusions must be understood in terms of the analysis undertaken. However, once LVL2 errors are detected and understood, the implications for other E859 measurements can be determined.

What follows is a scan of all of the $2\pi^-$ events rejected by the LVL2 trigger during the central Si+Au $\rightarrow 2\pi^-/\Lambda$ runs (11161–11164). This study is not a complete analysis for the trigger setting. It is, however, the relevant study for the two-pion analysis. There are two important distinctions between the LVL2 and PICD definitions of a pion track. There is, of course, a difference in resolution between the LVL2 online particle id and the full track reconstruction with offline timing calibrations. There is also a difference in the PID scheme utilized. We will return to these differences when discussing PICD pions that fall outside the LVL2 definition.

These runs contain a total of 2488 $2\pi^-$ events, of which a total of 32 or 1.3% were rejected by the trigger. The breakdown of these events into categories is given in Table B.1. The first two categories refer to pions which fail to record a hit on one of the two trigger chambers. The TR1 and TR2 chambers are known to be slightly inefficient, and it is expected that some tracks will be lost in this manner. No such inefficiency affects the TOF wall, which is required in any particle identification scheme. There is a subtle two-particle bias that results from the TR1/TR2 inefficiency, however. If there are two tracks that are close in X on the TOF wall, then one track may share the trigger chamber hit from the other. Thus, two pions which hit neighboring slats

are less likely to suffer from this inefficiency. The relative excess can be no greater than the total TR1/TR2 inefficiency of 0.3%. Such an enhancement is well below the statistical errors in a delta slat distribution, and attempts to discover such an enhancement were not successful. Furthermore, two tracks which share a hit on the trigger chambers will also share x-hits on T3 and T4, and the reconstruction algorithm may have difficulty finding both tracks.

Reason	Rejected events
TR1 hit missing	7
TR2 hit missing	1
SWI out of range	3
DS SLAT-hose	7
DS TOFD-hose	1
not PID'ed	12
multiple	1

Table B.1: Results of LVL2 bias study for Si+Au $\rightarrow 2\pi^-$ runs 11161–64.

The third category refers to particles which decay or multiple scatter on their way to the TOF wall, but are still reconstructed by AUSCON. An example of such an event is shown in Fig. B-1. In track number 2, the TOF hit is displaced from the straight-line track which AUSCON finds. LVL2 was unable to connect this hit with any pair of trigger chamber hits. In principle, all such tracks could be found by widening the search width. A search width (the number of adjacent wires on either side of the predicted wire which can be used with a TR1/TOF combination to form a valid track) of *1-2* was used for the event shown.

"DS SLAT-hose" and "DS TOFD-hose" refer not to the latest in latex fashion-wear, but to the one failure mode of the trigger which is not yet understood. The problem is consistent with a Data Stack entry that contains a repeat of the previous slat number. When the repeat overwrites the data words of a valid particle, that particle is lost by the trigger.

A small percentage of events were lost because the pion cuts used by the trigger were inconsistent with those used by the PICD particle identification scheme that later on became the collaboration standard. The PICD particle-id (Sec. 4.1.3) makes three sigma cuts in time-of-flight ($1/\beta$) for a given momentum. A momentum cut-off is applied where kaon and pion definitions begin to overlap. The LVL2 particle identification uses specified mass windows with a momentum cutoff. Fig. B-2 shows the discrepancy between the two methods of identifying pions and the AUSCON and LVL2 momentum and mass of particles that not identified as pions by LVL2. The figure employs an unusual convention to display the PICD cuts in the region where $\beta > 1$. Since the mass becomes

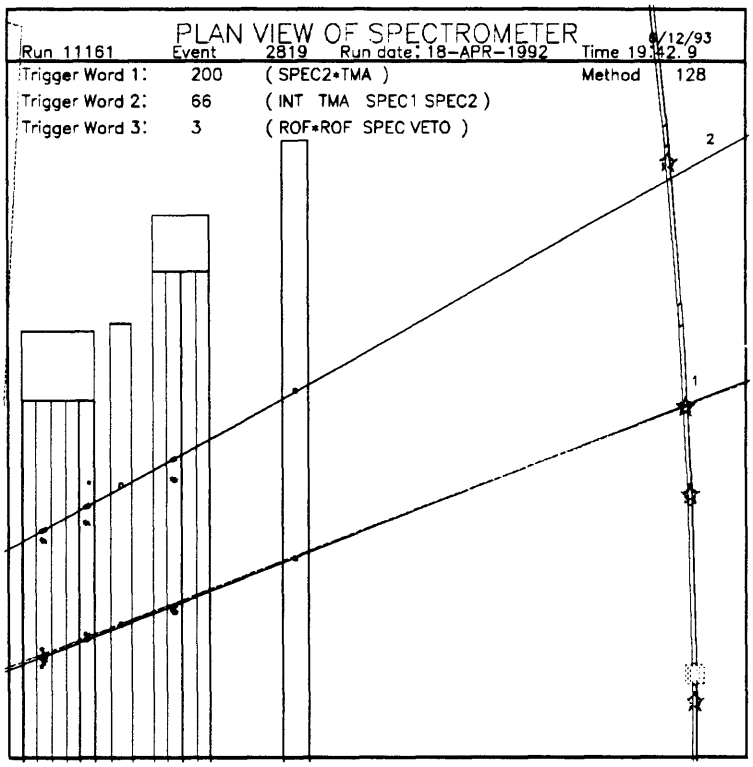

Figure B-1: A pion that scattered or decayed on its way to the TOF wall was reconstructed by AUSCON, but not found by LVL2.

imaginary in these region, we use the magnitude of the mass and flip the sign (negative pions now have a positive mass). The LVL2 uses mass cuts and accepts all $\beta > 1$ particles as pions. In the figure the solid line corresponds to the 300 MeV/c^2 cutoff for the LVL2 definition of a pion, and the dotted curves represent the PICD cuts. Note that all of the LVL2 points lie to the left of this line, indicating that they were not identified as pions by the trigger, and all of the PICD points fall within the PICD pion region.

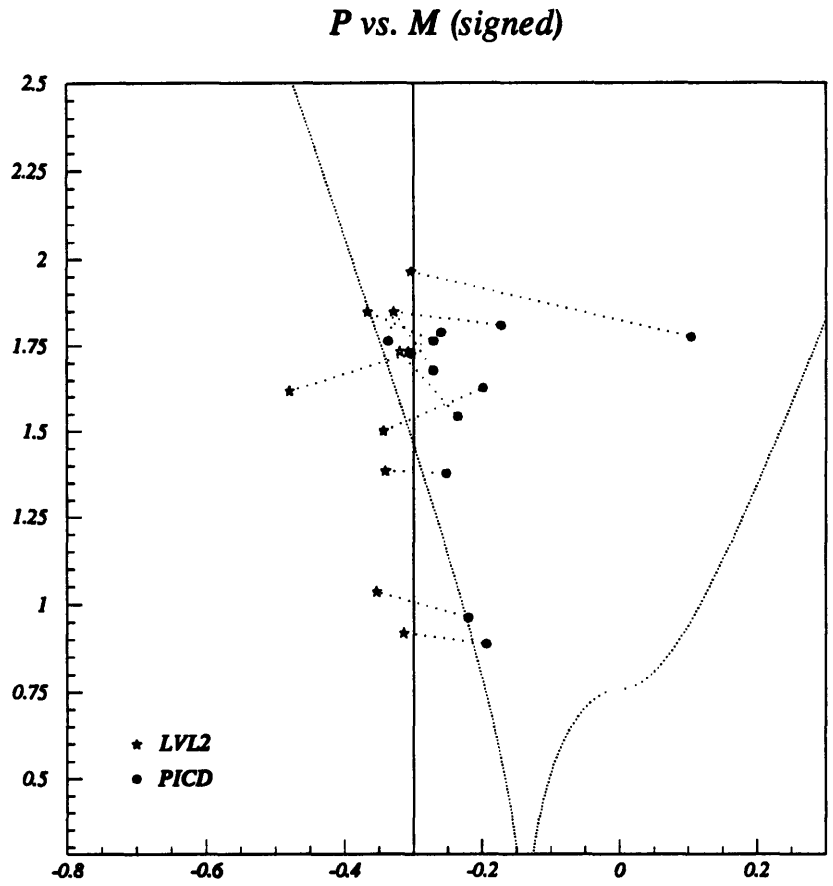

Figure B-2: Momentum vs. Mass for LVL2 and PICD identified pions. The LVL2 tracks (stars) are joined to their counterpart PICD tracks (filled circles).

The ultimate question for the two-particle correlation analyses is of course whether the trigger has introduced a bias in the relative momentum for identical particles. It is difficult to get an accurate measure of the relative momentum spectra from such a small number of particles. To obtain even a crude picture of this distribution for the rejected events it was necessary to combine pion pairs from

all of the systems for which veto-out runs were taken. The Q_{inv} distribution, along with the scaled distributions for each of the individual systems are shown in Fig. B-3. The distribution shows a very slight bias towards rejecting higher Q_{inv} tracks. This slight bias is in a rejection rate that is only 1%. The effect on the correlation function is negligible. However, in an attempt to understand this bias we have plotted the ratio of all of the LVL2 rejected events over all of the LVL2 accepted events in Fig. B-4. We have plotted this ratio for all events, and for those which do not contain a pion with momentum above 1.5 GeV/c. This cut appears to remove the slight bias, although the statistics are marginal. Nevertheless, it suggests that this slight bias may be understood in terms of the pid bias shown in Fig. B-2. It is the relation between high q and high momentum which then produces the observed bias in Q_{inv}.

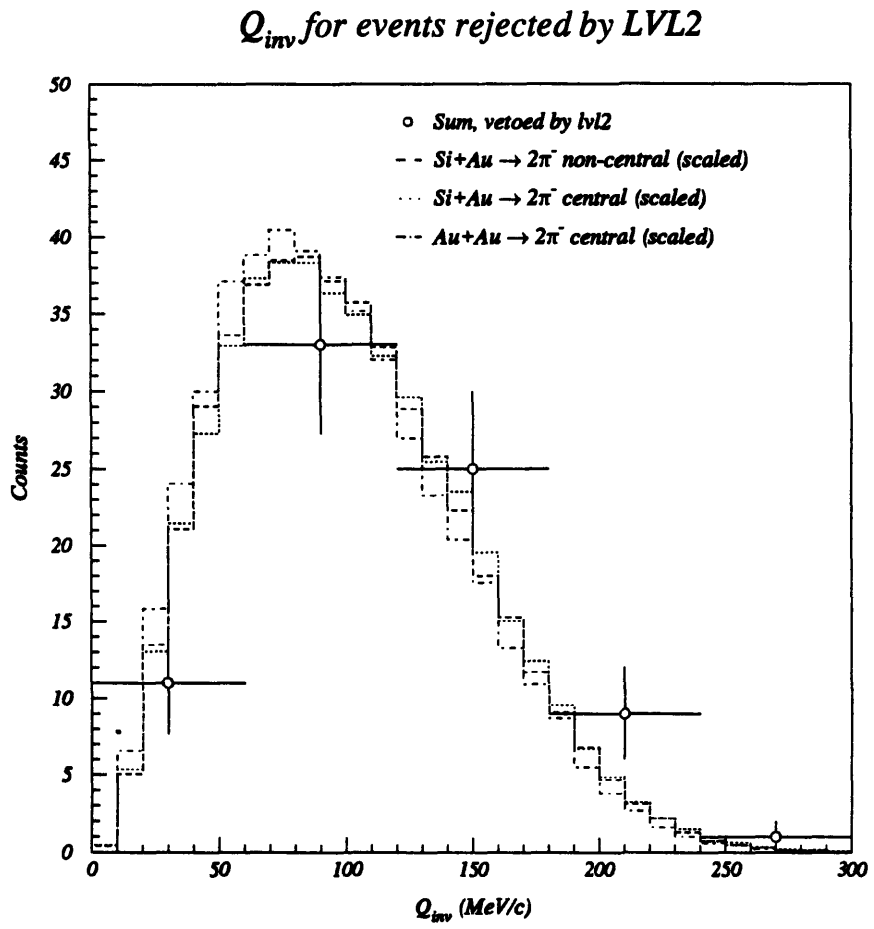

Figure B-3: Q_{inv} distributions for pion-pairs rejected by the trigger

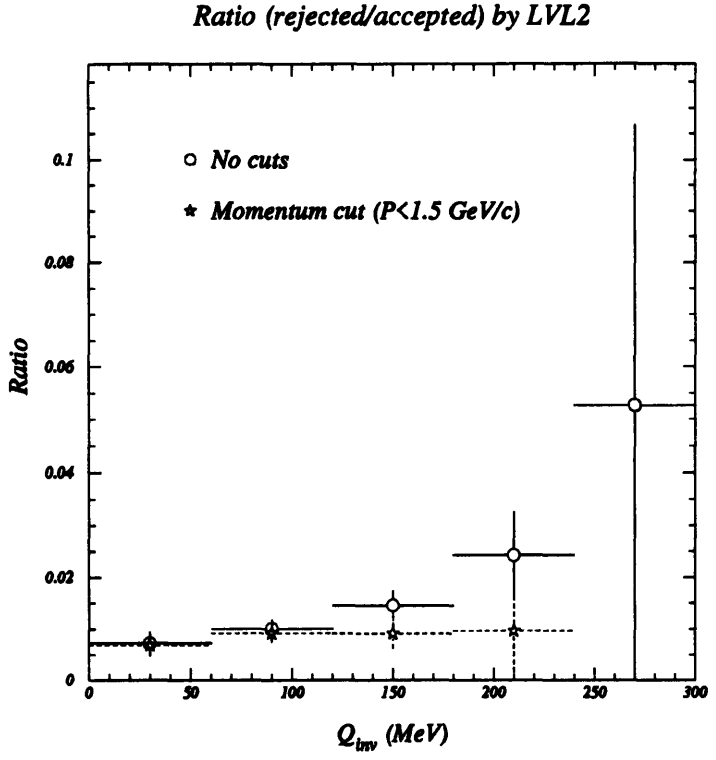

Figure B-4: Ratio of rejected over accepted (LVL2) pion pair events.

Appendix C

Background Errors Study

We suspect that the background errors are not the errors of a Poisson distribution for the following reason: Given an Actual (Poisson) distribution of N independent events, the relative errors in a bin are $1/\sqrt{Nf_i}$, where f_i is the fractional occupancy of the $i'th$ bin. Through event mixing we can form $M \approx N^2$ Background pairs.[1] Since no new independent information has been added, we expect the relative errors to be $\sim 1/\sqrt{Nf_i}$, rather than $\sim 1/\sqrt{Mf_i} = 1/\left(N\sqrt{f_i}\right)$ were the Background also a Poisson distribution. To demonstrate this formally, Zajc [Zaj82, Z$^+$84] developed a simple model which permits a type of background error to be derived through propagation of the errors of the actual distribution.

C.1 The Toy Box

In the model, Zajc derives the errors for a Monte Carlo calculation of the area of a rectangle, Ω, in which the x and y coordinates are both taken from a single array of N of random numbers. Here, l_x and l_y are the fractional lengths of the rectangle along x and y. If we form all possible pairs and count the number of points, n_Ω which fall inside the box, the fractional area is then,

$$\begin{aligned} A &= n_\Omega/N^2 \\ &= n_x n_y/N^2 \\ &= l_x l_y, \end{aligned}$$

[1] $N\left(N-1\right)/2$ pairs, to be exact.

and the error on the on the number of points in the box is,

$$\begin{aligned}\sigma_{n_\Omega}^2 &= \left(\frac{dn_\Omega}{dn_x}\right)^2 \sigma_{n_x}^2 + \left(\frac{dn_\Omega}{dn_y}\right)^2 \sigma_{n_y}^2 \\ &= n_y^2 n_x + n_x^2 n_y \\ &= N^3 \left(l_y^2 l_x + l_x^2 l_y\right).\end{aligned} \tag{C.1}$$

Here we have assumed that the errors on n_x, n_y are Poisson. One can derive a similar expression assuming binomial errors, however the Poisson errors are more easily applied to the relative momentum distributions of the data. Note that we have also assumed that our box does not intercept the diagonal; this would require the addition of the covariance terms to Eq. C.1. This expression is further simplified by making our rectangle a square ($l = l_x = l_y$),

$$\sigma_{n_\Omega}^2 = 2\,(lN)^3\,. \tag{C.2}$$

The relative error is,

$$\begin{aligned}\sigma_{n_\Omega}/n_\Omega &= \sqrt{2}\,(lN)^{3/2}/n_\Omega \\ &= \sqrt{2}/\left(n_\Omega\right)^{1/4}\end{aligned}$$

Despite combining x and y points from a single array, the relative errors are still proportional to $1/\sqrt{N}$. Had we instead formed $N/2$ truly independent pairs from the array of N points, then the number of points in the square would be only $l^2 N/2$, and the relative errors would be $\sqrt{2}/\left(l\sqrt{N}\right)$, instead of $\sqrt{2}/\sqrt{lN}$. Thus, in this context the event mixing reduces the relative errors by a factor of $\sqrt{l}$.

Zajc then replaces the fractional area of the box, l^2, with the fractional bin occupancy, f, in deriving the limit for which the contribution from the Background to the errors in the correlation function is non-negligible.

C.2 Generalization to Random Sampling

For the large numbers of Actual pairs in the E859 it is not feasible to generate the entire set of N^2 pairs ($> 10^{10}$ in some cases). For this reason we have generalized the likelihood-χ^2 fitting procedure

to accommodate non-negligible errors in the background (Sec. 4.4.3), and for this reason we[2] now generalize Zajc's toy model to the case in which a random subset of all possible background pairs are formed. In what follows there are two ensembles begin considered. We start with Eq. C.3, expressed as a sum over and ensemble of Q different event sets, each containing N events. The variance about the true area (A) follows the formula of Zajc because we are forming all pairs from each set of N events.

$$\sigma^2_{AN} \equiv \frac{1}{Q}\sum_{j=1}^{Q}\left(A_j N^2 - AN^2\right)^2 = 2\,(lN)^3\,. \tag{C.3}$$

The second ensemble consists of R backgrounds, each generated from a random sample of M pairs taken from the j^{th} event set. A_j is the empirical area as determined from one of the this event sets. It is defined by averaging over the R backgrounds, and *its* variance about its mean is Poisson.

$$\begin{aligned} < x_{ij} > \quad &\equiv \tfrac{1}{R}\textstyle\sum_{i=1}^{R} x_{ij} \quad &= A_j M \\ \sigma^2_{A_j M} \quad &\equiv \tfrac{1}{R}\textstyle\sum_{i=1}^{R}\left(x_{ij} - MP_j\right)^2 \quad &= A_j M. \end{aligned} \tag{C.4}$$

Now we wish to calculate the variance about the *true* area by summing over both ensembles. Thus, for each of the Q event sets, we form one all-pair background using all the pairs. Then, for each of these all-pair backgrounds, we randomly choose R subset backgrounds, each consisting of M pairs of points. Each of the all-pair backgrounds fluctuates about the *true* area, while each of the subset backgrounds fluctuates about the area one would get empirically from using its parent (all-pair) background. To calculate the fluctuations of the subset background about the *true* area, we must perform both sums,

$$\begin{aligned} \sigma^2_{AM} \quad &\equiv \quad \frac{1}{QR}\sum_{i=1}^{R}\sum_{j=1}^{Q}\left(x_{ij} - AM\right)^2 \\ &= \quad \frac{1}{Q}\sum_{j=1}^{Q}\underbrace{\sum_{i=1}^{R}\left(x_{ij}^2\right)}_{A_jM+(A_jM)^2} - (AM)^2 \\ &= \quad \underbrace{\frac{1}{Q}\sum_{j=1}^{Q}A_jM}_{AM} + \underbrace{\frac{1}{Q}\sum_{j=1}^{Q}(A_jM)^2}_{M^2\left(A^2+\frac{2l^3}{N}\right)} - (AM)^2 \end{aligned}$$

[2]This "We" refers to L. Ahle, V. Cianciolo, and the author.

$$= AM + M^2 \frac{2l^3}{N}. \tag{C.5}$$

The relative error is therefore,

$$\sigma_{AM}/AM = \sqrt{\frac{1}{AM} + \frac{2}{lN}}. \tag{C.6}$$

Note that this relative error has the appropriate limiting behavior:

$$\sigma_{AM}/AM = \begin{cases} \frac{1}{\sqrt{AM}} & N \gg M \quad \text{Poisson} \\ \frac{\sqrt{2}}{(AM)^{1/4}} & M \gg N \quad \text{Zajcian.} \end{cases} \tag{C.7}$$

Fig. C-1 examines the relative error as a function of the number of pairs, M. In this calculation, $N = 1000$, and $R = Q = 50$. The sides of the box have a fractional length of $\frac{1}{10}$. For $M \leq N$, the relative errors are well approximated by the errors of a Poisson distribution, whereas when M becomes large, the relative error approaches the Zajcian limit. Eq. C.5 is shown as a solid line; the more accurate binomial generalization provides a slightly better description of the Monte Carlo data points. The fluctuations for large M are not understood, but may be a result of relatively small values for R and Q.

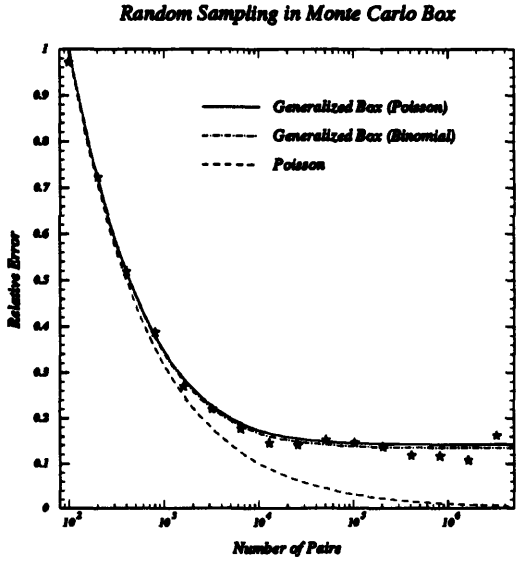

Figure C-1: Relative Errors for an off-diagonal box, 0.1 fractional length on a side as a function of the number of combinations formed from a 1000 element array.

C.3 Back to the Data

Encouraged by the success of Eq. C.6, we tested our formula against the data. The fractional area, $A = l^2$, was replaced by the fractional bin occupancy, f. The large central Si+Au $\rightarrow 2\pi^-$ Actual data set was subdivided into 200 event sets, and 200 backgrounds were generated from each. The relative errors on the mean were calculated from the sum over the two ensembles. It is worth noting that to arrive at the true relative error a sum must be performed over both the $\mathcal{R}$ and $\mathcal{Q}$ ensembles. If the errors are calculated from a sum over multiple backgrounds constructed from a single event set, this is equivalent to an empirical derivation of Eq. C.4. These relative errors correspond to the error in determining the number of all pairs that fall inside the box, and not the error in determining the true area of the box. This calculation will show the errors to be Poisson for any number of pairs that is significantly less than the maximum possible [Mor90, pp 147–151]. The results of performing a sum over both ensembles are shown in Fig. C-2. When all pairs are formed, the true errors are intermediate between those of a Poisson distribution and the predictions of the Zajc box model. For the case when the number of background pairs is limited to ten times the number of actual pairs, the distribution is well described by a Poisson. Thus, when applied to the data, both the box and generalized box formulas give rather conservative estimates for the relative errors per bin.

The data deviate from the toy model predictions for two reasons:

1. The two-dimensional shape formed by pairing the single particle momenta is much more complex than a square.

2. The single particle momentum distributions are not flat.

A closer examination of the shape of the event-mixed relative momentum bins illustrates why the true errors are much closer to Poisson than the toy model would have us believe. We return to Eq. C.1 of the original model. We can, with no loss of generality, divide the box into a grid $(u \times v)$ of smaller boxes.[3] The number of pairs which fall in the box is,

$$n_\Omega = \sum_{i=1}^{u} n_{x_i} \sum_{j=1}^{v} n_{y_j},$$

[3]This crucial piece of insight was provided free of charge by G.S.F. Stephans.

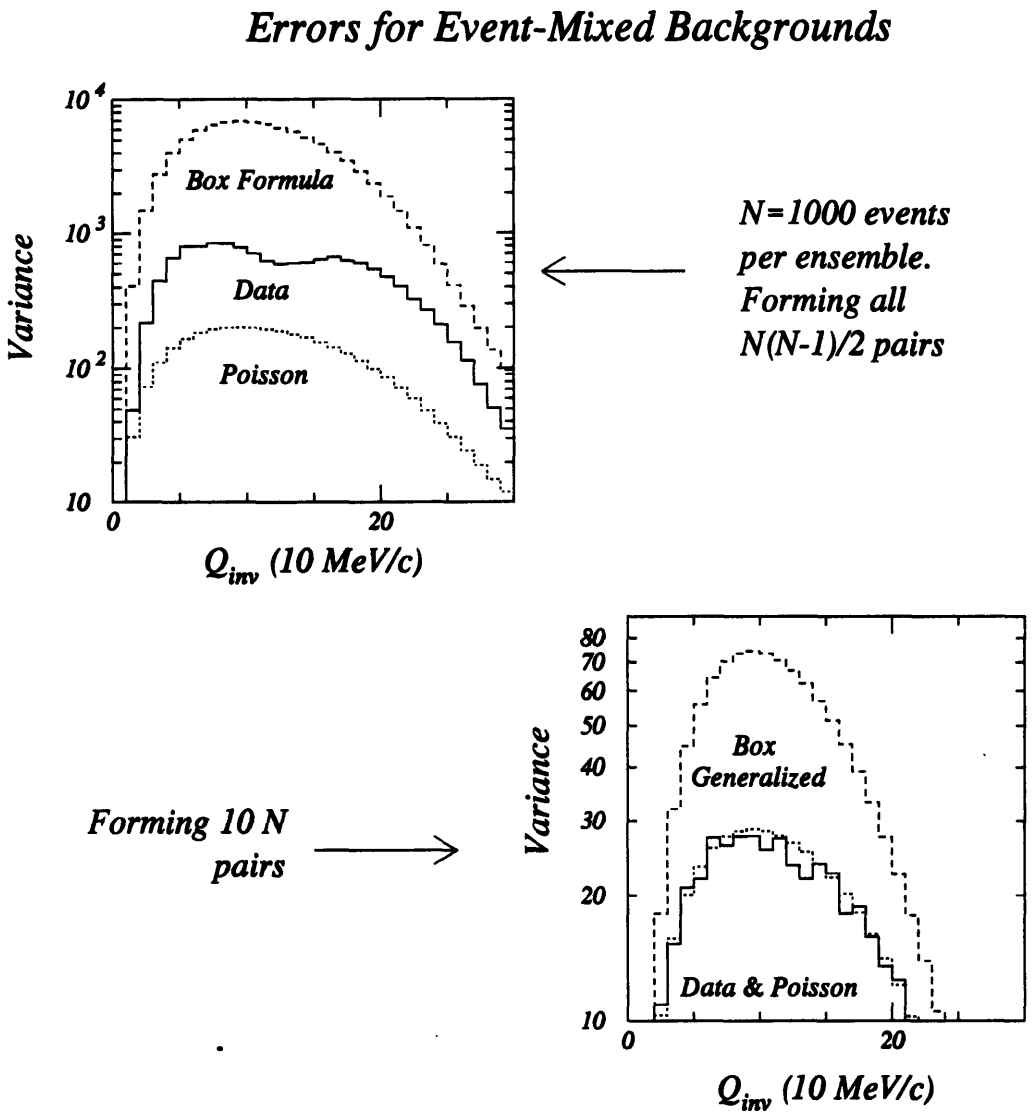

Figure C-2: Empirically determined errors for E859 Q_{inv} Background distributions.

and the variance on the mean is,

$$\sigma^2_{n_\Omega} = \sum_{i=1}^{u} \left(\frac{dn_\Omega}{dn_{x_i}} \right)^2 n^2_{x_i} + \sum_{j=1}^{v} \left(\frac{dn_\Omega}{dn_{y_j}} \right)^2 n^2_{y_j}. \tag{C.8}$$

This is an equivalent form of Eq. C.1 that can be generalized to irregular shapes. We use it to examine the errors for a distribution of one component (q_y) of the relative momentum. Fig. C-3 shows a crude grid applied to a distribution binned in q_y. According to our grid formula (Eq. C.8), grid boxes which do not overlap in their projections onto the axes are independent. Bins in relative momentum are described by grid boxes which lie along a diagonal, and are thus independent. In the limit of very narrow bins, each grid box will contain only a few points, and the errors per bin will be Poisson. Note, however, that we have completely neglected correlations between errors from different bins.[4] These will certainly be significant for background distributions generated by mixing all of the pairs.

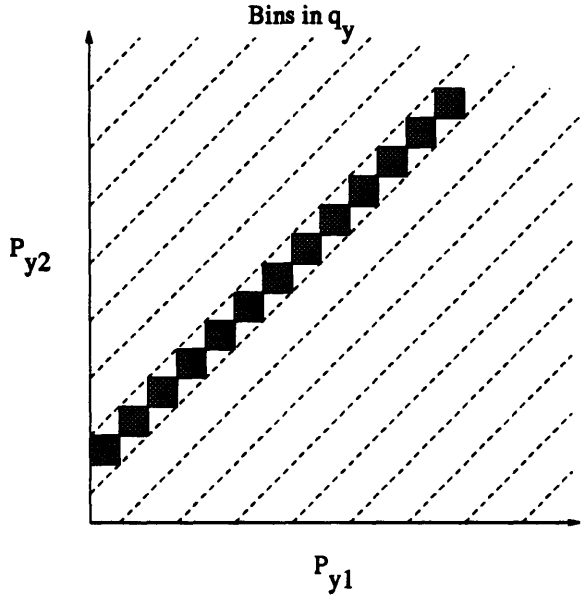

Figure C-3: A Box grid applied to a background distribution binned in q_y.

Some work has been done to incorporate the momentum distributions into understanding the errors of event mixed backgrounds, but we have yet to derive an analytic formula for this general case. The existence of such a general formula would be a significant contribution to all experimental physics analysis which makes use of event-mixed backgrounds. Here we have demonstrated that

[4] A subject for future study perhaps.

by limiting ourselves to a background that does not exceed more than ten times the statistics of the actual distribution, the errors for fluctuations within a bin are indeed Poisson.

Appendix D

Particle Identification Study

Table D.1 contains the parameters and correlation functions for the TOFID scheme compared side-by-side with the PICD results. Both ID schemes use a 1.82 GeV/c maximum pion momentum cut in this analysis. In most cases the fit parameters differ by not more then the sum of the separate standard deviations. The more stable of the two dimensional fits (R_T-R_L) shows no change in the parameter values. The R_T-R_L-τ fit parameters exhibit the largest discrepancy. We expect R_T and τ to be highly correlated (Sec. 5.1). Therefore it is not too surprising that an increase in one is accompanied by a decrease in the other. Our estimates of systematic error are intended for the two-dimensional fits, in which case the variation in these fit parameters is within the 10% estimate for systematic errors.

PID Scheme	$\lambda_{R-\tau}$	R	τ	$\lambda_{R_T-R_L}$	R_T	R_L
TOFID	0.49±0.02	2.35±0.10	2.79±0.19	0.49±0.02	3.15±0.10	2.32±0.12
PICD	0.50±0.02	2.18±0.11	3.19±0.19	0.49±0.02	3.13±0.11	2.32±0.12

PID Scheme	λ	R_L	R_{Tside}	R_{Tout}
TOFID	0.52±0.01	2.55±0.11	2.86±0.15	3.86±0.10
PICD	0.50±0.03	2.62±0.14	2.31±0.25	4.07±0.14

PID Scheme	λ	R_T	R_L	τ
TOFID	0.47±0.02	2.68±0.11	2.05±0.16	2.92±0.10
PICD	0.47±0.01	2.28±0.10	2.01±0.14	3.45±0.11

Table D.1: Fit parameters TOFID and PICD particle identification schemes.

Appendix E

RQMD Default Switch Settings

Switch	Value	Meaning
1	NA	*Unused*
2	NA	*Unused*
3	F	Use clock time for random number seed.
4	F	Pauli-blocking of collisions is performed
5	NA	*Unused*
6	T	Mean field is turned off.
7	NA	*Unused.*
8	T	Collisions between two nucleons in the same nucleus not permitted if neither has previously suffered a collision.
9	F	Many particles (Δ, ρ, η) are allowed to decay.
10	F	Pauli-blocking not enabled for resonance decay products.
11	F	No Pauli-blocking when building the nucleus.
12	F	Normal (T disables collisions to study mean field).
13	T	Ropes enabled.
14	F	Turns off phase space output on logical unit 7.
15	F	Normal (T performs Fritiof simulation)
16	F	All unstable non-strange hadrons decayed at end of event.
17	F	Participant and Spectator zones kept separate, but spectator zone heated by participants.
18	F	Particle/Jet system decay.
19	F	Normal (T disables transverse motion).
20	F	Elastic collisions not written to logical unit 9.
21	T	T turns off spectator calculations. This default setting is F, but if switch 23 is T (also default) then this becomes T.
22	F	Normal (T overwrites data statements with input file).
23	T	Fast cascade (sets switches 6,8,21 to T).
24	F	Normal (F used for pA with mean field).

Table E.1: RQMD (1.08) Switches.

Bibliography

[A+83] T. Akesson et al. Bose-Einstein correlations in $\alpha\alpha$, pp and $p\bar{p}$ interactions. *Phys. Lett.*, B129:269–272, 1983.

[A+85a] H. Aihara et al. Study of Bose-Einstein correlations in e^+e^- annihilation at 29 GeV. *Phys. Rev.*, D31:996–1003, 1985.

[A+85b] P. Avery et al. Bose-Einstein correlations in e^+e^- annihilations in the Υ region. *Phys. Rev.*, D32:2294–2302, 1985.

[A+86] M. Altoff et al. Bose-Einstein correlations observed in e^+e^- annihilation at a center of mass energy 34 GeV. *Z. Phys.*, C30:355–369, 1986.

[A+87a] T. Akesson et al. Evidence for directional dependence of Bose-Einstein correlations at the cern intersecting storage rings. *Phys. Lett.*, B187:420–424, 1987.

[A+87b] T. Akesson et al. Pion interferometry in jet events at the CERN Intersecting Storage Rings. *Z. Phys.*, C36:517–526, 1987.

[A+89] C. Albajar et al. Bose-Einstein correlations in $\bar{p}p$ interactions at $\sqrt{s}$=0.2 to 0.9 TeV. *Phys. Lett.*, B226:410–416, 1989.

[A+91] P.D. Acton et al. A study of Bose-Einstein correlations in e^+e^- annihilation at LEP. *Phys. Lett.*, B267:143–153, 1991.

[A+92a] T. Abbott et al. Bose-Einstein correlations in si+al and si+au collisions at 14.6 A $\cdot$ GeV/c. *Phys. Rev. Lett.*, 69:1030–1033, 1992.

[A+92b] L. Ahrens et al. The operational status of the booster injector for the AGS accelerator complex at BNL. In *XV Int. Conf. on High Energy Accelerators, Hamburg Germany 7/20-24/92*, 1992.

[A+93a] M.R. Adams et al. An investigation of Bose-Einstein correlations in muon-nucleon interactions at 490 GeV. *Phys. Lett.*, B308:418–424, 1993.

[A+93b] Y. Akiba et al. Bose-Einstein correlations in kaons in Si+Au collisions at 14.6 A · GeV/c. *Phys. Rev. Lett.*, 70:1057–1060, 1993.

[Abb90] Anthony S. Abbott. *Search for Intermittency in Central Collisions of ^{16}O+Cu at 14.6 GeV/c*. PhD thesis, University of California, Riverside, 1990.

[AH86] B. Andersson and W. Hoffmann. Bose-Einstein correlations and color strings. *Phys. Lett.*, B169:364–369, 1986.

[B+83a] D. Beavis et al. Pion interferometry analysis for 1.2 GeV/nucleon Ar on KCl. *Phys. Rev.*, C28:2561–2564, 1983.

[B+83b] D. Beavis et al. Pion source parameters in Ar on KCl collisions. *Phys. Rev.*, C27:910–913, 1983.

[B+86] D. Beavis et al. Expanding pion emitting source in Ar on Pb collisions. *Phys. Rev.*, C34:757–760, 1986.

[B+88] R. Bock et al. *Mod. Phys. Lett.*, A3:1745, 1988.

[B+89a] J.L. Baily et al. Bose-Einstein correlations for pions produced in pp collisions at 360 GeV/c. *Z. Phys.*, C43:341–348, 1989.

[B+89b] D. Beavis et al. A calorimeter for reltivistic heavy-ion experiments. *Nucl. Intrum. Methods A*, 281:367–372, 1989.

[B+89c] R. Bock et al. Source parameters deduced from Bose-Einstein correlations of two and three soft pions in symmetric heavy ion interactions at 650 A · MeV/c. *Z. Phys.*, A333:193–202, 1989.

[B+93] H. Bossy et al. Two-pion correlations and multiplicity effects in La on La collisions. *Phys. Rev. C*, 47:1659–1665, 1993.

[Bar86] J. Bartke. Size of the pion emission region in collisions of relativistic nuclei from intensity interferometry. *Phys. Lett.*, B174:32–34, 1986.

[Bay69] G. Baym. *Lectures on Quantum Mechanics*. The Benjamin/Cummings Publishing Company, Menlo Park, Califoria, 1969.

[Ber89] G. Bertsch. Pion interferometry as a probe of the plasma. *Nucl. Phys.*, A498:173c–180c, 1989.

[BG84] W. Busza and A.S. Goldhaber. Nuclear stopping power. *Phys. Lett.*, B139:235–238, 1984.

[Boa90] Jennings Boal, Gelbke. Intensity interferometry in subatomic physics. *Rev. Mod. Phys.*, 62:553–602, 1990.

[Bow88] M.G. Bowler. Extended sources, final state interactions and Bose-Einstein correlations. *Z. Phys.*, C39:81–88, 1988.

[Bow90] M.G. Bowler. Extended sources, final state interactions and Bose-Einstein correlations ii. resonances and multiparticle rescattering. *Z. Phys.*, C46:305–315, 1990.

[Bow91] M.G. Bowler. Bose-Einstein correlations in quark initiated jets. *Particle World*, 2:1–6, 1991.

[Bro74] R. Hanbury Brown. *The Intensity Interferometer*. Taylor and Francis Ltd., London, 1974.

[BT54] R. Hanbury Brown and R.Q. Twiss. A new type of interferometer for use in radio astronomy. *Phil. Mag.*, 45:663–682, 1954.

[BT56] R. Hanbury Brown and R.Q. Twiss. A test of a new type of stellar interferometer on Sirius. *Nature*, 178:1046–1048, 1956.

[BT57] R. Hanbury Brown and R.Q. Twiss. Interferometery of the intensity fluctuations in light i. basic theory: the correlation between photons in coherent beams of radiation. *Proc. R. Soc.*, A242:300–324, 1957.

[Bus94] Wit Busza, 1994. Public Communication.

[C+88] A.D. Chacon et al. Observation of a nonspherical pion source in relativistic heavy-ion collisions. *Phys. Rev. Lett.*, 60:780–783, 1988.

[C+92] W.B. Christie et al. Pion correlations in 1.8 A GeV Ar on KCl and La and 1.2 A GeV Xe on La. *Phys. Rev.*, C45:2836–2853, 1992.

[C+93] W.B. Christie et al. Pion correlations for 1.2 A GeV Lanthanum on Lanthanum. *Phys. Rev.*, C47:779–787, 1993.

[CC99] S. Steadman C. Chasman, H. Hamagaki. Studies of particle production at high baryon density using the au beam. Technical report, Brookhaven National Laboratory, 199? Proposal submitted to the AGS Program Committee.

[Cia93] V. Cianciolo. Pass3: How it worked. Technical report, Brookhaven National Laboratory, 1993. Internal Memo to the E859 Collaboration.

[Cia94] V. Cianciolo. *$2K^+$ Correlation Measurement.* PhD thesis, Massachusetts Institute of Technology, 1994.

[CL91] V. Cianciolo and R.J. Ledoux. The joys of triggering or ... how i learned to stop worrying and love pcos. Technical report, Brookhaven National Laboratory, 1991. Internal Memo #1 to the E859 Collaboration.

[Col92] Brian A. Cole. *Particle Production at High Transverse Momentum in Nucleus-Nucleus Collisions at the AGS.* PhD thesis, Massachusetts Institute of Technology, 1992.

[CSed] V. Cianciolo and R. Soltz. Vince and Ron's excellent HBT Memo. Technical report, Brookhaven National Laboratory, to be completed. Internal Memo to the E859 Collaboration.

[D+82] M. Deutschmann et al. A study of second-order interference for pions produced in various hadronic interactions. *Nucl. Phys.*, B204:333–345, 1982.

[Dav65] A.S. Davydov. *Quantum Mechanics.* Pergamon Press, London, 1965.

[DW87] R. Debbe and H. Wegner. New henry higgens field maps. Technical report, Brookhaven National Laboratory, 1987. Internal Memo #7 to the E802 Collaboration.

[ESO94] A. Oskarsson E. Stenlund, H. Gustafsson and I. Otterlund, editors. *Quark Matter '93*, volume A566 of *Nuclear Physics*, Amsterdam, June 20–24 1994. North-Holland. Proceedings of the Tenth International Converence on Ultra-RElativistic Nucleus-Nucleus Collisions, Bolänge, Sweden, June-20–24.

[F+78] S.Y. Fung et al. Observation of pion interferometry in relativistic nuclear collisions. *Phys. Rev. Lett.*, 41:1592–1594, 1978.

[FSf79] Frodesen, Skjeggestad, and Tøfte. *Probability and Statistics in Particle Physics*. Universitetsforlaget, Bergen, Norway, 1979.

[G+59] G. Goldhaber et al. Pion-pion correlations in antoproton annihilation events. *Phys. Rev. Lett.*, 3:181–183, 1959.

[G+60] G. Goldhaber et al. Influence of Bose-Einstein statisitics on the antiproton-proton annihilation process. *Phys. Rev.*, 120:300–312, 1960.

[Gam28] G. Gamow. *Zur Quantentheorie des Atomkernes*. *Z. Phys.*, 51:327, 1928.

[GK81] M. Gyulassy and S.K. Kauffmann. Coulomb effects in relativistic nuclear collisions. *Nucl. Phys.*, A362:503–533, 1981.

[GKW79] M. Gyulassy, S.K. Kauffmann, and L.W. Wilson. Pion interferometry of nuclear collisions I. Theory. *Phys. Rev.*, C20:2267–2292, 1979.

[Gol82] G. Goldhaber. Multipion correlations in e^+e^- annihilation at SPEAR. In J. Dias de Deus and J. Soffer, editors, *Proc. Int. Conf. High Energy Physics*. European Physical Society, 1982.

[GR93] H. Gutbrod and J. Rafelski, editors. *Particle Production in Highly Excited Matter*. Plenum Press, New York, 1993. Proceedings of a NATO Advanced Study Institute on Particle Production in Highly Excited Matter, July 12–24, 1992, Il Ciocco, Italy.

[Gri71] Podgoretskiĭ Grishin, Kopylov. Interference of identical particles in processes involving excited nuclei and resonances. *Sov. Journal of Nucl. Phys.*, 13:638, 1971.

[Gro90] Particle Data Group. Particle properties booklet. *Phys. Lett.*, B239, 1990.

[Gyu82] M. Gyulassy. Dynamics versus symmetrization in hadron interferometry. *Phys. Rev. Lett.*, 48:454–457, 1982.

[HS98] O. Hansen and S.Nagamiya. Studies of particle production at extreme baryon densities in nuclear collisions at the AGS. Technical report, Brookhaven National Laboratory, 198? Proposal submitted to the AGS Program Committee.

[HT93] S. Hayashi and Y. Tanaka. Pid859 user's manual. Technical report, Brookhaven National Laboratory, 1993. Internal Memo to the E859 Collaboration.

[Hua90] H. Z. Huang. *Semi-inclusive and Inclusive Spectra of Charged Pions, Kaons and Protons from Proton-Nucleus and Silicon-Nucleus Collisions at AGS Energy.* PhD thesis, Massachusetts Institute of Technology, 1990.

[Hum94] T.J. Humanic. Identified partilce interferometry in heavy-ion collisions: results from the CERN Na44 experiment. *Nucl. Phys.*, A566:115c–122c, 1994.

[J+89] I. Juricic et al. Bose-Einstein correlations in e^+e^- collisions. *Phys. Rev.*, D39:1–20, 1989.

[JCS86] R.V. Gaviai J. Cleymans and E. Suhonen. *Phys. Rep.*, 130:217, 1986.

[Kah93] S. Kahana. Physics at the AGS with a Relativistic Cascade. In G.S.F. Stephans, S.G. Steadman, and W.L. Kehoe, editors, *Heavy Ion Physics at the AGS*, pages 263–282, Cambridge, MA, January 1993.

[Koo77] S. Koonin. Proton pictures of high-energy nuclear collisions. *Phys. Lett. B*, 70:43–47, 1977.

[Kop72] Podgoretskiĭ Kopylov. Correlations of identical particles emitted by highly excited nuclei. *Sov. Journal of Nucl. Phys.*, 15:219, 1972.

[Kop74] G.I. Kopylov. Like particle correlations as a tool to study the multiple production. *Phys. Lett. B*, 50:472–474, 1974.

[KP74a] G. I. Kopylov and M. I. Podgoretskiĭ. Multiple production and interference of particles emitted by moving sources. *Yad. Fiz.*, 18:456–666, 1974.

[KP74b] G.I. Kopylov and M.I. Podgoretskiĭ. Mutual coherence functions of elementary particles and mutiple production. *Yad. Fiz.*, 19:434–446, 1974.

[L+81] J.J. Lu et al. Exploratory studies on relatvistic heavy-ion central collisions. *Phys. Rev. Lett.*, 46:898–902, 1981.

[LeC89] LeCroy Corporation. *ECLine Programmable Logic Data Handler Modules*, 1989.

[Lor89] B. Lorstad. Boson interferometry: A review of high energy data and its interpretation. *Int. J. Mod. Phys.*, A4:2861–2896, 1989.

[LR88] W.A. Zajc L.P. Remsberg, R.J. Ledoux. Studies of high-density baryon matter from extended measurements of particle momentum distributions and from high-precision two-particle correlations. Technical report, Brookhaven National Laboratory, 1988. Proposal submitted to the AGS Program Committee.

[M+84] C. De Marzo et al. Measurement of the average transverse momentum and of the pion-emission volume in proton-nucleus and antiproton-nulceus reactions at 200 GeV. *Phys. Rev.* , D29:363–367, 1984.

[Mor90] Richard J. Morse. *Bose-Einstein Correlation Measurements in 14.6* A · GeV/c *Nulceus-Nucleus Collisions*. PhD thesis, Massachusetts Institute of Technology, 1990.

[Mor92] R. Morse. Impact parameter dependence of Bose-Einstein correlations at 200 GeV/nucleon. Technical report, Lawrence Berkeley Laboratory, 1992. Internal Report, Nuclear Science Division.

[Mor94] Dave Morrison. *Kaon Production in 14.6* A · GeV/c *Nucleus-Nucleus Collisions*. PhD thesis, Massachusetts Institute of Technology, 1994.

[Mül85] B. Müller. *The Physics of the Quark-Gluon Plasma*. Springer Verlag, Heidelberg, Germany, 1985. and references therein.

[Osb88] L.S. Osborne. Measureing the shape of an excited hadron by use of the Bose-Einstein effect. *Phys. Rev. Lett.* , 60:987–990, 1988.

[P+94] T. Peitzmann et al. Effective source sizes of low rapidity soft particle emission. *Nucl. Phys.* , A566:519c–522c, 1994.

[Par93] C.G. Parsons. Stopping and Fermi/Bose Effects in 14.6 A · GeV/cNucleus-Nucleus Collisions. In G.S.F. Stephans, S.G. Steadman, and W.L. Kehoe, editors, *Heavy Ion Physics at the AGS*, pages 72–88, Cambridge, MA, January 1993.

[PB75] M.A. Preston and R.K. Bhaduri. *Structure of the Nucleus*. Addison-Wesley, Massachusetts, 1975.

[PGG90] S. Padula, M. Gyulassy, and S. Gavin. Pion interferometric tests of transport models. *Nucl. Phys.*, B329:357–375, 1990.

[Pra84] S. Pratt. Pion interferometry for exploding sources. *Phys. Rev. Lett.*, 53:1219–1221, 1984.

[Pra86] S. Pratt. Pion interferometry of quark-gluon plasma. *Phys. Rev.*, D33:1314–1327, 1986.

[Pra93] S. Pratt. Pion lasers from heavy ion collisions. In G.S.F. Stephans, S.G. Steadman, and W.L. Kehoe, editors, *Heavy Ion Physics at the AGS*, pages 390–396, Cambridge, MA, January 1993.

[Pra94] S. Pratt. Testing transport theories with correlation measurements. *Nucl. Phys.*, A566:103c–114c, 1994.

[R+94] G. Roland et al. Rapidity and Transverse Momentum Dependence of the two-π^- Correlation Function in 200 GeV/Nucleon S+Nucleus Collisions. *Nucl. Phys.*, A566:527c–530c, 1994.

[Rat94] Kevin Rathbun. Electron production in heavy ion collisions. Master's thesis, Massachusetts Institute of Technology, 1994.

[Ree94] K. Reece, 1994. Private Communication.

[Rot94] P. J. Rothschild. *Rapidity Dependence of Anti-Proton Production in Relativistic Heavy Ion Collisions at 14.6A GeV/c.* PhD thesis, Massachusetts Institute of Technology, 1994.

[S+86] T. Sugikate et al. 100 cm. ong time of flight scintillation counters with rms resolution of 50 ps. *Nucl. Instr. and Meth.*, A249:354–360, 1986.

[S+93] J. Sullivan et al. Bose-Einstein correlations of pion pairs and kaon pairs from Relativistic Quantum Molecular Dynamics. *Phys. Rev. Lett.*, 70:3000–3003, 1993.

[S+94] J.P. Sullivan et al. Calculations of Bose-Einstein Correlations from Relativistic Quantum Molecular Dynamics. *Nucl. Phys.*, A566:531c–534c, 1994.

[Sak92a] H. Sakurai. A New Tracking Code for E859 (TRCK3). Technical report, Brookhaven National Laboratory, 1992. Internal Memo #6 to the E859 Collaboration.

[Sak92b] H. Sakurai. *Study of Anti-Proton Production in* ^{28}Si + *A Collisions at 14.6* A · GeV/c. PhD thesis, University of Tokyo, 1992.

[Sar89] M. Sarabura. *Cluster Production in Relativistic Heavy-ion Collisions*. PhD thesis, Massachusetts Institute of Technology, 1989.

[Sau77] F. Sauli. Principles of operation of multiwire proportional and drift chambers. Technical report, CERN, 1977. Report 77-09.

[Sol91] R. Soltz. Exercising the track-finding trigger. Technical report, Brookhaven National Laboratory, 1991. Internal Memo #4 to the E859 Collaboration.

[Sol93] R. Soltz. Pass3 timing calibration: Strategic design and implementation. Technical report, Brookhaven National Laboratory, 1993. Internal Memo to the E859 Collaboration.

[Sor93] H. Sorge. Energy Dependence of Strangeness Production in Untrarelativistic pA and AA Collisions. In G.S.F. Stephans, S.G. Steadman, and W.L. Kehoe, editors, *Heavy Ion Physics at the AGS*, pages 283–303, Cambridge, MA, January 1993.

[Sun94] T. Sung. *Kaon Production in Relativistic Heavy-ion Collisions at 14.6 GeV/c per Nucleon*. PhD thesis, Massachusetts Institute of Technology, 1994.

[Suz87] M. Suzuki. Boson-einstein correlation and two-body final-state interaction of dipion. *Phys. Rev.* , D35:3359–3367, 1987.

[T$^+$88] P. Thieberger et al. Tandem injected relativistic heavy ion facility at brookhaven, preset and future. *Nucl. Instr. and Meth.* , A268:513–521, 1988.

[Tan85] I. Tanihata. Interaction cross sections and the radii of He isotopes. Technical Report 85-10, GSI, Darmstadt, October 1985. in Proc. 7'th High energy heavy ion Study.

[V$^+$94] O. Vossnack et al. Kaon correlation systematics in e859. *Nucl. Phys.* , A566:535c–538c, 1994.

[Vos94] O. Vossnack. *2K Correlations*. PhD thesis, Columbia University, 1994.

[Vut88] V. Vutsadakis. Description of the magnetic field of henry higgens. Technical report, Brookhaven National Laboratory, 1988. Internal Memo #19 to the E802 Collaboration.

[Vut92] V. Vutsadakis. *Small Relative Momentum Proton Correlations in Relativistic Heavy Ion Collisions*. PhD thesis, Massachusetts Institute of Technology, 1992.

[Wan94] Y. Wang. *Phi Production in Heavy Ion Collisions*. PhD thesis, Columbia University, 1994.

[X+94] Nu Xu et al. Pion interferometery in ^{28}Si+pb central collisions. *Nucl. Phys.*, A566:585c–588c, 1994.

[YK78] F. Yano and S. Koonin. Determining pion source parameters in relativistic heavy ino collisions. *Phys. Lett. B*, 78:556–559, 1978.

[Z+84] W.A. Zajc et al. Two-pion correlations in heavy ion collisions. *Phys. Rev. C*, 29:2173–2187, 1984.

[Zaj78] W.A. Zajc. Monte Carlo methods for the generation of events with Bose-Einstein correlations. *Phys. Rev.*, 35:3396–3408, 1878.

[Zaj82] W.A. Zajc. *Two-Pion Correlations in Heavy Ion Collisions*. PhD thesis, University of California, Berkeley, 1982.

[Zaj88] W.A. Zajc. Bose-Einstein correlations: From statistics to dynamics. In P. Carruthers, editor, *Hadronic Multiparticle Production*. World Scientific Press, 1988.

[Zaj91] W.A. Zajc. Extracting physics from the two-particle correlations. In M. Plümer, S. Raha, and R.M. Wiener, editors, *Correlations and Multiparticle Production*, Singapoor, 1991. World Scientific Press.

[Zaj92] W.A. Zajc. Overview of the E859 Level II Trigger. In W.T.H. Van Oers, editor, *Proceedings of the Fourth Conference on the Intersections between Particle and Nuclear Physics, Tucson Arizona, 24 May 1991*, New York, 1992. AIP.

[Zaj93] W.A. Zajc. A pedestrian's guide to interferometry. In Johann Rafelski Hans H. Gutbrod, editor, *Particle Production in Highly Excited Matter*, pages 435–459. Plenum Press, 1993. Proceeding of the NATO Advanced Study Institue on Particle Production in Highly Excited Matter, July 12–24, 1993, Il Ciocco, Tuscany, Italy.

Acknowledgements

It seems only fitting to begin by acknowledging the hard work and dedication of the MIT students in the heavy ion group who built the first Brookhaven experiment E802: Matt Bloomer, Huan Huang, Vasilios Vutsadakis, Martin Sarabura, Jim Costales, Chuck Parsons, Richard Morse, and Brian Cole. I owe a particular debt to Richard, who performed the first analysis of two-pion correlations for Si beams at the AGS. If Vince and I have contributed something unique to this field, it is because of the great strides Richard had made working by himself. Chuck has also had a great influence on our (Dave, Vince and myself) thinking. However, I fear that our combined abilities are not a match for Chuck's creative approach to solving problems; but then again, we also have never fused together the elements of a stove while making beer. Brian has given a great deal of his time and energy to the second generation experiment (E859) and the second generation students (us), at a time when his own interests would have been better served by hiding away and writing his thesis. Incidentally, Brian also brews beer.

Life for all the MIT students (past and present) would have been harder if not for the efforts of Dave Woodruff and Marge Neal. Overworked and underpaid Dave kept the computers up and running (most of the time) and Marge taught us how to string a wire chamber and provided companionship while we paid our daily dues in the detector lab. Then there is the person who is noticed the most when he *doesn't* do his job. Mr. Da Silva kept our floors vacuumed, and our trash cans clean. When he was gone for a week I learned what a bunch of pigs we truly are. I will miss his midnight companionship, despite his politically incorrect habit of throwing out the paper we had carefully placed in the recycling bin. During my stay in the heavy ion group, we went through a number of secretaries. None of them were quite like Barb. Barb is a person who's taste for the bizarre exceeds even my own. I owe her many thanks for the transparencies she has made for me, and hope she one can forgive my reluctance to use my thesis defense as an occasion to reveal to the audience a little-known tryst between Nixon and Elvis.

I am also grateful for the support we had at Brookhaven: Kenny Asselta and Henry Diaz were always willing, if not exactly eager, to help students scrounge for electronics, and Harvey Wegner never tired of teaching yet another graduate student how to wind cable. I would also like to thank Dana Beavis for his unique definition of an experimental physicist, "one who carries a pocket knife."

Then there are those physicists, not of the experimental sort, who go above and beyond the call of duty to share their expertise with the MIT graduate students. Heinze Sorge, who will never need a microphone, answered many questions on what goes on in a mysterious jumble of Fortran

statements known as RQMD. Scott Pratt, who has contributed much to the field (Sec. 2.1), never lost his patience explaining and re-explaining things to me and Vince. I regret that I did not have time to make proper use of his procedure to study two-pion correlations in the models.[1]

It is not possible to fully acknowledge help of the theoretical kind without also mentioning the help I've had from two newer members of the heavy ion group, Larry Ahle and Mark Baker. Larry, a younger graduate student, has provided key mathematical insights on a number of occasions. Mark is a convert (prisoner?) from high energy physics, has enriched the group with his perspective. I have enjoyed the many conversations we've had on the topic of Bose-Einstein correlations in jets.

Also, I wish to thank my thesis committee, Xiandong Ji and Wit Busza, for willingness to work with my last-minute approach to defending and finishing my thesis. Xiandong was very receptive to questions, and once gave me the benefit of a 5-minute derivation of second quantization. I appreciate the time that Wit spent reviewing and commenting on my introduction and review sections.

Working alongside Vince, Dave and myself were Ted Sung, Pete Rothschild, and Dan Zachary, who joined the group at a time when we were desperately in need of manpower. Ted jumped in to help work on the trigger monitoring, and Pete's contribution can be summed up in eight short words: he wrote the code that found the tracks. All three were the students of Steve Steadman, who helped me get the two-pion Au+Au request from the conference table to the experimental floor. There are also some new members of the heavy ion group who will have new challenges to overcome in the upcoming experiment, Craig Ogilvie, Eleanor Judd, and George Heintzelmann.

There are our colleagues from Livermore who added (and will add) to the fun of working on the experiment. Jim Thomas, Neil Namboodiri, John Luke, Shaheen Tonse, and Craig Sangster are best characterized as a rowdy bunch up to no good. I would also like to thank Jim Costales for leading the guys at Livermore to believe that all MIT grad. students are that good.

If there is one element of experiment E859 which can be said to embody its essence, it is the second level trigger; and the driving force behind the trigger was the combined talents of the E859 spokesman: Bob Ledoux, Bill Zajc, and Lou Remsberg. What is most remarkable about these men is that in addition to providing the necessary leadership, they viewed their primary task as the training young scientists. And this they did. Bob has greatly enriched my scientific vocabulary. There are many English words that one does not ordinarily associate with the scientific process which are in fact technical terms. Bill was also aware of this fact. In addition to his many contributions to our understanding of two-particle interferometry, Bill has also provided me with valuable career

[1] Sorry Scott.

advice at every juncture, always recommending that I choose whatever option puts the most distance between the two of us. Lou is perhaps best described by the following incident which replayed itself many times over: Vince, Dave, Ole and myself would work through the night trying to solve a certain problem with the trigger. Together we would come up with a solution only to find in the morning that Lou was able to reach the same conclusion in 5 minutes of casual thought during his daily commute!

And of course, working on the trigger would not have been nearly so much fun with anyone other than Vince Cianciolo, Dave Morrison, and Ole Vossnack. It is rare to find group of people who enjoy each others company so much both at and away from the lab. Ole, with his taste for the finer things in life, ordered 10 lbs of Pete's coffee for one run, and set up a miniature home entertainment center, including CD player and self-powered speakers, in the counting house. We have all appreciated his razor sharp wit, which is equally at home whether analyzing physics or poking fun. Working with Dave has been very *valuable*. I also *value* his friendship a great deal. It is *invaluable* to me. I have also benefited from his computer futzing, and learned from him that two particles are not necessarily more fun than one particle. Vince, my office-mate, has also been a very good teacher — I have learned more from him than from anyone else on the experiment — and a close friend. He also brews beer, as does Dave.

It is not possible for me to utter the words "enjoy Brookhaven" without thinking of Walter Kehoe. He taught us the importance of finding time to be civilized, and that there are places on Long Island where one can do this. No kidding. I also wish to thank Walter's wife, Nina, and their cat, Leila, for their hospitality. A relaxing dinner at Walter and Nina's place often did wonders to lift my moral during those times when I was beginning to believe that I would never actually finish. I am equally grateful for the hospitality and frienship of Maureen and Kunya. I also have my cousins, David and Tamar, to thank for giving me what I needed most during my final days of writing: a working fridge which I could freely use without fear of being verbally assaulted by an unstable roommate, and a place to crash at whatever odd hours my schedule happened to dictate. For the record, David also brews beer, but in a way that rivals some of the local micro-breweries. Look for the "Lazybones" label at your local liquor store.

Last among the professional acknowledgments is the debt I owe to my advisor, George Stephans. Research Scientist to the MIT physics community, to me he will always be Physics Analysis Guru, and friend. When everything else in my life was telling me to graduate and move on, George provided the additional kick that helped get me out the door. I would also like to thank both George

and Julie for the number of times that George came in on the weekends to pick up and read through the latest thesis copy.

Of all the personal sacrifices made to complete this thesis, none was greater than that of Susan, my wife. After waiting for one and a half years we are finally able to share the life we have chosen. A life that will include many simple things which we have both missed terribly, walks on the beach together, dinner and a movie, fighting over who gets the channel flipper. And now that I may have some free time on my hands, I too can brew some beer!

Rhapsody in Pions

A jazz compilation

1) New York Blues – Recorded at Nevis Studios
Featuring Shoji "Big Idea" Nagamiya on bongos
and Susan "Ever Patient" Huang on train whistle

2) LVL2 in Green (from the Kind of a Zoo disk)
Featuring John Coltrane on ADI
Bill Evans on ROF ROF
Dave "Cal Man" Morrison on INTER
and Lou "Big Trig" Remsberg on diagrams

3) Four Bit, Six Bit – Recorded at The Chill Room
Featuring Ole "Dutch" Vossnack on crimper
Vince "Big Boots" Cianciolo on air vent
and Leroy "Blue Box" LeCroy on CAMAC

4) Ron Runs the Beam Rate Down (off the Data Brew disk)
Featuring Miles Davis on ZCAL
Dave Holland on Spill Clock
and Chick Corea with Jim Cumming on electronics

5) Crossing TOF Zones (a special arrangement by Jim O'Dell)
With Shige "Three Sig" Hayashi on PID
and a satire duet by Akbar and Jeff

6) Count Your Background (off the Plus B album)
Featuring Sonny Rollins on Poisson
Clifford Brown on chi square
and Bill "Mr C2" Zajc on toy box

7) Somerville Baritone – Recorded at Studio 402
Featuring the quartet:
P. Soltz on dynamics
h. Soltz on correlations
D. Soltz on thesis
and, finally, R.A. "Doc Ron" Soltz back on sax!

Colophon

This thesis was typeset in 11pt New Century Schoolbook using the computer typesetting program LaTeX. While most of this thesis was written in person, the final edits and revisions were handled by the proofreading division of Stephans, Cianciolo & Morrison, Inc. of Cambridge, Massachusetts.